Development of a Liquid Xenon Time Projection Chamber for the XENON Dark Matter Search

Kaixuan Ni

Submitted in partial fulfillment of the
requirements for the degree
of Doctor of Philosophy
in the Graduate School of Arts and Sciences

COLUMBIA UNIVERSITY
2006

Development of a Liquid Xenon Time Projection Chamber for the XENON Dark Matter Search

Kaixuan Ni

Advisor: Professor Elena Aprile

Submitted in partial fulfillment of the
requirements for the degree
of Doctor of Philosophy
in the Graduate School of Arts and Sciences

COLUMBIA UNIVERSITY
2006

ABSTRACT

Development of a Liquid Xenon Time Projection Chamber for the XENON Dark Matter Search

Kaixuan Ni

This thesis describes the research conducted for the XENON dark matter direct detection experiment. The tiny energy and small cross-section, from the interaction of dark matter particle on the target, requires a low threshold and sufficient background rejection capability of the detector. The XENON experiment uses dual phase technology to detect scintillation and ionization simultaneously from an event in liquid xenon (LXe). The distinct ratio, between scintillation and ionization, for nuclear recoil and electron recoil events provides excellent background rejection potential. The XENON detector is designed to have 3D position sensitivity down to mm scale, which provides additional event information for background rejection.

Started in 2002, the XENON project made steady progress in the R&D phase during the past few years. Those include developing sensitive photon detectors in LXe, improving the energy resolution and LXe purity for detecting very low energy events. Two major quantities related to the dark matter detection, the scintillation efficiency and ionization yield of nuclear recoils in LXe, have been established. A prototype dual phase detector (XENON3) has been built and tested extensively in above ground laboratory. The 3D position sensitivity, as well as the background discrimination potential demonstrated from the XENON3 prototype, allows the construction of a 10 kg scale detector (XENON10), to be deployed underground in early 2006. With 99.5% electron recoil rejection efficiency and 16 keVr nuclear recoil energy threshold, XENON10 will be able to probe the WIMP-nucleon cross-section down to 2×10^{-44} cm^2 in the supersymmetry parameter space, after one month operation in the Gran Sasso underground laboratory.

Contents

1 Introduction 1

1.1 Introduction 1

1.2 The missing mass and modern cosmology 3

1.2.1 Galaxy rotational curves and dark matter 3

1.2.2 CMB, supernovae and galaxy clusters 4

1.2.3 Distribution of dark matter 9

1.3 Dark matter candidates and alternatives 10

1.3.1 Axion 11

1.3.2 Neutralino 12

1.3.3 Kaluza-Klein dark matter 13

1.3.4 MOND 13

1.4 Dark matter searches 14

1.4.1 Direct detection 14

1.4.2 Indirect detection 15

1.4.3 Search for WIMPs at accelerators 19

2 Direct detection of dark matter 20

2.1 Dark matter and supersymmetry 20

2.2 WIMP signals in a detector 21
    2.2.1 Velocity distribution 24
    2.2.2 Nuclear form factor 26
    2.2.3 Spin dependence 27
    2.2.4 WIMP event rate 31
    2.2.5 Annual modulation and directionality 31
2.3 Dark matter direct detection experiments 36
    2.3.1 NaI/CsI scintillator detectors 37
    2.3.2 Cryogenic detectors 39
    2.3.3 Cryogenic noble liquid detectors 44
    2.3.4 Other technologies 49
2.4 Low background requirements 52

3 Liquid xenon for particle detection 54

3.1 Physical properties of xenon 55
3.2 Ionization properties 58
    3.2.1 Particle interaction in xenon 58
    3.2.2 Ionization yield and its measurement 61
    3.2.3 Electron drift velocity and attachment 63
3.3 Scintillation properties 68
    3.3.1 Scintillation mechanism in liquid xenon 68
    3.3.2 Scintillation yield and its measurement 69
    3.3.3 Relation between ionization and scintillation 72
3.4 Proportional scintillation (electroluminescence) 73

4 Development of liquid xenon detectors 75

4.1 Proportional light in a dual phase chamber 76
  4.1.1 Single and dual phase operation 79
  4.1.2 Electron extraction and proportional scintillation . . . 81
  4.1.3 Ratio between proportional and direct light 86
4.2 Ionization for low energy γ rays 90
4.3 A continuous xenon purification system 100
4.4 Scintillation spectroscopy in liquid xenon 104
  4.4.1 Detector description and calibration 107
  4.4.2 Simulation of light collection efficiency 109
  4.4.3 Scintillation yield and energy resolution 112
  4.4.4 Field dependence of light yield 116
4.5 Novel UV photon detectors 123
  4.5.1 Silicon photo-multiplier (SiPM) 123
  4.5.2 Large area avalanche photodiode (LAAPD) 128
  4.5.3 CsI photocathode 141
4.6 Correlation between ionization and scintillation 147
  4.6.1 Field dependence of charge and light yield 151
  4.6.2 Anti-correlation of scintillation and ionization 154
  4.6.3 Energy resolution 160

5 Development for a sensitive dark matter search 163

5.1 Nuclear recoil scintillation efficiency in LXe 165
  5.1.1 Neutron scattering in LXe 165
  5.1.2 Scintillation efficiency and field dependence 168
  5.1.3 Lindhard and biexcitonic collision 173

5.2 Nuclear recoil ionization yield in LXe 177
  5.2.1 XeBaby: a small dual phase chamber 177
  5.2.2 Energy and field dependence 180
  5.2.3 Background discrimination 189
5.3 XENON3: a 3D sensitive XeTPC 192
  5.3.1 XY position sensitivity 195
  5.3.2 Energy calibration and position dependence 209
  5.3.3 Nuclear recoil ionization yield 216
  5.3.4 Background discrimination with position cut 221

6 The XENON10 Experiment 223

6.1 Detector design and operation 224
6.2 Light detection simulations 227
  6.2.1 Direct light detection 227
  6.2.2 Proportional light detection 232
  6.2.3 Expected XY position sensitivity 233
  6.2.4 Electron recoil rejection efficiency 238
6.3 Background consideration and sensitivity 239
  6.3.1 Gamma ray background 242
  6.3.2 Neutron background 245
  6.3.3 Projected sensitivity 247

List of Figures

1.1 Rotational curve of the spiral galaxy NGC 6503 (Begeman *et al.*, 1991). 5

1.2 Cosmological parameter space from high-redshift supernovae survey, galaxy cluster observation and cosmic microwave background measurement. 8

2.1 A schematic of WIMP elastic scattering off a target nucleus in a terrestrial detector. 22

2.2 Spin-independent nuclear form factor 27

2.3 Spin-dependent nuclear form factor 28

2.4 Calculated WIMP SI interaction (100 GeV and $\sigma_p = 5 \times 10^{-7}$ pb) differential event rate (solid lines) and total event rate (dashed lines) for recoil energy above a given threshold in keV for different target materials. 32

2.5 Calculated WIMP SD interaction rate for 100 GeV WIMP mass and $\sigma_p = 5 \times 10^{-2}$ pb (Na-23) or $\sigma_n = 5 \times 10^{-2}$ pb (Xe-129 and Si-29). Differential event rates are in solid lines and total event rates are in dashed lines, for recoil energy above a given threshold in keV on different target materials. 33

2.6 Expected WIMP annual modulation signals. 35
2.7 PSD by using time constants for γ (full line) and n (dashed line) events from NaI scintillation light. Figure from (Smith *et al.*, 1996) 38
2.8 DAMA annual modulation signal from a model independent fit to cosine function, showing a period of oscillation of 1.00 ± 0.01 year and offset t_0 at 140 ± 22 day. 40
2.9 Ionization yield versus recoil energy from CDMS ZIP detectors. Figure from (CDMS Collaboration, 2004) 43
2.10 Experimental results of spin-independent WIMP searches compared with theoretical SUSY predictions. Figure plotted from http://dmtools.brown.edu. 45
2.11 Design concept of the XENON dual phase LXeTPC with 3D position sensitivity for a WIMP dark matter search. 49
2.12 Illustration of possible signals from the LXeTPC and the difference between nuclear recoil and electron recoil events. . . . 50

3.1 Gamma ray interaction cross-section and mean free path ($\rho_{\mathrm{lxe}} = 2.98\mathrm{g/cm}^3$) in liquid xenon. Figure from (Ozone, 2005). 60
3.2 A simplified schematics of detection of ionization electrons by using charge pulse mode. 64
3.3 Electron drift velocity in liquid and solid xenon. Figure from (Miller *et al.*, 1968). 65
3.4 Electron diffusion coefficient in LAr and LXe as a function of density-normalized electric field. Figure from (Doke, 1982). . . 66

3.5 Electron attachment rate constant as a function of field for some impurity molecules in liquid xenon. Figure from (Bakale *et al.*, 1976). 67

3.6 Field dependence of scintillation (open symbols) and ionization (solid symbols) for 1 MeV conversion electrons in liquid xenon and liquid argon. Figure from (Doke *et al.*, 2002). . . . 73

4.1 Photo of the inner structure of the dual phase chamber. From the bottom are: cathode disk, grid and anode meshes. The Hamamatsu R6041 PMT is mounted above the anode mesh. . 77

4.2 A typical waveform directly from the PMT showing both direct light and proportional light generated by a gamma ray event from ^{207}Bi. 79

4.3 ^{207}Bi energy spectrum from direct scintillation light in LXe at zero electric field 80

4.4 Charge waveform triggered by the direct scintillation light of γ rays in LXe. 82

4.5 Charge amplitude as a function of drift time for ^{207}Bi radiation in LXe. 83

4.6 Electron extraction yield as a function of electric field in the gas phase. 84

4.7 Proportional light yield over gas pressure as a function of reduced field (field/pressure). 85

4.8 Energy spectra from proportional light in dual phase operation (top) and from ionization electrons in single-phase operation (bottom). 87

4.9 Grayscale image of the event density as a function of proportional and direct light yields. Events for a ^{207}Bi source at 1 kV/cm drift field in the liquid and 4 kV/cm in the gas phase. 88
4.10 Test pulse distribution for different input amplitudes. The input amplitudes, measured from the pulse height of an average of 1000 traces on scope, are shown on the top of each plot. . . 93
4.11 ADC amplitude versus input test pulse amplitude. A linear fit determines the ADC offset (-0.13 mV) and gain (59.2). . . . 94
4.12 Bi-207 spectrum from the Si detector. Each peak was fit by a Gaussian function. The energy of each peak is shown on the top of each plot. 95
4.13 Electron life time in liquid xenon at 1 kV/cm. An exponential fit of the 662 keV peak amplitude as a function of event drift time, was used to find the electron lifetime. 96
4.14 Charge spectrum of ^{137}Cs at 1 kV/cm. The 662 keV peak produces an average of 27,800 electrons, before the electron lifetime correction. 97
4.15 Charge spectrum of ^{57}Co at 1 kV/cm (top). The 122 keV peak produces an average of 4770 electrons, before the electron lifetime correction. Events for the charge distribution were selected within one sigma of the 122 keV peak from the light spectrum. 98
4.16 Charge spectrum of ^{22}Na at 1 kV/cm. The 511 keV and 1.274 MeV peaks produce an average of 20,300 and 57,200 electrons separately, before the electron lifetime correction. 99

4.17 A schematics of the xenon recirculation and purification system. 101

4.18 A picture showing working procedure of the purification system and detector. The arrows indicate the gas flow directions. 102

4.19 Charge collection for ionization of 662 keV γ rays in liquid xenon at different fields, before and after the recirculation (left). Electron lifetime in liquid xenon during recirculation (right). 103

4.20 The chamber innner structure for simultaneous scintillation and ionization detection (see text for illustration). 105

4.21 The detector schematics for simultaneous scintillation and ionization detection, and measurement of nuclear recoil scintillation efficiency in LXe (see text for illustration). 106

4.22 A typical event with signals from two PMTs and charge readout. Note that the sampling rate for the PMTs and charge waveforms are different. 108

4.23 Single photoelectron spectrum from Hamamatsu R9288 PMT operated at 900 V. 110

4.24 Distribution of total light collection efficiency for simulated events uniformly distributed in the LXe sensitive volume. . . 112

4.25 Dependence of light collection efficiency with event location in Z from simulation. 113

4.26 ^{57}Co scintillation light spectrum at zero field. A Gaussian fitting of the 122 keV peak shows a light yield about 6 pe/keV. 114

4.27 ^{22}Na scintillation light spectrum at zero field. 114

4.28 ^{137}Cs scintillation light spectrum at zero field. 115

4.29 LET dependence of scintillation light yield in liquid xenon for different energy γ rays (open squares from (Yamashita *et al.*, 2004) and solid squares from this paper), electrons and relativistic heavy ions (open circles from (Doke *et al.*, 2002)). . 117
4.30 ^{137}Cs scintillation light spectrum at 4 kV/cm electric field. The light yield is about 33% of that at zero field. The energy resolution of the 662 keV γ ray peak is at 9.0% (σ/E). 118
4.31 Scintillation light yield as a function of field for Co-57 and Cs-137. The light yield is normalized to that at zero field. . . 120
4.32 Energy resolution dependence on the γ ray energy. The solid symbols are the total energy resolution, while the open symbols represent the intrinsic energy resolution of liquid xenon scintillation light. The squares are measured in this work, and the circle points are from (Yamashita *et al.*, 2004). 122
4.33 The schematics of the detector for the SiPM test. 124
4.34 Amplitude distribution for ^{241}Am particle scintillations. Low amplitude part of the spectra. 126
4.35 Mean amplitude after pedestal subtraction versus peak number. Fit - linear function. The MCA offset from the channel number of zero photoelectron peaks in Figure 4.34 is subtracted.126
4.36 Amplitude distribution for ^{241}Am particle scintillations. Fit - Gaussian function. 127
4.37 Photograph of the assembled gridded ionization chamber electrodes, with the LAAPD mounted 6 mm above the anode grid. 130

4.38 DAQ schematics for the LAAPD setup for scintillation and ionization detection in liquid xenon. 131
4.39 LAAPD gain as a function of bias voltage measured at liquid xenon (-95°C) and room temperature (20°C). 132
4.40 Scintillation light spectrum from ^{207}Bi at zero electric field measured by LAAPD. 133
4.41 ^{241}Am scintillation light energy spectrum from 5.5 MeV alpha particles detected by the LAAPD in LXe. 135
4.42 Energy resolution as a function of LAAPD gain (thick line with experimental data points). 136
4.43 Field dependence of light yield for ^{241}Am 5.5 MeV alpha particles. 140
4.44 Ionization spectrum from ^{207}Bi radiation in liquid xenon at 1 kV/cm drift field with an LAAPD immersed in the liquid. . . 141
4.45 The picture on the top shows the vacuum cryostat integrated with gas filling line and a cryogenic cooler. The chamber structure and an array of seven PMTs on the top are shown below. 143
4.46 A typical waveform for 122 keV gamma ray from Co-57 showing S1-S4 signals. 144
4.47 S1-S4 signal size distribution for 122 keV gamma ray interaction in the dual phase chamber for a typical run with 3 kV/cm drift field and 8 kV/cm extraction field. 146

4.48 S4 versus S2 distribution (left) from the same data set as above shows that S4 starts to saturate when S2 signal is more than 20,000 photoelectrons. The S4/S2 distribution (right) shows a peak value of S4/S2 at 15.4. 147

4.49 CsI photocathode quantum efficiency in liquid xenon as a function of electric field. NIM94 (Aprile *et al.*, 1994), 3 kg - this measurement (note: 3 kg shall be 1 kg), small - a similar measurement performed as in NIM94 with the CsI photocathode in this dual phase measurement. 148

4.50 Waveforms of scintillation signal (left, sum of two PMTs) and ionization signal (right) of a 662 keV γ-ray event from ^{137}Cs at 1 kV/cm drift field. 150

4.51 Light and charge yields as a function of drift field for 662 keV γ-rays from ^{137}Cs. 152

4.52 Correlation between light yield and charge yield for 662 keV γ rays. 154

4.53 Energy spectra and anti-correlation between scintillation and ionization of ^{137}Cs 662 keV γ-rays signals at 1 kV/cm drift field in liquid xenon. 156

4.54 Energy spectra of ^{22}Na and ^{60}Co γ ray sources at 3 kV/cm, by combining charge and light signals. 161

4.55 Energy dependence of resolution measured from ^{22}Na, ^{137}Cs, and ^{60}Co at 3 kV/cm drift field. 162

5.1 Schematic view of the detector arrangement used to measure scintillation from nuclear recoils in LXe. 166

5.2 ^{57}Co scintillation light spectrum at zero field (solid line). A fit to the 122 keV peak gives a light yield of about 6 photoelectrons/keV, which is very close to the expected value from simulation (dashed line). 168

5.3 The measured LXe scintillation spectra (filled squares) for the 10.4 keV (left) and 56.5 keV (right) nuclear recoil data. The accidental spectrum is shown with filled circles. In both cases the uncertainties are statistical. 170

5.4 Simulated ToF between LXe and BC501A detectors for a scattering angle of 123 degrees. 172

5.5 Monte Carlo simulations of neutron scattering in the LXe detector for scattering angels of $\theta = 44°$ (left) and $\theta = 123°$ (right). 172

5.6 The LXe scintillation efficiency relative to the zero field, as a function of applied electric field, for 56.5 keV nuclear recoils (squares), 5.5 MeV alpha particles (circles) and 122 keV gamma-rays (triangles). Ionization data for alpha particles is also shown(stars). 174

5.7 Relative scintillation efficiency for nuclear recoils 176

5.8 A simplified schematics of inner structure of XeBaby chamber. 178

5.9 S1 and S2 from two typical nuclear elastic scattering event (left) and gamma ray electron recoil event (right). 179

5.10 A dual phase detector's (XeBaby) response to neutron (top) and gamma sources (bottom). 181

5.11 Energy dependence of nuclear recoil ionization yield at different drift field. 182

5.12 dE/dx for different energy γ rays, alpha particles and nuclear recoils. Data from SRIM (SRIM), ESTAR and ASTAR (NIST STAR). The solid lines are total stopping power. The dashed lines are electronic stopping for Xe recoils and alpha particles, and collisional stopping for electrons. 183

5.13 Ionization yield per keV as a function of recoil energy, fitted by equation 5.7. The errors in the data points are statistical only. 186

5.14 The field dependence nuclear recoil ionization yield parameters $\alpha(\varepsilon)$ and $\beta(\varepsilon)$. 187

5.15 Field dependence of scintillation and ionization yield in liquid xenon for 122 keV γ rays, 5.5 MeV alpha particles and 55 keV Xe nuclear recoils. 188

5.16 Electron recoil rejection efficiency as a function of electron equivalent energy with 80% acceptance window of nuclear recoils, for current detector (red, large square) and an optimized detector (green, small square) with only statistical distribution contributed to the background leakage. 190

5.17 Background rejection efficiency for events at different energy window, by comparing nuclear recoil event (blue, left peak) and electron recoil event (red, right peak). The dashed lines are the 80% acceptance windows of nuclear recoil events. The rejection efficiency values shown in the plots are assuming the leakage only from statistical contributions, according to the fit. 191

5.18 XENON3 inner chamber with 21 PMTs on top and 14 PMTs on bottom. 193

5.19 A simplified diagram of XENON3 DAQ. 194

5.20 Simulation of proportional light from a 100 keV electron recoil event near [-30, 0] mm in XENON3 detector. 196

5.21 Reconstructed positions relative to their actual position at [-30, 0] mm from Center of Gravity (left), Minimum Chisq (center) and Maximum Likelihood (right) methods for 10 keVee electron recoils. 200

5.22 Reconstructed positions relative to their actual position at [-30, 0] mm from Center of Gravity (left), Minimum Chisq (center) and Maximum Likelihood (right) methods for 10 keVr nuclear recoils. 201

5.23 XENON3 detector with 21 PMTs on top and PTFE on bottom. Square rings with 8 x 8 cm^2 openings were used for anode, grid and cathode. 202

5.24 S2 distribution for events at maximum drift time. The 5.3 MeV alpha events give about 100,000 photoelectrons for this run. 204

5.25 The reconstructed X&Y distribution for 5.3 MeV alpha events. 205
5.26 Co-57 positions for the calibration of XENON3 detector. . . . 206
5.27 Reconstructed XY positions for Co-57 at Position 1 (bottom), 2 (middle) and 3 (top), compared with expected positions from simulation. 207
5.28 Reconstructed XY positions (radial and angular distributions) for Co-57 from XENON3 detector with circular rings on top. . 208
5.29 Drift time dependence of S1 and S2 signals from Co-57 at position 1 (see Figure 5.26), with the detector operating at $V_{cathode} = 10kV$ and $V_{anode} = 4kV$. The pressure in the chamber was 2.6 atm and the gas gap is around 3 mm. 212
5.30 Energy spectra of S1 and S2 for Co-57 at 1 kV/cm. 213
5.31 Simulation of S2 light collection efficiency as a function of event radial position (left) and XY position dependency (right) for XENON3 detector. 214
5.32 Radial dependency of S1 and S2 signal for 122 keV γ rays in the XENON3 detector for $35mm < r < 50mm$. 215
5.33 S1 and S2 distributions for *40 keV line* at $r < 40$ mm (two on top) and $35mm < r < 45mm$ (two on bottom). Both S1 and S2 have been corrected for drift time dependency. 217
5.34 Neutron spectrum from Cf-252 source. 218
5.35 XENON3 response to Cf-252 source. 219
5.36 Nuclear recoil ionization yield, combined results from XENON3 and XeBaby detectors. 220

5.37 XENON3 background rejection efficiency with different position cut. 222

6.1 Baseline design of the XENON10 detector. 225
6.2 XENON10 inner detector illustration. 226
6.3 Simulated XENON10 light collection efficiency and its dependence on drift time. 229
6.4 Light collection efficiency for XENON10 after correcting for drift time dependency. 230
6.5 PMT coincidence distribution for 16 keV nuclear recoil events uniformly distributed in the sensitive target. 231
6.6 Low energy nuclear recoil trigger efficiency for XENON10. . . 232
6.7 S2 light collection efficiency for XENON10. Color unit is in %. 233
6.8 $1/\chi^2$ distribution for two simulated events from [0,0] mm (left) and [0,60] mm (right). The reconstructed X&Y positions (+ in the plot) and the χ^2_{min} values are shown on top of the plots. 235
6.9 Expected XY position sensitivity of XENON10 detector for 10 keV nuclear recoil events. The figure above shows the reconstructed event positions (red dots), compared with the original event positions (black dots). The figure below shows the dependence of position resolution (σ) on the event location. The resolution is best at the center (1.4 mm at r = 0), and becomes larger near the edge (2.4 mm at r = 9 cm). 236
6.10 The distribution of minimum chisq from position reconstruction for two-5keV-step nuclear recoil events with two steps separated by ΔL in XY. 237

6.11 Expected S2/S1 distribution for 16 keVr nuclear recoil events (and equivalent electron recoils) in XENON10 detector. 240
6.12 Expected electron recoil rejection efficiency vs. nuclear recoil acceptance at 16 keVr level for XENON10 detector. 241
6.13 Projected spin-independent WIMP sensitivity of XENON10 experiment. Plotted from http://dmtools.brown.edu. 249

List of Tables

3.1 Isotope components in natural xenon 56

3.2 Physical properties of noble elements 57

3.3 Ionization properties of noble gases and liquids 61

3.4 Properties related to scintillation of noble elements 70

4.1 Charge collection for γ ray ionization in liquid xenon 100

4.2 Light yield and energy resolution of γ rays in LXe. 115

4.3 Physical parameters for the light collection simulation. 138

4.4 LAAPD quantum efficiency measured from different sources. . 139

4.5 The meaning and values of symbols for S1–S4. 145

4.6 Resolution, correlation angle and coefficient from 662 keV γ-rays scintillation and ionization in LXe. 158

4.7 Intrinsic correlation coefficient and energy resolutions of scintillation and ionization in LXe. 160

5.1 The relative scintillation efficiency of xenon nuclear recoils in LXe to electron recoils. 171

5.2 Parameters assumed in the simulation of PMT's response to S2 signals. 198

6.1 Assumptions for the simulation of light collection efficiency. . . 228

6.2 Gamma ray background of XENON10 experiment. 245

ACKNOWLEDGMENTS

I would first thank my advisor, Prof. Elena Aprile, for giving me chance of participating in the XENON project. Her knowledge and experience, on liquid rare gas detectors and their applications to different area of physics, has broadened my view for experimental physics. I would also thank her for supporting me in every aspect during my years at Columbia.

I would thank Dr. Karl L. Giboni for giving me first hand experience on operating the detectors from my beginning in the group. I am so thankful for his ability and experience to turn ideas of radiation detector into working reality within a very short time scale, which made possible all the work described in this thesis.

I am very grateful to Dr. Masaki Yamashita, who has brought me tremendous help since he joined the group in 2003. I appreciate him for providing me so many special techniques, such as constructing the detector hardware and developing complex data analysis programs. His hardworking and endless effort to achieve a better detector performance impress me so much and teach me how to be an experimentalist.

My thanks also go to Prof. Richard Gaitskell, Prof. Dan McKinsey, Prof. Tom Shutt, Prof. Uwe Oberlack, Dr. Alexander Bolozdynya, Prof. Jose A. Matias Lopes, Prof. Yeongduk Kim and Prof. Laura Baudis, for their valuable information and suggestions to the XENON project and my work.

I feel so lucky to be working with a group of young and active colleagues, Dr. Alessandro Curioni, Dr. Masanori Kobayashi, Dr. Pawel Majewski, Dr. Richard Hasty, Angel, Dr. Bhartendu Singh, Luiz, Peter, Dr. Peter Shagin, Roman, Aaron, Jesse, David, Dr. Joerg Orboeck, Alfredo, John, Eric, Guillaume and Dr. Celeste Winant. I will never forget about the late nights in the lab and jokes you guys made. Without any of you, my work presented in this thesis will be incomplete.

I am indebted to my parents in China. They set me in a free environment to pursue a career that I think is right and worth to do. This thesis is dedicated to my wife, Xinyan Lu. Thanks for the love and encouragement during the past few years, when we shared the difficult times and happiness. Thanks for supporting me to be a physicist.

To Xinyan

Chapter 1

Introduction

1.1 Introduction

In the last century, intellectual advancement and experimental verification, especially from high energy accelerator experiments, have yielded a standard model of particle physics: there are three families of particles, each family consists of two leptons and two quarks (fermions), and force carrier particles (bosons). Although the model successfully describes the basic elements of our universe, there are still open questions, such as "why are there so many kinds of particles" and "is there a unification of the four forces", which puzzle and intrigue many physicists to pursue the answer.

Similar to the developments in particle physics, technological advancements in recent decades have allowed physicists and astronomers to measure the properties of the universe at the cosmological scale. Recent results from Cosmic Microwave Background (CMB), Large Scale Structure (LSS) and Type Ia supernovae observations have yielded a standard model of cosmology. In this very successful model, the universe consists of about 73% dark energy, about 23% non-baryonic dark matter, and about 4% baryons which constitute the ordinary matter. Answering the questions of "what is dark energy" and "what is dark matter" has become the most challenging task for physicists in the 21 century.

This thesis and underlying experiment were developed in the context of the emerging field of experimental astroparticle physics, which aims at probing the universe at an energy scale much higher than that achievable with existing or near-future human-made accelerators. In particular, the experimental effort of searching for hypothetical dark matter candidates has received the largest attention in recent years. A positive identification of a dark matter particles will provide both strong support of cosmological observations and predictions, and evidence for new physics beyond the standard model of particle physics.

In this section, we will first introduce the problem of the missing mass in the universe and the various evidence from cosmological observations for the existence of a large amount of dark matter in the universe. We then illustrate different theoretical explanations and models used to explain the mysterious dark matter problem, with focus on different particle candidates for dark matter. In the end, we will give a general review of various experimental efforts to search for dark matter with different approaches.

1.2 The missing mass and modern cosmology

1.2.1 Galaxy rotational curves and dark matter

Dark matter was introduced as a term to explain the observed gravitational effect with no associated luminous objects. The non-observable mass was usually accompanied by the inadequate instruments of older times. With the advancement of instrumentations and telescopes, evidence for dark matter was gathered from observations on various astronomical scales (Trimble, 1987). Usually Zwicky is referred to as the first person who proposed the idea of dark matter after he studied the velocity dispersion in galaxy clusters and found that more than 10 times the mass than that in the luminous galaxies themselves was needed to keep them together (Zwicky, 1933) . But in fact, almost a century before his time, in 1844, German astronomer and mathematician Friedrich Wilhelm Bessel had already concluded that there were invisible companions of mass comparable to Sirius and Procyon, by observing the variations and proper motions of these stars That invisible companion was seen as the white dwarf Sirius B later in 1862.

After Zwicky, many studies of galaxy mass as a function of radius showed the mass increasing linearly with radius up to 100 kpc and $10^{12}M_{\odot}$ for spiral and elliptical galaxies (Ostriker, Yahil & Peebles, 1974) and (Einasto, Kraasik & Saar, 1974), indicating that most of the matter in those galaxies were non-luminous. It is worth to mention the impressive historical review by Faber & Gallagher (1979), which gave convincing evidence of the existence of "invisible mass" by studying the mass-to-light ratio for various types of galaxies. Today, the flat rotation curves of spiral galaxies (Sofue *et al.*, 2001) out to large distance from the galaxy center (Fig. 1.1) are always referred to as the most convincing evidence of an extended halo of dark matter. The combined effect from the gas, the galaxy disk and an extended halo gives a very good explanation of the observed velocity distributions at large radii.

According to Newtonian dynamics, the rotational velocity of the galaxy at radius r should follow the equation below, with $M(r) = 4\pi \int \rho(r) r^2 dr$. $\rho(r)$ is the mass density profile. The flat rotational curve at large radius indicates a $M(r) \propto r$, which can only be explained with an extended halo, with $\rho(r) \propto 1/r^2$, beyond the optical disk.

$$v(r) = \sqrt{\frac{GM(r)}{r}} \tag{1.1}$$

1.2.2 CMB, supernovae and galaxy clusters

Dark matter was not only proposed to explain the gravitational effect of the galaxy rotational curves. Dark matter is an essential component of the big bang theory and is necessary to explain various cosmological effects, such as the polarization of cosmic microwave background (CMB) and the structure formation at large scale.

In recent years, cosmology has evolved to become a precise science with the availability of high precision observational data. Those include the observation of type Ia supernovae, cosmic microwave background (CMB) observations, and galaxy surveys. These observations can determine either the matter, the energy density, or both. They can also be used to determine parameters in cosmology models. These observations all point to a so called "standard cosmology model", with the universe made of about 30% of mat-

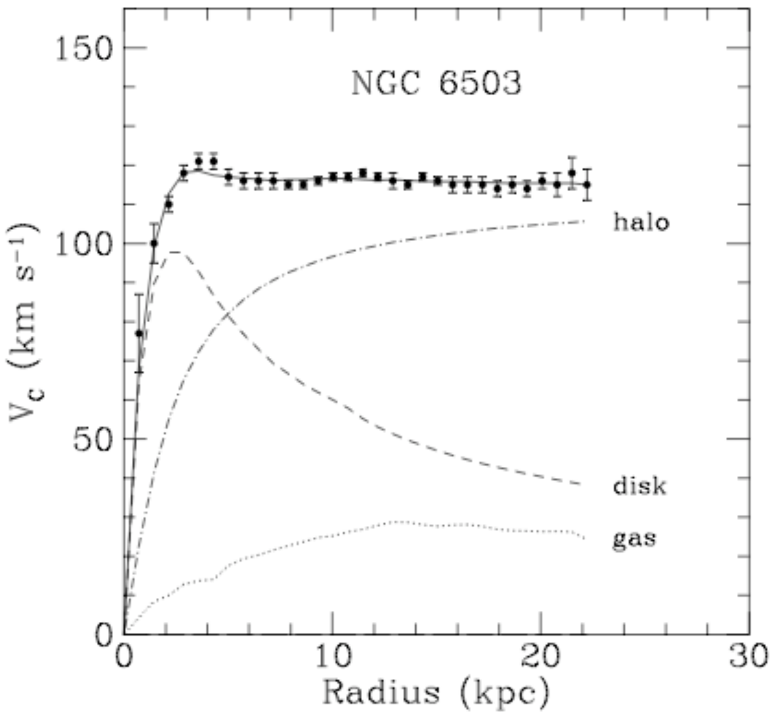

Figure 1.1: Rotational curve of the spiral galaxy NGC 6503 (Begeman *et al.*, 1991).

ter and 70% of energy, and the overall shape of the universe is flat. Other cosmological effects, such as gravitational lensing, can also be used to probe the matter-energy distribution in the universe.

The CMB radiation is left over from the big bang when the universe was cooled. The radiation is highly uniform across the sky. In 1992, NASA's COBE satellite detected tiny fluctuations (also called anisotropy) of the CMB radiation. A similar probe, the Wilkinson Microwave Anisotropy Probe (WMAP), with much higher sensitivity than COBE, reported much more accurate results in 2003 (WMAP Collaboration, 2003). The CMB anisotropy is associated with the fluctuations of matter density in the early universe, thus can be used to study the initial conditions of cosmic structure formation. The WMAP results fit a cosmological model with the matter density of the universe at $\Omega_m h^2 = 0.14 \pm 0.02$ and the baryon density at $\Omega_b h^2 = 0.024 \pm 0.001$, with Hubble constant $h = 0.72 \pm 0.05$ (WMAP Collaboration, 2003). Combined data of WMAP and Cosmic Background Imager (CBI) fit a flat cosmology model ($\Omega_{tot} = 1$) with $\Omega_b h^2 = 0.0233 \pm 0.0013$ and $\Omega_m h^2 = 0.109^{+0.012}_{-0.013}$ (Readhead *et al.*, 2004).

Recent observations and measurements of the distance-redshift relation of Type Ia supernovae brought clear evidence of the acceleration of the expansion of the universe. The acceleration of the universes expansion suggests an unknown type of energy - dark energy. A fit of the Type Ia supernovae observation data suggests a total energy density Ω_Λ around 0.7 and mass density of Ω_m around 0.3 (Schmidt *et al.*, 1998; Perlmutter *et al.*, 1999).

The gravitational instability and small fluctuations of the initial density field of the universe cause the formation of large-scale structure and the galaxy distribution in today's universe. Thus the measurement of the distribution of galaxy clustering at large scales can be used to determine the mass density of universe. This is particularly investigated by the 2dF Galaxy Redshift Survey (2dFGRS), which determines the total matter density times the Hubble parameter $\Omega_m h = 0.20 \pm 0.03$ and the baryon fraction $\Omega_b/\Omega_m = 0.15 \pm 0.07$ (Percival *et al.*, 2001). Combined with the CMB anisotropy measurement, 2dFGRS results favor a low-density universe with $\Omega_m \approx 0.3$ (Peacock *et al.*, 2001).

Combining the high-redshift supernovae survey, galaxy cluster observation and cosmic microwave background measurement, the normalized mass and energy densities Ω_m and Ω_Λ nicely converge in the cosmological parameter space, as shown in Figure 1.2, which indicates a inflationary and flat cosmological model. Figure1.2 is taken from the Supernova Cosmology Project website: http://panisse.lbl.gov/, based on results from (Allen *et al.*, 2002), (Spergel *et al.*, 2003), and (Knop *et al.*, 2003).

As already mentioned, other methods in observational cosmology , such as weak gravitational lensing , also led to the evidence of dark matter's existence. Lensing refers to the bending of the path of light from a distance galaxy as it passes though a gravitational potential. This effect results in distorted images of the background galaxies. By studying the surface brightness of the images of the background galaxies, the gravitational potential, thus the amount of mass in that potential can be inferred. Clowe *et al.* (2004) presented a weak-lensing mass reconstruction of the interacting cluster 1E 0657-558, from which they inferred direct evidence of the existence of dark matter.

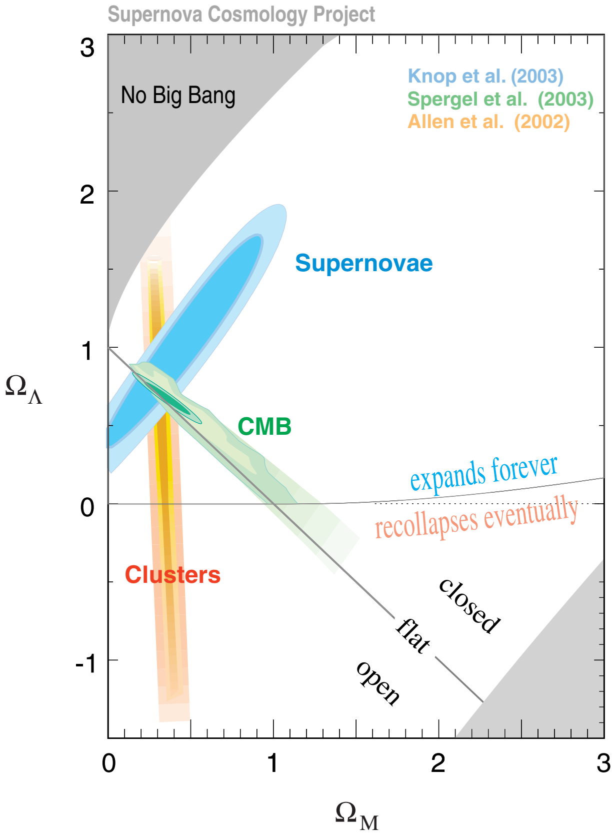

Figure 1.2: Cosmological parameter space from high-redshift supernovae survey, galaxy cluster observation and cosmic microwave background measurement.

1.2.3 Distribution of dark matter

Despite the compelling evidence that a large amount of dark matter exists in the universe, its distribution still needs to be established. The theoretical models have to be compared with the observed large-scale structure to nail down the parameters in the dark matter halo density profile $\rho(r)$.

Dark matter at cosmological scale

Modern advancement in computational speed allows the prediction of structure formation in the universe with high resolution details, utilizing N-body simulations. By specifying the initial density profile of the dark matter, the evolution of structure formation can be predicted with the gravitational potential between the simulated particles. Although different groups obtain different values for the initial mass density profile, it is convenient to write the profile in terms of $\alpha\beta\gamma$-profile (Diemand *et al.*, 2004),

$$\rho(r) = \frac{\rho_s}{(r/r_s)^\gamma[1+(r/r_s)^\alpha]^{(\beta-\gamma)/\alpha}} \tag{1.2}$$

where r_s is the scale radius and $\rho_s = \rho(r_s)$ is the density at this scale radius. With a fixed turnover parameter $\alpha = 1$ and outer slope parameter $\beta = 3$, Diemand *et al.* (2004) found the best-fit values to the data with $\gamma = 1.16 \pm 0.14$.

The current largest N-body simulation by (Springel *et al.*, 2005) tracks the growth of dark matter structure using 2160^3 particles, following them from redshift z = 127 to present, in a cube-shaped region 2230 billion light-years on a side. They show a tight network of cold dark matter clusters with a characteristic size $\sim 100h^{-1}$Mpc. In the scale of $\sim 3.9h^{-1}$Mpc, there are several hundred dark matter sub-structures, which are independent, gravitationally bound objects, orbiting within that scale. A recent simulation by (Diemand *et al.*, 2005) assumes the neutralino as the candidate for dark matter, and finds that numerous Earth-mass like dark matter halos are formed as the first objects in the early universe. These objects are stable against gravitational disruption, even in the center of the Milky Way. They expect that over 10^{15} of these dark matter mini-haloes are in the Galactic halo, with one passing through the Solar System every few thousand years.

The local dark matter density, as well as its velocity distribution, in the region of our solar system is very important in order to precisely calculate the interaction rate for both direct and indirect detection experiments. The local dark matter density is calculated from the distribution of rotation curve in the Milky Way. The best-fit values were obtained to be $\rho_0 = 0.23$ GeV/cm^3 by Caldwell *et al.* (1981) and $\rho_0 = 0.34$ GeV/cm^3 by Bahcall *et al.* (1983). The typical velocity of local dark matter is about 270 km/s (Jungman *et al.*, 1996).

1.3 Dark matter candidates and alternatives

Although there is plenty of convincing evidence that supports the existence of a dark component of mass in the universe, the nature of the dark matter is still a mystery. Proposals of dark matter candidates always involve some new physics and exotic new particles. Among these candidates, the neutralino, introduced by the supersymmetry model, is the most well studied theoretically and pursued experimentally. Axions and Kaluza-Klein particles are also very interesting candidates for dark matter. Although we now know that neutrinos have mass from neutrino oscillation experiments (Super-Kamiokande Collaboration, 1998; SNO Collaboration, 2002), the measured cosmological density of neutrinos is $\Omega_\nu h^2 < 0.0076$ (WMAP Collaboration, 2003), which is too little to account for the dark matter density in the universe. Here we will briefly discuss the major dark matter candidates, namely Axion, Neutralino, and Kaluza-Klein dark matter. We will not discuss other candidates, such as branons, which stem from the brane fluctuations in the context of string theory (Cembranos, Dobado and Maroto, 2003), scalar dark matter from little Higgs theories (Birkedal-Hansen and Wacker, 2004), WIMPzillas etc.. We refer to (Baltz, 2004), which lists most of the candidates covering 90 orders of the mass scale, for more details. In the end of this section, we will also discuss briefly the Modified Newtonian Dynamics (MOND) theory, which tries to resolve the galaxy rotation curve without introducing exotic dark matter particles.

1.3.1 Axion

The axion was proposed as a natural new light pseudo-scalar boson to solve the CP conservation problem of the strong interactions (Peccei & Quinn, 1977; Weinberg, 1978; Wilczek, 1978). CP invariance of strong interactions is violated in the context of quantum chromodynamics (QCD) theory, which is not the case from the experimental point of view. Although particle physics has no preference for the axion mass, laboratory experiments and implications from astrophysical and cosmological effects have excluded most of the mass range and left only two windows, $10^{-6}\mathrm{eV} \lesssim \mathrm{m_a} \lesssim 10^{-3}\mathrm{eV}$ and

$2\mathrm{eV} \lesssim \mathrm{m_a} \lesssim 5\mathrm{eV}$, for further exploration (Turner, 1990). A recent experiment using the Sikivie radio frequency cavity technique to probe the axion mass range of $2.3\mu\mathrm{eV} \leq \mathrm{m_a} \leq 3.4\mu\mathrm{eV}$ has given no positive signal (Asztalos *et al.*, 2002). Recent results from the CERN Axion Solar Telescope implies an upper limit to the axion-photon coupling $g_{a\gamma} < 1.16 \times 10^{-10}$ GeV^{-1} at 95% C.L. for an axion mass of $a_m \leq 0.02$eV (CAST Collaboration, 2005).

1.3.2 Neutralino

Neutralino is currently the best-motivated dark matter candidate in the framework of supersymmetry theory (Jungman *et al.*, 1996). Supersymmetry (SUSY) was proposed as an extension of the particle physics standard model to unify the four fundamental forces of nature (EM, weak, strong and gravitational). Each standard model particle has a superpartner in SUSY, which differs by half a unit of spin. Neutralino is the lightest supersymmetric particle (LSP), which is stable in SUSY models where R parity is conserved. Although particle physics experiments place some constrains on the SUSY parameter space (e.g. the g-2 muon anomalous magnetic moment experiment (Bennett *et al.*, 2002)), a clear signal from a laboratory discovery of a dark matter particle will significantly constrain the mechanisms (Salati, 2003), (Profume *et al.*, 2003), (Catena *et al.*, 2004), the calculation of the relic density and the neutralino candidates in MSSM (Minimal Supersymmetric Model). There remains a large parameter space to be probed by current technologies (Griest & Kamionkowski, 2000). Neutralino is the most popular dark matter candidate that is investigated by on-going direct detection experiments via its elastic scattering off a nucleon of the detector medium (see

Gaitskell (2004) for a recent review). Indirect neutralino searches, via their annihilation products, such as high energy neutrinos, antiprotons, positrons and gamma rays are also well pursued (Pacheco & Peirani, 2005). We will examine the details of these on-going experiments, as well as the possibility of neutralino detection in the accelerator-based experiments in Section 1.4.

1.3.3 Kaluza-Klein dark matter

Kaluza-Klein (KK) dark matter was named after Kaluza and Klein (Kaluza and Klein, 1921 and 1926), who suggested that extra space-time dimensions might exist. If standard model particles propagate in these extra dimensions and KK parity is conserved, the lightest KK particle is stable, becoming an excellent candidate for dark matter (Cheng, Feng, and Matchev, 2002). The mass of the first stable KK particle ranges from several hundred GeV to a few TeV, and can be detected via elastic scattering in the dark matter direct search experiments, or indirectly via annihilation products, such as positrons from the galactic halo, gamma rays from the galactic center, high energy neutrinos from the core of the Sun or the Earth, and antiprotons (Barrau *et al.*, 2005). Recent results from the HESS experiment reported a TeV gamma ray signal from the galactic center, which gives positive support of the KK dark matter with a mass of 1–10 TeV (Bergstrom, 2005).

1.3.4 MOND

The Modified Newtonian Dynamics model (MOND) was first proposed by Milgrom (1983). It assumes no baryonic dark matter, and explains the flat galaxy rotational curves at large radii as due to the modification of Newtonian dynamics at small accelerations. This model works quite well for spiral galaxies (Sanders *et al.*, 2002), but has problems to explain large scale structure formation (Nusser, 2002) and lensing of light. The initially proposed MOND theory is also not consistent with General Relativity, but recent development of relativistic MOND theory seems to agree with large-scale structure formation (Bekenstein, 2004). Measurement of the height of the third acoustic peak from CMB experiments will allow constrains of models without dark matter. Slosar *et al.* (2005) tested the MOND with recent Boomerang data and find that at least some cold dark matter component has to exist and that MOND is rather artificial even in its version capable of explaining the CMB results.

1.4 Dark matter searches

Although the nature of dark matter is still unknown, its existence is supported by many astronomical observations (Section 1.2). As the dark matter interaction cross section with normal matter is very small, at the level of the weak interaction, its mass must be large to account for its gravitational effect. Dark matter is usually referred to as WIMPs (Weakly Interacting Massive Particles).

1.4.1 Direct detection

As our Solar system moves in the galaxy, the earth encounters the dark matter halo with a relative speed. The WIMPs from the halo can make elastic scattering off the target nucleus of a terrestrial detector, and leave a small amount of energy (less than 100 keV) to the recoil nucleus. Successfully detecting this small amount of energy from the recoil nucleus will give a strong support as *direct* detection of WIMPs. The WIMPs may also make inelastic scattering off the target outer electrons, resulting in excitation and/or ionization in the target detector, with subsequent photons emission. The main challenge of the direct detection of WIMPs is the discrimination of a WIMP recoil event from a background event. The background gamma rays and neutrons will make electron and nuclear recoils, with energies similar to those from WIMPs. The direct detection of dark matter is among the most exciting and compelling experimental physics around the world. These experiments require a very low background environment, thus are usually located in deep underground laboratories. This thesis represents one of these direct detection experiments. We will discuss the details of WIMP event rate and background discrimination techniques for different experiments, and their underlying physics in Chapter 2.

1.4.2 Indirect detection

WIMPs can also be detected *indirectly* via their annihilation products in the Galactic halo, the Galactic center, in the core of the Sun and other regions. The detection of the annihilation products, such as gamma rays, neutrinos, positions and anti-protons, etc., from specific directions and locations will provide indirect information on the dark matter energy and distribution.

Gamma ray telescopes

Both space based gamma ray telescopes and ground based atmospheric Cherenkov telescopes can probe the gamma rays from WIMP annihilation (Fornengo *et al.*, 2004). In fact, the Energetic Gamma-Ray Experiment Telescope (EGRET) on the Compton Gamma-Ray Observatory has observed about 60% higher integral intensity for gamma rays above 1 GeV, than a model calculation of the emission based on dynamic balance and realistic interstellar matter and photon distributions from the galactic plane (Hunter *et al.*, 1997). Elsaesser & Mannheim (2005) compared the extragalactic gamma-ray background from EGRET data with high-resolution simulations of cosmic structure formation, and found a best-fit value of neutralino mass around 515 GeV. The next generation space-based gamma ray observatory GLAST (Gamma-Ray Large Area Space Telescope) is planned to be launched in 2007. It will be able to detect gamma rays up to 300 GeV, with a sensitivity 2×10^{-9} photons $\mathrm{cm}^{-2}\mathrm{s}^{-1}$ for gamma rays more than 100 MeV for a 2 year all-sky survey, a factor of 30 better than EGRET (GLAST, 1999).

The ground-based atmospheric Cherenkov telescopes detect the secondary particles originated from the electromagnetic cascade of primary energetic gamma rays, and the Cherenkov light from these secondary particles as they pass through the Earth's atmosphere. These detectors can also be used to detect very high energy cosmic rays, and their capability to distinguish between cosmic rays and gamma rays is required for a sensitive detection of gamma rays from the annihilation of dark matter particles. Complementary to space-based gamma ray telescopes, the ground-based Cherenkov telescopes will able to detect gamma rays in the TeV energy range and will have a much larger effective area.

Following the successful detection of Cherenkov light from gamma-ray emission of the Crab Nebula with the Whipple Observatory (Weekes *et al.*, 1989), many next generation Cherenkov telescopes are under construction, such as the VERITAS (Very Energetic Radiation Imaging Telescope Array System) (Weekes *et al.*, 2002). Some of them are already in operation, yielding interesting results. For example, the first survey from HESS (High Energy Stereoscopic System) finds a population of eight previously unknown sources of very high energy gamma rays (HESS Project, 2005). The HESS detection of a TeV gamma-ray signal from the direction of the galactic center may be explained by the annihilation of Kaluza-Klein dark matter (Bergstrom, 2005).

Neutrino telescopes

Large area neutrino telescopes can probe the high energy neutrino flux from the WIMP annihilation. These experiments use a large number of PMTs to detect Cherenkov light produced by muon tracks, originated from the high energy neutrino fluxes. Due to the large scale of these experiments, they usually need to use naturally existing sources as detection media. One example is the use of the Antarctic ice as a Cherenkov detector (Lowder *et al.*, 1991), like in the AMANDA (Antarctic Muon and Neutrino Detector Array) project, followed by a cubic-kilometer scale project such as IceCube (IceCube). IceCube will be sensitive to cold dark matter particles approaching TeV energy scale. A similar approach by the ANTARES Collaboration (ANTARES) uses a large area water Cherenkov detector in the deep Mediterranean Sea.

Antiproton and antideuteron detectors

WIMP self-annihilation will also produce particles such as positrons, antiprotons, antideuterons, etc.. The measured cosmic antiproton spectrum can provide information on the light neutralino and can be used to put stringent constraints on the supersymmetric configurations (e.g. (Bottino *et al.*, 2005)).

The search for antiprotons (or antideuterons) has been performed by the Balloon-borne Experiment with Superconducting Spectrometer (BESS). Its recent results based on the cosmic-ray antiproton spectrum suggest an unknown source of antiprotons below 1 GeV (Mitchell *et al.*, 2005). Annihilation of the lightest Kaluza-Klein particle (LKP) in the galactic halo may produce an antiproton flux at energies higher than about 10 GeV. The PAMELA satellite and experiments like AMS-02 will be able to access this energy range (Bringmann, 2005).

For the cosmic antideuteron search, BESS found no candidates from their data during four balloon flights from 1997 to 2000, and derived an upper limit of $1.9\times10^{-4}(\mathrm{m}^2\mathrm{s\ sr\ GeV/nucleon})^{-1}$ for the differential flux of cosmic-ray antideuterons, at the 95% confidence level, between 0.17 and 1.15 GeV/nucleon at the top of the atmosphere (Fuke *et al.*, 2005). The next generation antimatter detector GAPS (the General Antiparticle Spectrometer) identifies antimatter through the characteristic X-rays emitted by antimatter when it is captured into the target forming exotic atoms (Hailey *et al.*, 2004). Their recent test of a prototype with an antiproton beam indicated that the X-rays yield is consistent with prior expectations (Hailey *et al.*, 2005) giving sufficient sensitivity of detecting antideuterons.

1.4.3 Search for WIMPs at accelerators

Future high energy accelerators will be able to produce weakly interacting massive particles. WIMPs produced in electron positron colliders, or hadron colliders will escape the detectors without being detected. The ”missing energy”, will be a signature for the WIMPs (Birkedal *et al.*, 2004).

There are also considerations of gravitino as the lightest supersymmetric particle (LSP). The future Large Hadron Collider (LHC) and International Linear Collider (ILC) will be able to produce the next-to-lightest supersymmetric particle (NLSP), most favored being charged sleptons, with a decay time of one year or less. These NLSPs can be trapped in a large-scale detector (kton scale) outside of the collider and be studied from their decay products (Feng & Smith, 2005; Hamaguchi *et al.*, 2004).

Chapter 2

Direct detection of dark matter

In the last two decades, the direct detection of dark matter has become an exciting field in astroparticle physics with several new technologies and proposed experiments. Specifically, many of these efforts are focused on searching for the dark matter particles, namely WIMPs, from the supersymmetry (SUSY) scenario. In this chapter, we will first describe some of the SUSY model predictions for dark matter particles and discuss in detail the various factors and mathematical formulae that govern the signal and detection rate of WIMPs in an earth-based direct detection system. We will then review various technologies that are used in the dark matter direct detection, where we will introduce the XENON dark matter search experiment.

2.1 Dark matter and supersymmetry

Supersymmetry (SUSY) is a hypothetical symmetry in particle physics developed in order to unify the four known fundamental forces in nature. SUSY requires that every fundamental particle in the standard model of particle physics has a superpartner, which differs by half a unit of spin. Leptons and quarks have superpartners called sleptons and squarks. Gauge bosons have their superpartners named gauginos, and the Higgs bosons have higgsinos. The mass scale of these superparticles must be much higher than their corresponding standard model particles, otherwise they would have already been discovered in nature. Thus, SUSY must be broken at some energy scale. In practice, the superparticle masses are governed by a set of parameters describing the SUSY breaking.

The lightest supersymmetric particle (LSP) is particularly interesting, as it must be stable and neutral (without charge) and an excellent candidate for WIMP dark matter if SUSY is true. It is suggested by Goldberg (1983) that the photino $\tilde{\gamma}$, the supersymmetric partner of the photon, is the LSP. Ellis *et al.* (1984) further considered that the LSP may also be two higgsinos ($\tilde{H}_1^0$ and $\tilde{H}_2^0$). In fact, the LSP may be a superposition of the photino $\tilde{\gamma}$, two higgsinos $\tilde{H}_1^0$, $\tilde{H}_2^0$, and the zino $\tilde{Z}$, the supersymmetric partner of Z gauge boson, as in equation 2.1. Such a combination is generically referred to as a neutralino χ.

$$\chi = N_1\tilde{\gamma} + N_2\tilde{Z} + N_3\tilde{H}_1^0 + N_4\tilde{H}_2^0 \tag{2.1}$$

2.2 WIMP signals in a detector

The detectability of WIMP dark matter was first proposed by Goodman & Witten (1985). As discussed in section 1.4, different target materials are used for the direct detection of the WIMPs. The energy spectra, from the WIMP elastic scattering off the target nucleus (Figure 2.1), are exponentially falling with typical average energy of 10-100 keV. To identify a true WIMP signal, we have to compare the expected WIMP event rate with the background subtracted spectra from experiment. We will review the mathematical frameworks of dark matter direct detection experiment in the following section, based on the work by Lewin & Smith (1996).

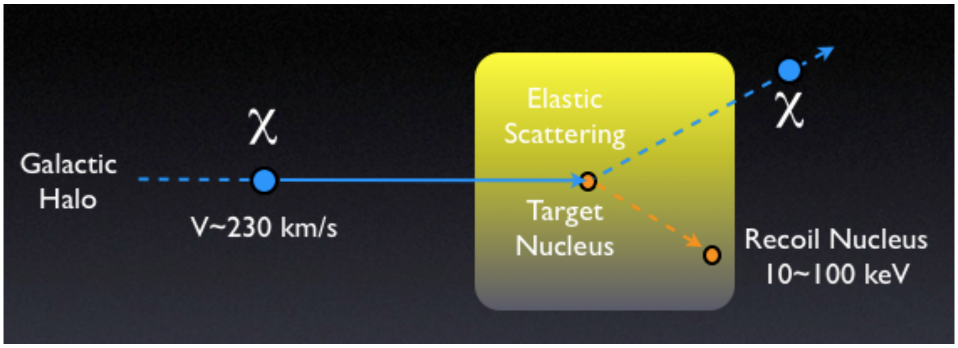

Figure 2.1: A schematic of WIMP elastic scattering off a target nucleus in a terrestrial detector.

With N_A as the Avogadro number (6.02×10^{26} kg^{-1}), cross-section σ, particle velocity v, and particle density n, the event rate per unit mass (kg) on a target of atomic mass number A is

$$dR = \frac{N_A}{A}\sigma v dn \tag{2.2}$$

The total event rate per unit mass is

$$R_0 = \int_{v=0}^{v_{esc}} dR = \int_{v=0}^{v_{esc}} \frac{N_A}{A}\sigma v dn \tag{2.3}$$

v_{esc} is the local Galactic escape velocity, and dn is the differential particle density, which is given by:

$$dn = \frac{n_0}{k} f(\vec{v}, \vec{v}_e) d\vec{v} \tag{2.4}$$

where

$$k = \int_0^{2\pi} d\phi \int_{-1}^{+1} d(\cos\theta) \int_0^{v_{esc}} f(\vec{v}, \vec{v}_e) v^2 dv \tag{2.5}$$

is the normalization constant, such that integrated particle density with speed less than the local Galactic escape velocity v_{esc} is equal to the mean WIMP number density n_0. $n_0 = \rho_\chi / M_\chi$, with ρ_χ and M_χ as the WIMP density and mass. $f(\vec{v}, \vec{v}_e)$ is the dark matter velocity distribution, where $\vec{v}$ is the WIMP velocity and $\vec{v}_e$ is the earth velocity, relative to the dark matter halo. Assuming a Maxwellian dark matter velocity distribution

$$f(\vec{v}, \vec{v}_e) = e^{-(v+v_e)^2/v_0^2} \tag{2.6}$$

with v_0 for the most likely WIMP velocity, we can calculate the total event rate per unit mass, based on equation 2.3-2.6 and assuming $v_e = 0$ and $v_{esc} = \infty$,

$$R_0 = \frac{2}{\pi^{1/2}} \frac{N_A}{A} \frac{\rho_\chi}{M_\chi} \sigma v_0 \tag{2.7}$$

We can normalize R_0 to $\rho_\chi = 0.3$ GeVc^{-2}cm^{-3} and $v_0 = 230$ km/s^{-1} in unit of evts/kg/day.

$$R_0 = \frac{377}{M_\chi M_t} \left(\frac{\sigma_0}{1\text{pb}}\right) \left(\frac{\rho_\chi}{0.3\text{GeVc}^{-2}\text{cm}^{-3}}\right) \left(\frac{v_0}{230\text{kms}^{-1}}\right) \tag{2.8}$$

where M_χ and M_t are in GeVc^{-2}. $M_t = 0.932A$ is the mass of target nucleus (e.g. for natural xenon with atomic mass of 131.29, $M_t = 122.4$GeVc^{-2}).

The typical differential energy spectrum of WIMP nuclear recoils in a direct WIMP search detector is expected to be as follows (for the simplest case that the detector is stationary in the Galaxy),

$$\frac{dR}{dE_R} = \frac{R_0}{E_0 r} e^{-E_R/E_0 r} \tag{2.9}$$

where E_R is the recoil energy, R_0 is the total event rate as discussed above, E_0 is the kinetic energy of the WIMP, and r is a kinematics factor shown in equation (2.10).

$$r = \frac{4M_\chi M_t}{(M_\chi + M_t)^2} \tag{2.10}$$

The expected WIMP energy spectrum can be derived from the right side of equation 2.9. For a realistic WIMP energy spectrum calculation, we need to take into account various corrections, such as the WIMP velocity distribution, nuclear form factor, and quenching factor. In addition, spin-dependent(SD) and spin-independent (SI) WIMP interactions shall be studied separately.

2.2.1 Velocity distribution

Only WIMPs with velocity $v_e < v < v_{esc}$ can be detected by the target on earth. From equation 2.2, 2.4 and 2.7, we derive

$$dR = R_0 \frac{\pi^{1/2}}{2k} \frac{v}{v_0} f(\vec{v}, \vec{v}_e) d\vec{v} \tag{2.11}$$

From equation 2.12 and 2.6, we get:

$$k = k_0 \left[\mathrm{erf}\left(\frac{v_{esc}}{v_0}\right) - \frac{2}{\pi^{1/2}} \frac{v_{esc}}{v_0} e^{-v_{esc}^2/v_0^2} \right] \tag{2.12}$$

where $k_0 = (\pi v_0^2)^{3/2}$ is for k at $v_{esc} = \infty$. We can write the equation 2.11 as:

$$dR = R_0 \frac{k_0}{k} \frac{v}{2\pi v_0^4} f(\vec{v}, \vec{v}_e) d\vec{v} \tag{2.13}$$

Integrating the above equation with different range for v gives:

$$\frac{R(0, v_{esc})}{R_0} = \frac{k_0}{k} \left[1 - \left(1 + \frac{v_{esc}^2}{v_0^2} e^{-v_{esc}^2/v_0^2} \right) \right] \tag{2.14}$$

$$\frac{R(v_e, \infty)}{R_0} = \frac{1}{2} \left[\pi^{1/2} \left(\frac{v_e}{v_0} + \frac{1}{2} \frac{v_0}{v_e} \right) \operatorname{erf} \left(\frac{v_e}{v_0} \right) + e^{-v_e^2/v_0^2} \right] \tag{2.15}$$

$$\frac{R(v_e, v_{esc})}{R_0} = \frac{k_0}{k} \left[\frac{R(v_e, \infty)}{R_0} - \left(\frac{v_{esc}^2}{v_0^2} + \frac{1}{3} \frac{v_e^2}{v_0^2} + 1 \right) e^{-v_{esc}^2/v_0^2} \right] \tag{2.16}$$

The truncated differential event rate can now be written as:

$$\frac{dR}{dE_R} = \int_{E_{min}}^{E_{max}} \frac{1}{Er} dR(E) = \frac{1}{E_0 r} \int_{v_{min}}^{v_{max}} \frac{v_0^2}{v^2} dR(v) \tag{2.17}$$

where $E_0 = \frac{1}{2} M_\chi v_0^2$, thus v_{min} is the minimum dark matter particle velocity corresponding to $E_{min} = E_R/r$, which is the smallest energy to produce a recoil energy of E_R. Combining equation 2.13 gives:

$$\frac{dR(0, v_{esc})}{dE_R} = \frac{k_0}{k} \frac{R_0}{E_0 r} \left(e^{-E_R/E_0 r} - e^{-v_{esc}^2/v_0^2} \right) \tag{2.18}$$

$$\frac{dR(v_e, \infty)}{dE_R} = \frac{R_0}{E_0 r} \frac{\pi^{1/2}}{4} \frac{v_0}{v_e} \left[\operatorname{erf} \left(\frac{v_{min} + v_e}{v_0} \right) - \left(\frac{v_{min} - v_e}{v_0} \right) \right] \tag{2.19}$$

$$\frac{dR(v_e, v_{esc})}{dE_R} = \frac{k_0}{k} \left[\frac{dR(v_e, \infty)}{dE_R} - \frac{R_0}{E_0 r} e^{-v_{esc}^2/v_0^2} \right] \tag{2.20}$$

The above equations can be used to derive the annual modulation in the WIMP event rate, which will be discussed in section 2.2.5. For practical use, the differential energy spectrum can be approximated as:

$$\frac{dR(v_e, \infty)}{dE_R} = c_1 \frac{R_0}{E_0 r} e^{-c_2 E_R/E_0 r} \tag{2.21}$$

where $c1$ and $c2$ are constant, which are related to each other by

$$\frac{c_1}{c_2} = \frac{R(v_e, \infty)}{R_0} \tag{2.22}$$

For most practical use, we can take fixed values c1 = 0.751, and c2 = 0.561. A complete table of $c1$ and $c2$ values in different months of the year can be found in (Lewin & Smith, 1996).

2.2.2 Nuclear form factor

The cross-section σ in equation 2.8 depends on the nuclear form factor $F(q)$ as,

$$\sigma = \sigma_0 F^2(q) \tag{2.23}$$

where σ_0 is the cross-section at zero momentum transfer. The nuclear form factor contains the information pertaining to the drop in the effective cross-section when the momentum transfer $q = (2M_t E_R)^{1/2}$ is large enough that the wavelength h/q is smaller than the nuclear radius. The effect is significant for target media with large atomic mass M_t (such as ^{131}Xe). Thus a clear understanding of $F(q)$ is important to predict the sensitivity of the WIMP detectors. In practice, the form factor is the Fourier transform of the ground state mass density distribution $\rho(r)$.

$$F(q) = \frac{4\pi}{q} \int_0^\infty r \sin{(qr)} \rho(r) dr \tag{2.24}$$

For $\rho(r)$, Lewin & Smith (1996) considered a thin shell model approximating the spin-dependent (SD) case and a solid sphere model for the spin-independent (SI) case, and obtained the results as below,

$$F_{SD}(q) = \sin(qr_e)/qr_e \tag{2.25}$$

$$F_{SI}(q) = 3[\sin(qr_e) - qr_e \cos(qr_e)]/(qr_e)^3 \tag{2.26}$$

where r_e is the effective nuclear radius. If we take the simplest approximation as $r_e \approx 1.0A^{1/3}$fm, the SD and SI nuclear form factors from the above equations are plotted in Figure 2.2 and Figure 2.3 for different target materials. Note that more realistic nuclear form factors are discussed in (Lewin & Smith, 1996) and (Engel, 1991).

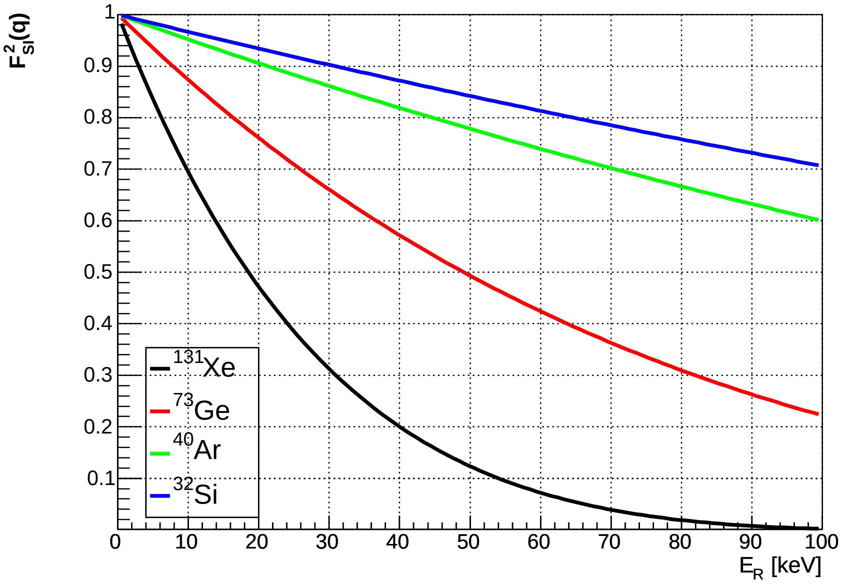

Figure 2.2: Spin-independent nuclear form factor

2.2.3 Spin dependence

The total WIMP-nucleus cross section at zero momentum transfer σ_0 is described as (Jungman *et al.*, 1996)

$$\sigma_0 = 4G_F^2\mu_t^2 C \tag{2.27}$$

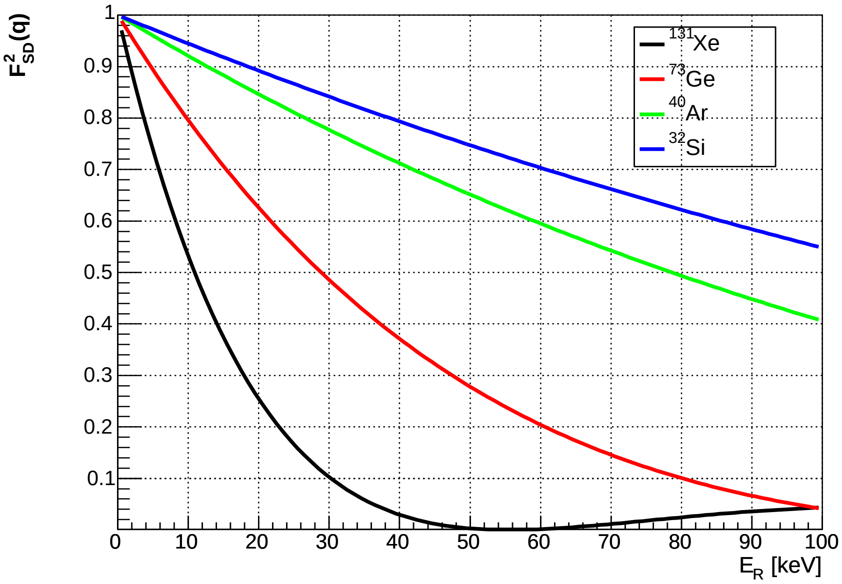

Figure 2.3: Spin-dependent nuclear form factor

where $\mu_t = M_\chi M_t/(M_\chi + M_t)$ is the WIMP-target reduced mass in the center-of-momentum frame. $G_F/(\hbar c)^3 = 1.166\text{GeV}^{-2}$ is the Fermi coupling constant. C is a dimensionless number that carries all the particle-physics model information. In the following, we use C_{SD} and C_{SI} for the two cases of spin-dependent and spin-independent interactions.

In spin-dependent case,

$$C_{SD} = (8/\pi)\Lambda^2 J(J+1) \tag{2.28}$$

where

$$\Lambda = (1/J)[a_p\langle S_p\rangle + a_n\langle S_n\rangle] \tag{2.29}$$

with a_p and a_n the effective WIMP-proton and WIMP-neutron couplings, and $\langle S_p\rangle$ and $\langle S_n\rangle$ the expectation values of the proton and neutron spins in the nucleus. J is the total nuclear spin.

In order to derive experimental limits in a model independent way, one can separate the proton and neutron contributions to C_{SD} as (Tovey *et al.*, 2000),

$$C_{SD}^{p,n} = \frac{8}{\pi}[a_{p,n}\langle S_{p,n}\rangle]^2\frac{J+1}{J} \tag{2.30}$$

Thus the proton and neutron contributions $\sigma_0^{p,n}$ to the total cross section σ_0 are,

$$\sigma_0^{p,n} = 4G_F^2\mu_t^2 C_{SD}^{p,n} \tag{2.31}$$

with $\sigma_0 = (\sqrt{\sigma_0^p} \pm \sqrt{\sigma_0^n})^2$. The WIMP-proton and WIMP-neutron cross section limits $\sigma_{p,n}^{lim}$ that corresponding to WIMP-nucleus cross section limit σ_0^{lim} are,

$$\sigma_{p,n}^{\text{lim}} = \sigma_0^{\text{lim}}\frac{\mu_{p,n}^2}{\mu_t^2}\frac{1}{C_{SD}^{p,n}/C_{p,n}} \tag{2.32}$$

in which, the use of $C_{SD}^{p,n}/C_{p,n} = 4/3\langle S_{p,n}\rangle^2(J+1)/J$ cancels out the WIMP-dependent terms a_p^2 and a_n^2. Table 2.2.3 lists the spin-dependent values of typical nuclei used in the direct dark matter detectors (Tovey *et al.*, 2000).

Nucleus	Z	Odd Nucleon	J	$\langle S_p\rangle$	$\langle S_n\rangle$	C_{SD}^p/C_p	C_{SD}^n/C_n
^{19}F	9	p	1/2	0.441	-0.109	7.78×10^{-1}	4.75×10^{-2}
^{23}Na	11	p	3/2	0.248	0.020	1.37×10^{-1}	8.89×10^{-4}
^{27}Al	13	p	5/2	-0.343	0.030	2.20×10^{-1}	1.68×10^{-3}
^{29}Si	14	n	1/2	-0.002	0.130	1.60×10^{-5}	6.76×10^{-2}
^{35}Cl	17	p	3/2	-0.083	0.004	1.53×10^{-2}	3.56×10^{-5}
^{39}K	19	p	3/2	-0.180	0.050	7.20×10^{-2}	5.56×10^{-3}
^{73}Ge	32	n	9/2	0.030	0.378	1.47×10^{-3}	2.33×10^{-1}
^{93}Nb	41	p	9/2	0.460	0.080	3.45×10^{-1}	1.04×10^{-2}
^{125}Te	52	n	1/2	0.001	0.287	4.00×10^{-6}	3.29×10^{-1}
^{127}I	53	p	5/2	0.309	0.075	1.78×10^{-1}	1.05×10^{-2}
^{129}Xe	54	n	1/2	0.028	0.359	3.14×10^{-3}	5.16×10^{-1}
^{131}Xe	54	n	3/2	-0.009	-0.227	1.80×10^{-4}	1.15×10^{-1}

Table 2.2.3: Values of spin-dependent parameters for various target nuclei.

The spin-independent case is much simpler,

$$C_{SI} = \frac{1}{\pi G_F^2}[Zf_p + (A-Z)f_n]^2 \tag{2.33}$$

where f_p and f_n are effective WIMP-proton and WIMP-neutron couplings. Z and $A-Z$ are numbers of protons and neutrons. In most instances, $f_p \simeq f_n$, then we have,

$$C_{SI} = \frac{1}{\pi G_F^2}(Af_p)^2 \tag{2.34}$$

To compare the cross section limits from experiments with different target nuclei, the WIMP-proton cross section is used. It can be seen that the WIMP-nucleus interaction cross section σ_0 is proportional to the A^2. The WIMP coherent scattering is enhanced for a target with large atomic mass unit.

$$\sigma_p^{\lim} = \sigma_0^{\lim} \frac{\mu_p^2}{\mu_t^2} \frac{C_p}{C_{SI}} = \sigma_0^{\lim} \frac{\mu_p^2}{\mu_t^2} \frac{1}{A^2} \tag{2.35}$$

2.2.4 WIMP event rate

Based on the discussion above, we can calculate the WIMP event rate according to equation 2.8, 2.23 and 2.27. For the spin independent case, we calculated the WIMP event rate as shown in Figure 2.4, for an assumed WIMP mass of 100 GeV and WIMP-nucleon cross-section $\sigma_p = 5 \times 10^{-7}$ pb (5×10^{-43}cm^2). The differential rate unit is dru (evts/keV/kg/day). A detector with Xe as target material would be able to reach a total event rate of about 0.1 event/kg/day for an energy threshold above 15 keVr, the highest among the calculated target materials. The WIMP event rate for the spin-dependent case for target materials containing Xe-129, Na-23 and Si-29 isotopes is shown in Figure 2.5. The WIMP-nucleon cross-section for spin dependent case is chosen here such that it will give a similar total rate (above 15 keV recoil energy) as the spin independent case for a detector with Xe as target.

2.2.5 Annual modulation and directionality

As shown in equation 2.8, the WIMP event rate in an earth-based detector is dependent on the detector's relative velocity to the halo. During the earth's

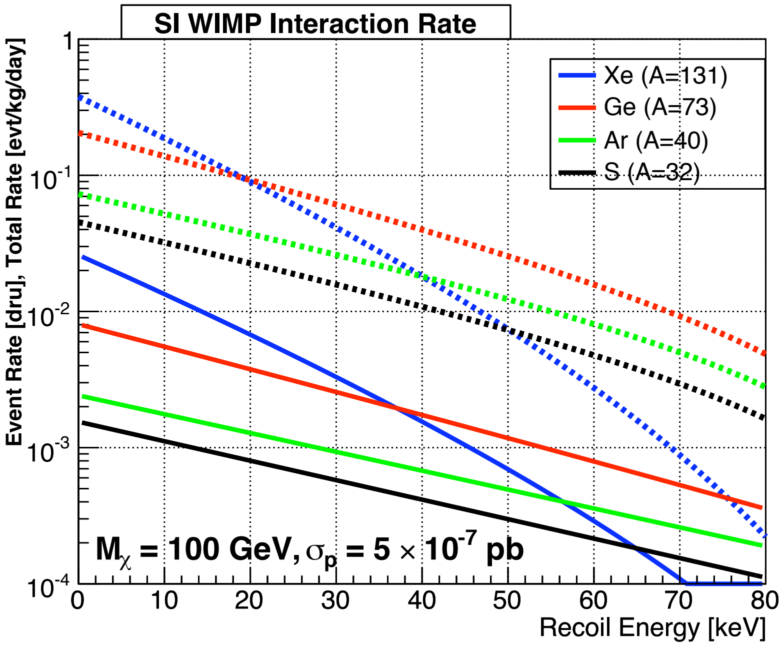

Figure 2.4: Calculated WIMP SI interaction (100 GeV and $\sigma_p = 5 \times 10^{-7}$ pb) differential event rate (solid lines) and total event rate (dashed lines) for recoil energy above a given threshold in keV for different target materials.

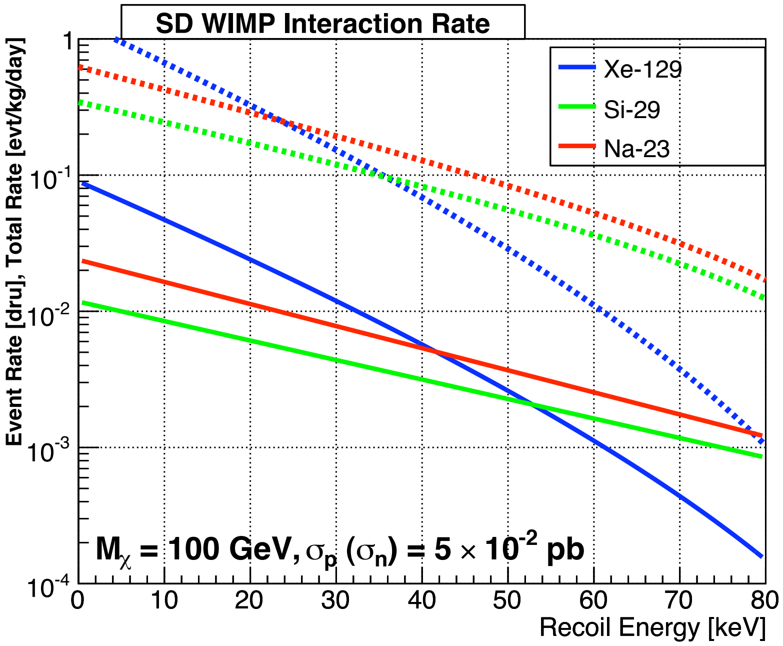

Figure 2.5: Calculated WIMP SD interaction rate for 100 GeV WIMP mass and $\sigma_p = 5 \times 10^{-2}$ pb (Na-23) or $\sigma_n = 5 \times 10^{-2}$ pb (Xe-129 and Si-29). Differential event rates are in solid lines and total event rates are in dashed lines, for recoil energy above a given threshold in keV on different target materials.

annual rotation around the Sun, the detector's relative velocity to the halo changes, which affects the event rate in the detector. This is usually referred as a WIMP annual modulation signal. See (Drukier *et al.*, 1986; Spergel, 1988) for more discussions. The annual modulation of the event rate in the detector will give additional support for WIMP events from the galactic halo, in contrast to the background events originating from earth's environment, which usually have no annual modulation in event rate.

The relative velocity of an earth-based detector to the galactic halo as a function of time in the year, $v(t)$, is shown as in equation 2.36, with $\theta = 62.5^o$ the inclination of the Solar system plane to the direction of Sun's motion. t_0 is the time when the Earth's velocity relative to the halo is the highest (around June 2rd), and ω is the annual rotation velocity of the Earth v_e in the solar system. v_s is the Sun's velocity relative to the Galactic halo. The modulation of the count rate during the year is shown in Figure 2.6 (Drukier *et al.*, 1986). The v_{min} corresponds to the energy threshold of the detector with $E_{th} = \frac{4M_\chi M_T}{(M_\chi + M_T)^2} \cdot \frac{1}{2} M_\chi v_{min}^2$.

$$v(t) = v_s + v_e \cos\theta \cos[\omega(t - t_0)] \tag{2.36}$$

Since the Sun moves in the halo, the rates of forward and backward going recoils relative to the Sun's motion would be different. Some detectors, with the capability of detect the direction (front/back discrimination) of an events, would be thus have additional sensitivity to WIMP events.

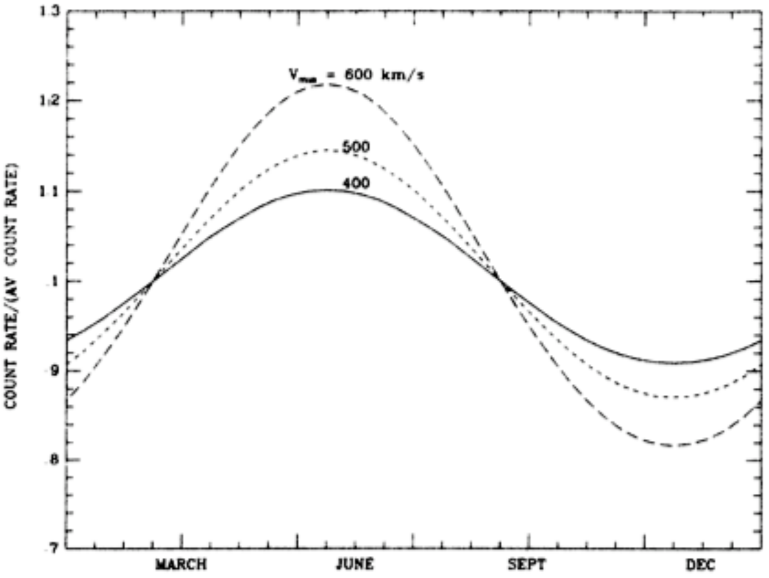

Figure 2.6: Expected WIMP annual modulation signals.

2.3 Dark matter direct detection experiments

The first attempts to detect WIMP dark matter directly began in the 1980's. Early experiments used existing detector technology, primarily high purity Ge and Si ionization detectors. By suppressing the background activities in an underground environment and with shielding, the event rates in those detectors were counted and compared with the estimated background rate.

The experiments in 1990's began to use techniques with the potential to discriminate between nuclear recoils and electron recoils by using some parameters from the detector, such as the pulse-shape discrimination (PSD) applied in experiments using NaI scintillator. The large mass of NaI/CsI scintillator allowed the study of annual modulation signals, but the poor discrimination made it hard to identify true nuclear recoil events from WIMPs. Cryogenic detectors, developed in the late 1990's started to show much better background discrimination and today they still provide the best sensitivity for direct dark matter detection.

Regarding the future dark matter search experiments, the search sensitivity will be determined by the mass and exposure time of the detector system. A ton scale detector seems very necessary to probe the major SUSY parameter space. Although the cryogenic detectors have shown very nice background suppression technology, the deployment and operation of ton scale detectors at such a low temperature seems to be difficult. New technologies, such as cryogenic noble liquid detectors, especially liquid xenon and liquid argon, have the advantage of realizing a large scale detector rather rapidly. These detectors, however, still need to prove their background rejection capabilities.

Some novel technologies, such as gas time projection chamber (TPC) for a directional dark matter search and superheated bubble chambers, are also developed in recent years.

An excellent review of up-to-date technologies and experiments for direct dark matter detection can be found at (Gaitskell, 2004). In the following sections, we will discuss briefly the major experimental results and some recent progress in the field.

2.3.1 NaI/CsI scintillator detectors

Dark matter searches using NaI scintillator have been performed since the mid 1990's and some large scale experiments are still running. The nuclear recoil events can be distinguished from electron recoil events, based on the scintillation light pulse shape (PSD), as shown in Figure 2.7. The experiments based on the PSD could reach sensitivity to nuclear recoils a factor of 10–30 below the gamma background, and some of the results showed better spin-independent WIMP sensitivity than conventional Ge ionization detectors. The NaI scintillator also allows for spin-dependent searches of WIMPs. The final result from the UKDMC (UK Dark Matter Collaboration) NAIAD (NaI Advanced Detector) experiment has set limits on the WIMP-nucleon spin-independent cross sections and also placed the most stringent constraints on the spin-dependent WIMP-proton cross section (UKDMC Collaboration, 2005a). In recent years, similar PSD technique has been used with CsI(Tl) crystal detectors, which showed better PSD performance than NaI scintillator (KIMS Collaboration, 2005).

The increasing amount of mass for the NaI detectors allowed the study of WIMP annual modulation with enough statistics. The DAMA Collaboration

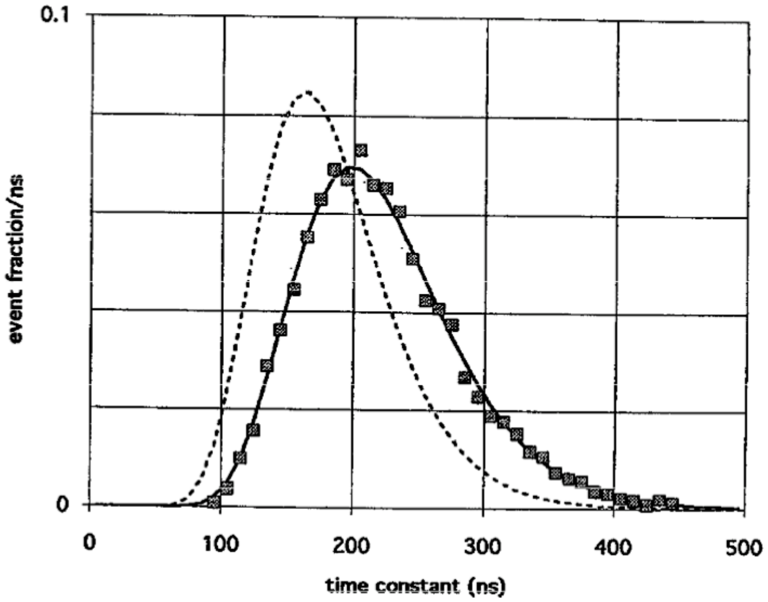

Figure 2.7: PSD by using time constants for γ (full line) and n (dashed line) events from NaI scintillation light. Figure from (Smith *et al.*, 1996)

reported positive annual modulation signals (without PSD discrimination of nuclear and electron recoils) based on 100 kg NaI(T*l*) crystals with an total exposure of 108,000 kg–days for a seven-year period run ended in July 2002 (Bernabei *et al.*, 2003). They showed an annual modulated signal (Figure 2.8) with 6.3σ CL, and claimed a detection of WIMP signal at a WIMP-nucleon cross section at $\sigma_p \approx 10^{-6} \sim 10^{-5}$ pb for a WIMP mass of 60 GeV/C^2 (Bernabei *et al.*, 2000; Belli, 2002). DAMA is currently the only experiment that claims a positive WIMP detection. While many suggestions have been made to resolve the conflict of the DAMA result with other experiments with even better sensitivity to WIMP spin-independent searches, there remains doubt as to whether the annual modulation signal from DAMA experiment might be from some systematic effect in the experiment itself, with an annual cycle rather than a WIMP signal. See chapter 5.1 of (Gaitskell, 2004) for some discussions on this topic.

2.3.2 Cryogenic detectors

Cryogenic detectors operated in sub-Kelvin temperature have achieved to-date the best performance and sensitivity for WIMP dark matter searches. These detectors use two signals, thermal phonons and ionization in the case of cryogenic Ge and Si detectors, and phonons and scintillation in the case of scintillator Ca_2WO_4, measured simultaneously to discriminate between nuclear recoils and electron recoils.

The EDELWEISS Collaboration uses neutron transmutation doped (NTD) Ge heat sensors to read the thermal phonon signal from a recoil event. The phonon signal has no quenching for nuclear recoil events and is used to get

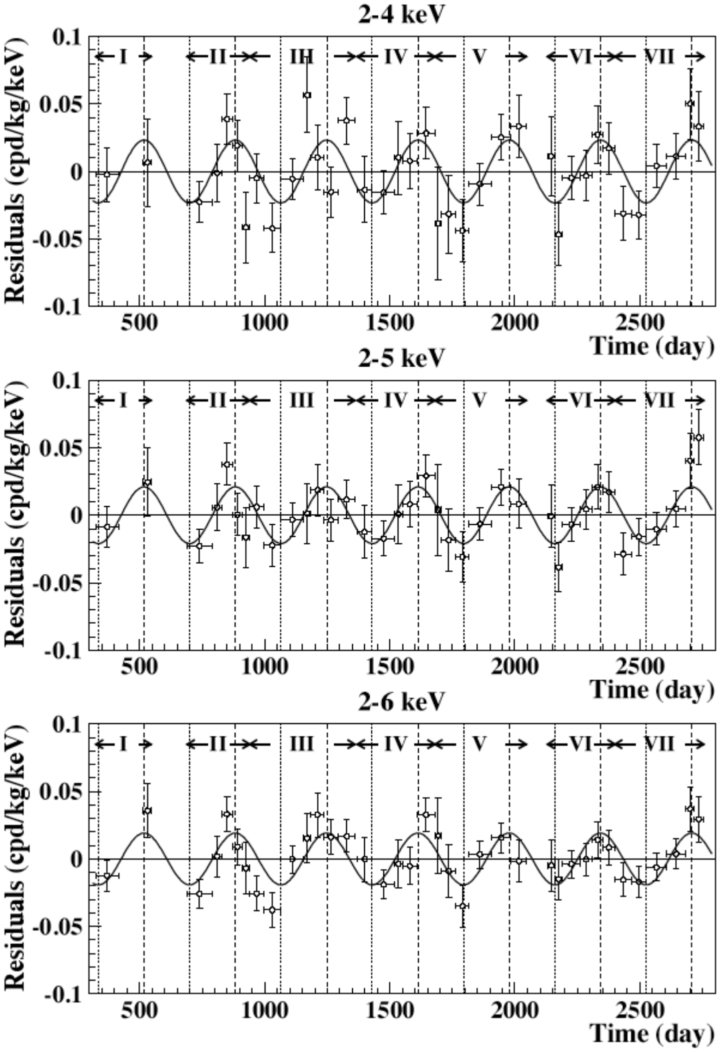

Figure 2.8: DAMA annual modulation signal from a model independent fit to cosine function, showing a period of oscillation of 1.00 ± 0.01 year and offset t_0 at 140 ± 22 day.

the energy of an event. The ionization from nuclear recoils will be reduced by the quenching factor, which allows the separation of the nuclear recoil events from electron recoil events. Since their first result based on a 320 g Heat-and-Ionization Ge detector (EDELWEISS Collaboration, 2001), the EDELWEISS has improved the sensitivity for spin-independent WIMP searches (EDELWEISS Collaboration, 2002), with the final result from three 320 g detectors over four-month of stable operation with total exposure of 62 kg d (EDELWEISS Collaboration, 2005a). The Ge detector used by the EDEWEISS Collaboration contains 7.8% natural ^{73}Ge isotope with high-spin. They have also reported competitive results compared with other spin-dependent WIMP search experiments (EDELWEISS Collaboration, 2005b).

Although EDELWEISS has a long detector exposure, an insufficient background cut due to surface events limited its sensitivity. The similar sensitivity limit was also faced by the first CDMS experiment at Stanford Underground Facility (SUF), which reported its first result in (CDMS Collaboration, 2000). The sensitivity of CDMS SUF was improved by using a combination of Al Schottky contacts on a thin amorphous Si layer (Shutt *et al.*, 2000), with better neutron shielding and increased exposure time. The results from CDMS SUF data from 1998 and 1999 yielded 23 WIMP candidate events, but those events were confirmed to be neutrons from background (CDMS Collaboration, 2002, 2003).

The recent CDMS detectors, which use low-temperature 250 g Ge and 100 g Si ZIP technology, were moved to the Soudan Mine in 2003 for a lower background environment (CDMS II). The first result from the CDMS II experiment shows no nuclear recoil events (Figure 2.9) with 53 live-day exposure (CDMS Collaboration, 2004). The events due to background photons are rejected with 99.99% efficiency. The previous surface events with low ionization yield, which mimicked nuclear recoil events, were rejected with >96% efficiency by using additional rise time information from the phonon pulse shape. The result is the world's lowest limit of spin-independent WIMP interaction, with a minimum WIMP-nucleon elastic scattering cross section at $4 \times 10^{-43}\mathrm{cm}^2$ for a WIMP mass at 60 GeVc^{-2}, and a minimum spin-dependent WIMP-neutron elastic scattering cross section at $2 \times 10^{-37}\mathrm{cm}^2$ for a WIMP mass at 50 GeVc^{-2} (CDMS Collaboration, 2005a). The experiment has been running with two towers, each consisting of six detectors, with total exposures of 34 kg-d for germanium and 12 kg-day for silicon targets after cuts. The latest results have lowered the sensitivity limit for both spin-independent WIMP interaction (CDMS Collaboration, 2005b) and spin-dependent WIMP searches (CDMS Collaboration, 2005c).

The cryogenic detectors, operated by the CRESST Collaboration, use Ca_2WO_4 scintillator to detect the scintillation light from nuclear or electron recoil events. The thermal phonon is detected by using a single-element superconducting phase transition (SPT) thermometer. The phonon gives the energy calibration of the detector. Due to the quenching factor of nuclear recoil scintillation light, the events from background γ rays can be efficiently rejected. Recent CRESST results (CRESST Collaboration, 2005) give a similar WIMP-nucleon spin independent interaction limit to that of the latest EDELWEISS result.

The cryogenic detectors have made great progress in the last few years and their results have placed the world's current lowest exclusion limit for the

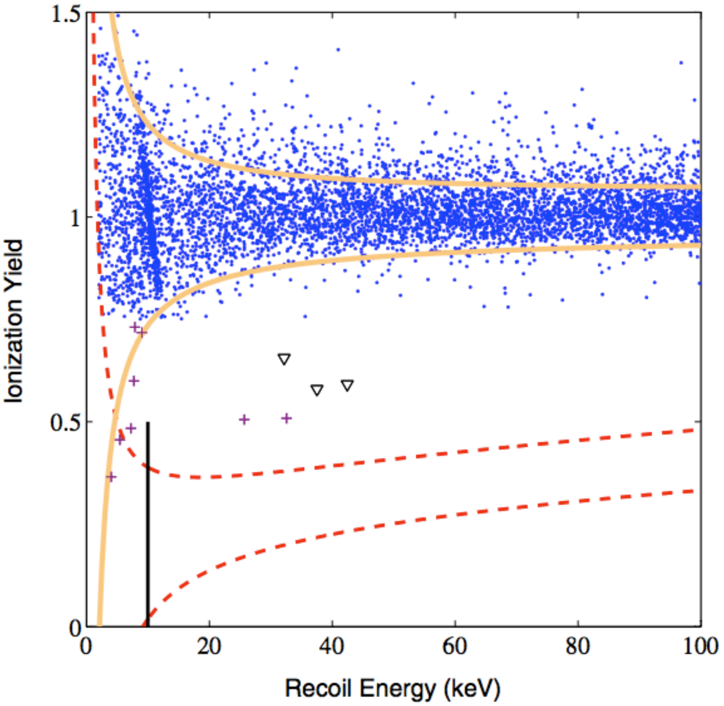

Figure 2.9: Ionization yield versus recoil energy from CDMS ZIP detectors. Figure from (CDMS Collaboration, 2004)

spin-independent WIMP dark matter searches (Figure 2.10). The experimental data from top to bottom are from DAMA (Bernabei *et al.*, 2000), EDELWEISS (EDELWEISS Collaboration, 2005a), ZEPLIN I (UKDMC Collaboration, 2005b) and CDMS (Soudan) (CDMS Collaboration, 2004). The shaded regions are theoretical predictions from (Bottino *et al.*, 2004), (Ellis *et al.*, 2005) and (Baltz & Gondolo, 2003). The cryogenic Ge detectors will face the difficulty and cost of operating at a large mass (ton-scale) detector. In this respect, the cryogenic noble liquid detectors seem more promising, while a clear proof of their potential of background rejection has to be demonstrated.

2.3.3 Cryogenic noble liquid detectors

The liquid noble elements are excellent scintillators, while at the same time a sufficient amount of ionization signals can be collected with an applied electric field. The experiments using the pure scintillation light from liquid noble elements exploit similar pulse shape discrimination (PSD) as the NaI scintillator based experiments, to discriminate between nuclear and electron recoil events. Since this kind of detectors only use one phase (liquid) as the working medium, we refer to them as *single phase detectors.* Due to the different ionizing density of nuclear and electron recoils in liquid noble elements, the background discrimination can be realized by measuring simultaneously the ionization and scintillation signals from the liquid. Usually the ionization produced in this kind of detector is detected via the proportional scintillation produced in the gas phase, thus using both liquid and gas as working medium. We refer to this kind of detector as *dual phase detectors.*

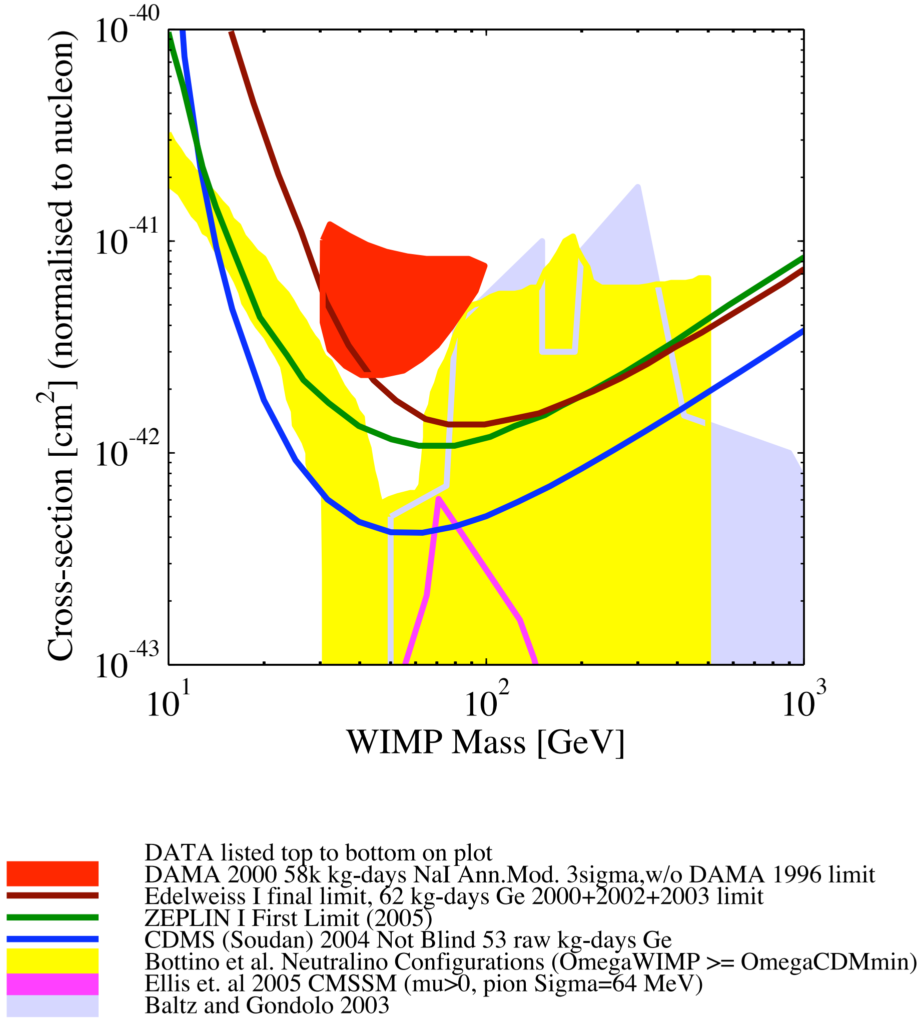

Figure 2.10: Experimental results of spin-independent WIMP searches compared with theoretical SUSY predictions. Figure plotted from http://dmtools.brown.edu.

Single phase detectors

The single phase cryogenic noble liquid detectors use PSD to discriminate between nuclear and electron recoil events. The initial attempt by the DAMA/Xe experiment used Kr-free xenon enriched ^{129}Xe at 99.5%, which also allows the study of spin-dependent WIMP interactions (Bernabei *et al.*, 1998). The weighted mean times $\tau = \sum_i h_i t_i / \sum_i h_i$ (where h_i is the scintillation pulse height at time t_i) were used to define a gamma ray discrimination quality factor as $DQF = (\tau_\gamma - \tau_n)/\tau_\gamma$. The DQF ranges from 7% to 20% for energies of 10–50 keV. Although this result was published in 1998, no significant improvement of this kind of technology was achieved for several years. Recently, the ZEPLIN I experiment published their first result based on the PSD of liquid xenon scintillation light (UKDMC Collaboration, 2005b) with a detector operating at the UK Boulby Mine and for an exposure of 293 kg d. Based on a neutron calibration run, they found a time constant, a value fitted from a scintillation pulse distribution function, to be about 0.5 for nuclear recoils relative to that for electron recoils. events with same electron (or nuclear) equivalent energy. With no significant population of shorter pulses, they derived a 90% CL upper limit of the spin-independent WIMP nucleon cross-section at a minimum of 1.1×10^{-6} pb (1.1×10^{-42}cm^2). The PSD method can also be applied to other noble elements (neon (Boulay *et al.*, 2004) and argon) for detecting WIMP dark matter, such as WARP (WARP Collaboration, 2004), ArDM (Kaufmann, 2006), and CLEAN experiment (McKinsey *et al.*, 2005c). Instead of using PSD for background discrimination, a larger scale liquid xenon detector, such as XMASS single phase (Namba *et al.*, 2004), would also be able to reject background based on a volume cut and selecting events only in the center of the detector. This would allow a sufficient background rejection if the position of the events in the detector is accurately reconstructed.

Dual phase detector

Compared to the single phase cryogenic noble liquid detectors, the dual phase detectors using xenon and argon have been actively studied in recent years. As discussed above, these detectors measure the scintillation and the ionization signals simultaneously from an event. The direct scintillation light is detected by photon detectors, usually photo-multiplier tubes (PMTs) as $S1$ signal. The number of primary ionization electrons, from nuclear recoil events in these liquid noble element, is very small and can't be detected efficiently with charge-sensitive devices. In these experiments, the primary electrons are drifted from the liquid to gas phase with a drift field E_d in the liquid. Once they reach the gas phase, the signal is amplified by means of proportional scintillation (or electroluminescence) by a strong field in the gas phase. The proportional scintillation is also detected by the PMTs as $S2$ signal. The distinct ratio between the scintillation and ionization, $S2/S1$, for nuclear recoil events and electron recoil events provides background rejection for the WIMP dark matter searches. The experiments using this technology include the XMASS dual phase in Japan (Yamashita, 2003a,b), ZEPIN II (UKDMC Collaboration, 2002) and ZEPLIN III (UKDMC Collaboration, 2001) in the United Kingdom, and the XENON experiment (XENON Collaboration, 2002) in the United States. All of these experiments are using dual phase xenon detectors. The same principle is also used in the dual phase argon detector of WARP (WARP Collaboration, 2004; Grandi, 2005) experiment at the Gran Sasso Laboratory in Italy and ArDM experiments.

The XENON experiment was proposed in 2002 using the dual phase time projection chamber (TPC) approach to detect the WIMP dark matter directly by observing their unique recoil signature relative to that from background electrons. The goal of the XENON experiment is to have 1-ton of liquid xenon distributed in ten identical LXeTPCs (Liquid Xenon Time Projection Chambers). Each LXeTPC (see Figure 2.11) contains 100 kg of ultra pure liquid xenon as the target for WIMP interaction, with photon sensors on both top and bottom of the LXe target for a good light collection, which will determine the energy threshold of the detector. The $S1$ and $S2$ signal from one event will be separated by a drift time (see Figure 2.12) of the order of $\sim 50\mu$s for a detector with 10 cm depth. The drift time gives information on the event's Z position in the detector. The $S2$ signal, originating from the cloud of ionization electrons created by an event, is very localized in X&Y. By using an array of photon sensor in the gas phase, the event X&Y position can be well reconstructed with a precision of less than 1 cm (or even better). The 3D position sensitivity of the detector will ultimately help to make sufficient cuts to reject background events, especially for events near the edge and surface of the detector. It will give additional background event rejection capability for this kind of detector. The XENON experiment is finalizing the calibration of a detector with about 15 kg target mass (XENON10), which was deployed underground in the Gran Sasso National Underground Lab in Italy in early 2006. At a background level below 0.14 events/keVee/kg/day and a background rejection potential of 99.5%, XENON10 experiment will be able to detect WIMP events, or set an upper limit, at the level of WIMP-nucleon cross-section as low as 2×10^{-44} cm^2. This limit is more than an order of magnitude lower than the current lowest WIMP-nucleon spin-independent cross-section limit set by the CDMS II experiment.

Figure 2.11: Design concept of the XENON dual phase LXeTPC with 3D position sensitivity for a WIMP dark matter search.

2.3.4 Other technologies

Directional searches using gas TPCs

As discussed in (Spergel, 1988), the Sun's motion around the galactic center, and its relative motion in the WIMP halo (note that the WIMPs are nondis-

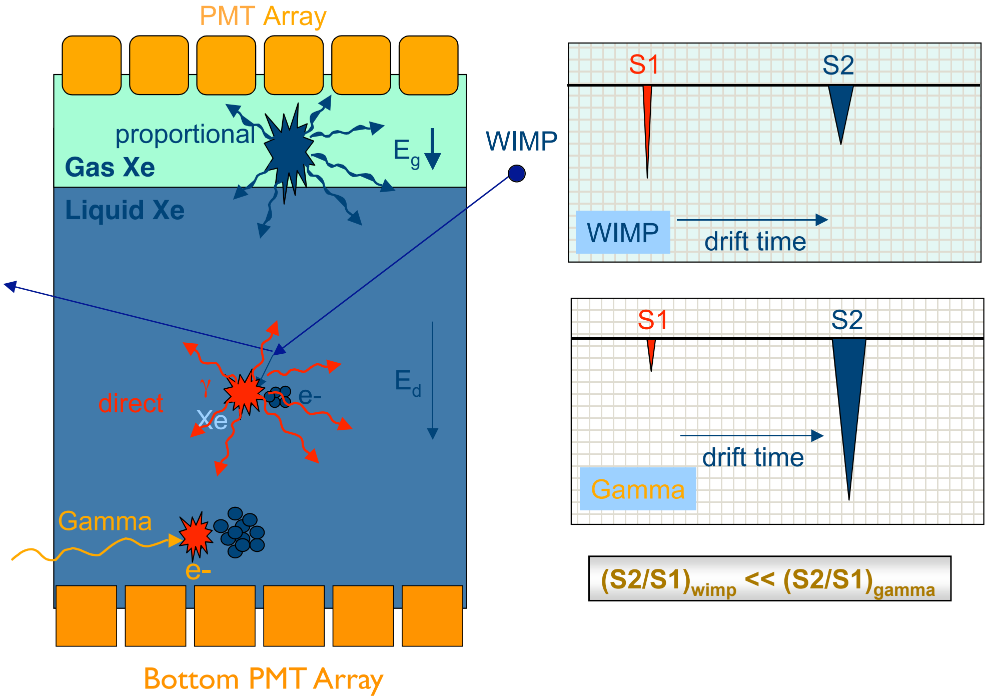

Figure 2.12: Illustration of possible signals from the LXeTPC and the difference between nuclear recoil and electron recoil events.

sipative particles, and usually described with a random velocity distribution, instead of rapidly rotating as the Sun), indicates that the WIMPs coming towards the earth have preferred directions. The study of the arrival direction of the WIMP could provide additional support of a positive identification of WIMPs.

The experiments discussed in the previous sections will not have the sensitivity to study the directionality of the WIMP events. By using gas time projection chambers (gas TPCs), a recoil event with a few keV will make a trajectory in the gas medium, providing information on the direction of the incoming particles. The electron recoils in the medium will have much smaller stopping power dE/dX than that from nuclear recoils. This indicates that with the same energy deposited and converted into ionization, the ranges for electron and nuclear recoils are different. The background rejection can be achieved by measuring both the range and ionization in these gas TPCs (Snowden-Ifft *et al.*, 2000, 2003). This is the principle of operation for the DRIFT-I experiment (Paling *et al.*, 2004) using CS_2 as the gas medium. A similar approach is being investigated by the MIMAC-He3, a MIcro-tpc MAtrix of Chambers of Helium-3, experiment by using ^{3}He as the gas medium, which is also sensitive to WIMP search via spin-dependent interactions (Moulin *et al.*, 2005).

Superheated droplet/liquid detectors

An alternative approach to rapidly increase the mass of a WIMP detector to a ton scale with simplicity of the design has been pursued by using the bubble chamber concept, where an ionizing particle deposits its energy in a superheated liquid and produces vaporization along its wake, and the bubble detector (also known as superheated droplet detector), where small drops of liquid with radius about 10 μm are uniformly dispersed in a gel or viscoelastic medium, which extends the lifetime of the superheated states. The technology can be used to detect the WIMP dark matter, such as in the SIMPLE (Collar *et al.*, 2000; Giuliani, 2005), PICASSO (Boukhira *et al.*, 2000; PICASSO Collaboration, 2005) and COUPP experiment (Collar *et al.*, 2005).

2.4 Low background requirements

At the current stage, dark matter direct detection experiments are mainly focused on how to clearly identify a WIMP signal from the background, which can be $\alpha/\beta/\gamma$ and neutrons from the environment and the detector itself.

The environmental γ ray activity is largely due to the decay chains of ^{238}U and ^{232}Th and from decay of ^{40}K. Those γ rays can be reduced by placing the detector inside shielding (i.e. Pb), which can reduce the level down to 0.1–1 events/keV/kg/day (dru). The radioactivity contained in the detector's construction material is more serious, as it can't be shielded and will give a significant amount of γ ray background if the construction materials are not carefully selected for low activity.

Neutron events will make nuclear recoils in the target, very similar to that from WIMPs. The level of neutron activity from (α, n) reactions in the rock can be reduced by using shielding with low-Z material (such as polyethylene). Neutron elastic scattering events can also be identified if the event makes multiple scatters in a detector with position sensitivity.

Neutrons generated by cosmic ray muons in the surrounding rock with energies more than 20 MeV are difficult to be moderated by shielding. Placing the detector in a deep underground site, where the muon flux is greatly attenuated, can reduce this neutron flux. More details on background sources and reduction will be discussed in Section 6.3.

Chapter 3

Liquid xenon for particle detection

Liquid noble elements, especially liquid argon and liquid xenon, have been used for particle detection since several decades ago (Doke, 1981; Schmidt, 1997). Their good ionization and scintillation properties have been extensively studied and application of this detection medium has been extended from high energy experiments to astrophysics, astroparticle physics and medical imaging in recent years (Doke *et al.*, 1999; Lopes *et al.*, 2003). Xenon, as one of the noble elements with high atomic mass, and highest scintillation and ionization yield, has been developed for several specific applications, such as for the LXePET (LXe for Positron Emission Tomography) (Chepel *et al.*, 1997) in medical imaging, the LXeGRIT (LXe Gamma Ray Imaging Telescope) in MeV γ ray astrophysics (Xu, 1998; Aprile *et al.*, 2002), and several particle-astrophysics experiments use liquid xenon for double beta decay (Danilov *et al.*, 2000), solar neutrino detection (Georgadze *et al.*, 1997) and

WIMP dark matter detection (see Section 2.3.3) in.

In this chapter, we will first review the general properties of xenon. The properties for the particle detection, specifically the ionization and scintillation properties of condensed xenon, will be discussed further, in details. While the detection of particles with very small kinetic energy (a few tens of keV) in liquid xenon has attracted a lot of interest in recent years, the properties of low energy events (either nuclear or electron recoils) in liquid xenon were generally not well studied.We will also include some of the studies carried out during the R&D work of this thesis.

3.1 Physical properties of xenon

Among the noble gases, xenon has the highest atomic mass (except radon which hasn't been studied so far for radiation detection). Xenon exists in the air with a very small concentration (less than 0.1 ppm). Natural xenon contains different isotopes, as listed in Table 3.1 (WebElements), with the odd spin component ^{129}Xe and ^{131}Xe. It can be obtained as a byproduct from liquefaction and separation of air. Liquid xenon has the largest density and smallest radiation length among the noble liquids (except radon). Table 3.2 compares the general properties of liquid xenon to other noble gases, most of the values are adapted from the elements website (WebElements) and (NIST Fluid).

Xenon costs (about $1k/kg), more than other noble gases, especially Ar, which is also usually cooled by LAr itself and can be discarded after the experiment, at least if small volumes are involved. The operation pressure of

Table 3.1: Isotope components in natural xenon

Isotope	Atomic Mass	Natural Abundance [atom %]	Nuclear Spin (I)	Magnetic Moment
^{124}Xe	123.9	0.09	0	
^{126}Xe	125.9	0.09	0	
^{128}Xe	127.9	1.92	0	
^{129}Xe	128.9	26.4	1/2	-0.778
^{130}Xe	129.9	4.08	0	
^{131}Xe	130.9	21.2	3/2	0.692
^{132}Xe	131.9	26.9	0	
^{134}Xe	133.9	10.4	0	
^{136}Xe	135.9	8.87	0	

Table 3.2: Physical properties of noble elements

Property	He	Ne	Ar	Kr	Xe
Atomic Number (Z)	2	10	18	36	54
Atomic Weight (A)	4.00	20.18	39.95	83.80	131.29
Boiling Point T_b at 1 atm [K]	4.22	27.1	87.3	119.9	165.0
Melting Point T_m at 1 atm [K]	0.95	24.6	83.8	115.8	161.4
Gas Density at 1 atm&298 K [g/l]	0.16	0.82	1.63	3.43	5.40
Gas Density at 1 atm&T_b [g/l]	16.6	9.56	5.77	8.89	9.99
Liquid Density at 1 atm&T_b [g/cm^3]	0.12	1.21	1.40	2.41	2.94
Critical Temperature T_c [K]	5.19	44.4	150.8	209.4	289.7
Critical Pressure P_c [atm]	–	–	48.3	54.3	57.6
Critical Density [g/cm^3]	–	–	0.54	0.91	1.10
Dielectric Constant of Liquid	–	–	1.51	1.66	1.95

a liquid xenon detector is usually between 1 and 3 atm, corresponding to an equilibrium temperature between 165 K (-108°C) and 187 K (-86°C). Usually a copper cold finger with liquid nitrogen cooling bath is used. For a more stable operation, a cryogenic refrigerator is needed and the development of a Pulse Tube Refrigerator (PTR) optimized for LXe temperature (Haruyama *et al.*, 2004) has led to a very efficient, reliable and practical cooling system for LXe detectors as large as many hundreds of kg (MEG Collaboration, 2003).

3.2 Ionization properties

When a particle passes through matter, it will lose energy and be stopped or scattered. The type of interaction and amount of energy loss depends on the energy and type of the incident particle, as well as the detection medium. In this section, we will first discuss different type of particle interactions in liquid xenon and specific experimental techniques of detecting the energy deposited in the *ionization* channel. We will talk about detection of *scintillation* light in the next section.

3.2.1 Particle interaction in xenon

Different particles, such as alpha particles, relativistic electrons, γ rays and neutrons, interacting in liquid xenon involve totally different mechanisms, as discussed in details in (Knoll, 2000).

Due to the positive charge of alpha particles, they will interact with the orbital electrons of the medium atoms, via the Coulomb force. As a result of the interaction,an orbital electron can either be lifted to a higher-level shell within the atom *excitation*, or can be completely removed from the atom *ionization*. The alpha particle will encounter many of this type of interactions and convert its energy either to the ionization, or excitation. Since the interaction occurs in all directions simultaneously and the particle is not affected by a single interaction, the path of the alpha particle is usually a straight line. Unlike alpha particles, the path of relativistic electrons can be quite tortuous since they have the same mass as the orbital electrons. The rate of their energy loss is also slower than that of alpha particles.

For γ rays, there are three main type of interactions with matter: *photoelectric absorption*, *Compton scattering* and *pair production*. The photoelectric absorption occurs when a γ ray is completely absorbed by the atom and an energetic electron is ejected from one of the bound shells of the atom. It has the highest cross-section from low energy γ rays (such as 122 keV γ rays from ^{57}Co). The Compton scattering occurs when the incident γ ray is deflected and transfers part of its energy to an electron. This usually happens in the γ ray energy around 1 MeV (e.g. 662 keV γ ray from ^{137}Cs). The pair production process will produce an electron-positron pair from the incident γ ray. It occurs when the γ ray energy exceeds twice the rest-mass energy of an electron (1.02 MeV). The effect becomes dominant for γ rays with energy of several MeV. Figure 3.1 shows the interaction cross-section as a function of γ ray energy in liquid xenon, as well as the mean free path of γ rays in LXe as a function of energy. The mean free path for 122 keV γ rays is less than 3 mm in LXe.

Depending on their energy, neutrons interact differently in liquid xenon.

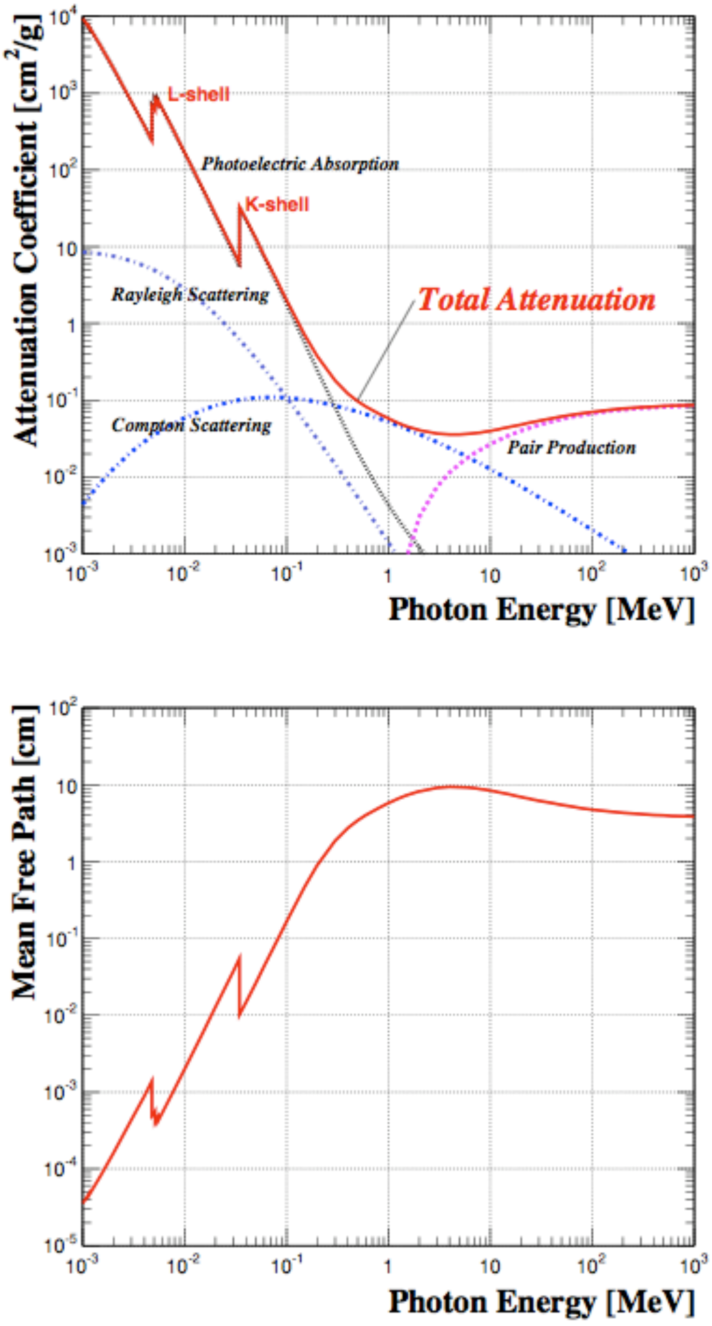

Figure 3.1: Gamma ray interaction cross-section and mean free path ($\rho_{\mathrm{lxe}} = 2.98\mathrm{g/cm^3}$) in liquid xenon. Figure from (Ozone, 2005).

For *fast neutrons*, energy is transferred via *elastic scattering* to a *recoil nucleus* of the target material. If its energy is high enough, a neutron can also suffer an *inelastic scattering*, which elevates the recoil nucleus to an excited state. The energy transferred to the excited state is released to a γ ray during the de-excitation of the nucleus. The interactions of *slow neutrons* are mainly via elastic scattering, with barely enough energy deposit to be detected, and neutron-induced nuclear reactions [mostly radiative capture reactions (n, γ)]. Much of the population of slow neutrons will be found as *thermal neutrons*, which have an average energy of 0.025 eV at room temperature.

Table 3.3: Ionization properties of noble gases and liquids

Property	He	Ne	Ar	Kr	Xe
1st ionization energy [eV]	24.6	21.6	15.8	14.0	12.1
2nd ionization energy [eV]	54.5	41.0	27.7	24.4	21.2
3rd ionization energy [eV]	–	63.6	40.8	37.0	32.2
$W - value$ in liquid for relativistic e^-	–	–	23.6	20.5	15.6
$W - value$ in gas for relativistic e^-	41.3	–	26.4	–	21.9
$W - value$ in gas for α particles	42.7	–	26.3	–	–
Fano factor in liquid	–	–	0.06	0.07	0.12
Electron binding energy (K) [keV]	0.025	0.87	3.21	14.33	34.56

3.2.2 Ionization yield and its measurement

Ionization is the stripping of orbital electrons from an atom. The 1st ionization energy is the energy required to strip one electron from the neutral atom, the 2nd ionization energy is the energy required to strip another electron after the first has been removed, and so on. When a particle passes through the detection medium, not all of its energy is transferred via *ionization.* Part of the energy is transferred to *excitation* of the atom. The average energy needed to produce an electron-ion pair, usually called $W - value$, is defined and used in experimental physics. It is dependent on the radiation particle and the medium atom. The 1st to 3rd ionization energy, as well as the $W - value$ for different noble gas elements are listed in Table 3.3. The ionization energies are from (WebElements). The $W - values$ for relativistic electrons in LAr, LKr and LXe are from (Miyajima *et al.*, 1974; Takahashi *et al.*, 1975) and references therein. We note that the measurement from (Aprile *et al.*, 1993) shows a slightly smaller $W - value$, 18.4 eV, in LKr. The $W - values$ for relativistic electrons and α particles in GHe and GAr are from (Knoll, 2000).

The fluctuation of the number of electron-ion pairs is of interest, as it will determine the energy resolution of the measurement. If the stripping of each electron from the atom is independent, then the fluctuation should follow the Poisson statistics distribution as the square root of the number of electron-ion pairs. A smaller fluctuation than the Poisson prediction is expected for noble liquid elements. A value, called *Fano factor* F, is used to describe the energy resolution of the detector as $\sigma/E = \sqrt{F/(E/W)}$, where E is the energy of the radiation. The values of $Fanofactor$ from theoretical calculations are listed in Table 3.3 for some of the noble liquid elements, values for some noble gas elements from (Knoll, 2000), based on (Alkhazov *et al.*, 1967). The small Fano factor in liquid noble elements indicates a very good energy resolution (about 0.1% for 1 MeV electrons in liquid xenon), while the experimental measured resolution is much worse. For example, see (Ichinose, 1992). Some studies of this discrepancy were carried out during the period of this thesis by studying the energy resolution of the combined signal from ionization and scintillation in liquid xenon (see Section 4.6).

After the creation of electron-ion pairs by the primary ionizing particle, the electron and ion tend to *recombine* to a neutral atom. By applying an electric field across the detector medium, the electron and ion can be separated and collected individually. Usually a gridded ionization chamber in charge pulse mode (see illustration in Figure 3.2) is used to detect the ionization electrons. The rise time T_r of the output pulse corresponds to the time that the electrons cloud drift between grid and anode. The decay time corresponds to the value of the $R_F C_F$ circuit in the charge preamplifier. The pulse height is proportional to the number of collected electrons from ionization. A known test pulse V_{tp} and calibrated feedback capacitor C_{tp} are used to determine the conversion factor from the output pulse height to the number of charges. The pulse from the preamplifier can be fed into a spectroscopy amplifier, and further into a Multi-Channel Analyzer (MCA), or be saved as raw pulse waveforms to a computer via a flash ADC (Analog to Digital Converter) for further waveform analysis (see Section 4.2 for an example).

3.2.3 Electron drift velocity and attachment

In liquid xenon, the electrons created by the ionizing particle remain as a localized small cloud during their drifting along the electric drift line. Their

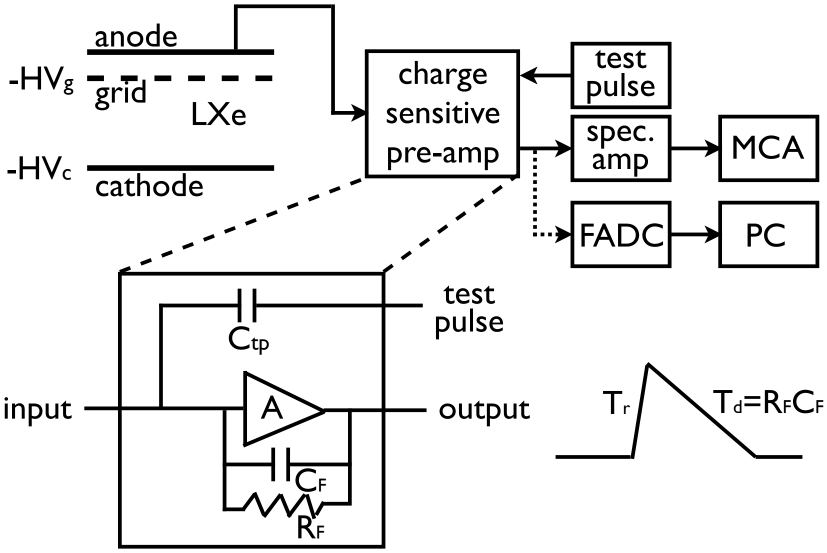

Figure 3.2: A simplified schematics of detection of ionization electrons by using charge pulse mode.

drift velocity has been measured in a wide range of electric fields and liquid temperature and tends to be saturated above a few kV/cm (Figure 3.3). At 1 kV/cm, the electron drift velocity is about 2 mm/μs. This value is quite useful and is used to derive the event position in Z direction in the TPC (time projection chamber) where the time of the event can be precisely determined. The electrons from the cloud tend to diffuse from the high-density part during their drifting. The diffusion is described by the diffusion coefficient D, which is defined in $\sigma = \sqrt{2Dt}$, with σ the standard deviation of the electron cloud distribution projected onto an arbitrary orthogonal axis (x, y, or z) (Knoll, 2000). The diffusion coefficient as a function of density-normalized electric field is shown in Figure 3.4.

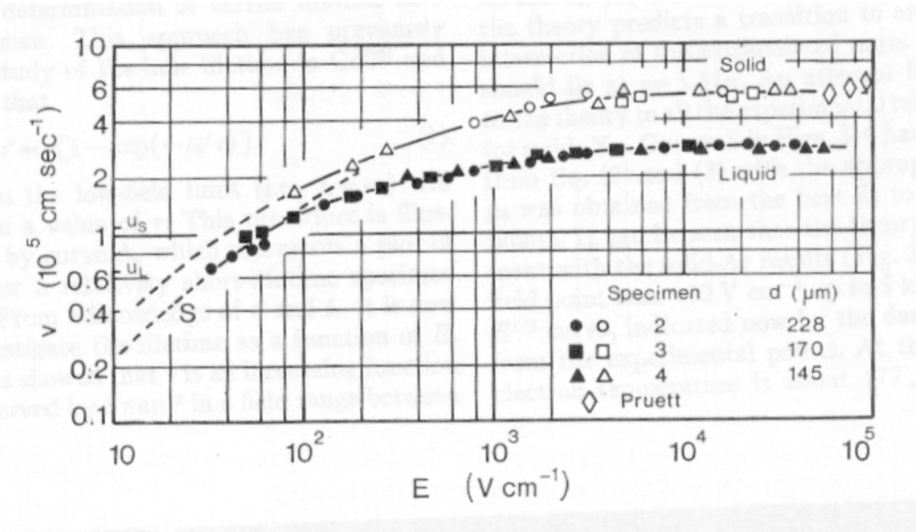

Figure 3.3: Electron drift velocity in liquid and solid xenon. Figure from (Miller *et al.*, 1968).

Among the noble liquid detectors, the liquid xenon ones are operated

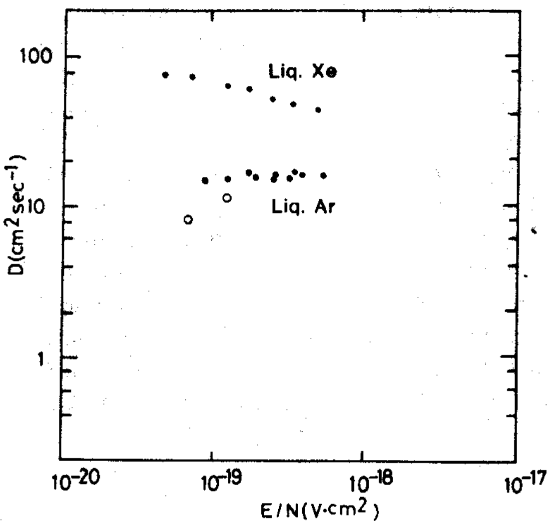

Figure 3.4: Electron diffusion coefficient in LAr and LXe as a function of density-normalized electric field. Figure from (Doke, 1982).

at the highest temperature. Some of the impurities are not frozen out. The main content of the impurity is O_2, whose attachment rate to electrons can be reduced by increasing the electric field, while other impurities, such as N_2O goes in the reverse direction. Figure 3.5 shows the electron attachment rate constant of some impurity molecules in liquid xenon. Thus the purification of liquid xenon is extremely important, in order to minimize the loss of electrons during their drifting towards the collection electrode. To achieve a purity level that is sufficient for electron detection and stable operation, a continuous xenon gas purification system is necessary (see Section 4.3 for a description of such an system).

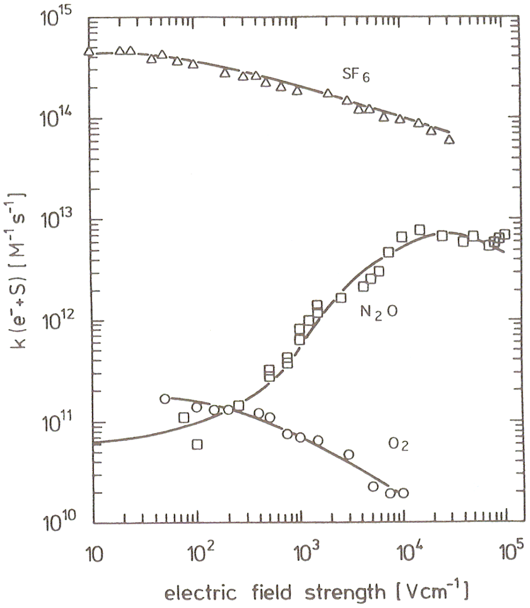

Figure 3.5: Electron attachment rate constant as a function of field for some impurity molecules in liquid xenon. Figure from (Bakale *et al.*, 1976).

3.3 Scintillation properties

Scintillation light from liquid xenon represents another very useful signal for particle detection in liquid xenon. The light can be used as a trigger. Sufficient light detection with optimized detector geometry and readout will give additional information and can be used for particle identification and improvement of detector performance.

3.3.1 Scintillation mechanism in liquid xenon

The *excitation* states of rare gas atoms will return to the ground state by emitting a photon, which gives *scintillation* light. The recombination of electron-ion pair from the *ionization* process will also produce excitation states, leading to scintillation photons. The two processes can be illustrated as following for the case of scintillation in liquid xenon (Doke *et al.*, 2002).

$$\mathrm{Xe}^* + \mathrm{Xe} \rightarrow \mathrm{Xe}_2^* \tag{3.1}$$

$$\mathrm{Xe}_2^* \rightarrow 2\mathrm{Xe} + \mathrm{h}\nu \tag{3.2}$$

$$\mathrm{Xe}^+ + \mathrm{Xe} \rightarrow \mathrm{Xe}_2^+ \tag{3.3}$$

$$\mathrm{Xe}_2^+ + \mathrm{e}^- \rightarrow \mathrm{Xe}^{**} + \mathrm{Xe} \tag{3.4}$$

$$\mathrm{Xe}^{**} \rightarrow \mathrm{Xe}^* + \mathrm{heat} \tag{3.5}$$

$$\mathrm{Xe}^* + \mathrm{Xe} \rightarrow \mathrm{Xe}_2^* \tag{3.6}$$

$$\mathrm{Xe}_2^* \rightarrow 2\mathrm{Xe} + \mathrm{h}\nu \tag{3.7}$$

The scintillation light of liquid xenon is peaked at 178 nm (Jortner *et al.*, 1965). It has two decay time components, 4.3 ns and 22.0 ns, corresponding to the decay of two excited molecular states ($^1\Sigma_u^+$ and $^3\Sigma_u^+$) separately (Hitachi *et al.*, 1983).

Table 3.4 lists various properties of scintillation in noble elements (gas or liquid). The data for liquid helium are from (McKinsey *et al.*, 2005b) and references therein. The data for liquid argon and xenon are from (Doke *et al.*, 2002) and references therein.

3.3.2 Scintillation yield and its measurement

Similar to the definition of $W - value$ for ionization, we use $W_{ph} - value$ as the average energy to produce a scintillation photon. The value was found to be quite different for different types of particles (α, electron and heavy ions) (see Table 3.4). The W_{ph} for α particles in gas and liquid xenon are measured to be 49.6 and 16.3 eV, respectively (Miyajima *et al.*, 1992).

Maximum light yield per MeV was found for relativistic heavy particles (Doke *et al.*, 2002) while the scintillation from α and relativistic electrons is largely suppressed, which resulted in less light yield and thus, larger W_{ph}. The possible explanation of this light quenching is due to the biexcitonic collision $[\mathrm{Xe}^* + \mathrm{Xe}^* \rightarrow \mathrm{Xe} + \mathrm{Xe}^+ + \mathrm{e}^-(\mathrm{k.e.})]$ of two excitons in dense ionizing regions of the medium (Hitachi *et al.*, 1992). The result is that two excitons will produce one electron-ion pair, which carries away kinetic energy. The electron will finally lose its energy and recombine with an ion, producing only one UV photon. Due to this effect, the light yield is not linear with the energy of particle. Even γ rays with different energy will give different scintillation

Property	He	Ne	Ar	Kr	Xe
Peak wavelength [nm]	80	80	129	147	178
Decay time constant in liquid	1 ns, 13 s	–	7.0 ns, 1.6μs	–	4.3 ns, 22.0 ns
Refractive Index of Liquid	1.03	–	–	–	1.57, 1.69
W_{ph} in gas for α's [eV]	–	–	–	–	49.6
W_{ph} in liquid for α's [eV]	–	–	27.1	–	16.3, 17.9
W_{ph} in liquid for relativistic e^- [eV]	–	–	24.4	–	21.6
W_{ph} in liquid for relativistic heavy ions [eV]	–	–	19.5	–	13.8
Absorption length	–	–	–	–	$>$ 100 cm
Rayleigh scattering length	–	–	–	–	29 cm to 50 cm

Table 3.4: Properties related to scintillation of noble elements

yields (Yamashita *et al.*, 2004). Our studies also indicate a higher light yield for lower energy γ rays (see Section 4.4).

Some other properties related to the detection of liquid xenon scintillation light are: the refractive index of liquid xenon for its UV light, and the absorption and scattering lengths of the light in liquid xenon. The refractive index of liquid xenon was measured to be 1.57 (Barkov *et al.*, 1996) and 1.69 (Solovov *et al.*, 2004). The large refractive index of liquid xenon makes it difficult to efficiently detect the scintillation in a dual phase detector with only light detectors in the gas phase, due to total internal reflection at the liquid-gas interface.

The absorption length λ_{abs} of the UV light in liquid xenon depends on the purity level. The main impurities are water and oxygen. Recently, the MEG collaboration reported an increase of λ_{abs} up to 1 meter after purification in a 100 liter liquid xenon γ-ray detector (Baldini *et al.*, 2005). Thus a small-scale detector ($\sim$10 cm) should be transparent to its own scintillation light. We use this value ($\lambda_{\mathrm{abs}} = 1$ m) for the input of detector simulations. The Rayleigh scattering length λ_{sca} of the scintillation light will deflect the direction of the light, but will not reduce the light collection. λ_{sca} value was measured between 29 and 50 cm (Braem *et al.*, 1992; Chepel *et al.*, 1994; Ishida *et al.*, 1997; Solovov *et al.*, 2004). We adopt a value $\lambda_{\mathrm{sca}} = 30$ cm from theoretical calculation (Seidel *et al.*, 2002) for the detector simulations.

Usually, photon detection devices with enhanced UV light detection are used for the detection of the scintillation light in liquid xenon. These include PMTs, LAAPDs (large area avalanche photodiodes), CsI photocathodes and more recently, silicon photo-multiplier (SiPM). See Section 4.4 and 4.5 for some studies during this thesis.

3.3.3 Relation between ionization and scintillation

By applying an electric field in the liquid, the recombination of electron-ion pairs is reduced, thus the scintillation light is also reduced. The electric-field effect of scintillation quenching was first observed in liquid xenon and argon by Kubota *et al.* (1978). It is accompanied by the increase of ionization electron collection. Figure 3.6 shows the relative yield of light detection with electric field E, compared to that at zero field, $S(E)/S_0$, as a function of field strength for 1 MeV conversion electrons. The charge collection, $Q(E)/Q_0$, is defined as the percentage of charge collection to that at infinite field (i.e. $Q_0 = E/W$). At high fields, the scintillation light yield is less than 40% of that at zero field.

More recently, the correlation between ionization and scintillation signals in liquid xenon was measured and a clear evidence of *anti-correlation* was found (Conti *et al.*, 2003). For a given electron recoil energy and at a given electric field, the smaller scintillation light signal is always accompanied by a larger ionization yield. This anti-correlation makes it possible to improve the energy resolution in a liquid xenon detector. Our recent experiment based on the measurement of charge and light for different energy of γ rays, has confirmed the strong *anti-correlation* effect and the improvement of the energy resolution of liquid xenon to the level predicted by the Fano factor (see section 4.6 for more details).

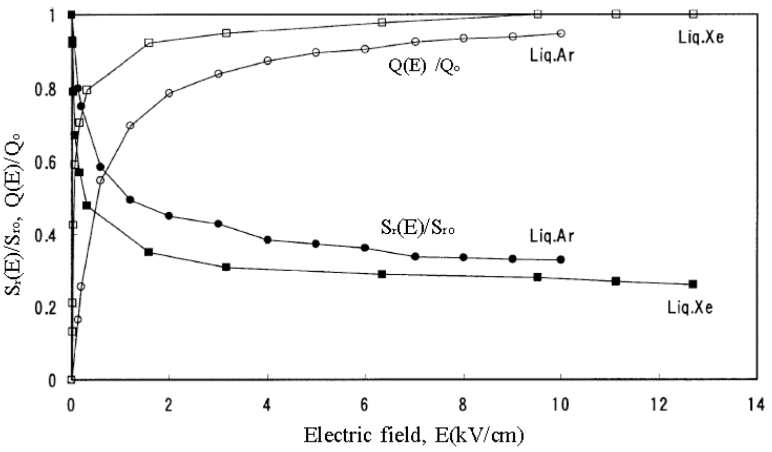

Figure 3.6: Field dependence of scintillation (open symbols) and ionization (solid symbols) for 1 MeV conversion electrons in liquid xenon and liquid argon. Figure from (Doke *et al.*, 2002).

3.4 Proportional scintillation (electroluminescence)

In a dual phase emission detector, ionization electrons extracted from a non-polar liquid into the gas phase, are accelerated by an applied electric field in the gas, resulting in electroluminescence or proportional scintillation (Bolozdynya, 1999). Measurement of proportional scintillation light, rather than charge, provides an amplified signal and thus a low energy threshold, while maintaining the same energy resolution obtained with the charge measurement in the liquid. Detecting both the direct scintillation light and the proportional scintillation is the main technique on which the detectors for the XENON dark matter search experiment are based. A study has been carried out to study the properties of proportional scintillation, the electron extraction efficiency from the liquid to the gas phase, and a comparison of the energy resolution of proportional light and direct charge measurement (Section 4.1).

Chapter 4

Development of liquid xenon detectors

In order to study the properties of liquid xenon for the WIMP dark matter detection, various R&D has been carried out during the last few years. The operation of a small dual phase xenon chamber was performed to study the various properties of proportional scintillation (electroluminescence) and electron emission (Section 4.1). The small recoil signal produced by the WIMP elastic scattering in liquid xenon requires the detector to be sensitive to very low energy events. The measurement of ionization and scintillation from low energy γ rays (122 keV) was performed (Section 4.2 and 4.4). The measured values determine the energy calibration of a liquid xenon dark matter detector. To detect the small amount of ionization electrons from the nuclear recoil of a few 10 keV, an ultra pure liquid xenon environment has to be achieved. A continuous xenon purification and circulation system was developed to satisfy this requirement (Section 4.3). To achieve a low energy threshold, the direct scintillation light collection has to be optimized. UV reflective materials and PMTs, which were developed specifically for this application, were studied (Section 4.4). Several novel UV photon detectors were also tested as possible alternatives to PMTs for light detection (Section 4.5). Finally, the improvement of the energy resolution, which will ultimately determine the background rejection efficiency of a liquid xenon dark matter detector, was observed by combining the scintillation and ionization signals from liquid xenon (Section 4.6).

4.1 Proportional light in a dual phase chamber

To have a good understanding of dual phase operation of a xenon detector, a small chamber was built to study various properties, such as the extraction of electrons from the liquid to the gas phase and gain (number of photons per electron) in the gas.

A photo of the assembled electrodes and PMT, is shown in Figure 4.1. The cathode is a 6 cm diameter stainless steel (SS) disk with a ^{207}Bi source deposited in the center. Two SS etched meshes, also 6 cm in diameter, are mounted 10 mm above the cathode. They define the gas amplification region of 5 mm, or work as a shielding grid and anode when operating the chamber in single phase mode. The meshes have 0.1 mm bar thickness and 1 mm spacing. Four PTFE spacers hold the three electrodes in place.

The PMT (Hamamatsu R6041), mounted 7 mm above the anode mesh, was originally developed for the LXe detectors used by the Columbia and

Figure 4.1: Photo of the inner structure of the dual phase chamber. From the bottom are: cathode disk, grid and anode meshes. The Hamamatsu R6041 PMT is mounted above the anode mesh.

Waseda University groups. It has a 2-inch diameter quartz window and is less than 4 cm long, due to its metal channel construction. The initial version of the tube, as used in these measurements, suffers from a poor QE, typically less than 8% at 178 nm. Further development of the same PMT for the MEG collaboration [1] has yielded a new version of the same metal channel PMT (Hamamatsu R9288) with QE improved to 20%.

In order to minimize the impact of impurities from the PMT we replaced the standard HV base with a custom designed base made of ceramic. Tests carried out with another LXe ionization chamber (Aprile *et al.*, 2003) have previously confirmed a good level of purity with the R6041 and its HV base fully immersed in LXe.

The assembled structure and PMT is enclosed in a SS vessel of about 0.5 liter volume. Hermetic HV and signal feed-throughs, the pumping port and the gas filling line are provided on the vessel's flange. A charge sensitive preamplifier (ClearPulse Model 580) is coupled to the anode, to detect the signal of drifting electrons. The energy spectrum of the ^{207}Bi source can be directly measured by feeding the preamplifier signal to a spectroscopy amplifier (ORTEC 450) and to a Multi-Channel Analyzer. Xe gas, purified by a SAES getter, is condensed into the vessel by a cold bath of liquid nitrogen and alcohol mixture. At the typical operating temperature of -95°C, the vapor pressure of the gas above the LXe is 2 atm.

---

[1] MEG Website: http://meg.icepp.s.u-tokyo.ac.jp/

4.1.1 Single and dual phase operation

As Xe gas is condensed in the chamber, we monitor the liquid level with the light signals detected by the PMT. With no field applied, only direct scintillation light from the ^{207}Bi electrons and gamma radiation can be seen, as soon as the cathode is covered by LXe. With an applied field, the amount of direct light signal is reduced as recombination is reduced. Simultaneously, ionization electrons start to drift. During this filling phase we apply a drift field of 0.5 kV/cm between cathode and grid and a field of 4 kV/cm between grid and anode. The field is not large enough to extract the drifting electrons from the liquid to the gas phase. Therefore only the fast direct scintillation light is seen at this stage.

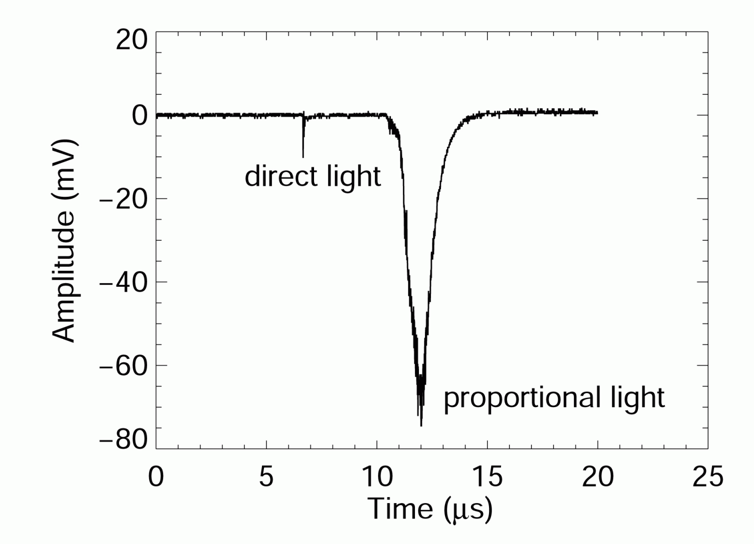

Figure 4.2: A typical waveform directly from the PMT showing both direct light and proportional light generated by a gamma ray event from ^{207}Bi.

As soon as the liquid level covers the grid, the ionization electrons can

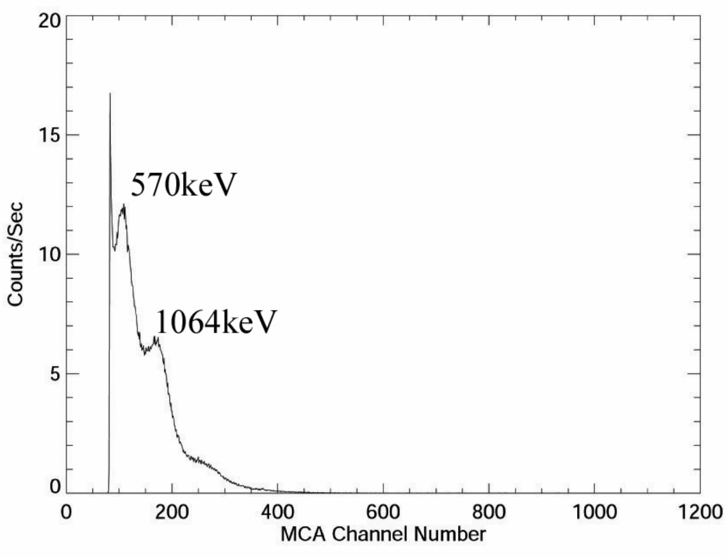

Figure 4.3: ^{207}Bi energy spectrum from direct scintillation light in LXe at zero electric field

be extracted to the gas phase at the high field of 4 kV/cm. At such a high field, these drifting electrons excite the Xe molecules and produce scintillation light. The amount of this scintillation light is proportional to the reduced field (field over gas pressure). The proportional light signal is also determined by the gas gap across which it is produced. In our case, this gap is around 4 mm by assuming the error of controlling the liquid level is around 1 mm. In this dual phase operation, both direct and proportional scintillation was seen by the PMT. The light waveform registered with a fast digital scope at 500 MHz (LeCroy Waverunner LT374) is shown in Figure 4.2. The time between the direct light and the proportional light is 4.5 μs, which is the electron drift time in the 10 mm liquid xenon gap.

The chamber can be filled even further with xenon, such that the liquid covers the anode mesh and the PMT window. In this case, the detector operates in single-phase mode, in which only direct scintillation light is seen and all drifting electrons are collected by the anode. The ^{207}Bi spectrum obtained from the direct scintillation light, at zero field, is shown in Figure 4.3. The measurement was performed by replacing the spacers with a solid ring of PTFE [$\sim$92% reflectivity for Xe light (Yamashita *et al.*, 2004)].

By analyzing individual charge waveforms (Figure 4.4) triggered by the direct light, we can measure the purity of the LXe. After several passages of the gas through the getter, we were able to achieve a long electron lifetime, demonstrating the compatibility of all materials, including PTFE and PMT HV divider, with high purity LXe. Figure 4.5 shows the distribution of charge amplitude for the ^{207}Bi 570 keV gamma-ray line as a function of drift time. The corresponding fit with the function $Q(t) = Q(0)exp(-t/\tau)$, with Q(t) the charge amplitude at drift time t, indicates a good purity level (τ $\sim$1.5 ms).

4.1.2 Electron extraction and proportional scintillation

Due to the negative value of the ground state energy of the quasi-free electrons in liquid xenon (Bolozdynya, 1999), an electric field is needed to 'heat' the electrons and extract them from the liquid to the gas phase. The extraction yield as a function of field in the gas is measured by following steps.

First we operated the detector in the single phase, and set the drift field (field between cathode and grid) at a value E_d. The field between anode and grid is set at a value E_c, which is always greater than E_d, allowing

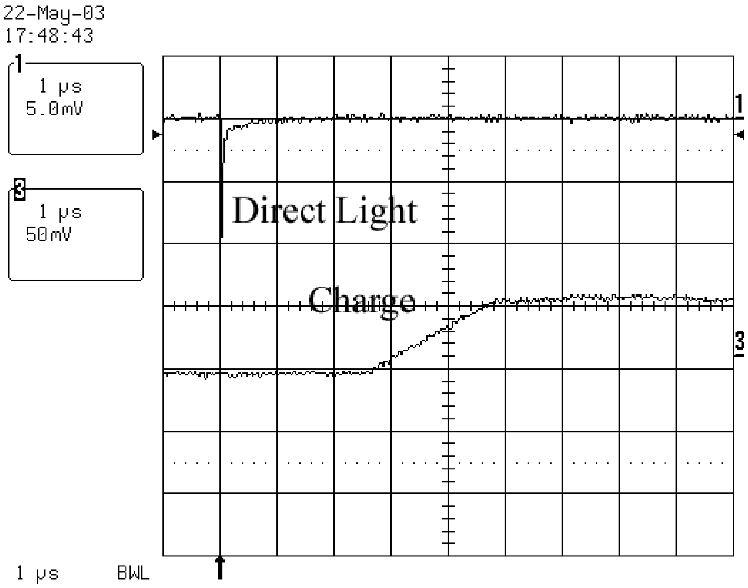

Figure 4.4: Charge waveform triggered by the direct scintillation light of γ rays in LXe.

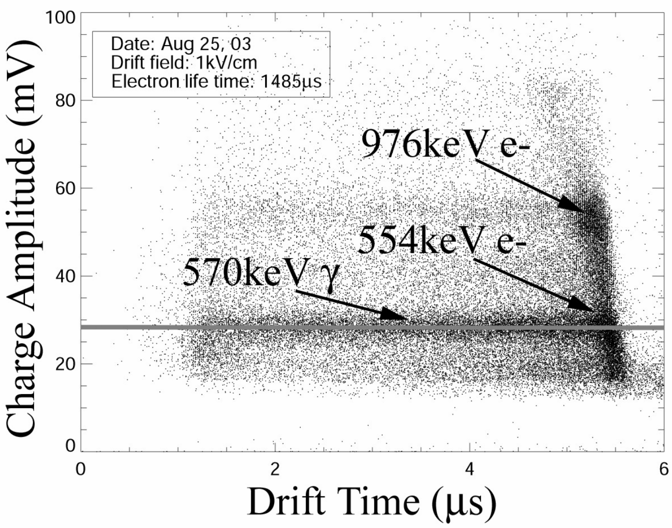

Figure 4.5: Charge amplitude as a function of drift time for ^{207}Bi radiation in LXe.

electron transmission through the grid mesh. We took the charge spectrum with the MCA and measured the peak position p_1 of 570 keV gamma ray line. After that, we removed some xenon, and operated the detector in the dual phase mode. We adjusted the HV values for the grid and cathode so that the drift field was kept at E_d and the field in the gas between anode and the liquid surface is $E_g = \epsilon E_c$, where ϵ is the dielectric constant of liquid xenon. The value for ϵ is quite different (between 1.87 and 2.85) from various publications (Marcoux, 1970; Seidel *et al.*, 2002). We used an approximate value of $\epsilon = 2.0$ to estimate the field. The thickness of the liquid layer above the grid is negligible, and the field in this liquid layer is E_c, allowing a same electron transmission rate through the grid mesh as in the single-phase mode. We took the charge spectrum again and measured the peak position p_2 of

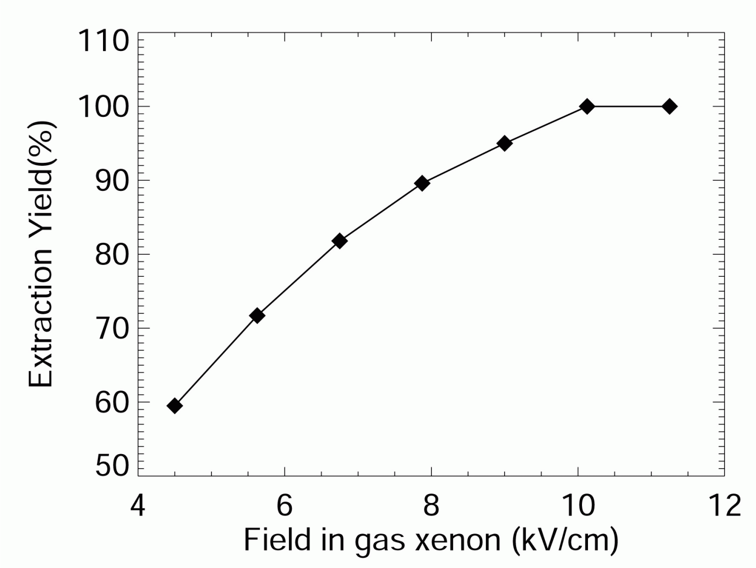

Figure 4.6: Electron extraction yield as a function of electric field in the gas phase.

the same gamma ray line. The ratio $Y = p_2/p_1$ gives the extraction yield through the liquid-gas interface. The electron extraction yield as a function of the field in the gas phase is shown in Figure 4.6. At a field higher than 10 kV/cm, the electron extraction efficiency is 100%.

Extracted electrons drift in the gas phase, and excite Xe molecules and produce proportional light. The number of UV photons produced in this process depends on the gas pressure p in atm, the electric field E in kV/cm and the electrons drift distance d in cm, in the gas as the following empirical equation (Bolozdynya, 1999),

$$N_\gamma = \alpha N_e (E/p - \beta) p d \tag{4.1}$$

Here N_e is the number of electrons extracted from the liquid to the gas

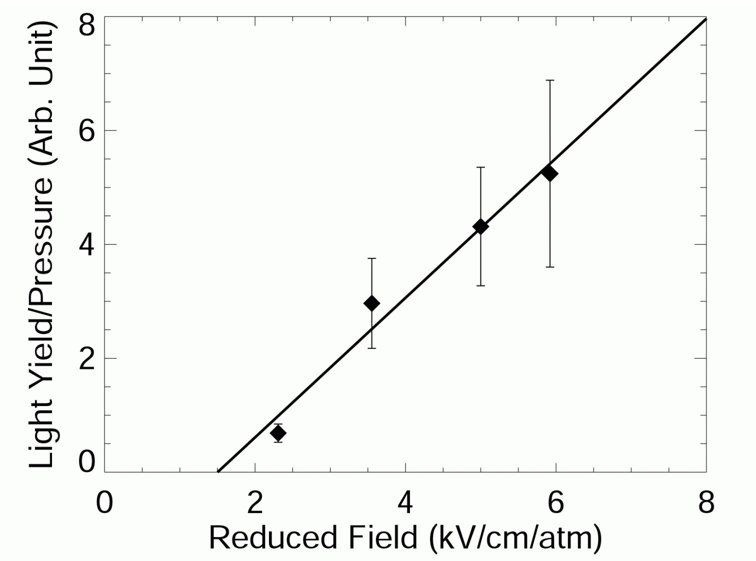

Figure 4.7: Proportional light yield over gas pressure as a function of reduced field (field/pressure).

phase, N_γ is the number of proportional scintillation photons produced, α and β are two parameters determined by the experiment conditions. α is the amplification factor, and β is the threshold of reduced field for proportional light production.

In our experiments, the gas pressure was kept at 2 atm. The gap for proportional light production was about 0.4 cm. Once the gas pressure and field are kept stable, the amount of proportional light is proportional to the number of ionization electrons. As can be seen in Figure 4.8, the energy spectrum from the proportional light is similar to that obtained from the charge spectrum taken in the single phase. The peak around 80 keV in the proportional light spectrum is attributed to the low energy X-rays from ^{207}Bi.

The dependence of the proportional light yield was measured for a reduced electric field from 2.25 to 6 kV/cm/atm. Figure 4.7 shows the amplitude of proportional light for the ^{207}Bi X-ray peak around 80 keV as a function of field. A linear fit gives a threshold value of β about 1.3 kV/cm/atm.

4.1.3 Ratio between proportional and direct light

The technique of a dual phase xenon detector for background discrimination between electron recoils and nuclear recoils are based on the ratio of proportional $S2$ and direct light $S1$. The ratio is determined by the light collection efficiency, the electric field, the gap for proportional light and the drift field in the liquid. It can be described by the following equation.

$$\frac{S2}{S1} = \frac{\alpha_2 Q_e Y \cdot N_\gamma / N_e}{\alpha_1 L_e} \cdot \frac{W_{ph}}{W} \tag{4.2}$$

ε is the energy deposited in the liquid xenon. W and W_{ph} are the W-values in liquid xenon for charge and light, respectively. For electron recoils, W_e is 15.6 eV (Takahashi *et al.*, 1975) and W_{ph} is 23.7 eV (Doke *et al.*, 1999). Q_e is the charge collection efficiency, which is about 80% at 1 kV/cm drift field, and L_e is the electric field quenching of $S1$, which is 40% at 1 kV/cm drift field (see section 3.3). α_1 and α_2 are the light collection efficiencies for $S1$ and $S2$. They are estimated to be around 10% and 50% separately. Y is the electron extraction yield. At 4 kV/cm in the gas phase, Y is about 50%, as shown in Figure 4.6.

Figure 4.9 is a grayscale image of the event density as a function of proportional and direct light yields. Events are for ^{207}Bi at 1 kV/cm drift field and with 4 kV/cm in the proportional scintillation gap, with Xe gas pressure at 2 atm and d at 0.4 cm. Reading from this plot, the proportional light

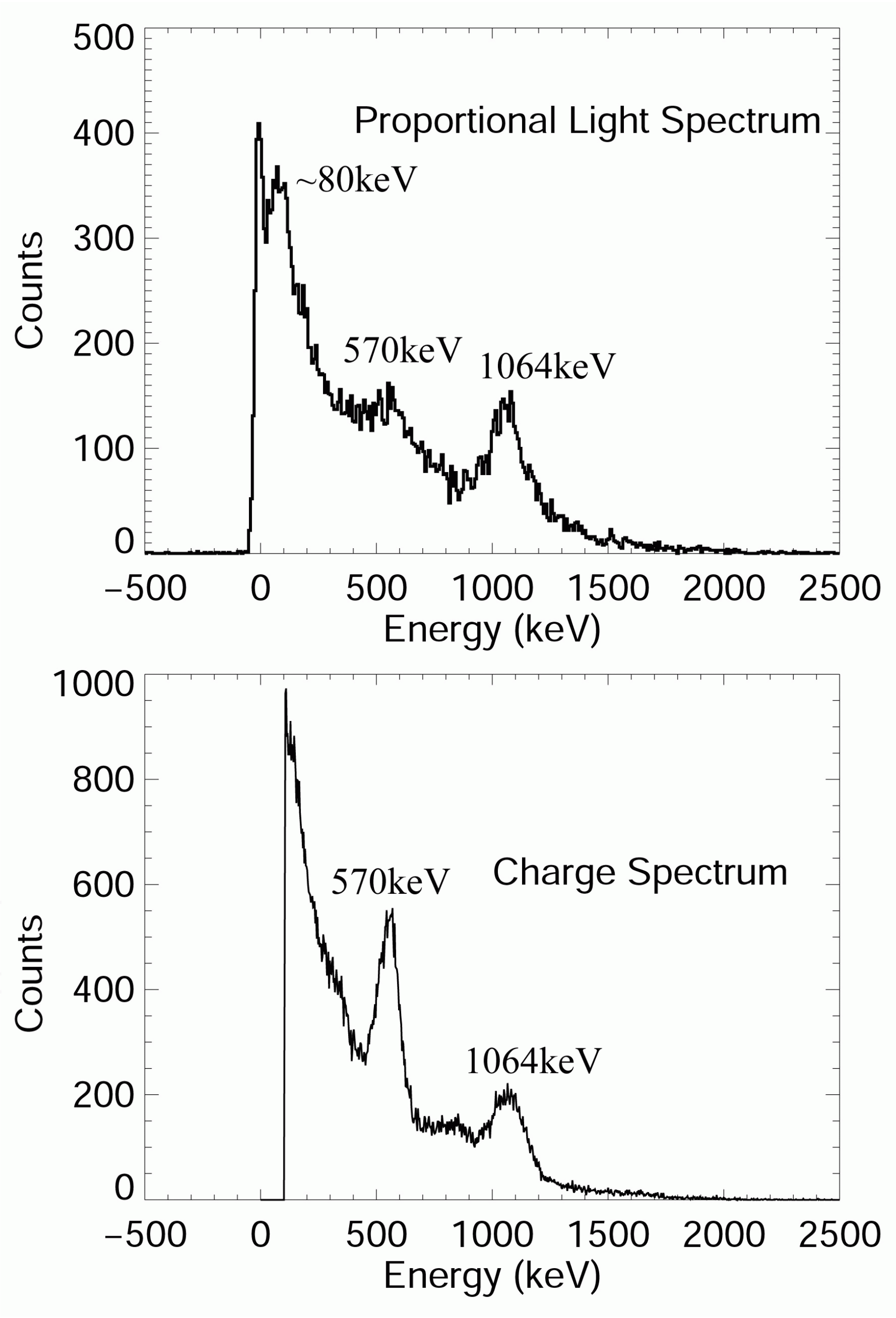

Figure 4.8: Energy spectra from proportional light in dual phase operation (top) and from ionization electrons in single-phase operation (bottom).

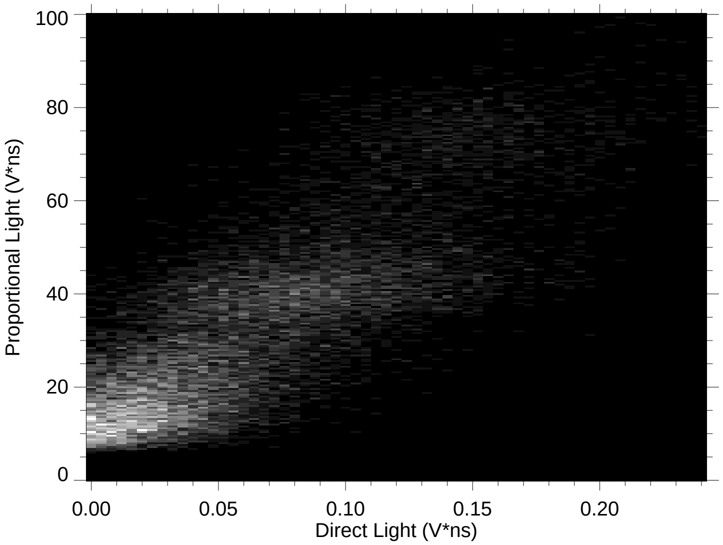

Figure 4.9: Grayscale image of the event density as a function of proportional and direct light yields. Events for a ^{207}Bi source at 1 kV/cm drift field in the liquid and 4 kV/cm in the gas phase.

yield for 570 keV gamma ray is around 40 (unit: $V \cdot ns$), and the direct light yield is around 0.08 (unit: $V \cdot ns$). These two values give the ratio $S2/S1$ of equation 4.2 at about 500. Based on these values and according to equation 4.2, we estimated a rough value of the amplification parameter α to be around 120. Note this value is very crude and we should mention that α is around 70 in (Bolozdynya, 1999).

4.2 Ionization for low energy γ rays

The γ-ray ionization yield in liquid xenon is an important property for liquid xenon particle detectors. Although the $W - value$ has been determined decades ago (Takahashi *et al.*, 1975), the ionization electrons are difficult to be detected fully because the recombination of electrons and ions can't be fully suppressed, even at a very high electric field. The charge collection, $Q(E)/Q_0$ is defined as the percentage of electrons that is finally detected $Q(E)$ over the total electron-ion pair created Q_0.

The charge collection has been measured extensively for 1 MeV conversion electrons, 570 keV and 662 keV γ rays (Aprile *et al.*, 1991a, 2002b) and alpha particles (Aprile *et al.*, 1991b; Ichinose, 1991). There is indication that the charge collection for low energy γ rays (e.g. 122 keV from ^{57}Co) is different from that of MeV γ rays due to the different ionizing density in liquid xenon. The study of the charge collection of low energy γ rays thus becomes interesting, especially for calibration of detectors looking at low energy events, such as for the detection of WIMP dark matter particles.

During the work for this thesis, a measurement of the low energy γ rays (122 keV from ^{57}Co) charge collection was conducted, along with γ rays at other energies (511 keV and 1.27 MeV from ^{22}Na, and 662 keV from ^{137}Cs), at different drift fields (1 and 2 kV/cm).

The measurement was performed with the XeBaby detector (Figure 5.8) in a single-phase operation (i.e. anode was covered by LXe), with two PMTs viewing the sensitive liquid from top and bottom for detecting the scintillation light. High voltage is separately supplied to the cathode and grid. Proper field ratio is chosen to ensure a full charge transmission through the grid. The charge signal was read out from the anode by a preamplifier (ClearPulse 580). The pulses from preamplifier were linearly amplified by a gain of 5 and fed directly into a flash ADC and were saved to computer for further analysis. The full waveforms of both charge and light were recorded. The pulse height of the charge waveform was used to determine the charge yield, which was calibrated with known test pulses, following equation 4.3, where V_γ and V_{to} are the ADC pulse amplitude from γ-ray and test pulse output separately. V_{tp} is the input amplitude of test pulse, and C_{tp} is the test pulse feedback capacitance in the preamplifier. Q_γ is the measured value of charge from γ-ray ionization. The light amplitude is given by the integrated light waveforms (see section 4.6 for a detailed description). The charge and light correlation gives additional information for event selection.

$$Q_\gamma = \frac{V_\gamma}{V_{to}} \cdot (V_{tp} \cdot C_{tp}) \tag{4.3}$$

There are at least five important factors that limit the precision of charge measurement: charge loss due to non optimized *field ratio* for maximum electron transmission through the grid, *ADC offset*, precision of *test pulse feedback capacitance* value, charge loss due to *impurities in liquid xenon* and *charge leakage*, due to field lines not ending-up on anode wires.

In the current measurement, the first three factors were well measured and determined. According to Bunemann's equation (Bunemann *et al.*, 1947), the ionization charges can't be fully transmitted through the grid if the ratio between the field above E_c and below E_d the grid is less than a certain threshold. Here E_c is the collection field between anode and grid, and E_d is the drift field between grid and cathode. A rough calculation from Bunemann's equation requires a field ratio of at least 1.5 for a 100% charge transmission for the grid configuration of XeBaby. However, the geometry of wire meshes as used in XeBaby can't be fully described by the Bunemann's equation. The field ratio was thus determined experimentally and set to the value of 2. The measurement of 662 keV γ-ray charge collection as a function of field ratio shows that at field ratio above 2, the charge collection is saturated, which indicates a full charge transmission through the grid. The ADC offset was measured by using test pulses at different amplitudes. Figure 4.10 shows the pulse height distribution from recorded waveforms for different test pulse amplitudes. The test pulse amplitudes were very precisely measured on the scope from an average of 1000 traces. From the width of the test pulse distribution, the equivalent noise charge (ENC) was calculated, which is about 1200 e^- in this experiment. Figure 4.11 shows that the ADC has a very small offset (-0.13 mV).

To precisely determine the feedback capacitance for the test pulse, a Si detector with a ^{207}Bi source is used. The γ-ray lines (570 keV and 1064 keV) and internal conversion lines (481 keV and 976 keV) from ^{207}Bi are used for the calibration (Figure 4.12). A W value of 3.62 eV (Knoll, 2000) for Si at room temperature is used to calculate the number of charges produced from the γ and electron lines. We use the 976 keV line (corresponding to 43.1 fC of charge) to calibrate the test pulse feedback capacitance. According to equation 4.3, we got $C_{tp} = 1.025$ fC.

Liquid xenon purity is an important factor that affects the charge collection measurement. A bad purity will result in a much lower charge collection. The knowledge of electron lifetime in liquid xenon will give a measurement of

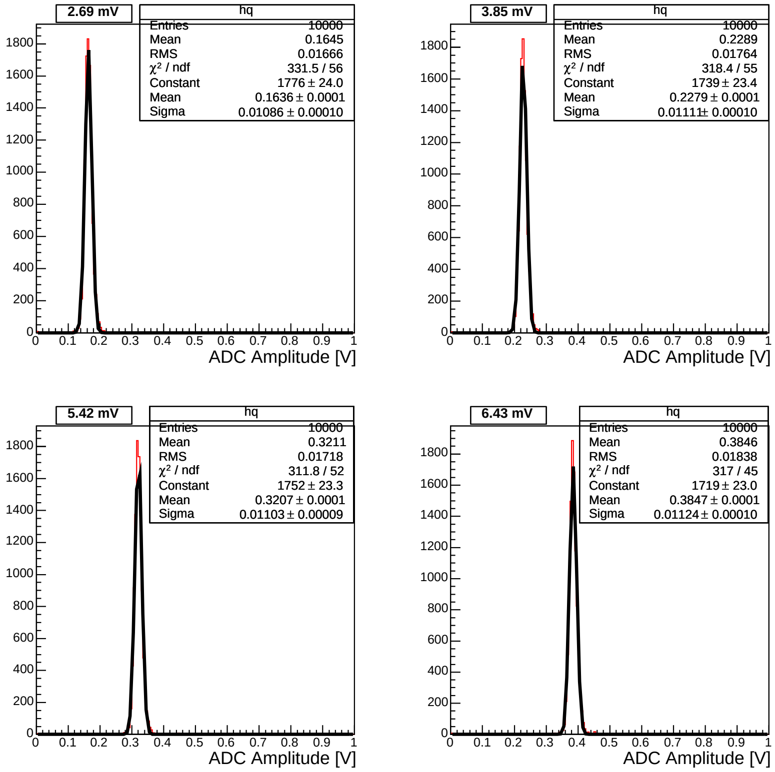

Figure 4.10: Test pulse distribution for different input amplitudes. The input amplitudes, measured from the pulse height of an average of 1000 traces on scope, are shown on the top of each plot.

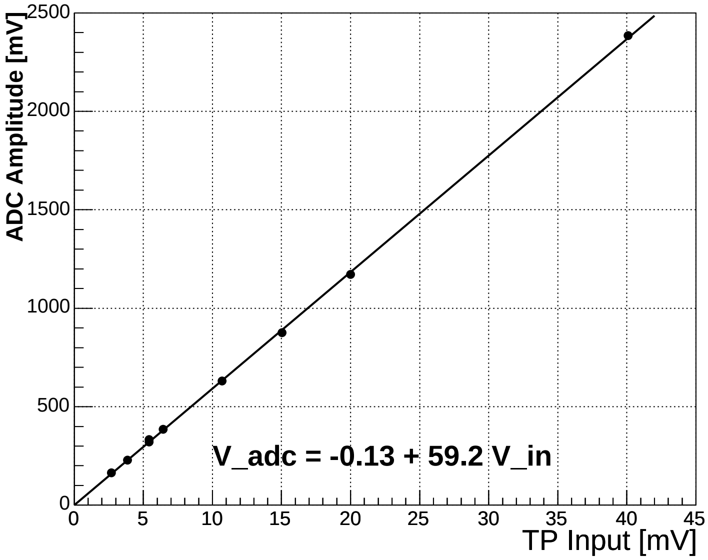

Figure 4.11: ADC amplitude versus input test pulse amplitude. A linear fit determines the ADC offset (-0.13 mV) and gain (59.2).

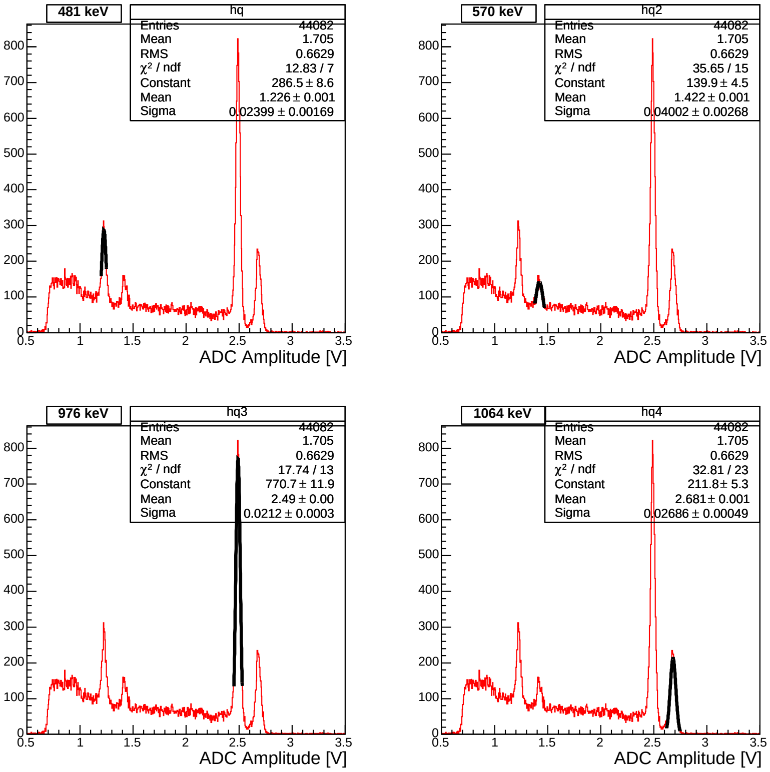

Figure 4.12: Bi-207 spectrum from the Si detector. Each peak was fit by a Gaussian function. The energy of each peak is shown on the top of each plot.

liquid xenon purity, and we can use the lifetime to correct the charge signals. In the current measurement, we use the charge amplitude as a function of drift time from 662 keV γ-ray events to measure the electron lifetime (Figure 4.13). The fit gives an electron lifetime about $t_e = 114\ \mu$s at 1 kV/cm at the time when the measurement was performed. The events were uniformly distributed in the 2 cm drift region. They have an average drift time of $t_d = 5\ \mu$s. Thus a correction factor of $1/\exp(-\mathrm{t_d}/\tau) \sim 1.045$, with an error less than 1%, is needed for the current charge measurement.

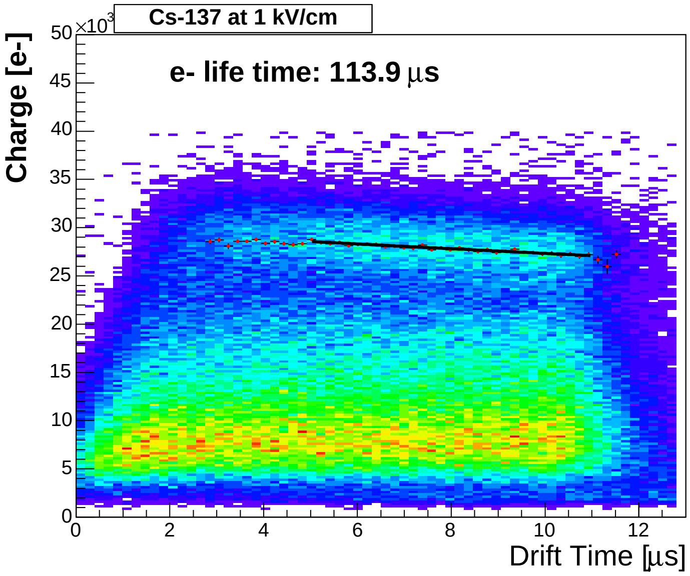

Figure 4.13: Electron life time in liquid xenon at 1 kV/cm. An exponential fit of the 662 keV peak amplitude as a function of event drift time, was used to find the electron lifetime.

The charge spectra from ^{57}Co, ^{22}Na and ^{137}Cs at 1 kV/cm drift field were shown below (Figure 4.14-4.15). For ^{57}Co charge spectrum, we selected

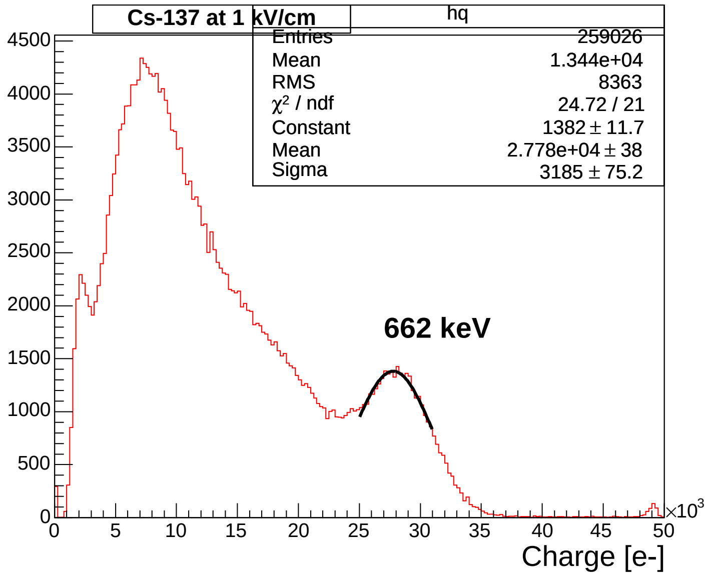

Figure 4.14: Charge spectrum of ^{137}Cs at 1 kV/cm. The 662 keV peak produces an average of 27,800 electrons, before the electron lifetime correction.

events within 1σ of the 122 keV peak from its measured scintillation light distribution.

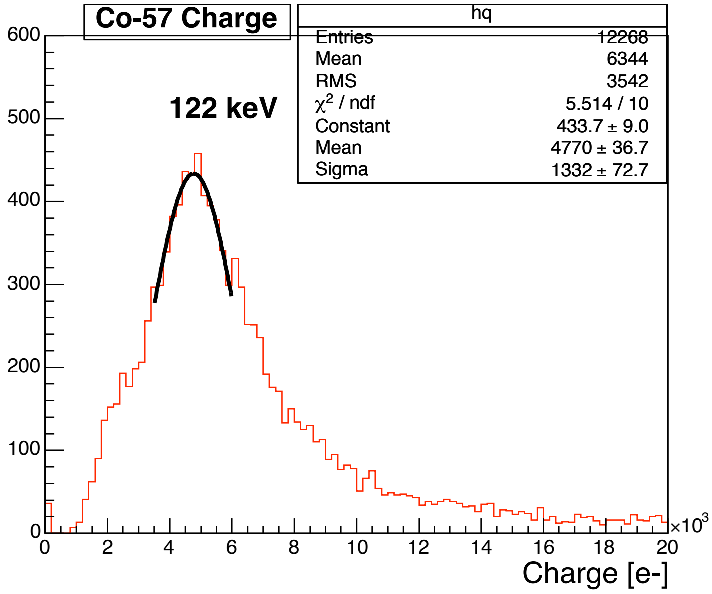

Figure 4.15: Charge spectrum of ^{57}Co at 1 kV/cm (top). The 122 keV peak produces an average of 4770 electrons, before the electron lifetime correction. Events for the charge distribution were selected within one sigma of the 122 keV peak from the light spectrum.

By including the correction factor (1.045) due to LXe purity, Table 4.1 lists the number of collected electrons per keV for different energy γ rays and at different drift fields, together with charge collection $Q(E)/Q_0$ with $Q_0 = \varepsilon/W$. ε is the γ ray energy. The results have been corrected for the electron lifetime measurement by using ^{137}Cs at each field. The statistical errors are less than 3%.

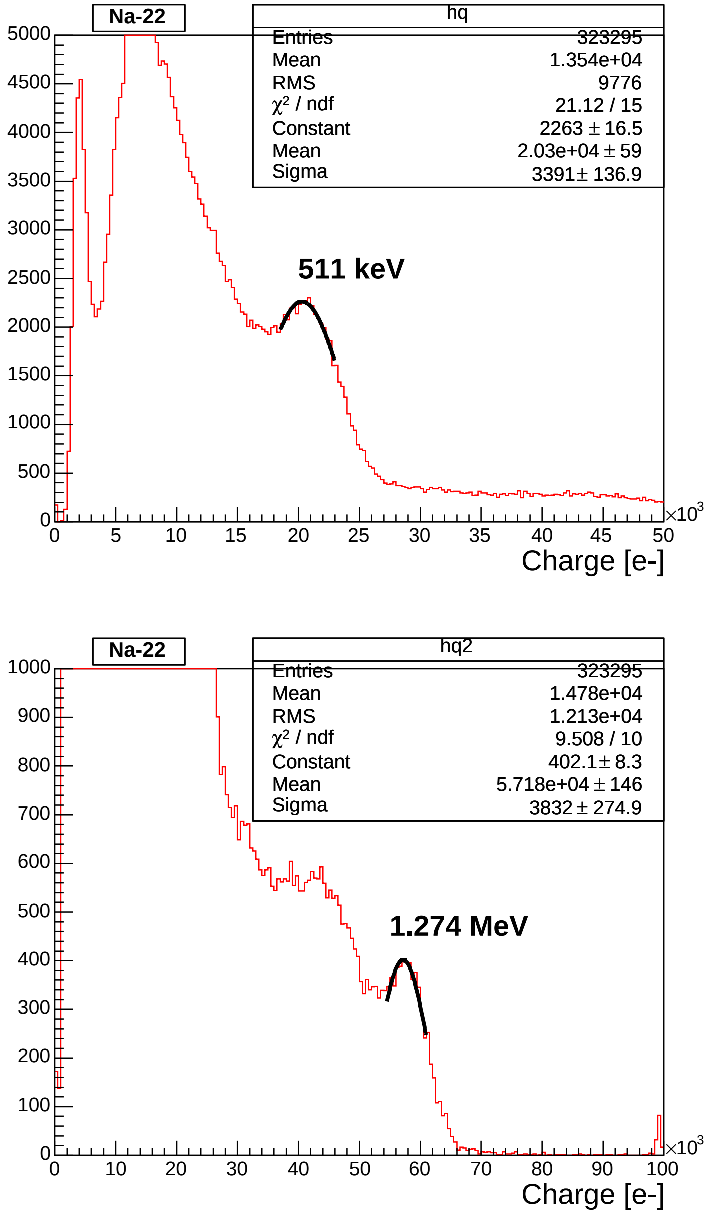

Figure 4.16: Charge spectrum of ^{22}Na at 1 kV/cm. The 511 keV and 1.274 MeV peaks produce an average of 20,300 and 57,200 electrons separately, before the electron lifetime correction.

Table 4.1: Charge collection for γ ray ionization in liquid xenon

Field [kV/cm]	Source	Energy [keV]	Electrons/keV	Charge Collection
1.0	^{57}Co	122	40.8	63.7%
1.0	^{22}Na	511	41.5	64.8%
1.0	^{137}Cs	662	43.9	68.4%
1.0	^{22}Na	1274	46.9	73.2%
2.0	^{57}Co	122	46.0	71.8%
2.0	^{137}Cs	662	46.3	72.2%

4.3 A continuous xenon purification system

One of the challenges of using liquid xenon for low energy event detection is the purity. A small amount of electron-negative impurity, such as O_2, H_2O and N_2O, will suppress the charge collection. Thus to keep a high purity level of the liquid is essential for the XENON experiment. The conventional method of purifying xenon gas is to let it go through a hot getter (SAES) before filling into the detector. On the other hand, impurities internal to the detector will destroy the xenon gas purity and require several cycles of purification and a long period to achieve a good xenon purity. A more efficient way of purifying the xenon is to use a continuous purification system, which was developed under the XENON R&D program.

As illustrated in Figure 4.17, after filling the detector with sufficient amount of liquid xenon, a diaphragm pump is used to take the xenon out

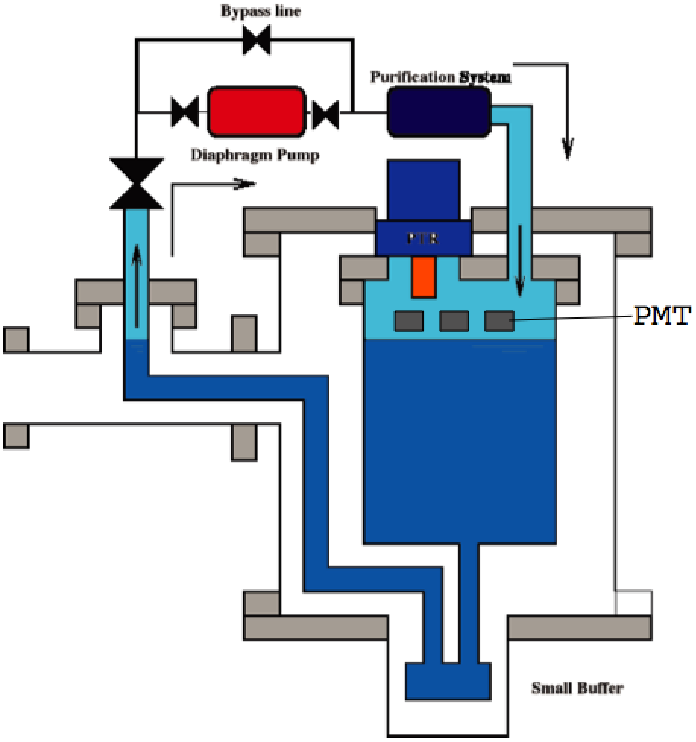

Figure 4.17: A schematics of the xenon recirculation and purification system.

of the bottom of the detector, pass it again through the purification system (SAES getter), and refill and condense the purified xenon gas in the detector. The speed of this setup was only limited by the purification capability of the getter (5 STL/minute). The recirculation system, combined with the actual xenon detector is shown in Figure 4.18.

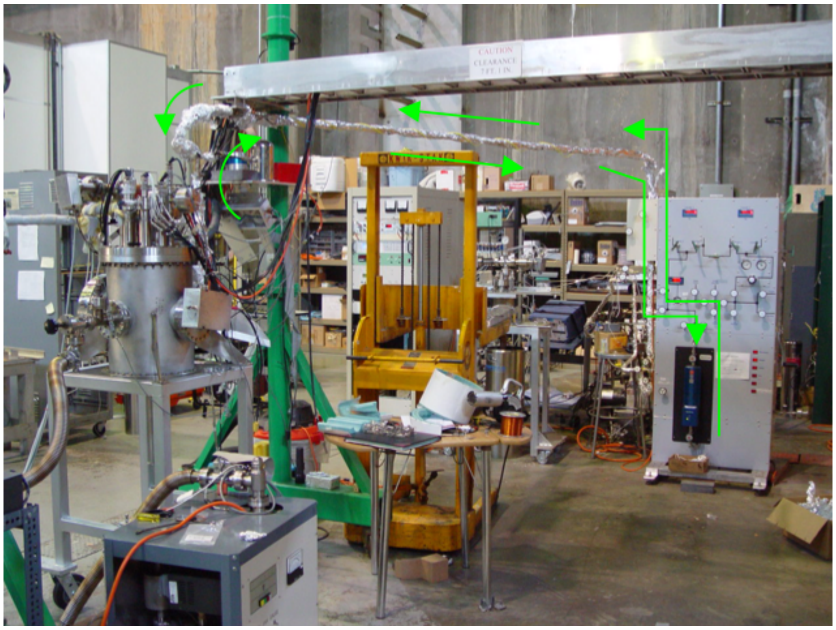

Figure 4.18: A picture showing working procedure of the purification system and detector. The arrows indicate the gas flow directions.

A simple way to check the liquid xenon purity is from the charge collection of a known energy γ ray line(e.g. 662 keV γ rays from Cs^{137}) (see section 3.2 for details). If the impurity level is high, the charge collection is small and possibly decreases at high drift field (Figure 4.19). With the additional signal of the fast scintillation light from the PMTs, the drift time (or event location along Z-axis) can be identified. The electron lifetime τ can be found by fitting the data with a function $Q(t) = Q_0 \times \exp(-t/\tau)$, where $Q(t)$ is the charge amplitude at drift time t (see section 3.2 for an example of the fit). For a detector with a few kg of liquid xenon, it normally takes a few days to reach a good electron lifetime, up to a few hundred μs. Once the detector is clean, the next experiment will require much less time of purification to reach good xenon purity (see Figure 4.19 right).

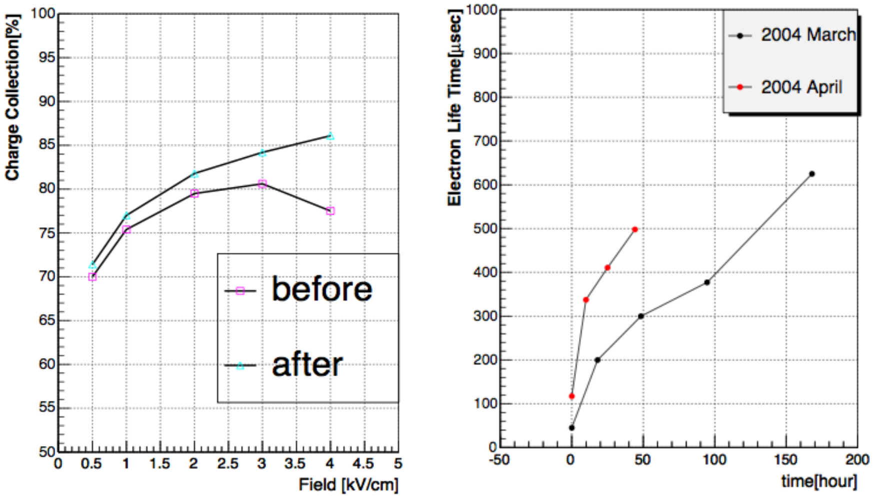

Figure 4.19: Charge collection for ionization of 662 keV γ rays in liquid xenon at different fields, before and after the recirculation (left). Electron lifetime in liquid xenon during recirculation (right).

4.4 Scintillation spectroscopy in liquid xenon

Liquid xenon (LXe) has been used for many applications for its good ionization properties, while applications based on its scintillation light are not fully developed, mostly due to the poor light collection efficiencies (LCE). Some of the current applications based on the LXe scintillation light (e.g. MEG(MEG Collaboration, 2003)) are using photomultiplier tubes (PMTs) in the liquid to optimize the LCE. But adding materials in the liquid xenon will bring impurities, which limit the detection of ionization signals. The future experiments based on liquid xenon require efficient detection of both ionization and scintillation signals at very low energy threshold (XENON Collaboration, 2002), which needs a high light collection efficiency, and at the same time, a high purity level to drift free electrons in the liquid xenon.

Our group started to develop a new system with PMTs immersed in LXe to increase the light collection efficiency (Aprile *et al.*, 2003) a few years ago. But various components on the PMTs brought many impurities into the liquid xenon and it was difficult to detect ionization signals at that time. Recently we have developed a xenon gas recirculation and purification system, which allows to maintain a good purity level (see Section 4.3). With such a system, we were able to construct a chamber with the highest light collection efficiency ever reached by a similar size of liquid xenon detector, while at the same time, we could still keep the liquid xenon at a high purify level for detection of ionization signals.

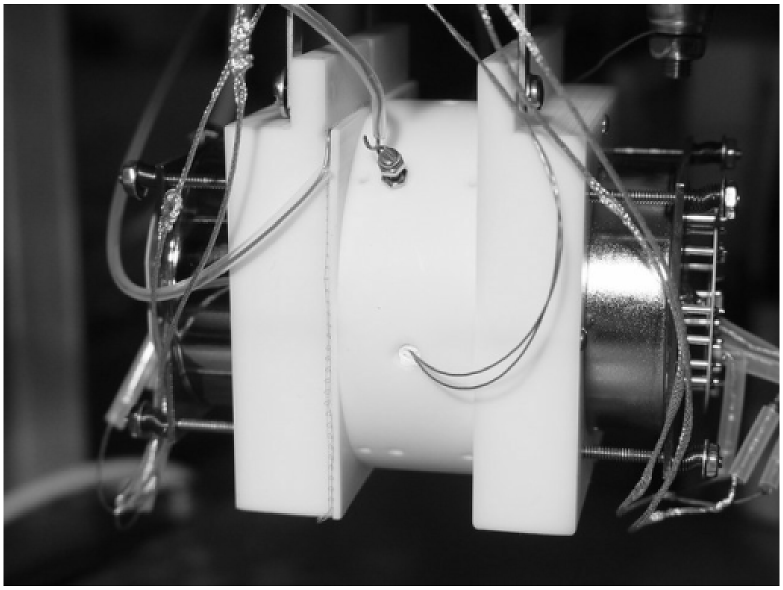

Figure 4.20: The chamber innner structure for simultaneous scintillation and ionization detection (see text for illustration).

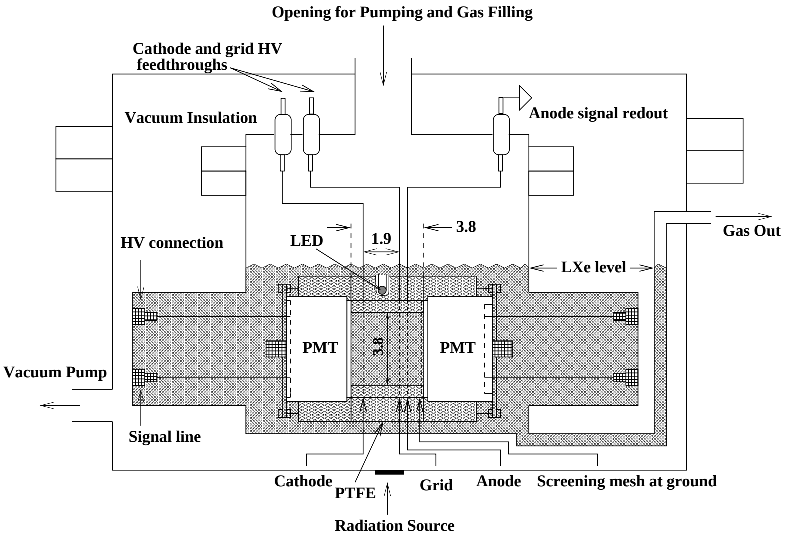

Figure 4.21: The detector schematics for simultaneous scintillation and ionization detection, and measurement of nuclear recoil scintillation efficiency in LXe (see text for illustration).

4.4.1 Detector description and calibration

As shown in Figure 4.20 and Figure 4.21, the gridded ionization chamber electrodes are enclosed by a PTFE tube, viewed by two Hamamatsu R9288 PMTs from the sides. The electrodes are three meshes, which serve as cathode, grid and anode. The optical transparency of these meshes are 95%. By applying high voltages on the cathode and grid, we can collect ionization signals from the anode with a charge sensitive preamplifier. There is one additional mesh covering the surface of the PMT, which is close to the anode mesh. The use of this addtional mesh is to shield the anode from the PMT photocathode, to reduce the induction signals from the PMT on the charge signals (see Figure4.50 for more details).

The 1.9 cm drift region between cathode and grid defines the liquid xenon sensitive volume. The distance between grid and anode is 3 mm. The whole structure is immersed in liquid xenon during the experiment. The structure is mounted in a stainless steel vessel, surrounded by a vacuum cryostat for thermal insulation.

The whole scintillation light waveforms from the two PMTs are recorded by a LeCroy digital oscilloscope (model LT374) with a time sampling of 1 ns. We also record the ionization signals from the pre-amplifier to a LeCroy 2262 waveform recorder, with a time sampling of 200 ns/pt. The ionization signals were used for charge measurement, which also gives the information of the event location from drift time. The coincidence of the two PMTs signals are used for the triggering. Figure4.50 shows the charge and light waveforms of a 662 keV γ event from ^{137}Cs.

The ultra-pure liquid xenon is filled the detector through a high temperature SAES getter, to remove electron-negative impurities. After filling the chamber with enough liquid xenon, the xenon was continuously circulated through the purification system, originally designed for the XENON dark matter search experiment (see (XENON Collaboration, 2004) or section 4.3 for details), to achieve the best xenon purity level. During the recirculation of xenon, we monitored the charge and light yield as a function of recirculation time. Although we noticed significant improvements of the charge collection within a few days, the light yield seemed not change much. This indicates that the attenuation of scintllation light in liquid xenon is much longer than the size of our chamber, even before the purification of xenon.

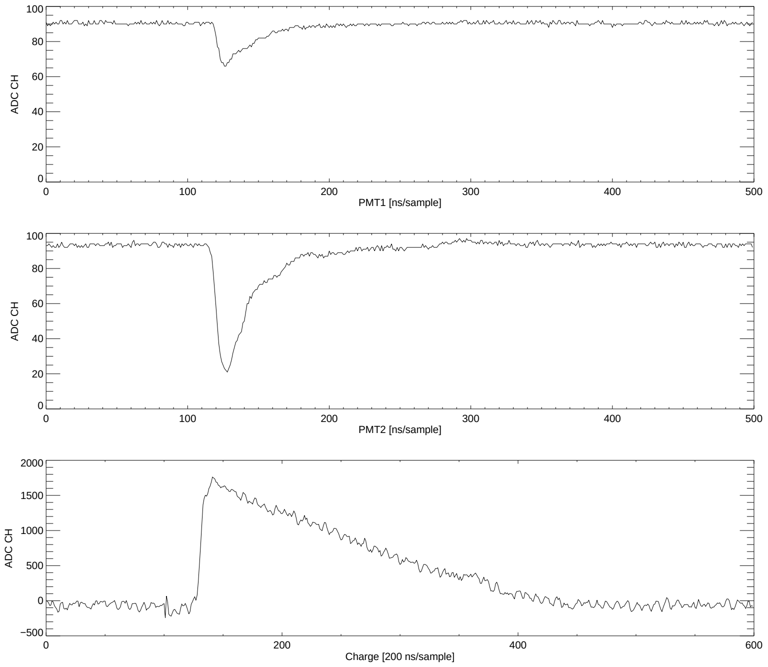

Figure 4.22: A typical event with signals from two PMTs and charge readout. Note that the sampling rate for the PMTs and charge waveforms are different.

$$N_{pe} = \frac{\int V(t)dt/R}{q \cdot g} \tag{4.4}$$

The integrated pulse area (see equation 4.4) of the light waveforms give the number of photoelectrons (N_{pe}) produced by the scintillation light on the photocathodes of the two PMTs. In equation 4.4, $R = 50\Omega$ is the impedence for the PMT signals. q is the elementary electronic charge and g is the PMT gain, which is calibrated by the single photoelectron peaks from LED. A test pulse generator was used for the LED power supply. The test pulse amplitude is adjusted small enough such that the light from the LED generates mostly zero or single photoelectrons in the PMT photocathodes. A typical single photoelectron (PE) spectrum is shown in Figure 4.23. The single PE peak gives about 4.7×10^6 electrons, which is the gain of the PMT at the operating voltage of 900 Volts .

4.4.2 Simulation of light collection efficiency

A Monte Carlo simulation, based on Geant4, has been developed to trace the scintillation photons produced in the liquid xenon. The PTFE reflectivity, the mesh transparency, and UV light absorption (attenuation) length and scattering (Rayleigh) length are taken into account in the simulation. The PTFE reflectivity is more than 99% over the spectral range of 350∼1800 nm (Weidner & Hsia, 1981). Yamashita et al. (Yamashita *et al.*, 2004) reported values of 88%∼95% for the liquid xenon scintillation light. The mesh transparency was measured at $95 \pm 1\%$. The stability of light yield confirms that the absorption length of UV light is very long. We use a value of 100 cm, reported in (Baldini *et al.*, 2005). The scattering length was

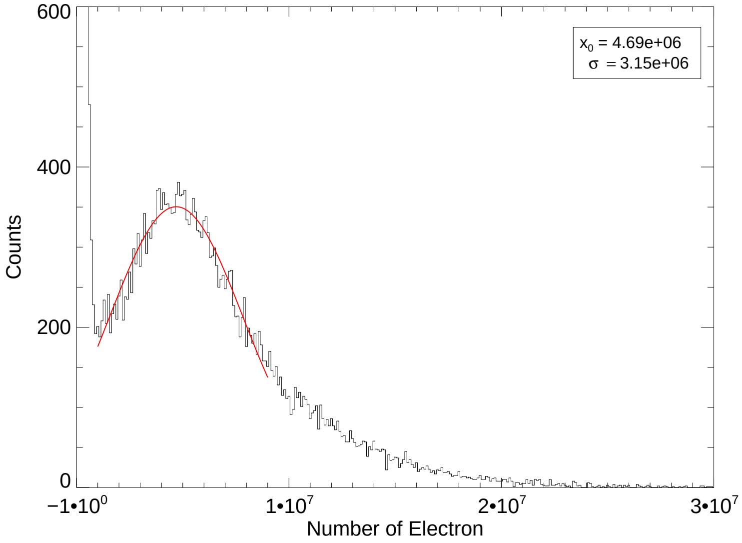

Figure 4.23: Single photoelectron spectrum from Hamamatsu R9288 PMT operated at 900 V.

calculated to be about 30 cm (Seidel *et al.*, 2002). Since the structure in our setup is completely enclosed by the PTFE reflector, and the absorption and scattering lengths are much longer than the scale of our setup, change in their values has very little impact on the light collection efficiency. The major uncertainty for calculating the light collection efficiency is from the PTFE reflectivity.

Figure 4.24 shows the light collection efficiency for events uniformly distributed in the LXe sensitive volume , which is defined as the region between cathode and grid meshes, for PTFE reflectivity at 92% and mesh transparency at 95%. A total light collection efficiency of 67% can be achieved. A 3%(σ) variation was found for events at different locations in the LXe sensitive volume. We performed similar simulations by varying the PTFE reflectivity between 88% and 95% and mesh transparency between 94% to 96%, and an overall light collection efficiency is estimated at $63 \pm 4\%$.

Depending on the event location, the light collection for each of the PMTs varies from 14% to 60% (see Figure 4.25), while combining signals from these two PMTs significantly reduce the non-uniformity. At zero drift field, there is no drift time information from the charge signal. Thus we use a cut based on the two PMT signals asymmetry, which is the signal difference over total, to select those events in the center (mostly between cathode and grid). The drift time selection for the data with field on allows us to select events within 0.4 mm in Z. In Figure 4.25, the light collection reduction due to the absorption from mesh is clearly shown. The down and up triangles are for the right and left PMTs, respectively. The squares are for the combined value. The four vertical dashed lines indicate the location of cathode, grid, anode and

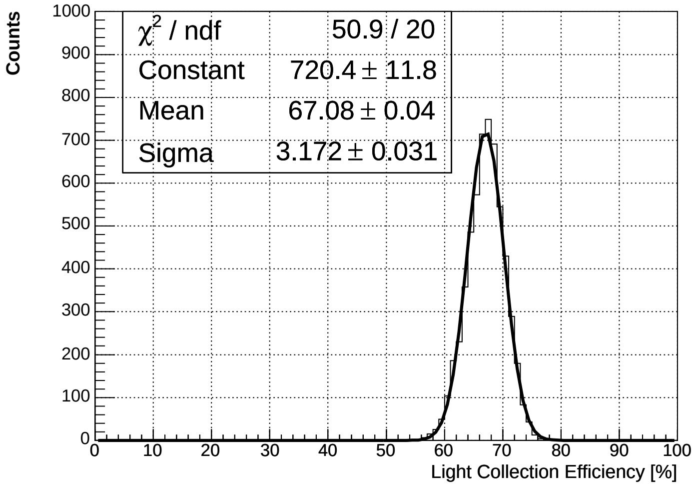

Figure 4.24: Distribution of total light collection efficiency for simulated events uniformly distributed in the LXe sensitive volume.

shielding grid, accordingly.

4.4.3 Scintillation yield and energy resolution

The number of photoelectrons (N_{pe}) from a given energy (E) gamma ray photo-absorbed in LXe can be calculated as,

$$N_{pe} = \frac{E}{W_{ph}} \times L_c \times QE \tag{4.5}$$

where L_c is the light collection efficiency, and QE is the PMT quantum efficiency. Based on the measured value of N_{pe}, we can estimate the value of W_{ph} from the above equation. One of the main errors of this estimation comes from the light collection efficiency. The quantum efficiency of the

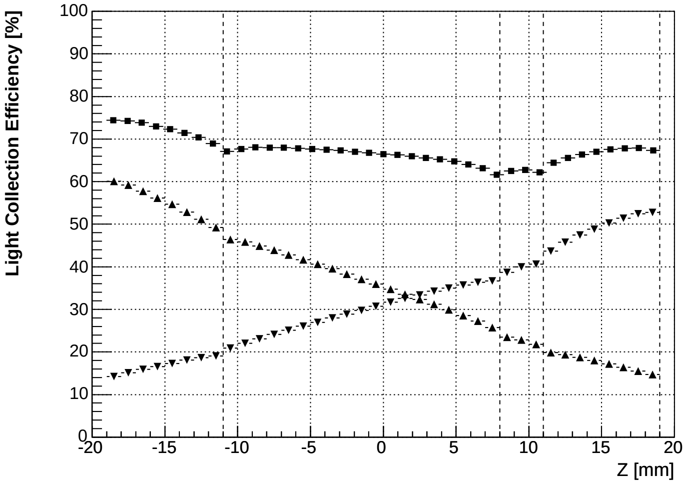

Figure 4.25: Dependence of light collection efficiency with event location in Z from simulation.

PMTs is about $0.7 \times (22 \pm 2)\%$ [2], where a factor of collection efficiency (0.7) is included.

Figure 5.2 is the ^{57}Co scintillation light spectrum in the scale of number of photoelectrons, at zero field. The 122 keV produced about 726 pe, which correspond to about 6.0 pe/keV. The W_{ph} is estimated to be 16.3±1.9 eV. The error comes from the light collection efficiency and PMT quantum efficiency. This meausurement was repeated for 662 keV from ^{137}Cs (Figure 4.28) and 511 keV from ^{22}Na (Figure 4.27) γ rays. The results are listed in Table 4.2.

Our measured energy dependence of the scintillation light yield for gamma rays is shown in Figure 4.29, which is consistent with the results reported in (Yamashita *et al.*, 2004). The linear energy transfer (LET) values are

---

[2] A value of about 20% at room temperature is provided from Hamamatsu Corporation. At LXe temperature, the QE usually increases by about 10%.

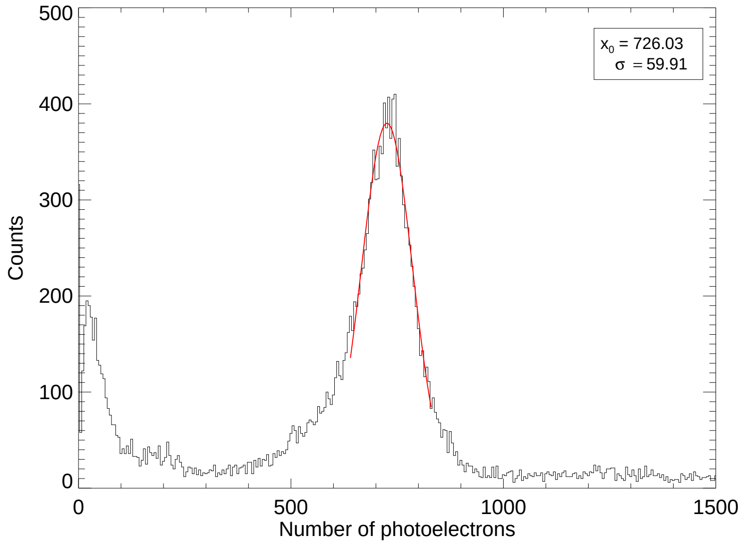

Figure 4.26: ^{57}Co scintillation light spectrum at zero field. A Gaussian fitting of the 122 keV peak shows a light yield about 6 pe/keV.

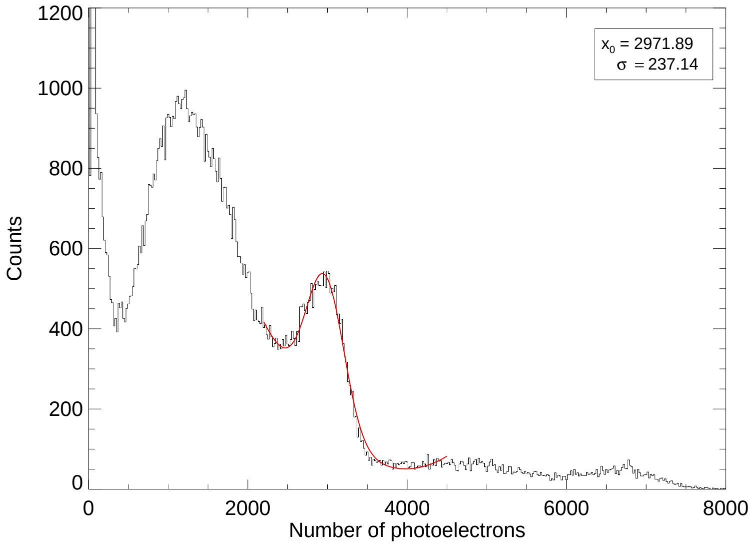

Figure 4.27: ^{22}Na scintillation light spectrum at zero field.

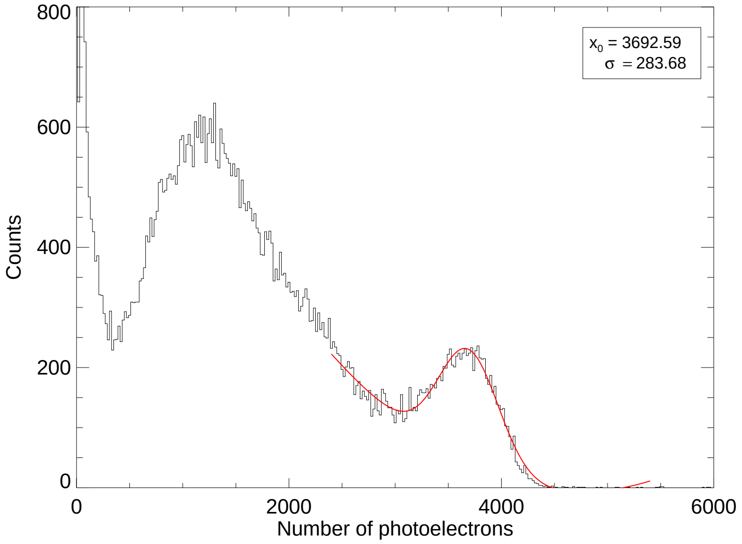

Figure 4.28: ^{137}Cs scintillation light spectrum at zero field.

Table 4.2: Light yield and energy resolution of γ rays in LXe.

Source	Energy [keV]	Light yield [pe/keV]	W_{ph} [eV]	Energy resolution [σ/E]
^{57}Co	122	5.95	16.3 ± 1.9	$8.8 \pm 0.6\%$
^{22}Na	511	5.82	16.7 ± 2.0	$8.0 \pm 0.3\%$
^{137}Cs	662	5.58	17.4 ± 2.0	$7.9 \pm 0.3\%$

obtained from (NIST STAR). The relative light yield from unit energy for 122 keV γ rays is about 7% higher than that for 662 keV γ rays. The relative scintillation yield per unit energy, $(dL/dE)_{rel}$, as a function of LET, dE/dx, is given by the following equation (Doke, 2001),

$$(dL/dE)_{rel} = \frac{A(dE/dx)}{1 + B(dE/dx)} + \eta_0 \tag{4.6}$$

where $(dL/dE)_{rel}$ is normalized to the light yield at the flat top level, measured from relativistic heavy ions. A, B and η_0 are free parameters. In the case of zero LET, $(dL/dE)_{rel}$ is equal to C. At $dE/dx \to \infty$, $A/B + \eta_0 = 1$. The relation between A and η_0, and B and η_0, can be calculated with experimental values from 1 MeV electrons, previously measured. We fit the experimental values, by combining our results, with those from (Yamashita *et al.*, 2004) and (Doke *et al.*, 2002). The best fit gives an η_0 value at 0.55 for low energy gamma rays, such as Co-57. For gamma rays with more than 500 keV, such as from Cs-137, the fitted parameter η_0 prefers a zero value. In any case, the η_0 found here in liquid xenon, is smaller than that in liquid argon ($\sim$ 0.75 (Doke *et al.*, 2002)), which is expected from theoretical considerations (Doke & Masuda, 1994).

4.4.4 Field dependence of light yield

Due to the reduction of electron-ion recombination with an electric field, the scintillation light yield from γ ray electron recoils is significantly reduced at high field. Thanks to the high light collection efficiency in our detector, we were able to observe good light spectra despite the reduction due to the field. Figure 4.30 shows a ^{137}Cs scintillation spectrum at 4 kV/cm field. In

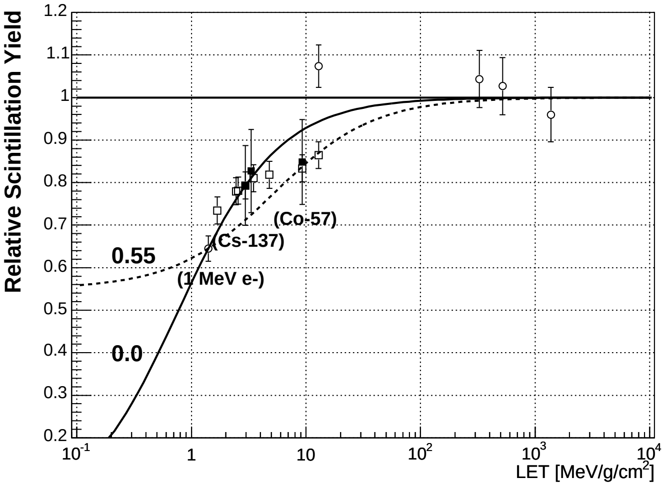

Figure 4.29: LET dependence of scintillation light yield in liquid xenon for different energy γ rays (open squares from (Yamashita *et al.*, 2004) and solid squares from this paper), electrons and relativistic heavy ions (open circles from (Doke *et al.*, 2002)).

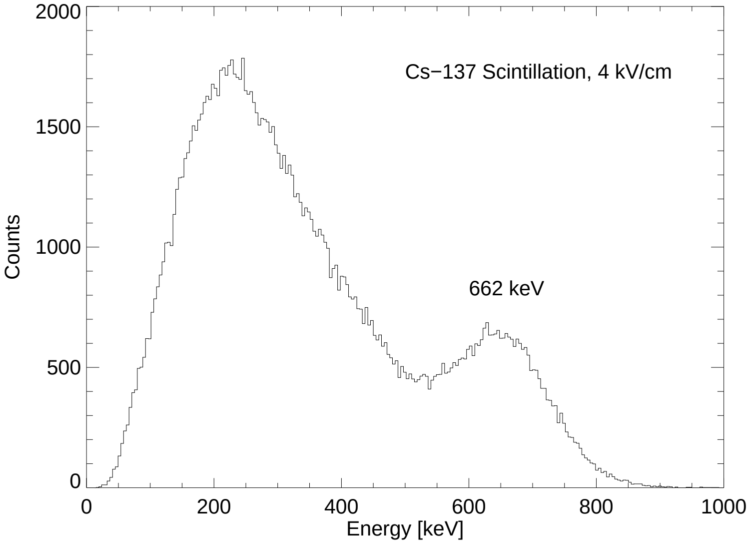

Figure 4.30: ^{137}Cs scintillation light spectrum at 4 kV/cm electric field. The light yield is about 33% of that at zero field. The energy resolution of the 662 keV γ ray peak is at 9.0% (σ/E).

principle, the field dependence of light yield is related to the field dependence of charge collection. A realistic model of the charge collection as a function of field is as follows (Thomas *et al.*, 1988),

$$\frac{Q(E)}{Q_0} = c\frac{ln(1+\xi_0)}{\xi_0} + (1-c)\frac{ln(1+\xi_1)}{\xi_1} \tag{4.7}$$

where $Q(E)$ is the charge collection at drift field E and Q_0 is the maximum charge collection at infinite field. ξ_0 and ξ_1 are parameters describing the charge density along the minimum ionizing part, and at the maximum ionizing part, of an electron track, respectively. $\xi_i = N_0\alpha_i/4a^2u_{-}E$ $(i = 0, 1)$, where E is the magnitude of the drift field, u_{-} is the electron mobility, N_0 is the charge per unit cell of dimension a and α_i are the recombination coefficients.

Based on the scintillation mechanism as described in (Doke *et al.*, 2002), the relation between light yield and charge collection and their dependence on the electric field is written as,

$$\frac{S(E)}{S_0} = \frac{1 + N_{ex}/N_i - Q(E)/Q_0}{1 + N_{ex}/N_i - \chi} \tag{4.8}$$

where $S(E)$ and S_0 are the light yield at field E and zero field, separately. N_{ex}/N_i is the ratio of number of excitons and ion pairs produced by an ionizing particle. χ is the ratio of the number of escaping electrons at zero field and N_i. A simultaneous fit to the scintillation light yield as a function of drift field for 122 keV γ rays (^{57}Co) and 662 keV γ rays (^{137}Cs), by equation 4.8, is shown in Figure 4.31. The best fit parameters obtained are $N_{ex}/N_i = 0.11 \pm 0.05$ and $\chi = 0.47 \pm 0.05$. We note that the N_{ex}/N_i was estimated at 0.06 from the optical approximation by using the absorption spectrum of solid rare gases(Miyajima *et al.*, 1974). This value is rather smaller than our best fit value, but still within the uncertainty. The χ value obtained here is much similar to that reported in (Doke *et al.*, 2002).

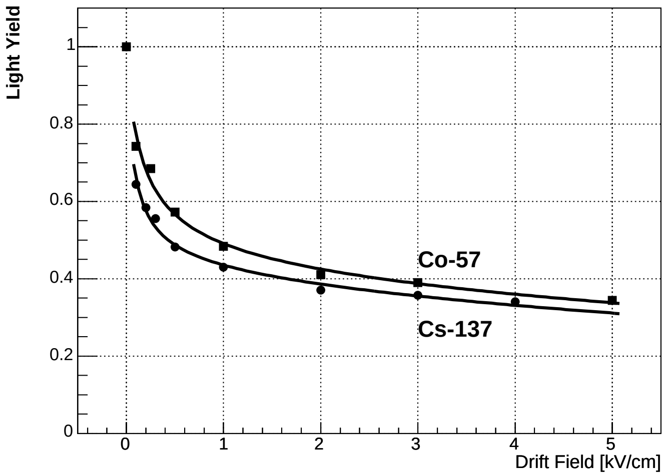

Figure 4.31: Scintillation light yield as a function of field for Co-57 and Cs-137. The light yield is normalized to that at zero field.

The energy resolution of the scintillation spectra was studied for different energies of γ rays (see Figure 4.32). The energy dependence of the resolution is also listed in Table 1, where the errors are from different measurements. The overall energy resolution R of a liquid xenon scintillation detector is a combination of light collection variation due to the detector geometry R_g, the statistical fluctuation of number of photoelectrons from the PMTs R_s, and liquid xenon scintillation intrinsic energy resolution R_i, which can be written as,

$$R^2 = R_g^2 + R_s^2 + R_i^2 \tag{4.9}$$

Based on simulations of our detector, R_g for the 511 keV γ from ^{22}Na and 662 keV γ from ^{137}Cs are about 4.7%, and due to much localized interactions,

R_g is about 2.5% for 122 keV γ from ^{57}Co. R_s can be simply calculated as $R_s = 1/\sqrt{N_{pe}}$, where N_{pe} is the number of photoelectrons from the PMT. The intrinsic energy resolution R_i as a function of γ ray energy is also plotted in Figure 4.32, compared to the results in (Yamashita *et al.*, 2004). Due to the much higher light collection efficiency, the contribution from statistical fluctuation R_s in our chamber is much less than the detector used in (Yamashita *et al.*, 2004). This explains the better energy resolution we obtained for 122 keV γ rays. For higher energy γ rays, the energy resolution contribution from R_s is reduced, leaving the intrinsic energy resolution as the dominant component. The intrinsic energy resolution should not depend on the detector itself, as shown from the consistent results between this work and (Yamashita *et al.*, 2004). We should mention that the intrinsic energy resolution measured here, 6-8%(σ) for 122 to 662 keV γ rays, is higher than that calculated in (Doke, 2001).

The field dependence of the energy resolution was also studied by applying drift fields up to 4 kV/cm. By combining the charge and light signal with a certain correlation angle, a much better energy resolution, compared to that of charge or light spectrum only, can be achieved (see section 4.6).

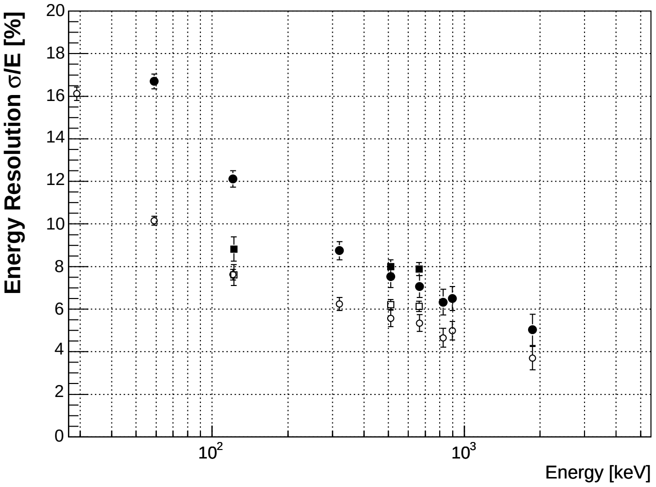

Figure 4.32: Energy resolution dependence on the γ ray energy. The solid symbols are the total energy resolution, while the open symbols represent the intrinsic energy resolution of liquid xenon scintillation light. The squares are measured in this work, and the circle points are from (Yamashita *et al.*, 2004).

4.5 Novel UV photon detectors

Several types of UV photon detectors were investigated during the XENON R&D program. The main purpose is to improve the light collection, in order to achieve a lower energy threshold. These devices include a silicon photomultiplier tube (SiPM), a large area avalanche photo diode (LAAPD) and a CsI photocathode.

4.5.1 Silicon photo-multiplier (SiPM)

The SiPM (Bondarenko *et al.*, 2000; Buzhan *et al.*, 2003) is a promising Avalanche Photodiode (APD) variant consisting of 576 silicon micro pixels per square mm of detector surface. Each pixel is a $21 \times 21\mu\mathrm{m}^2$ independent photon micro-counter operating in limited Geiger mode with gain of 10^6. All SiPM pixels are connected to the common load, so the output signal is the sum of all signals. Thus a proportional signal is created by the sum of the digital micro-APD (pixel) signals. The main features of SiPM are low excess noise factor, low bias voltage (50V), and excellent timing (30 ps for 10 photoelectrons). SiPMs have a low excess noise factor comparable to the Hybrid Photodiode (HPD) (Cushman *et al.*, 2000) because the gain mechanism relies on counting how many of the micro-APDs have fired. The SiPM noise is high at room temperatures, but is reduced significantly when operated at cryogenic temperatures. The photon detection efficiency is similar to a PMT, but comes from the product of a higher quantum efficiency (QE) multiplied by the ratio of sensitive area to the total detector area. It is thus well-suited to a purely solid state solution to LXe scintillation detection. The SiPM is another very promising device, which can detect a small amount of light with a very good single photoelectron detection capability. Here we summarize our first attempt to detect liquid xenon scintillation light with a small SiPM immersed in liquid xenon.

Experimental apparatus

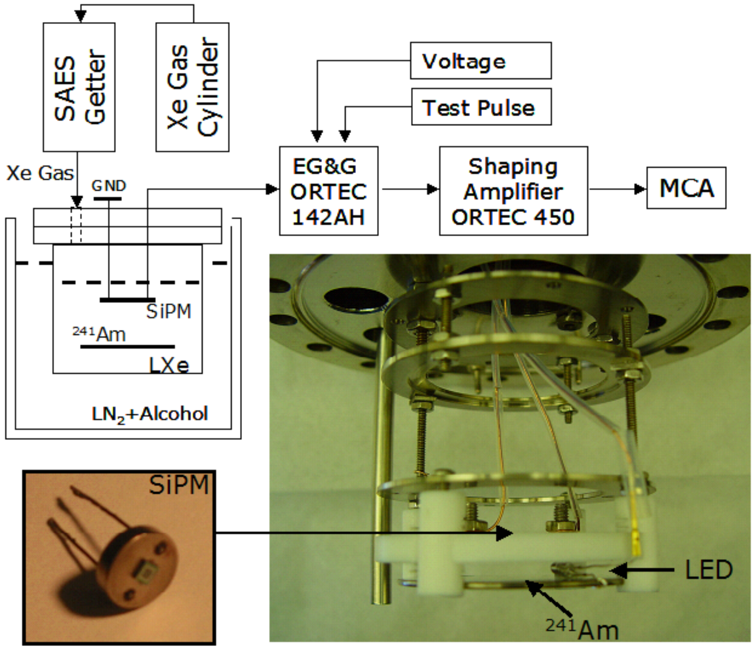

Figure 4.33: The schematics of the detector for the SiPM test.

The LXe detector used for the test of the SiPM is the same one used for testing different light sensors, including the Hamamatsu metal channel PMT (Aprile *et al.*, 2004) and the LAAPD (Ni *et al.*, 2005). The detector consists of a 6 cm diameter stainless steel electrode with a radioactive alpha source ^{241}Am deposited in its center. The 1 × 1mm^2 SiPM (type Z, serial number 217) was mounted on a Teflon support plate facing the source plate. A blue LED was also mounted on the Teflon plate. The distance between source and SiPM was 4.7 mm. The detector was pumped down to a vacuum level of 10^{-8} Torr and baked out for 36 hours before filling with LXe. Xe gas, purified through a SAES getter, was condensed in the detector vessel, cooled by a bath of liquid nitrogen and alcohol mixture at -95^{o}C. Figure 4.33 shows a schematic of detector, gas system and electronics.

The scintillation photons, absorbed by the SiPM, produce photoelectrons which are consequently amplified inside the silicon via a Geiger mode avalanche. The SiPM electrical signal is fed into a charge sensitive preamplifier, followed by an ORTEC 450 shaping amplifier. A test pulse generator is used to calibrate electronics chain system.

Experimental results

The great advantage of a SiPM is that it is self-calibrating, since its single photoelectron sensitivity can be used for calibration. The resulting low amplitude part of the α-source spectrum is shown in Figure 4.34. Note the excellent resolution (low excess noise factor) that allows up to 11 photoelecton peaks to be clearly distinguished. Each single photoelectron peak is fitted using a Gaussian function. The fitted mean value is plotted versus peak number (number of photoelectrons) in Figure 4.35, clearly showing a linear behavior.

We have estimated the SiPM gain g with a calibrated test pulse signal as follows:

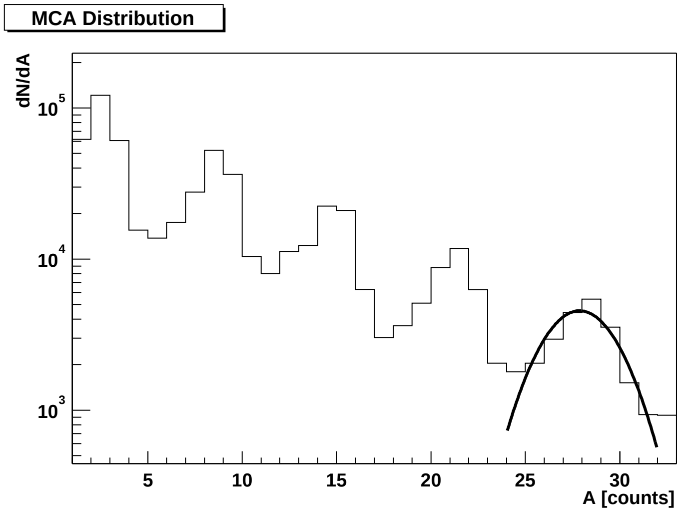

Figure 4.34: Amplitude distribution for ^{241}Am particle scintillations. Low amplitude part of the spectra.

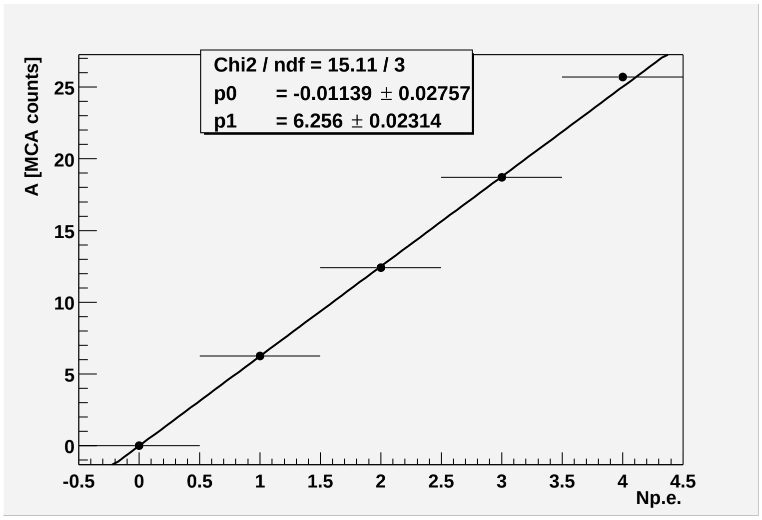

Figure 4.35: Mean amplitude after pedestal subtraction versus peak number. Fit - linear function. The MCA offset from the channel number of zero photoelectron peaks in Figure 4.34 is subtracted.

$$g = \frac{V_t C}{qA} \cdot \frac{M_1}{M_t} \tag{4.10}$$

where V_t and M_t are the test pulse amplitude and channel number in the MCA spectrum, respectively. C is the capacitance of the charge sensitive pre-amplifier. $M_1 \approx 6.2$ is number of channels corresponding to a single photoelectron and q is the elementary electronic charge. $A \approx 27$ is the gain of the amplification system used in this measurement. Based on these values, the SiPM gain is estimated to be around 1.8×10^6 at the operation voltage of 52 V.

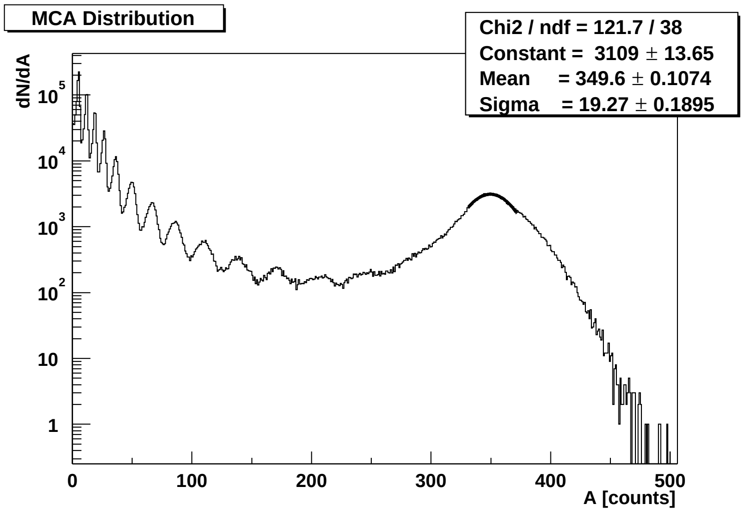

Figure 4.36: Amplitude distribution for ^{241}Am particle scintillations. Fit - Gaussian function.

In Figure 4.36 the ^{241}Am α-source energy spectrum, measured with the SiPM bias voltage at 52 V, is shown. The average number of photoelectrons detected from LXe scintillation light induced by ^{241}Am α particles is determined to be 55 p.e.

The total number of scintillation photons striking the SiPM can be calculated using the energy of α particle (5.48 MeV), the average energy needed to produce single scintillation photon in LXe (19.6 eV for α particle (Doke *et al.*, 2002)), and the geometrical acceptance of the SiPM detector. For the detector geometry used in the tests, the average number of scintillation photons produced by one 5.48 MeV α particle striking the SiPM surface is $N_{ph} = 1006$ photons. Thus the measured photon detection efficiency is $\varepsilon = \frac{55 p.e.}{1006 ph.} = 5.5\%$. The quantum efficiency of the SiPM (QE) can be calculated as $\varepsilon = QE \times A$, where A is the active area ratio of the device. Assuming $A = 0.254$ (Buzhan *et al.*, 2003), we infer a $QE = 22\%$ including the probability of initiating the Geiger avalanche.

4.5.2 Large area avalanche photodiode (LAAPD)

In recent years, large area avalanche photodiodes (LAAPD) have been successfully applied as photo detectors for a variety of scintillators (Lopes *et al.*, 2001; Kapusta, 2002; Moszynski *et al.*, 2003), including liquid xenon (LXe) (Solovov *et al.*, 2002). On the other hand, for a practical application of LAAPDs, especially for dark matter searches, several issues remain to be addressed. The primary concern is the capability of a light readout based on LAAPDs to achieve the low energy threshold of a few tens of keV required for high sensitivity. Other issues include long term stability of operation, impact on LXe purity, as well as readout complexity and cost. The experiments presented here aimed at confirming the high QE for LXe scintillation reported in the literature, and at verifying the compatibility of LAAPDs immersed in the liquid with the requirement to detect tiny ionization signals, at the single electron level.

Experimental setup

The 16 mm diameter, windowless LAAPD tested in these experiments was mounted inside a gridded ionization chamber, filled with high purity LXe. A photograph of the assembled electrodes and LAAPD is shown in Figure 4.37. The cathode is a 6 cm diameter stainless steel plate with either a gamma ray source (^{207}Bi) or an alpha source (^{241}Am) deposited on its center. The shielding grid and the anode grid are made with stretched wires on stainless steel frames, with a thickness of about 0.8 mm. The wire spacing is 2 mm, and the wire diameter is 60 μm. The separation between cathode and grid is 1 cm, which defines the maximum drift gap for ionization electrons. The grid to anode separation is 3 mm. The spacing between electrodes was maintained with rings made of PTFE, for its high reflectivity in the UV region (Yamashita *et al.*, 2004). The LAAPD, originally glued by API Inc. on a thin ceramic substrate, was mounted on a PTFE disk, facing the anode grid at a distance of 6 mm above. We note that the LAAPD had been exposed to air for several months prior to its use in LXe. Hermetic feedthroughs are used for cathode and grid HV lines and for anode signal readout via a charge sensitive amplifier. Additional feedthroughs are used to bias the LAAPD and to connect its output to a separate charge sensitive amplifier.

A schematic drawing of the detector system and electronics readout is shown in Figure 4.5.1. The ionization electrons, which are created from gamma rays or alpha particles in the drift region, are drifted upward by the applied electric field, and are collected by a charge sensitive pre-amplifier

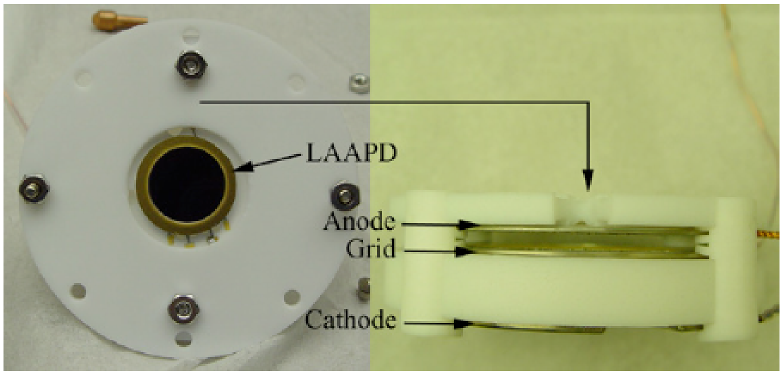

Figure 4.37: Photograph of the assembled gridded ionization chamber electrodes, with the LAAPD mounted 6 mm above the anode grid.

(ClearPulse Model 580) connected to the anode. The scintillation light hits the LAAPD and produces photoelectrons, which are amplified by the avalanche process. The avalanche electrons are collected by an AmpTek 250 pre-amplifier. The charge and light signals, either from ClearPulse 580 or AmpTek A250, are fed into a low-noise shaping amplifier (ORTEC 450). The amplified signals are further fed into a PC-based multi-channel analyzer (MCA) for spectroscopy analysis. Known test pulses are used to calibrate the DAQ system, for both light and charge signals. The capacitances in the pre-amplifiers were calibrated with a silicon detector. We used an open bath cooling apparatus with a liquid nitrogen and alcohol mixture to condense the xenon gas. The vessel enclosing the assembled detector was filled with high purity LXe, covering completely the LAAPD.

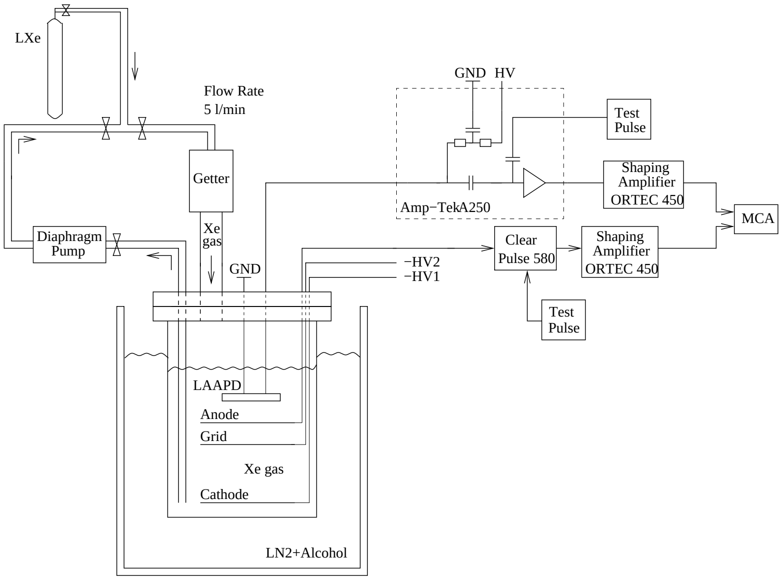

Figure 4.38: DAQ schematics for the LAAPD setup for scintillation and ionization detection in liquid xenon.

Experimental measurements

The gain of the LAAPD was measured in a different set-up configuration, which optimizes the light collection efficiency by placing the LAAPD very close (about 3.5 mm) to the source plate, at -95°C (Figure 4.39). The direct scintillation from a 5.5 MeV alpha source (^{241}Am) was measured as a function of applied voltage on the LAAPD up to about 1500 V. Unitary gain was determined from the average amplitude in the 300 to 500 V range (Fernandes *et al.*, 2004a). The typical reduction in applied voltage, for a constant gain, when reducing temperature (Solovov *et al.*, 2000) was observed, corresponding to an average voltage variation of about 2.4 V/°C at a gain of 100.

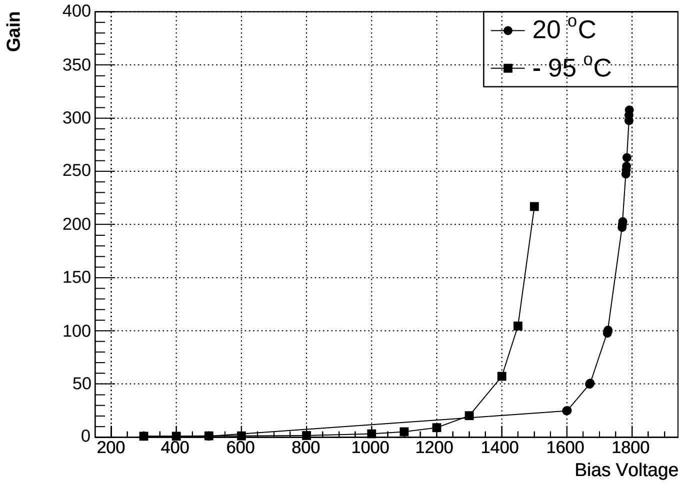

Figure 4.39: LAAPD gain as a function of bias voltage measured at liquid xenon (-95°C) and room temperature (20°C).

The scintillation light spectrum of the ^{207}Bi radiation in LXe was measured, as shown in Figure 4.40. Due to the small liquid xenon sensitive volume, the energy from most of the 1064 keV gamma rays of ^{207}Bi is not fully deposited. The second peak on the spectrum is mostly contributed by the 976 keV internal conversion electrons. As the gamma rays interact at any point in the liquid xenon active volume, light collection in the LAAPD varies accordingly to the interaction position. Using PTFE reflectors, the variation in light collection can be reduced to less than 1%, without compromising the energy resolution. The energy resolution for the 976 keV electrons of ^{207}Bi is 7.5% (σ), which is comparable to the energy resolution obtained earlier by using a PMT in the same chamber with similar geometry (Aprile *et al.*, 2004). The spectrum was accumulated at zero electric field to maximize light output from LXe.

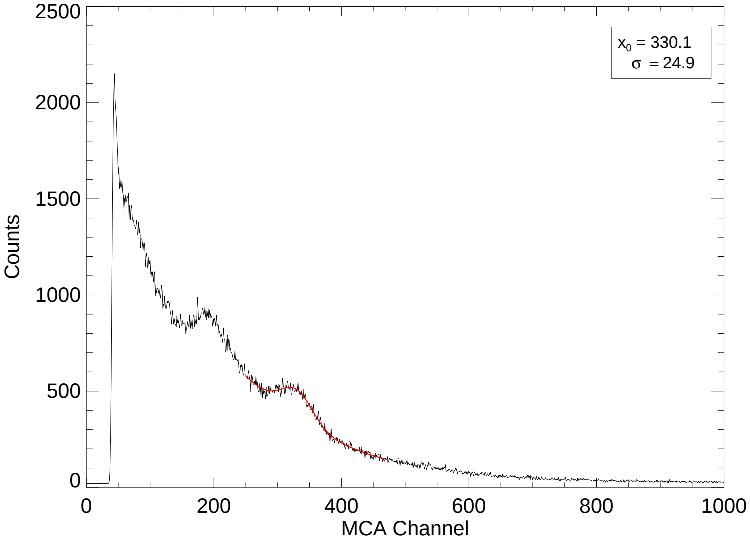

Figure 4.40: Scintillation light spectrum from ^{207}Bi at zero electric field measured by LAAPD.

To better evaluate the LAAPD performance in liquid xenon, larger amounts of scintillation light are necessary. The 5.5 MeV alpha particles from ^{241}Am provide typically one order of magnitude larger scintillation pulse and their interaction is very localized in liquid xenon, contributing to a clear scintillation light spectrum. To get the best possible energy resolution, the gain of LAAPD and shaping time on the amplifier were optimized and finally a gain of 57 was selected for this measurement as shown in Figure 4.41. A very good energy resolution of 2.6% (σ) (with PTFE walls) and 3.0% (σ) (without PTFE walls) was obtained. To compare the performance of LAAPD with other photon detection devices, the alpha spectrum was also measured using a 2-inch diameter Hamamatsu R9288 PMT with less than 20% QE at 178 nm wavelength. A value of 2.5% energy resolution was obtained.

The energy resolution as a function of LAAPD gain can be written as follows,

$$\sigma/E = \sqrt{\left(\frac{N_e}{N_0 M}\right)^2 + \frac{F-1}{N_0} + \delta^2} \tag{4.11}$$

The first term in this equation is contributed from electronic noise. N_e is the noise equivalent charge, which can be measured from the distribution of a known test pulse. N_0 is the number of primary electron-hole pair produced from the scintillation light in the photodiode surface. M is the LAAPD gain. The second term is from the fluctuations of the gain and is inherent to the electron avalanche process of the LAAPD, where F is the excess noise factor. The experimental value for F is approximately written as $F = 1.7003 + 0.0021M$ (Fernandes *et al.*, 2004b) for $M > 30$. The third term

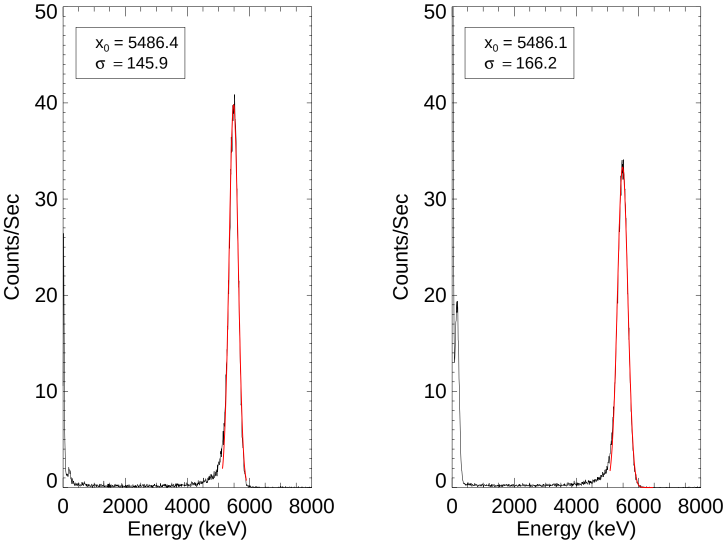

Figure 4.41: ^{241}Am scintillation light energy spectrum from 5.5 MeV alpha particles detected by the LAAPD in LXe.

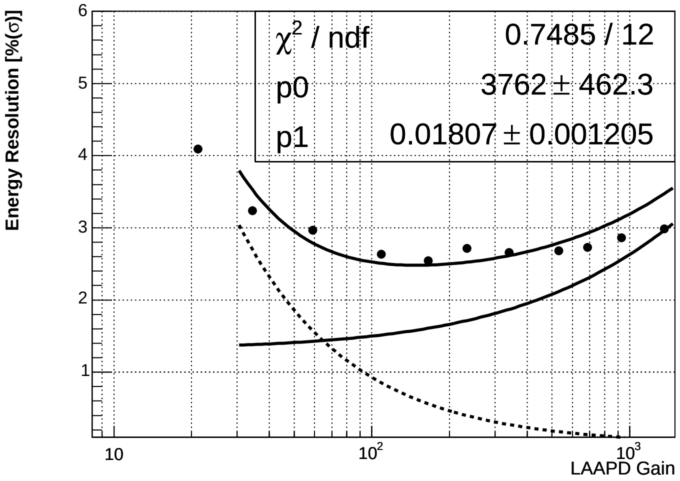

Figure 4.42: Energy resolution as a function of LAAPD gain (thick line with experimental data points).

δ is contributed from the scintillation process in the liquid xenon, including statistical fluctuations of scintillation photon production, and photoelectrons created in the LAAPD. Using the gain measurement with the LAAPD at 3.5 mm from the source plate, we fit the results with the above equation with N_e and δ as free parameters (Figure 4.42), while fixing F from the experimental value (Fernandes *et al.*, 2004b). The noise equivalent charge N_e from the fit agrees well with the measured value with a calibrated test pulse. From the fitted values, we infer that the statistical fluctuations contribute 1.8% to the energy resolution, with a contribution of about 1.6% ($1/\sqrt{N_0}$, $N_0 \approx 4000$) from fluctuations in the number of photoelectrons.

Quantum efficiency

The quantum efficiency (η) of a LAAPD can be calculated by the following equation,

$$\eta = \frac{N_0}{N_p} = \frac{N_d/M}{\alpha N_{tot}} \tag{4.12}$$

Here N_0 is the number of photoelectrons from the LAAPD, N_p is the number of photons reaching the LAAPD surface, M is the LAAPD gain, N_d is the number of electron charges detected by the pre-amplifier and N_{tot} is the total number of scintillation photons produced by an event. N_{tot} is approximately equal to E/W_{ph}, where E is the energy of the event, and W_{ph} is the average energy required to produce a scintillation photon in liquid xenon. The W_{ph} values are 21.6 eV (Doke *et al.*, 2002) and 19.6 eV (Doke *et al.*, 1999) for gamma and alpha events respectively. α is the light collection efficiency, which is defined as the percentage of the total LXe light yield reaching the LAAPD surface. We have estimated the light collection efficiency by using a light tracing simulation program in GEANT4 (GEANT4) with the assumptions listed in Table 4.3.

The estimated light collection efficiency from the simulation is $7.0 \pm 0.7\%$ for the structure with 1 cm thick PTFE wall between the cathode and grid. The error indicates the different reflectivity values used in the simulations. In the case of no PTFE walls, the light collection efficiency was calculated by simply using the solid angle for alpha particles and ignoring the reflectivity of stainless steel. As result, 3.3% light collection efficiency was obtained. Considering a 20% stainless steel reflectivity, 4.1% light collection efficiency

Table 4.3: Physical parameters for the light collection simulation.

Item	Value	Ref.
PTFE reflectivity	90-95%	(Yamashita *et al.*, 2004)
Light absorption length	100 cm	(Baldini *et al.*, 2005)
Rayleigh scattering length	30 cm	(Seidel *et al.*, 2002)

was obtained. In order to estimate the number of photons incident on the LAAPD surface, an average value for light collection efficiency was used, as presented in Table 4.4.

From the above considerations, we estimated the QE of the LAAPD for different measurements, which are shown in Table 4.4. The main uncertainty is from the estimation of the light collection efficiency. The different values obtained from electron and alpha events may be due to the uncertainty in W_{ph} and the LAAPD gain values. In conclusion, we use the average of the QE values from the electron and alpha measurements, which is $45 \pm 5\%$.

Field dependence of light yield

The liquid xenon scintillation light yield depends on the strength of the applied electric field (Doke *et al.*, 2002). The dependence of the scintillation yield of liquid xenon for alpha particles has been measured by the Columbia group several years ago, using an external PMT coupled to a LXe volume via a CaF_2 window (Aprile *et al.*, 1990). In the current setup, we were able to measure this field dependence with a LAAPD. For comparison, we also

Table 4.4: LAAPD quantum efficiency measured from different sources.

Measurement	PTFE	Light Col. Eff.(%)	Bias V	APD Gain	QE(%)
976 keV e^-	with	7.0 ± 0.7	1460	146	50 ± 5
5.5 MeV α	with	7.0 ± 0.7	1400	57	39 ± 4
5.5 MeV α	without	3.7 ± 0.4	1400	57	39 ± 4

measured this field dependence with a Hamamatsu R9288 PMT immersed in liquid xenon, in the same chamber. Figure 4.43 shows the combined results.

The LAAPD gain varies considerably with temperature, and our simple alcohol-LN_2 cooling bath does not keep the liquid temperature stable enough to avoid temperature dependent gain variations. The gain of the PMT is not much affected by such small temperature fluctuations. The data from the LAAPD and the PMT are in good agreement, but the result with the LAAPD has more fluctuations due to its acute temperature dependence, which is obvious from the curve.

Impact of LAAPD on LXe purity

One challenge involving photon detection devices immersed in liquid xenon is their compatibility with the high purity required for electron drift, if a combined charge and light readout is implemented. Our experience with LXe detectors shows that the light yield of LXe is not very sensitive to the purity level, unlike the charge yield. Many efforts have been made in the

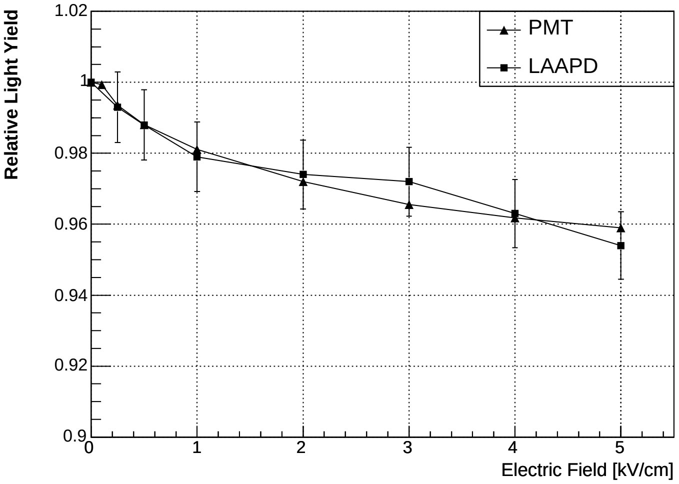

Figure 4.43: Field dependence of light yield for ^{241}Am 5.5 MeV alpha particles.

past to detect both ionization and scintillation, using PMTs, in liquid xenon (Aprile *et al.*, 2003). Currently we have developed a xenon recirculation and purification system (XENON Collaboration, 2004), which continuously removes impurities from the liquid xenon during experiment. Depending on the size of the detector, we can achieve a sufficient purity level for drifting ionization electrons within two to tens of hours. During the first experiment with the LAAPD immersed in the LXe, we used this recirculation system to purify the xenon, continuously. We measured the 976 keV peak position of the ^{207}Bi to monitor the charge collection. Within a few hours of recirculation and purification, we achieved a high charge collection of 75%. The ionization spectrum of ^{207}Bi at 1 kV/cm drift field shown in Figure 4.44 is comparable to that measured in a liquid xenon ionization chamber with an external PMT (Aprile *et al.*, 1991a). From the second experiment, we observed the same level of charge collection even without using the recirculation system, which indicates that the LAAPD is clean and does not bring any impurities into the liquid xenon.

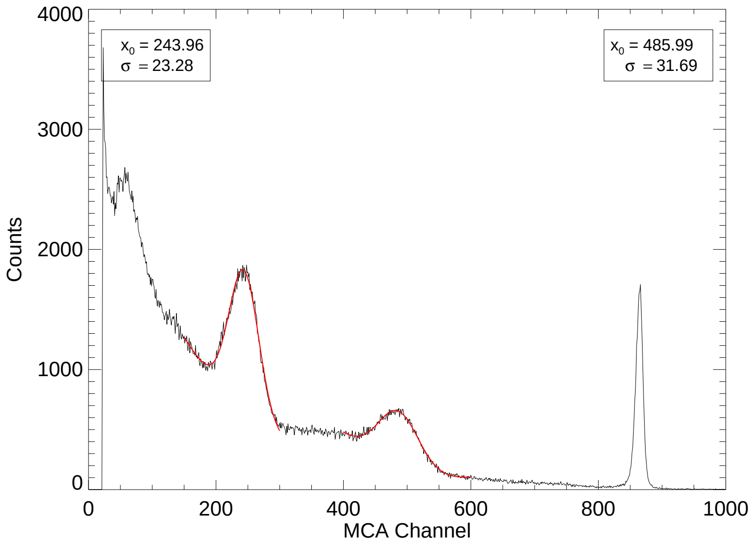

Figure 4.44: Ionization spectrum from ^{207}Bi radiation in liquid xenon at 1 kV/cm drift field with an LAAPD immersed in the liquid.

4.5.3 CsI photocathode

One of the approaches proposed for the XENON detector is to use a CsI photocathode on the bottom of the liquid xenon drift volume, in order to achieve low energy threshold by increasing the detection of direct scintillation light (S1), while minimizing radioactivity intrinsically very high in PMTs, as well as cost. This requires both stable operation of a CsI photocathode in liquid xenon, and good quality cathode with high quantum efficiency. The experiment with a CsI photocathodes was performed within the XENON R&D program, by using a dual phase xenon detector with about 1 kg sensitive liquid xenon target (Figure 4.45). The chamber with 3.7 cm drift length, was equipped with an 8 x 8 cm^2 CsI photocathode on the bottom. Seven 2-inch-diameter PMTs (Hamamatsu R9288) were installed in the gas phase, to detect the direct scintillation signal (S1), proportional scintillation signal (S2), and proportional scintillation signal from extracted photoelectrons from CsI photocathode (S3).

A recoil in the liquid xenon sensitive volume (LXeSV) produces both scintillation and ionization signals. The direct scintillation light is detected either by the PMT array (S1) on the top in the gas phase, or the CsI photocathode (CsIPC) on the bottom in the liquid phase. The ionization electrons drift under the applied electric field E_d and are extracted from the liquid to the gas phase, where they produce proportional scintillation light, which is also detected by the PMT array (S2). The photoelectrons from CsIPC, produced by the direct scintillation light, drift up the whole liquid xenon gap, and again produce proportional light. The PMT array detects this light as S3. The photon-electron-photon process keeps going on if no external interference is used to stop the feedback, which will result in a larger and larger S4, S5, etc.. We used the HV switching device (Model PVX4130 from Directed Energy, Inc.) to stop the signal up to S4 in the experiment. A typical waveform from 122 keV gamma rays is shown in Figure 4.46. The signal size distributions for S1-S4 are shown in Figure 4.47.

The integrated area for each signal (S1-S4) corresponds to the number of photoelectrons (see equations below). The meaning and values of the symbols

Figure 4.45: The picture on the top shows the vacuum cryostat integrated with gas filling line and a cryogenic cooler. The chamber structure and an array of seven PMTs on the top are shown below.

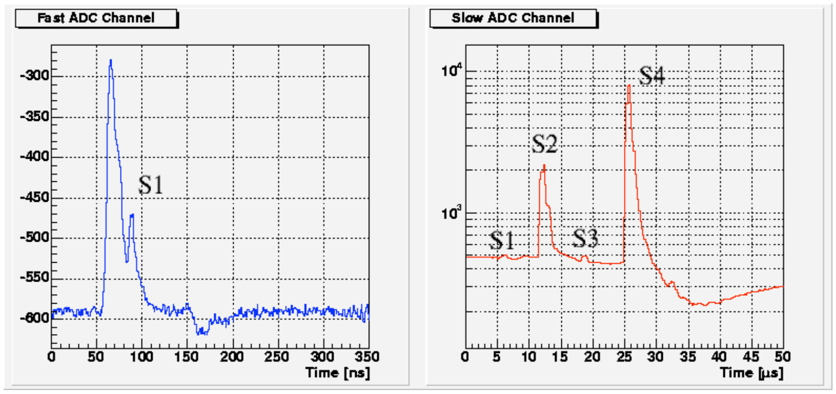

Figure 4.46: A typical waveform for 122 keV gamma ray from Co-57 showing S1-S4 signals.

are listed in Table 4.5. α_{1-4} is from simulation. E is the recoil energy, W and W_{ph} are the average energies to produce one electron or photon in liquid xenon.

$$S1 = \alpha_1 Q_{PMT} n_p \tag{4.13}$$

$$S2 = (\alpha_2 Q_{PMT})(\gamma_{gas}\varepsilon_{ex}\varepsilon_d)n_e \tag{4.14}$$

$$S3 = (\alpha_2 Q_{PMT})(\gamma_{gas}\varepsilon_{ex}\varepsilon_d^{'})(\alpha_3 Q_{CsI})n_p \tag{4.15}$$

$$S4 = (\alpha_2 Q_{PMT})(\gamma_{gas}\varepsilon_{ex}\varepsilon_d^{'})(\alpha_4 Q_{CsI})(\gamma_{gas}\varepsilon_{ex}\varepsilon_d)n_e \tag{4.16}$$

From the equations above, we can estimate the QE of CsI (Q_{CsI}) photocathode by following two methods - S4/S2 and S3/S1 (see equation 4.17 and 4.18). The accuracy of both methods is determined by the estimation of the gas gain, extraction efficiency and light collection efficiency from simulation. The two methods should give similar results. The values on the right end of equation 4.17 and 4.18 are for a typical run with 3 kV/cm drift field and 8 kV/cm extraction field at which we assume $\varepsilon_{ex} = 90\%$ (Aprile *et al.*, 2004), $\gamma_{gas} = 210$ (Bolozdynya, 1999), and $\varepsilon_d^{'} = 100\%$.

$$Q_{CsI} = \frac{S4/S2}{\gamma_{gas}\varepsilon_{ex}\varepsilon_d^{'}} \cdot \frac{1}{\alpha_4} = (1.24 S4/S2)\% \tag{4.17}$$

$$Q_{CsI} = \frac{S3/S1}{\gamma_{gas}\varepsilon_{ex}\varepsilon_d^{'}} \cdot \frac{\alpha_1}{\alpha_2\alpha_3} = (0.19 S3/S1)\% \tag{4.18}$$

Table 4.5: The meaning and values of symbols for S1–S4.

Item	Meaning	Value
α_1	direct light collection efficiency for PMT	3.3%
α_2	proportional light collection efficiency for PMT	13%
α_3	direct light collection efficiency for CsI	70%
α_4	proportional light collection efficiency for CsI	42%
Q_{PMT}	quantum efficiency of PMT (including CE)	14%
Q_{CsI}	quantum efficiency of CsI	to be measured
γ_{gas}	gas gain - photons per electron in gas	>200
ε_{ex}	electron extraction efficiency from liquid to gas	90-100%
ε_d	charge collection efficiency	~70%
$\varepsilon_d^{'}$	charge drifting efficiency from CsI	<100%
n_e	number of electrons from event site	E/W
n_p	number of photons from event site	E/W_{ph}

We used ^{57}Co on the bottom of the detector for the measurement. From the mean value of the signals, we got S3/S1 = 100 and S4/S2 = 5.5, which gives a QE of 19% and 7% respectively, according to equation 4.17 and 4.18 above. The disagreement between these two values is due to the S4 signal saturation (see Figure 4.48 for explanation). By seeing only the low energy events, the S4/S2 value is equal to 15.4. This corrected value gives QE of CsI at 19%, which is the same as that calculated from the S3/S1 method. The combined QE values as a function of field are shown in Figure 4.49. A value of at least 19% can be reached at 3 kV/cm.

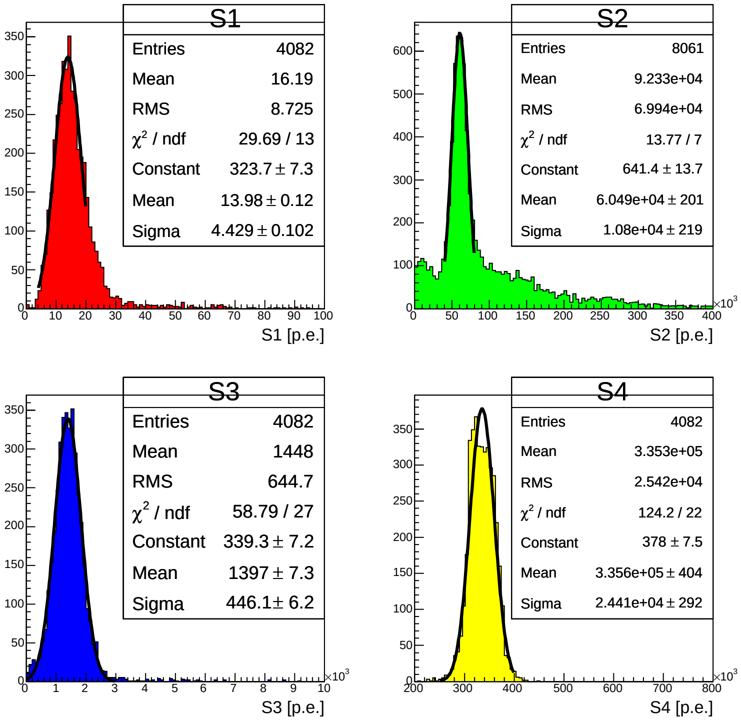

Figure 4.47: S1-S4 signal size distribution for 122 keV gamma ray interaction in the dual phase chamber for a typical run with 3 kV/cm drift field and 8 kV/cm extraction field.

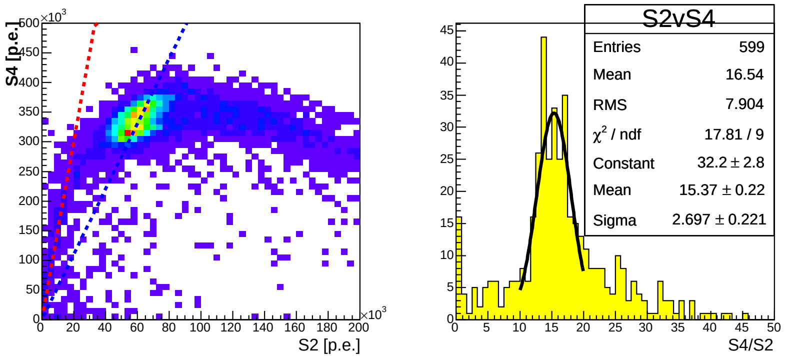

Figure 4.48: S4 versus S2 distribution (left) from the same data set as above shows that S4 starts to saturate when S2 signal is more than 20,000 photoelectrons. The S4/S2 distribution (right) shows a peak value of S4/S2 at 15.4.

4.6 Correlation between ionization and scintillation

The energy resolution in liquid xenon, at the operating field of 1 kV/cm, was measured at 4.2% (σ) at 1 MeV (Aprile *et al.*, 2001). The fair energy resolution has been a major limitation of the LXeTPC realization as a Compton telescope. Improving the energy response of liquid xenon with a more efficient use of the scintillation signal, along with the ionization signal, was proposed (Aprile *et al.*, 2003). The work presented here is our first attempt to improve the energy resolution of LXe.

The anti-correlation of scintillation and ionization signals in LXe was first observed by Kubota et al. (Kubota *et al.*, 1978) and its potential to improve the energy resolution was proposed by Seguinot et al. many years

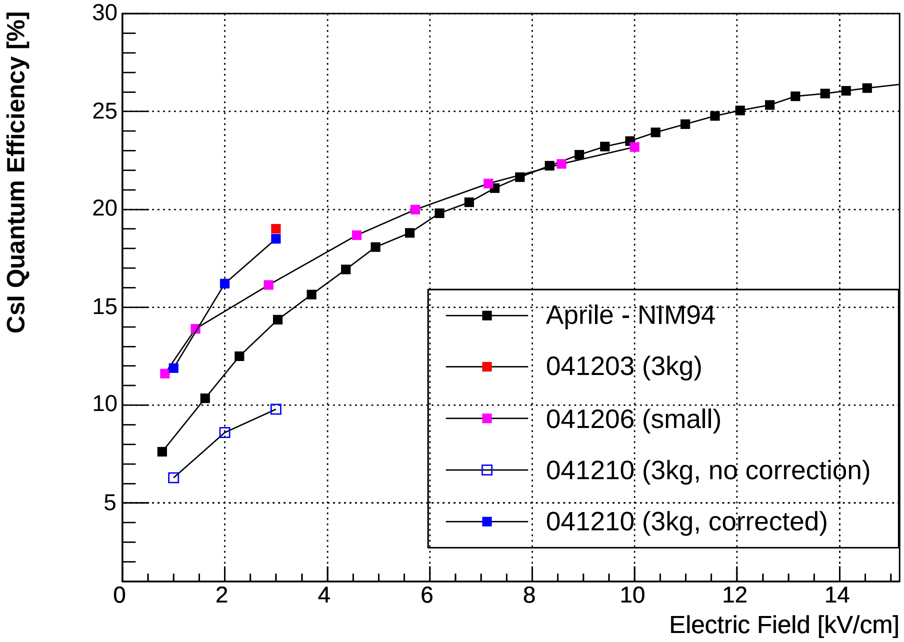

Figure 4.49: CsI photocathode quantum efficiency in liquid xenon as a function of electric field. NIM94 (Aprile *et al.*, 1994), 3 kg - this measurement (note: 3 kg shall be 1 kg), small - a similar measurement performed as in NIM94 with the CsI photocathode in this dual phase measurement.

ago (Seguinot *et al.*, 1992). But this promise has been hard to realize at that time, given the difficulty of efficiently detecting the 178 nm xenon scintillation light under the constraints of efficient charge collection. The improved light collection with a new type of PMT (see Section 4.4) has shown promising applications of LXeTPC in the direct dark matter search experiment for low energy events (XENON Collaboration, 2004).

The LXe chamber for this study was equipped with two Hamamatsu R9288 PMTs immersed in liquid xenon and a gridded ionization structure enclosed by a PTFE wall (Figure 4.21). There are three high optical tranparent meshes, which serve as cathode, grid and anode for ionization detection. The 1.9 cm drift region between cathode and grid defines the liquid xenon sensitive volume. The distance between grid and anode is 3 mm. The ionization electrons are drifted up and collected by the anode mesh. A charge-sensitive pre-amplifier (ClearPulse Model 580) is connected to the anode mesh to detect the ionization signals. The ionization signals are recorded by a waveform digitizer (LeCroy 2262), with a time sampling of 200 ns. The scintillation light waveforms from the two PMTs were recorded by a digital oscilloscope (LeCroy Model LT374) with a time sampling of 1 ns. The time difference between the scintillation and ionization signals gives the electron drift time information. The coincidence of the two PMT signals were used to give the event trigger. Figure 4.50 shows the scintillation and ionization waveforms of a 662 keV γ-ray event from ^{137}Cs. The number of photoelectrons, N_{pe}, detected by the PMTs are calculated by using the PMT gain calibration by using LED. The charge waveform is well described by the Fermi-Dirac threshold function in equation 4.19. The pulse height A, drift time t_d, rise time

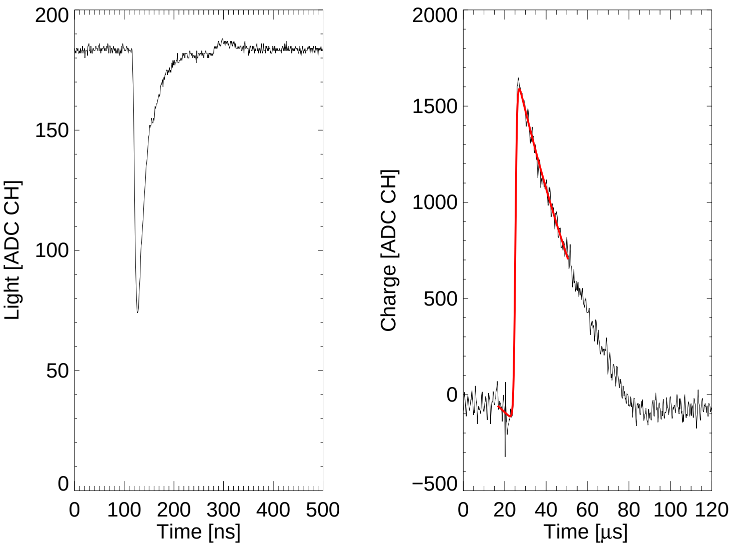

Figure 4.50: Waveforms of scintillation signal (left, sum of two PMTs) and ionization signal (right) of a 662 keV γ-ray event from ^{137}Cs at 1 kV/cm drift field.

t_r and fall time t_f are determined from a fitting of the charge waveform to equation 4.19. A known test pulse was used to calibrate the charge readout system and the number of collected electrons, N_e, was calculated from the pulse height of the charge waveform.

$$Q(t) = A \cdot \frac{e^{-(t-t_d)/t_r}}{1+e^{-(t-t_d)/t_f}} \tag{4.19}$$

The whole inner structure is immersed in liquid xenon during the experiment. The structure is mounted in a stainless steel vessel, surrounded by a vacuum cryostat for thermal insulation. The chamber is kept at LXe temperature at about –95°C. The xenon gas filling and purification system is the same as that in our previous publication regarding the detection of γ-rays with a 3.5 liter liquid xenon ionization chamber (Aprile *et al.*, 2002b). In addition to that, a xenon gas recirculation system (XENON Collaboration, 2004) is installed to purify the xenon continuously until a sufficient charge collection (or electron lifetime) is reached.

4.6.1 Field dependence of charge and light yield

The anti-correlation of charge and light yield is due to the recombination of electron-ion pairs created from a particle irradiation in liquid xenon. Figure 4.51 shows the field dependences of both light yield and charge yield, measured up to 4 kV/cm for 662 keV γ rays from ^{137}Cs in our correct setup. The increasing of charge yield as a function of field is usually described by the Thomas-Imel model (Thomas *et al.*, 1988) as in equation 4.20,

$$\frac{Q(E)}{Q_0} = c\frac{ln(1+\xi_0/E)}{\xi_0/E} + (1-c)\frac{ln(1+\xi_1/E)}{\xi_1/E} \tag{4.20}$$

where Q_0 is the charge collection at infinite field. Q_0 can be calculated as E_γ/W, where E_γ is the γ-ray deposited energy and $W = 15.6$ eV (Takahashi *et al.*, 1975) is the average energy required to produce an electron-ion pair in liquid xenon. $Q(E)$ is the charge collection at drift field E. As described in (Thomas *et al.*, 1988), the ionization track contains a core with high ionizing density and a penumbra produced from δ-ray ionization along the track. The electron-ion pairs in the core have strong recombinations, in which one electron-ion pair recombines and produces a UV photon (Doke *et al.*, 2002). The electron-ion pairs from δ-ray ionization have much less recombination because of its low ionizing density. In equation 4.20, ξ_0 and ξ_1 describes the strength of recombination for the two ionizing parts. A fitting of equation

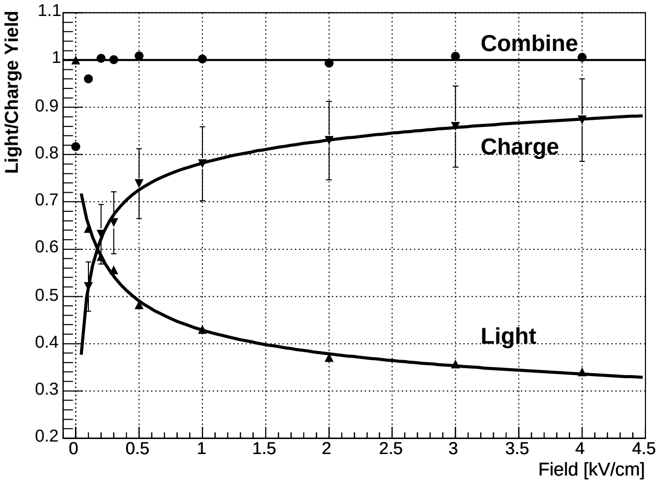

Figure 4.51: Light and charge yields as a function of drift field for 662 keV γ-rays from ^{137}Cs.

4.20 to the charge yield data (Figure 4.51) gives $c = 0.76 \pm 0.21$, $\xi_0 = 0.11 \pm 0.11$ kV/cm and $\xi_1 = 9.1 \pm 23.6$ kV/cm. The errors are only from statistics of the fitting. Note the large errors for the parameters. If the charge collection is 10% lower, we obtain $c = 0.70 \pm 0.15$, $\xi_0 = 0.12 \pm 0.09$ kV/cm and $\xi_1 = 23 \pm 55$ kV/cm.

The light yield, in contrast to charge yield, decreases as the drift field is increased. Equation 4.21 describes the field dependence of light yield $S(E)/S_0$, where $S(E)$ and S_0 are the light collection at drift field E and zero field separately. It was proposed by Doke et al. (Doke *et al.*, 2002) to explain the scintillation light reduction at low LET (linear energy transfer) region, by introducing the model of escaping electrons. The escaping electrons do not recombine with the ions for an extended time (>ms) even at zero field.

$$\frac{S(E)}{S_0} = \frac{1 + N_{ex}/N_i - Q(E)/Q_0}{1 + N_{ex}/N_i - \chi} \tag{4.21}$$

In equation 4.21, N_{ex}/N_i is the ratio of number of excitons and ion pairs produced by a γ-ray irradiation. χ is the percentage of escaping electrons from N_i. N_{ex}/N_i and χ can be determined by fitting a linear function to the relation between charge and light yields according to equation 4.21 (Figure 4.52), which gives $N_{ex}/N_i = 0.20 \pm 0.13$ and $\chi = 0.22 \pm 0.02$. The errors are from the uncertainty of charge collection only. The N_{ex}/N_i was estimated theoretically at 0.06 from the optical approximation by using the absorption spectrum of solid rare gases (Miyajima *et al.*, 1974). Doke et al. (Doke *et al.*, 2002) estimated $N_{ex}/N_i = 0.20$ and $\chi = 0.43$ from the data obtained for 1 MeV conversion electrons. The N_{ex}/N_i value is similar to our result. The different values of χ between this study and (Doke *et al.*, 2002) might be related to the different γ-ray irradiation energies.

A fitting of equation 4.21 to the light yield as a function of field (Figure 4.51) gives $c = 0.45 \pm 0.02$, $\xi_0 = 0.51 \pm 0.06$ kV/cm and $\xi_1 = 179 \pm 95$ kV/cm. In the fitting, N_{ex}/N_i and χ were set equal to 0.20 and 0.22, as determined above. If we assume the charge collection is 10% lower, N_{ex}/N_i and χ are 0.07 and 0.20 separately. By set N_{ex}/N_i and χ at these values, we obtain $c = 0.52 \pm 0.04$, $\xi_0 = 0.12 \pm 0.04$ kV/cm and $\xi_1 = 38 \pm 17$ kV/cm from the fitting of the light yield data. These parameters are more consistent with those from fitting of charge yield if the charge collection is 10% lower.

The two signals can be combined by following equation,

$$C(E) = a\frac{Q(E)}{Q_0} + b\frac{S(E)}{S_0} \tag{4.22}$$

with $a = 1/(1 + N_{ex}/N_i)$ and $b = 1 - a\chi$, which gives a constant $C(E) = 1$, regardless of field differences. The combined valules are also plotted in Figure 4.51. Note at zero field or very low field, equation 4.21 and 4.22 are not valid as escaping electrons are not fully collected.

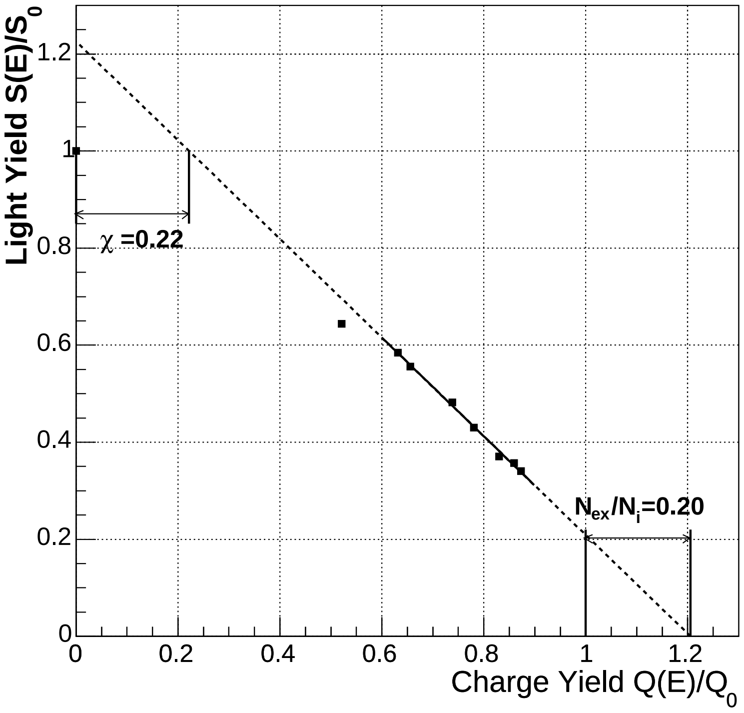

Figure 4.52: Correlation between light yield and charge yield for 662 keV γ rays.

4.6.2 Anti-correlation of scintillation and ionization

The field dependence of charge and light anti-correlation and their linear relationship implicate a way to improve the energy resolution by combining signals from scintillation and ionization channels with proper coefficients. The strong charge and light anti-correlation at a given drift field was first observed in liquid argon from relativistic La ions (Crawford *et al.*, 1987). It was recently observed in liquid xenon for 570 keV γ-rays from ^{207}Bi (Conti *et al.*, 2003). With an insufficient light collection efficiency by using an external PMT to detect the scintillation light, the best energy resolution was achieved at 3% at 4 kV/cm by combining the charge and light signals. In our detector, the improved light collection with two PMTs immersed in liquid xenon gives better results.

The strong anti-correlation of charge and light signals for 662 keV γ-rays from ^{137}Cs at 1 kV/cm is shown in Figure 4.53. The energy resolutions from light spectrum and charge spectrum for 662 keV peak are 10.3% and 4.8% separately. The charge-light correlation angle, θ, is defined as the angle between the major axis of the charge-light ellipse and the X-axis for light, after normalizing the charge and light in the same scale (i.e., in this case we normalize the charge scale to the number of photoelectrons for 662 keV line on the light spectrum). θ can be calculated as $\tan^{-1}(R_q/R_s)$, where R_s and R_q are the energy resolutions of the 662 keV peak from scintillation and ionization spectra separately. θ can also be found by a 2D gaussian fit on the charge-light ellipse of the 662 keV peak. A better energy resolution can be achieved by combining the charge and light signals as,

$$\varepsilon_c = \frac{\sin\theta \cdot \varepsilon_s + \cos\theta \cdot \varepsilon_q}{\sin\theta + \cos\theta} \tag{4.23}$$

where ε_c is the combined signal, normalized to the 662 keV line on the light spectrum in number of photoelectrons. ε_s and ε_q are scintillation light and charge values normalized to the same scale in number of photoelectrons. The charge-light combined energy resolution of 662 keV line is significantly improved to 1.7%.

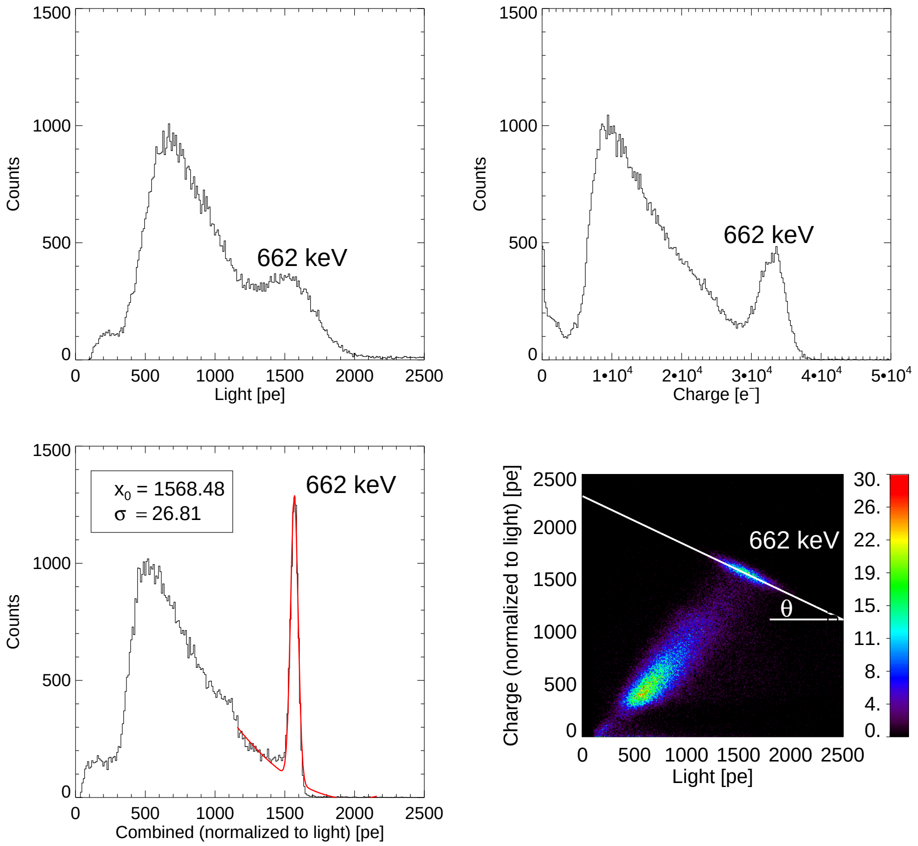

Figure 4.53: Energy spectra and anti-correlation between scintillation and ionization of ^{137}Cs 662 keV γ-rays signals at 1 kV/cm drift field in liquid xenon.

The energy resolution from charge-light combined spectrum, R_c, can be derived from equation 4.23 as (Bevington & Robinson),

$$R_c^2 = \frac{\sin^2\theta \cdot R_s^2 + \cos^2\theta \cdot R_q^2 + 2\sin\theta\cos\theta \cdot R_{sq}}{(\sin\theta + \cos\theta)^2} \tag{4.24}$$

where R_s and R_q are the energy resolutions from scintillation and ionization spectra separately. The covariance R_{sq} is the contribution from the correlation of the two signals. The magnitude of R_{sq} indicates the strength of anti-correlation (or correlation) between the scintillation and ionization signals. It is usually expressed in terms of correlation coefficient ρ_{sq},

$$\rho_{sq} = R_{sq}/(R_s R_q) \tag{4.25}$$

A value of ρ_{sq} closing to -1 (or 1) indicates a very strong anti-correlation (or correlation) of scintillation and ionization signals, while a zero ρ_{sq} means no correlation. In equation 4.24, R_s and R_q can be expressed as,

$${R_s}^2 = R_{si}^2 + R_{sg}^2 + R_{ss}^2 \approx R_{si}^2 + R_{ss}^2 \tag{4.26}$$

$${R_q}^2 = R_{qi}^2 + R_{qe}^2 \tag{4.27}$$

where R_{si} and R_{qi} are the intrinsic energy resolutions of scintillation and ionization in liquid xenon. R_{sg} is from the geometrical fluctuation of light collection. It is negligible in our result since only events in the center of the detector were selected for the analysis. R_{ss} is from the statistical fluctuation of number of photoelectrons N_{pe} in PMTs. R_{ss} is approximately equal to $1.1/\sqrt{N_{pe}}$, by considering the gain fluctuations of the PMTs. R_{qe} is from the noise equivalent charge (ENC) from charge readout. ENC was measured to be between 600 and 800 electrons, depending on the drift field, from a test pulse distribution. $R_{qe} = ENC/N_e$, where N_e is the number of collected charges from the 662 keV peak.

Table 4.6 lists the energy resolutions of the 662 keV γ-ray peak from ionization, scintillation, and charge-light combined spectra at different drift fields. Statistical errors are shown for the energy resolution values. The correlation angles and coefficients at each field are also presented. The energy resolutions are getting better with increasing fields for both scintillation and ionization, while the charge-light combined energy resolution are about the same at different fields. The best value achieved in this study is 1.7% at 1 kV/cm drift field. We would mention that during the scope of this work, we observed improvement of energy resolutions for both light and combined spectra with improved light collection efficiency from a better structure of PTFE reflectors, while the energy resolution from the charge spectrum was not changed.

Table 4.6: Resolution, correlation angle and coefficient from 662 keV γ-rays scintillation and ionization in LXe.

Field [kV/cm]	R_s(%)	R_q(%)	R_c(%)	θ	ρ_{sq}
1	10.3±0.4	4.8±0.1	1.7±0.1	24.8°	-0.87
2	10.5±0.3	4.0±0.1	1.8±0.1	20.8°	-0.80
3	10.0±0.3	3.6±0.1	1.9±0.1	19.7°	-0.74
4	9.8±0.3	3.4±0.1	1.8±0.1	19.1°	-0.74

The different values of charge-light correlation coefficients at different fields indicate a more fundamental intrinsic correlation coefficient of ionization and scintillation in liquid xenon. In fact, the energy resolution R_c from charge-light combined signals comes from two factors. One is the liquid xenon intrinsic resolution R_{ci}. Another factor, R_{ce}, is contributed from external sources, such as the fluctuations of light collection and electronic noise from the charge readout. The charge-light combined energy resolution can be written as below,

$$R_c^2 = R_{ci}^2 + R_{ce}^2 \tag{4.28}$$

$$R_{ci}^2 = \frac{\sin^2\theta \cdot R_{si}^2 + \cos^2\theta \cdot R_{qi}^2 + 2\sin\theta\cos\theta \cdot R_{sqi}}{(\sin\theta + \cos\theta)^2} \tag{4.29}$$

$$R_{ce}^2 \approx \frac{\sin^2\theta \cdot R_{ss}^2 + \cos^2\theta \cdot R_{qe}^2}{(\sin\theta + \cos\theta)^2} \tag{4.30}$$

In these equations R_{si}, R_{qi} are the liquid xenon intrinsic energy resolution from scintillation and ionization separately, as previously discussed. R_{sqi} indicates the intrinsic correlation between ionization and scintillation signals. We can define the intrinsic correlation coefficient, ρ_{sqi}, of liquid xenon scintillation and ionization, similar to equation 4.25 for the overall charge-light correlation coefficient.

$$\rho_{sqi} = R_{sqi}/(R_{si}R_{qi}) \tag{4.31}$$

The intrinsic energy resolution for scintillation, R_{si}, and ionization, R_{qi}, can be calculated based on equation 4.26 and 4.27, from the measured values of correlation angle θ, statistical fluctuation of light detection R_{ss} and electronic noise contribution R_{qe}. The calculated values are listed in Table 4.7. Table 4.7 also shows the intrinsic and external contributions, R_{ci} and R_{ce}, to the charge-light combined energy resolution. The values of R_{ci} and R_{ce} are calculated from equation 4.28-4.30. The intrinsic correlation coefficients from equation 4.31 are also shown.

Table 4.7: Intrinsic correlation coefficient and energy resolutions of scintillation and ionization in LXe.

Field [kV/cm]	$R_{si}(\%)$	$R_{qi}(\%)$	$R_{ce}(\%)$	$R_{ci}(\%)$	ρ_{sqi}
1	9.9±0.4	4.3±0.1	1.6±0.1	< 0.2	-1.00
2	10.1±0.3	3.5±0.1	1.7±0.2	< 0.6	-0.98
3	9.5±0.3	3.0±0.1	1.8±0.2	< 0.5	-0.98
4	9.3±0.3	2.8±0.1	1.8±0.2	< 0.3	-1.00

The intrinsic energy resolution in liquid xenon by combining scintillation and ionization signals is less than 1%. It's hard to make a precise estimation at such a small value. Thus only the upper limits are given here. The intrinsic correlation coefficients are very close to -1, which indicates that a much stronger intrinsic anti-correlation between ionization and scintillation in liquid xenon. An even better energy resolution can be achieved, by combining scintillation and ionization signals, if the external contribution to energy resolution can be further reduced.

4.6.3 Energy resolution

The same method of improving energy resolution by combining scintillation and ionization signals was performed for γ-rays at different energies from ^{22}Na (511 keV and 1.28 MeV), ^{137}Cs (662 keV) and ^{60}Co (1.17 MeV and 1.33 MeV) at 3 kV/cm drift field (Figure 4.54). The energy resolutions (before noise subtraction) from charge, light and charge-light combined spectra are shown in Figure 4.55. The data was fit by an empirical function, $\sigma/E = \alpha/\sqrt{(E/MeV)}$, with parameter α equal to (8.6±0.4)%, (3.0±0.4)%

and (1.9±0.4)% for light, charge and combined spectra separately in the current detector.

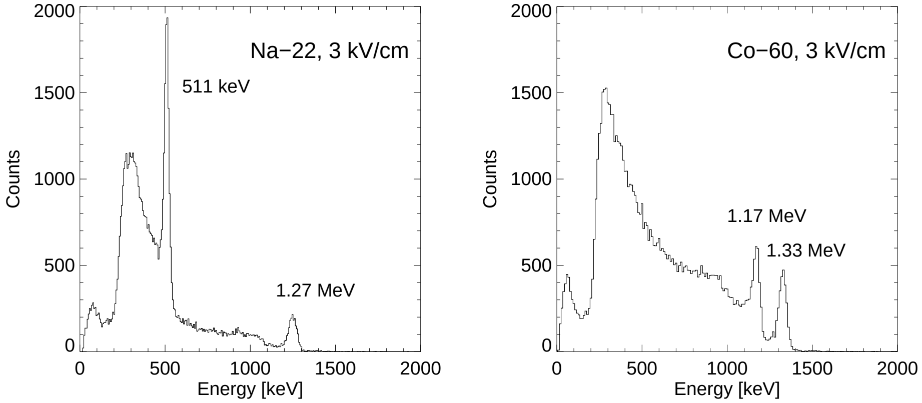

Figure 4.54: Energy spectra of ^{22}Na and ^{60}Co γ ray sources at 3 kV/cm, by combining charge and light signals.

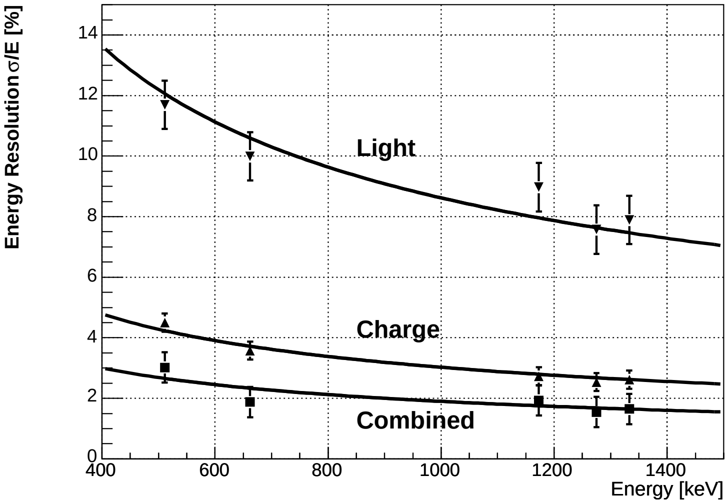

Figure 4.55: Energy dependence of resolution measured from ^{22}Na, ^{137}Cs, and ^{60}Co at 3 kV/cm drift field.

Chapter 5

Development for a sensitive dark matter search

The performance demonstrated in Chapter 4, with various liquid xenon detectors, guided the design of the first dual phase xenon TPC prototype for the XENON dark matter search. The properties, namely scintillation and ionization, of liquid xenon to low energy nuclear recoils remained to be precisely measured, to provide information of a WIMP recoil event. These important measurements were carried out and are presented in this chapter.

We will first describe the measurement of nuclear recoil scintillation efficiency and ionization yield in liquid xenon, before introducing the first XENON TPC prototype and its results A nuclear recoil, unlike an electron recoil, deposits most of its energy to the atomic motion (heat). Only part of its energy is transferred to ionization (or excitation) of xenon atoms to be observed via ionization charge (or scintillation light). The scintillation efficiency of nuclear recoils is defined as the ratio of the *observable* energy to the total *recoil* energy. The field dependence of the scintillation efficiency is also needed to be well studied, as in the XENON detector concept an electric field is applied. The measurement was performed with the detector already described in the previous chapter. Section 5.1 summarizes the measurement, as a detailed description has been published (Aprile *et al.*, 2005b).

The nuclear recoil ionization yield in liquid xenon represents another not-established parameter that essentially determines the performance of the dual phase XeTPC for dark matter search. Our first measurement based on a small dual phase detector (in section 5.2) shows that the ionization yield is higher than previously expected from heavily ionizing particles, such as α particles. This property would definitely make it easier to detect the ionization charges from very small energy nuclear recoils. On the other hand, it will also affect the background discrimination capability of the dual phase xenon detector. A study of the background discrimination thus has been carried out.

Finally, we report results from a 2.2 kg dual phase XENON TPC prototype, with 3D position sensitivity. Using an array of PMTs right above the gas gap, where proportional scintillation happens, the event XY position can be reconstructed. XENON3 represents the first xenon detector with 3D position sensitivity in the XENON dark matter search program. The performance of the position sensitivity, as well as confirmation of nuclear recoil ionization yield and background rejection potential of such a detector are presented in section 5.3.

5.1 Nuclear recoil scintillation efficiency in LXe

In order to determine the energy of nuclear recoils in liquid xenon, the absolute scintillation yields from nuclear recoils has to be precisely known. Because the excitation density of nuclear recoils in LXe is higher than that of electron recoils of the same energy, the scintillation yield is expected to be different. Knowledge of the ratio of these two scintillation yields is important for the determination of the sensitivity of LXe-based detectors to WIMP dark matter. The ratio has been previously measured(Akimov *et al.*, 2002; Bernabei *et al.*, 2001; Arneodo *et al.*, 2000; Bernabei *et al.*, 1996), but data do not cover the lowest recoil energies, which are of interest to sensitive dark matter experiments. Here we report results obtained with a LXe detector exposed to a neutron beam to measure Xe recoil scintillation efficiency in the energy range from 10.4 keV to 56.5 keV. Since some of the LXe dark matter experiments operate with an external electric field to simultaneously detect the scintillation and ionization signals produced by nuclear recoils, we have also measured the scintillation yield as a function of applied electric field up to 4 kV/cm.

5.1.1 Neutron scattering in LXe

The experiments were carried out in the Radiological Research Accelerator Facility at the Columbia Nevis Laboratory. Fast neutrons were produced by bombarding a tritiated target with 3.3 MeV protons. A nearly monoenergetic neutron beam with an average energy of 2.4 MeV in the forward

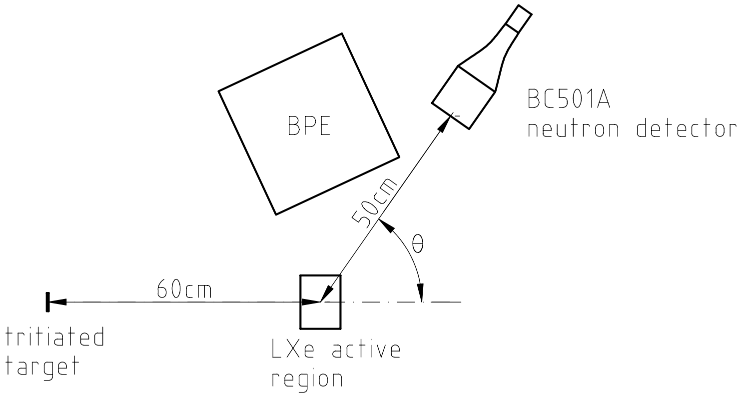

Figure 5.1: Schematic view of the detector arrangement used to measure scintillation from nuclear recoils in LXe.

direction was obtained through the $\mathrm{T(p,n)^3He}$ reaction. The energy spread of the neutrons due to the finite thickness of the tritium target was less than 10% FWHM. A liquid xenon detector was placed 60 cm from the neutron source in the forward direction.

The energy of xenon recoil can be determined simply from kinematics. The recoil energy E_r transferred to a xenon nucleus when a neutron with energy E_n scatters through an angle θ is approximately

$$E_r \approx E_n \frac{2M_n M_{Xe}}{(M_n + M_{Xe})^2}(1 - \cos\theta), \tag{5.1}$$

where M_n is the mass of a neutron and M_{Xe} is the mass of a xenon nucleus. The energy transferred is the maximum for back-scattered neutrons. A BC501A liquid scintillator (7.5 cm diameter, 7.5 cm long) with pulse shape discrimination was used to tag the neutrons scattered in the LXe detector.

The position and size of the neutron detector determine the average and spread of the xenon recoil energy of the tagged events. Data were taken with the center of the BC501A detector at neutron scattering angles of 123, 117, 106, 72, 55 and 44 degrees. The distance between the BC501A and LXe detectors was near 50 cm for all angles. To minimize the chance of direct neutron scattering in the liquid scintillator, the path between the neutron source and the neutron detector was shielded with 30-cm-thick borated polyethylene (5% by weight natural boron). The LXe detector arrangement is shown in Figure 5.1. The energy spread due to the finite solid angle of the BC501A neutron detector was approximately 10% FWHM.

The LXe detector allows a simultaneous measurement of ionization and scintillation signals produced by radiation in its active 21 cm^3 volume. A schematic of the LXe detector is shown in Figure 4.21. For measurements of the LXe purity and for energy calibration, we used gamma rays from radioactive sources such as ^{57}Co and ^{22}Na, placed directly underneath the cryostat. To demonstrate the excellent light sensitivity of this detector, which enabled us to measure recoils with kinetic energy as low as 10 keV, Figure 5.2 shows the scintillation light spectrum of ^{57}Co gamma-rays at zero electric field. When the 122 keV peak location in the light spectrum is combined with the gain measurement from the single photoelectron peak, the sensitivity is found to be 6 photoelectrons/keV. The measured sensitivity and spectrum are in good agreement with a simulation of the detector response, which takes into account the light collection efficiency and its spatial distribution as described in (Aprile *et al.*, 2005a).

The data acquisition was done with a digital oscilloscope (LeCroy LT374). The analog signals from the LXe PMTs and the BC501A PMT were split, with one copy going to a discriminator for each channel. The amplification

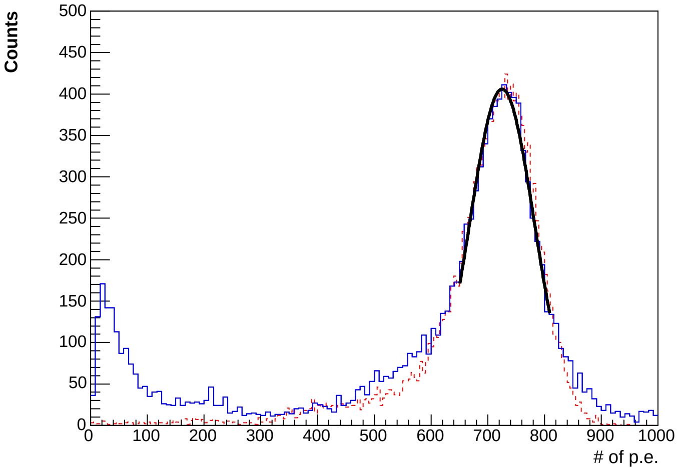

Figure 5.2: ^{57}Co scintillation light spectrum at zero field (solid line). A fit to the 122 keV peak gives a light yield of about 6 photoelectrons/keV, which is very close to the expected value from simulation (dashed line).

and discrimination on the LXe channels was set to achieve a single photoelectron threshold. A coincidence unit was used to trigger the oscilloscope on triple coincidences among the two LXe PMTs and the BC501A PMT within 150 ns. The recorded waveforms were transferred to a computer for later analysis.

5.1.2 Scintillation efficiency and field dependence

The scintillation efficiency for Xe nuclear recoils is defined as the ratio of the light produced by a nuclear recoil to the light produced by an electron recoil of the same energy. In practice, the peak in the nuclear recoil spectrum measured at each scattering angle is converted to an electron equivalent energy scale and compared to the expected nuclear recoil energy at that angle. The electron equivalent scale is determined by calibrating the LXe detector with 122 keV gamma rays from ^{57}Co. In this low energy region, the scintillation response of LXe is not linear, like in many other scintillators(Yamashita, 2003b). However we chose to calibrate with ^{57}Co gamma rays in order to compare our data directly to previous works(Akimov *et al.*, 2002; Arneodo *et al.*, 2000). The expectation value of the nuclear recoil energy is calculated from the geometry of the LXe and BC501A detectors, as in equation 5.1.

The selection of nuclear recoil events is based primarily on time of flight between the LXe and the BC501A detectors. For elastic scattering events where the neutron scatters directly from a Xe nucleus to the BC501A detector, the time of flight is approximately 2 ns for every centimeter of separation. Neutron and gamma coincidences are well separated in the time of flight (ToF) spectrum. Because of the finite size of the detectors, the ToF for neutrons that only scatter once in the active LXe varies by 6 ns. Neutron events in which multiple scattering occurs will generally have a longer ToF than single scattering events, and they also contribute to a tail on the neutron peak in the ToF spectrum. Only events within the first 6 ns of the neutron peak are accepted, and pulse-shape discrimination in the BC501A detector(Marrone *et al.*, 2002) is used to further reduce gamma backgrounds.

The electron equivalent energy spectra for nuclear recoil events with the lowest (10.4 keV) and highest (56.5 keV) recoil energies are shown in Figure 5.3, together with the accidental spectrum. The peaks are fit with the sum of a Gaussian and an exponential distribution. The peak location of the Gaussian is divided by the expected recoil energy to determine the scintillation efficiency. The resulting relative scintillation efficiency, as a function of

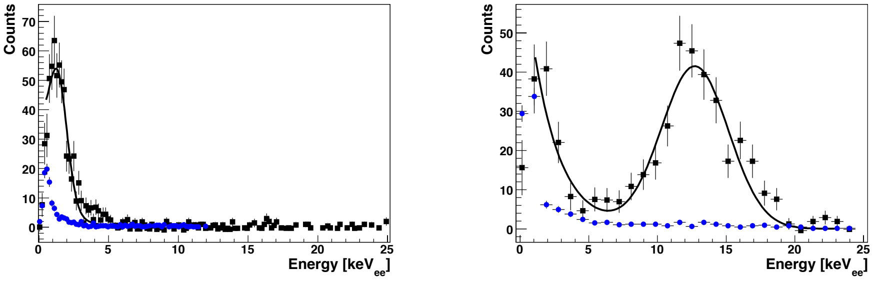

Figure 5.3: The measured LXe scintillation spectra (filled squares) for the 10.4 keV (left) and 56.5 keV (right) nuclear recoil data. The accidental spectrum is shown with filled circles. In both cases the uncertainties are statistical.

nuclear recoil energy, is shown in Table 5.1. The average scattering angle of the neutrons is given by θ. The average recoil energy of the xenon nucleus is given by E_r. Uncertainties include both systematic and statistical contributions. For recoil energies below 40 keV, where no prior measurements have been reported, the scintillation efficiency drops to 0.13. The errors include both statistical and systematic uncertainties, of similar sizes. The dominant systematic uncertainties are due to the uncertainty in the position of the detectors and the effects of multiple scattering.

The effect of multiple scattering of neutrons in the LXe detector and surrounding materials on the location of the nuclear recoil peak was investigated with a Monte Carlo simulation, using the GEANT4 LHEP-PRECO-HP physics package(Agostinelli *et al.*, 2003). A comparison of the simulated recoil spectra including multiple scattering events with the spectra generated with only single scattering events is used to estimate the significance of mul-

Table 5.1: The relative scintillation efficiency of xenon nuclear recoils in LXe to electron recoils.

θ (degrees)	E_r (keV)	Relative Efficiency
44	10.4	0.130 ± 0.024
55	15.6	0.163 ± 0.023
72	25.6	0.167 ± 0.021
106	46.8	0.238 ± 0.030
117	53.2	0.240 ± 0.019
123	56.5	0.227 ± 0.016

tiple scattering. These Monte Carlo simulations included a 6 ns ToF cut, which is identical to that used in the analysis of the real data. The effectiveness of the ToF cut for reducing multiple scattering backgrounds is shown in Figure 5.4. The unshaded histogram is for all single and multiple scattering events, while the shaded histogram is for single scattering events in LXe, followed by scattering in the BC501A detector.

The multiple scattering has little effect on the location of the peak found by fitting the nuclear recoil spectrum, as shown in Figure 5.5 where the results for single scattering are drawn in a scaled histogram. For each geometry, the single scattering spectrum is fit with a Gaussian distribution to determine the peak location; the multiple scattering spectrum is fit with a Gaussian and an exponential distribution. The difference in the peak location is less than five percent for every geometry. Simulated spectra for the lowest and highest energy deposition geometries are shown in Figure 5.5.

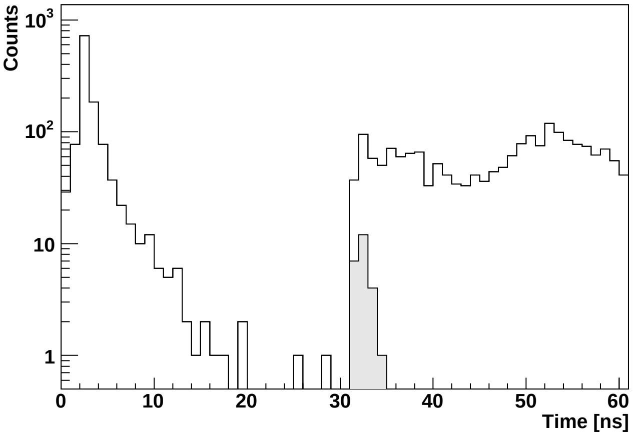

Figure 5.4: Simulated ToF between LXe and BC501A detectors for a scattering angle of 123 degrees.

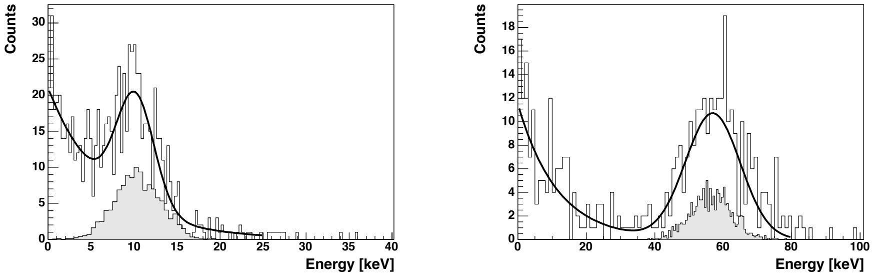

Figure 5.5: Monte Carlo simulations of neutron scattering in the LXe detector for scattering angels of $\theta = 44°$ (left) and $\theta = 123°$ (right).

To investigate the dependence of the nuclear recoils scintillation yield on the electric field applied in the liquid xenon, we used the geometry corresponding to 56.5 keV recoils. At each field, the scintillation efficiency is calculated relative to the scintillation efficiency at zero field, which eliminates uncertainties associated with the determination of the recoil energy. The data are shown in Figure 5.6. The error bars include a 10% systematic error due to the variation in the gain of the PMTs immersed in LXe, under prolonged neutron irradiation. The figure also shows the scintillation yield measured with the same detector under 5.5 MeV alpha particles irradiation and under 122 keV gamma-rays irradiation. The ionization yield for alpha particles is shown as well.

5.1.3 Lindhard and biexcitonic collision

For recoils with energy in the range of 10.4 to 56.5 keV, we find the relative scintillation efficiency to be in the range 0.13 to 0.23. Compared to the scintillation yield due to electron or alpha particle excitation, the scintillation yield due to nuclear recoil excitation is significantly reduced. Our results are shown in Figure 5.7, along with previous measurements by other groups(Arneodo *et al.*, 2000; Akimov *et al.*, 2002; Bernabei *et al.*, 2001, 1996). The predicted curves from theoretical models from Lindhard (Lindhard, 1963) and Hitachi(Hitachi, 2004) are also shown as solid and dotted lines, respectively. The scintillation efficiency of LXe is about 15% less than the Lindhard prediction. Hitachi explains this difference by estimating the additional loss in scintillation yield that results from the higher excitation density of nuclear recoils.

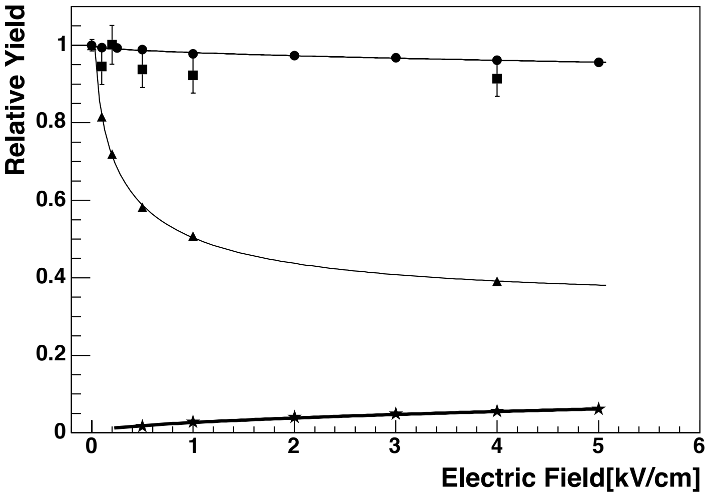

Figure 5.6: The LXe scintillation efficiency relative to the zero field, as a function of applied electric field, for 56.5 keV nuclear recoils (squares), 5.5 MeV alpha particles (circles) and 122 keV gamma-rays (triangles). Ionization data for alpha particles is also shown(stars).

Rapid recombination in LXe under high Linear Energy Transfer (LET) excitation(Hitachi *et al.*, 1983, 1992) provides a mechanism for reducing the scintillation yield of nuclear recoils in addition to that of nuclear quenching treated by Lindhard. In order to estimate the total scintillation yield, Hitachi considers biexcitonic collisions, or collisions between two *free* excitons that emit an electron with a kinetic energy close to the difference between twice the excitation energy E_{ex} and the band-gap energy E_g (i.e. $2E_{ex}$-E_g):

$$\mathrm{Xe}^* + \mathrm{Xe}^* \quad \rightarrow \quad \mathrm{Xe} + \mathrm{Xe}^+ + \mathrm{e}^- \tag{5.2}$$

The electron then loses its kinetic energy very rapidly before recombination. This process reduces the number of excitons available for VUV photons since it requires two excitons to eventually produce one photon. It is therefore considered the main mechanism responsible for the reduction of the total scintillation yield in LXe under irradiation by nuclear recoils. As shown in Figure 5.7, our data are in good agreement with the Hitachi prediction.

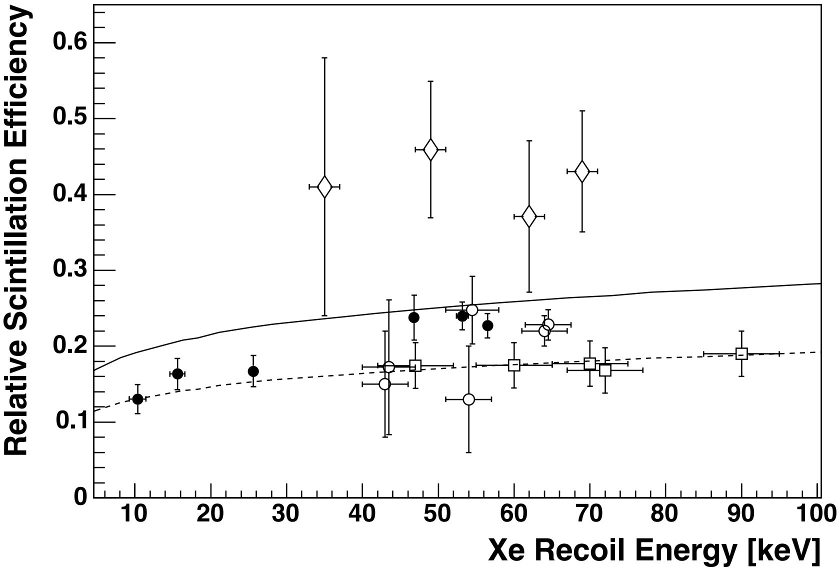

Figure 5.7: The relative scintillation efficiency for nuclear recoils for different recoil energies from all the published results: this experiment (full circle), Akimov *et al.* (2002) (open circles), Arneodo *et al.* (2000) (open squares) and Bernabei *et al.* (1996) (open diamonds). The solid line is from Lindhard (Lindhard, 1963) and the dotted line is from Hitachi's (Hitachi, 2004) theoretical model.

5.2 Nuclear recoil ionization yield in LXe

A direct measurement is needed for the ionization yield of Xe recoils in LXe, which has been carried out with a dedicated dual phase (liquid/gas) Xe detector. The nuclear recoil ionization yield as a function of recoil energy and applied electric field was measured.

5.2.1 XeBaby: a small dual phase chamber

A dual phase xenon chamber (Fig. 5.8) with 65 g of sensitive liquid xenon target mass was constructed to detect the ionization and scintillation signals simultaneously. It uses a liquid nitrogen-cooled cold finger system, with temperature control, to condense the gas and to maintain a stable liquid temperature. The detector was operated with vapor pressure between 2 and 2.8 atm, with stability better than 1%. The high purity of the LXe in the detector was achieved with the continuous gas purification through a high temperature getter. The direct scintillation light (S1) was detected by two UV sensitive photo-multiplier tubes (PMT) in the chamber immediately following an event in the sensitive target. The ionization electrons were drifted up with a field in liquid xenon, and were extracted to the gas phase with a stronger field in the gas. The extracted electrons produce proportional scintillation light in the gas. The proportional scintillation light was detected by the PMTs as a delayed signal (S2). The details of operating the dual phase xenon detector can be found in Section 4.1. The waveforms of S1 and S2 (see Figure 5.9) were recorded with a fast ADC (1 GHz) and a slow ADC (5 MHz) separately. Either the S1 coincidence from the two PMTs, or a single signal from the bottom PMT, was used for the trigger.

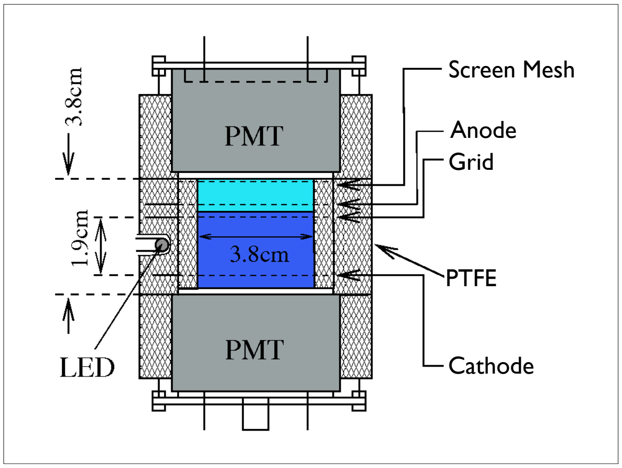

Figure 5.8: A simplified schematics of inner structure of XeBaby chamber.

The nuclear recoil elastic scattering events were produced by irradiating the liquid xenon target with a 5 Ci AmBe source, borrowed from another group, at 50 cm away from the chamber. The neutron source was shielded with 10 cm lead blocks to reduce the γ ray activity. Figure 5.10 shows the chamber's response to the AmBe source, compared with its response to low energy electron recoils from Compton scattering of 662 keV γ rays (an external ^{137}Cs source was used). Both plots are for the same drift field of 2 kV/cm. Due to the different ionizing density for nuclear recoils and electron recoils in liquid xenon, the recombination rate of electron-hole pairs are significantly different. The high recombination of nuclear recoil ionizations reduces the number of collected charges (S2), while the scintillation signal S1 is not much affected. For electron recoils from γ rays, the recombination rate of electron-hole pairs is much smaller. The S2/S1 ratio for electron re-

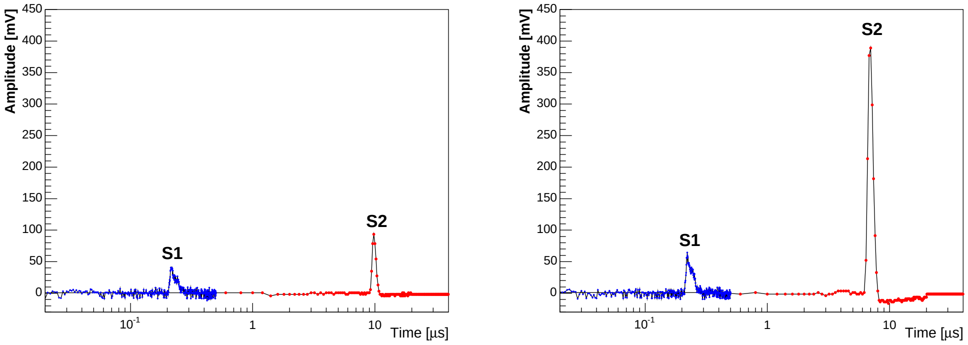

Figure 5.9: S1 and S2 from two typical nuclear elastic scattering event (left) and gamma ray electron recoil event (right).

coils thus becomes much larger than that for nuclear recoils from neutron elastic scattering. In the top plot of Fig. 5.10, the nuclear recoil band is clearly separated from the γ band. There are events from neutron inelastic scattering on ^{129}Xe (40 keV gamma). Additional gamma ray events are due to neutron inelastic scattering on ^{131}Xe, and ^{19}F contained in PTFE. The detector's response to ^{137}Cs irradiation shows a clear gamma ray band.

Both S1 and S2 signals were calibrated with an external ^{57}Co source emitting 122 keV γ rays. The calibration values for S1 are about 5.2 photoelectrons/keV at zero field, and 2.2 photoelectrons/keV at 2 kV/cm drift field. The amplitude (and time characteristics) of the S2 signal depends on the gas pressure, gas gap, and the field applied in the gas (Bolozdynya, 1999). The 122 keV γ ray calibration data acquired with 2 kV/cm drift field and 3.5 kV on the anode for the this detector gave about 4.7×10^4 pe for S2 signal. The number of collected ionization electrons from 122 keV γ rays is about 5.6×10^3 at 2 kV/cm drift field (see Section 4.2 and also (Shutt *et al.*, 2005)).

This gives a S2 calibration of about 8.4 pe/electron.

5.2.2 Energy and field dependence

The ionization yield is defined as the number of observed electrons per unit recoil energy (e^-/keVr). The number of electrons from S2 is calculated based on the calibration value from ^{57}Co. The recoil energy E_r is calculated from $E_r = E_e/f_q \cdot L_e/L_n$, where E_e, in unit of keVee, is based on S1 calibration from ^{57}Co. L_n and L_e are scintillation light quenching due to drift field, compared to the zero field value, for nuclear recoils and 122 keV γ rays respectively. The value for L_e is measured in this experiment, to be about 42% at 2 kV/cm. The value for L_n has only been measured for 56 keVr nuclear recoils (Aprile *et al.*, 2005b), which was found to be about 95% and does not change much with electric field. In the data presented here, we have assumed that the field dependence is similar at other recoil energies. Ongoing measurements with a large volume dual phase XENON prototype at Columbia will clarify this assumption. f_q is the nuclear recoil scintillation efficiency in liquid xenon at zero field. From our recent measurements of this quantity down to 10 keVr (Aprile *et al.*, 2005b), we infer the empirical energy dependence as $f_q = 0.06E_r^{0.34}$. The nuclear recoil ionization yield for different recoil energies and different drift fields is shown in Fig. 5.11 from the XeBaby detector. The uncertainty on the yield is dominated by the systematic error from ^{57}Co S2 calibration (5–6%). The statistical error is much smaller.

Due to the high ionizing density and strong recombination of nuclear recoil ionization in liquid xenon, it was previously considered that the amount of observed electrons would be very small and is similar to that from alpha

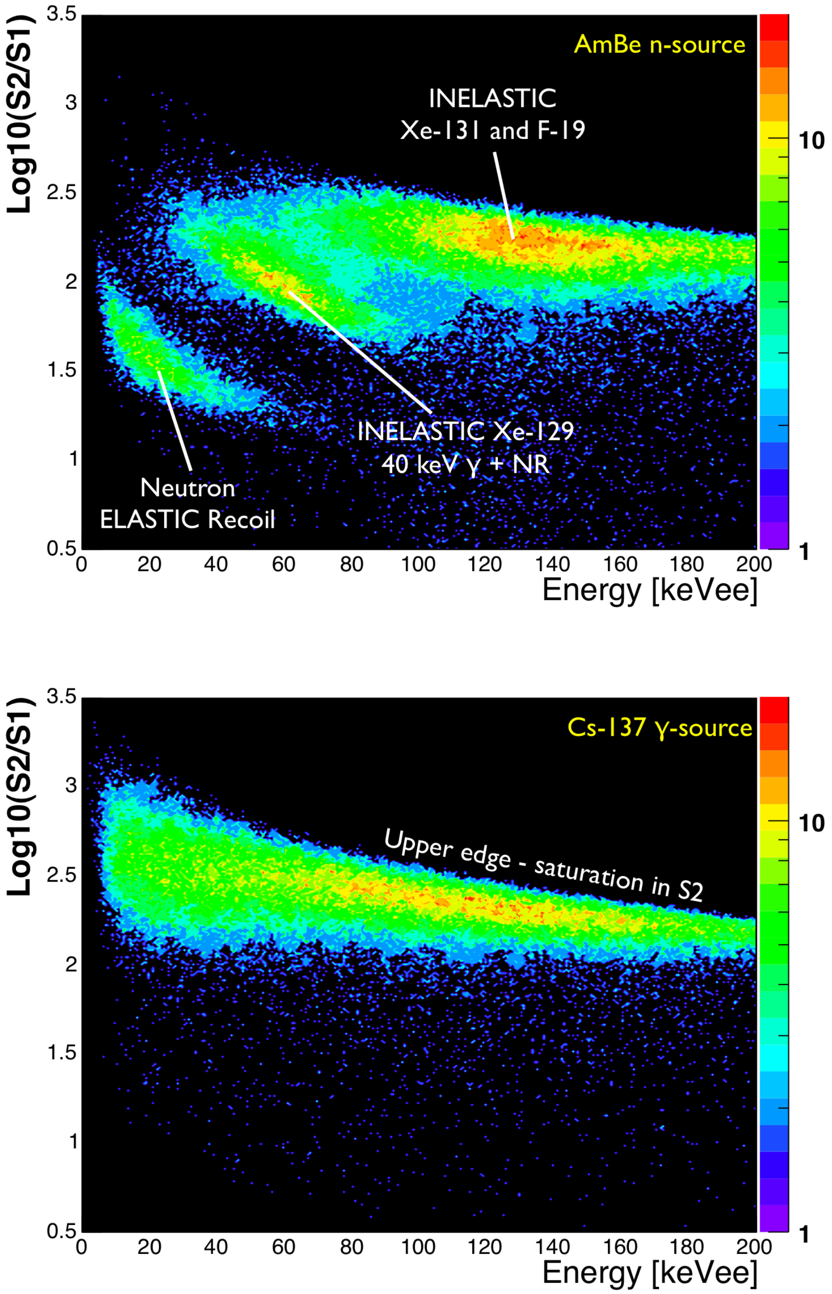

Figure 5.10: A dual phase detector's (XeBaby) response to neutron (top) and gamma sources (bottom).

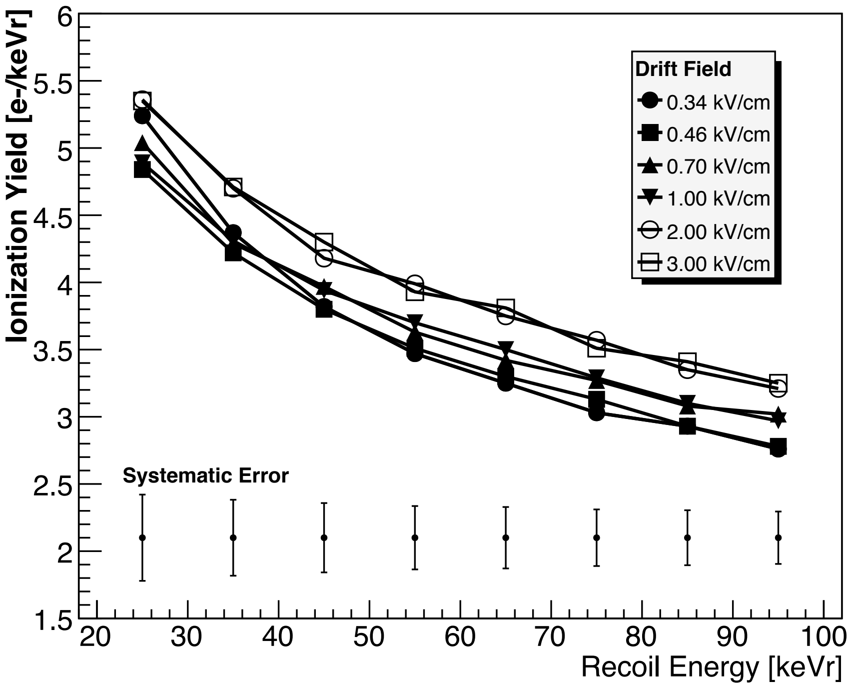

Figure 5.11: Energy dependence of nuclear recoil ionization yield at different drift field.

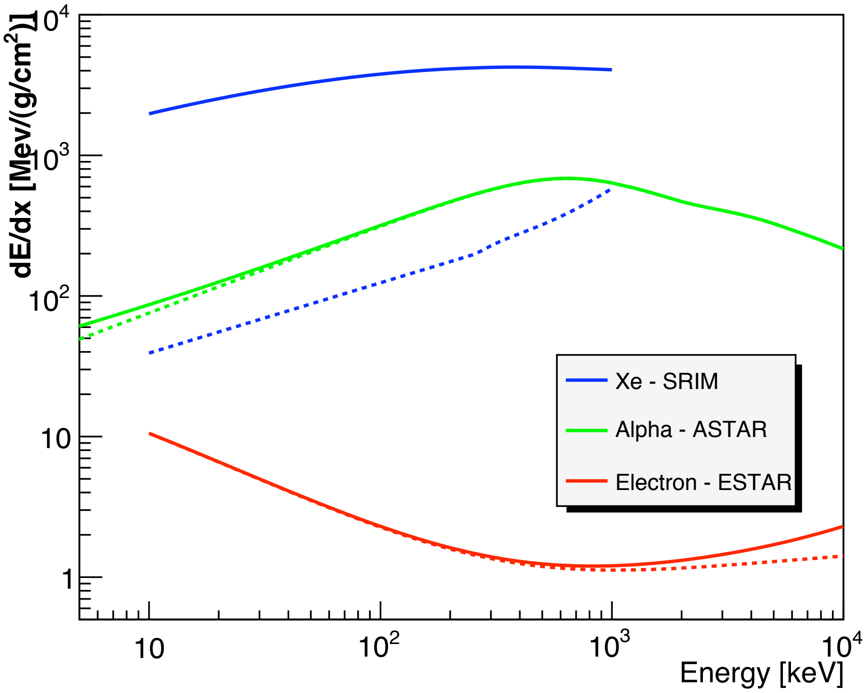

Figure 5.12: dE/dx for different energy γ rays, alpha particles and nuclear recoils. Data from SRIM (SRIM), ESTAR and ASTAR (NIST STAR). The solid lines are total stopping power. The dashed lines are electronic stopping for Xe recoils and alpha particles, and collisional stopping for electrons.

particle ionization in liquid xenon, which is typically in the range of 1 electron per 5 keV at a drift field of 2 kV/cm (Aprile *et al.*, 1991b). While our data indicate that for low energy nuclear recoils in the range of 10–100 keV, the number of observed electrons is between 2.5 to 5.5 electrons per keV, which is much higher than previously expected. This can be explained by their smaller ionizing density, which is specified as dE/dx, compared to alpha particles (see Figure 5.12).

A simple model is used to describe the energy and field dependence of the ionization yield as in equation 5.3–5.5, where ε (kV/cm) and E (keV) are the values of drift field and nuclear recoil energy. N_e is the number of observed electrons (i.e. collected charges).

$$N_e(E,\varepsilon) = \alpha(\varepsilon)E^{\beta(\varepsilon)} \tag{5.3}$$

$$\alpha(\varepsilon) = \frac{\alpha_1\varepsilon}{\alpha_2\varepsilon - 1} \tag{5.4}$$

$$\beta(\varepsilon) = \frac{\beta_1\varepsilon}{\beta_2\varepsilon + 1} \tag{5.5}$$

If we assume the ionization yield per unit energy, N_e/E, is inversely proportional to the recombination rate R, and R is proportional to the ionizing density, which is proportional to the electronic stopping power $(dE/dx)_e$, we get $N_e/E \propto (dE/dx)_e^{-1/2}$. At this low energy ($E < 100$ keV), the electronic stopping power $(dE/dx)_e$ from Xe recoils in liquid xenon is proportional to $E^{1/2}$ (Lindhard, 1963). Thus we would expect $N_e \propto E^{1/2}$ (equation 5.6), and the parameter β should be around 0.5. For the field dependence of α and β (equation 5.4 and 5.5), we assume $\alpha(0) = 0$ and $\beta(0) = 0$, and $\alpha(\varepsilon \rightarrow \infty)$ and $\beta(\varepsilon \rightarrow \infty)$ are finite values.

$$N_e/E \propto R^{-1} \propto (dE/dx)_e^{-1} \propto E^{-1/2} \rightarrow N_e \propto E^{1/2} \tag{5.6}$$

A modified version of equation 5.3 to describe the number of observed electron *per unit energy* as a function of energy is as below.

$$N_e(E, \varepsilon)/E = \alpha(\varepsilon) E^{\beta(\varepsilon)-1} \tag{5.7}$$

We fit the ionization yield at different fields according to equation 5.7 and the results are shown in Figure 5.13. The lowest energy point is 25 keV for most of the data sets, except for field of 0.25 kV/cm. For the field of 3.0 kV/cm, we used only one of the dataset for the fitting, as the other one might have been suffered from poor charge collection due to liquid xenon impurity.

The fitted parameter α is larger at lower drift field. It may due to the assumption that the field dependence of nuclear recoil scintillation yield at different recoil energy is the same as that of nuclear recoils at 56.5 keV. The scintillation yield for lower energy recoils might suffer more field quenching than that of at higher recoil energy. But there are no available measurement at these energies. The field dependence of $\alpha(\varepsilon)$ and $\beta(\varepsilon)$ according to the fitting of equation 5.4 and 5.5 is shown in Figure 5.14. The errors of α and β are statistical only as shown in the fitting parameters in Figure 5.13.

Figure 5.15 summarizes the results obtained to-date, on both the relative light yield and charge yield as a function of drift field for different particles in LXe: 122 keV γ rays from (Aprile *et al.*, 2005a; Shutt *et al.*, 2005), 55 keV Xe nuclear recoils from (Aprile *et al.*, 2005b) and this measurement, and 5.5 MeV α particles (Aprile *et al.*, 1991b). The relative light yield $S(E)/S_0$ is simply the light yield relative to that at zero field S_0. The relative charge

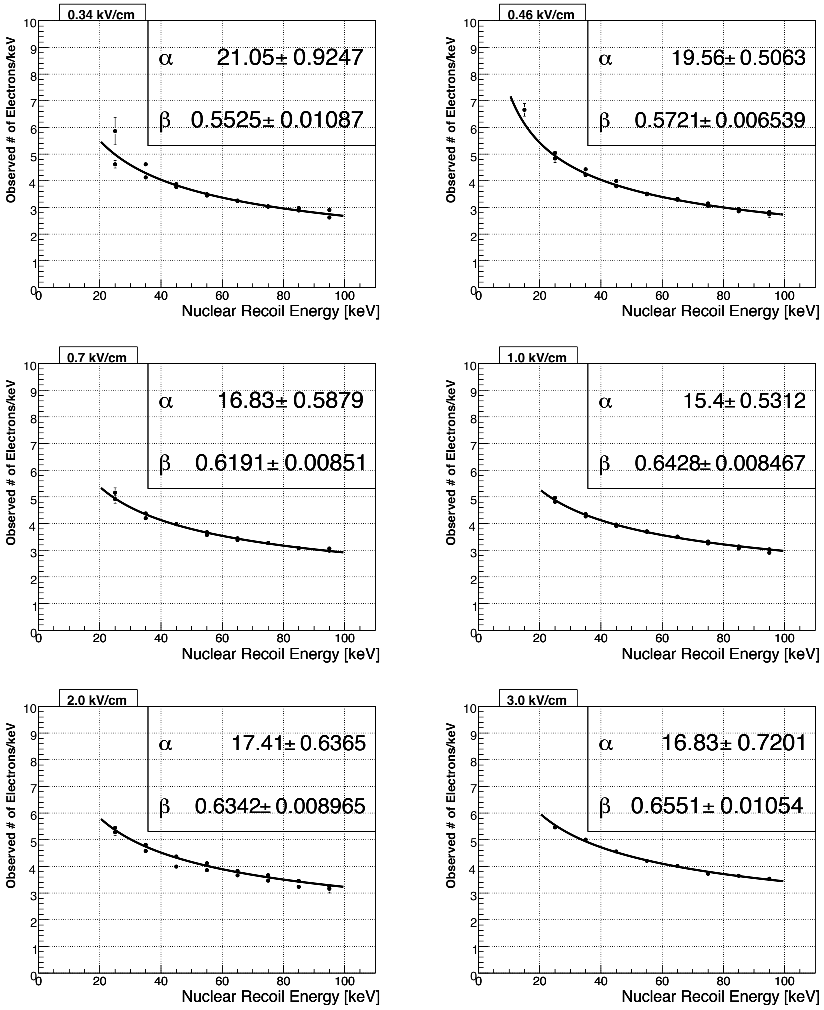

Figure 5.13: Ionization yield per keV as a function of recoil energy, fitted by equation 5.7. The errors in the data points are statistical only.

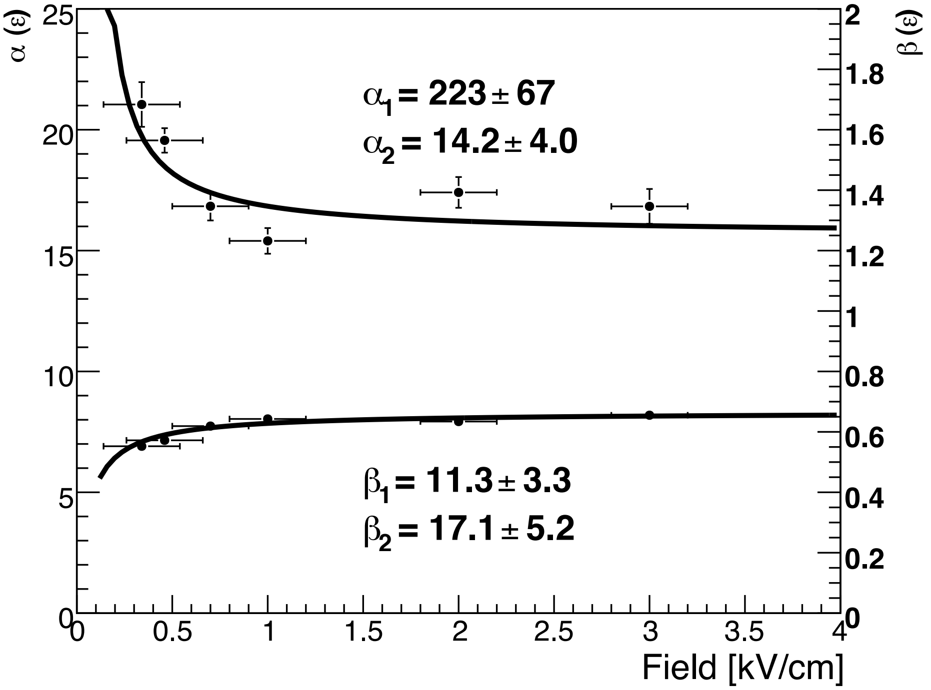

Figure 5.14: The field dependence nuclear recoil ionization yield parameters $\alpha(\varepsilon)$ and $\beta(\varepsilon)$.

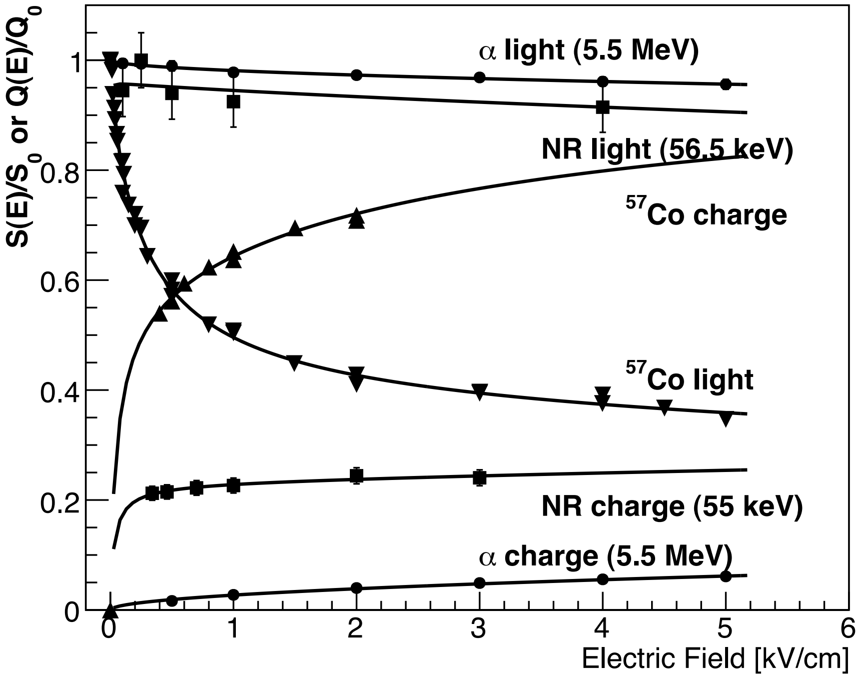

Figure 5.15: Field dependence of scintillation and ionization yield in liquid xenon for 122 keV γ rays, 5.5 MeV alpha particles and 55 keV Xe nuclear recoils.

yield $Q(E)/Q_0$ is the charge collected relative to that at infinite field Q_0. For nuclear recoils, $Q_0 = E_r \cdot q_n/W_e$, where E_r is the recoil energy, q_n is the nuclear quenching factor predicted by Lindhard theory (Lindhard, 1963). $W_e = 15.6$ eV (Takahashi *et al.*, 1975) is the average energy required to produce an electron-ion pair in LXe. For 122 keV gammas and 5.5 MeV alpha particles, we use simply the energy divided by the W value to obtain the charge at infinite field.

5.2.3 Background discrimination

The different values of S2/S1 between nuclear recoils and electron recoils makes liquid xenon an excellent target to discriminate between these two kinds of interactions. Figure 5.17 shows the S2/S1 distributions for nuclear recoil (AmBe source) and electron recoil (^{137}Cs) events at different electron equivalent energy (5 to 50 keVee) windows. Both datasets were taken at the same field configurations (4 kV on anode and 4 kV on cathode). Those rejection efficiency values are all obtained with 80% nuclear recoil acceptance $[-2\sigma, 1\sigma]$ from the Log10(S2/S1) distribution. Electron recoil events outside of this acceptance window are rejected. The background rejection efficiency can be further optimized by adjusting the acceptance of nuclear recoil events and optimize the detector's performance.

The data from the current small detector shows some population of electron recoil events leaking into the nuclear recoil region. This leakage seems from the detector itself, not from the statistical fluctuation. It may due to the field non-uniformity near the edge of the detector's sensitive volume. According to a Gaussian distribution by fitting the Log10(S2/S1) distribution from electron recoils, a much better background rejection efficiency can be obtained by assuming that the leakage of the electron recoil events into nuclear recoil acceptance region is only caused by statistical fluctuation. The improvement of the detector performance can be made by improving the uniformity of the electric field. Additional XY position sensitivity of the detector can be used to make fiducial volume cut to remove the edge events (see section 5.3.4).

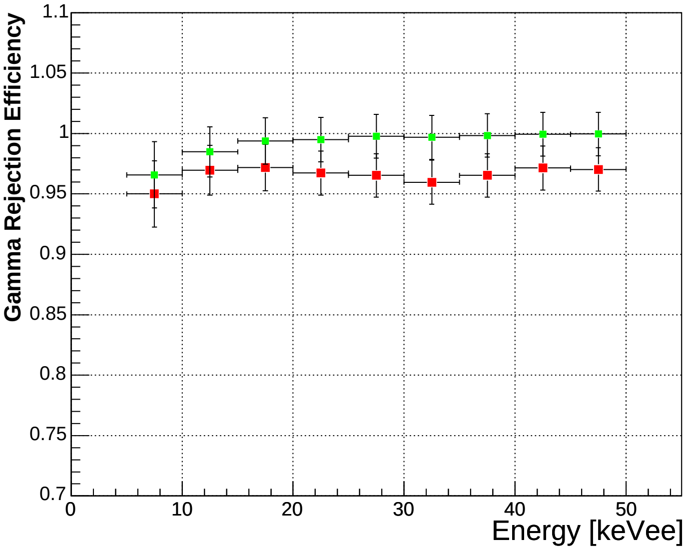

Figure 5.16: Electron recoil rejection efficiency as a function of electron equivalent energy with 80% acceptance window of nuclear recoils, for current detector (red, large square) and an optimized detector (green, small square) with only statistical distribution contributed to the background leakage.

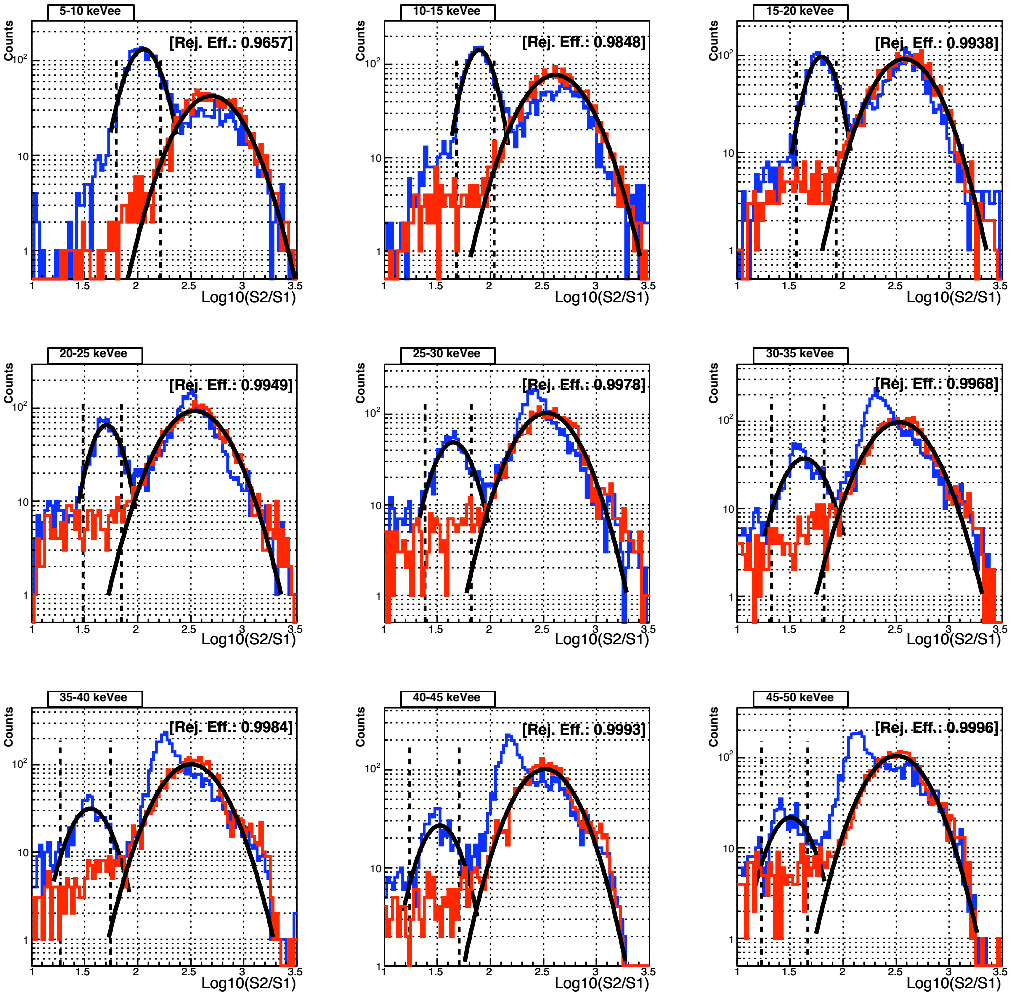

Figure 5.17: Background rejection efficiency for events at different energy window, by comparing nuclear recoil event (blue, left peak) and electron recoil event (red, right peak). The dashed lines are the 80% acceptance windows of nuclear recoil events. The rejection efficiency values shown in the plots are assuming the leakage only from statistical contributions, according to the fit.

5.3 XENON3: a 3D sensitive XeTPC

As a first approach towards a larger scale XENON detector, a fully operational dual phase xenon TPC with 3D position sensitivity was constructed. The detector's inner chamber (as shown in Figure 5.18) consists a cylindrical PTFE tube with about 10 cm inner diameter and 10 cm drift length between cathode and grid. The anode is 5 mm above the grid, which defines the gas gap where proportional scintillation occurs. Both anode and grid are made with wires stretched across rings with inner diameter of 10 cm. Field shaping rings are used to maintain field uniformity in the drift region. There are 21 PMTs on the top above the anode, and 14 PMTs on bottom below the cathode. All PMTs are Hamamatsu R8250 with 1-inch-square surface.

The chamber is placed inside of a vacuum cryostat. It is cooled by a pulse-tube refrigerator, to keep a stable operating pressure between 1 and 3 atm, with fluctuations less than 0.05 atm during the experiment. The cryostat and refrigerator system are shown in Figure 4.45.

The waveform from each of the 35 PMTs is fed into a charge amplifier (x10, Phillips 776) with two outputs. One output from the fan in/out unit is fed into a FADC channel (STRUCK SIS3301, 100 MHz, 14 bit with 2 V dynamic range) and another output is sent to a discriminator (CAEN V814). A coincidence of at least 3 PMTs is required to give a trigger for most cases. The DAQ diagram is shown in Figure 5.19. An additional gate delay generator (Phillips 7194) is used to hold the trigger off for a period of time ($\sim$200 mus) after one trigger, to wait until the PMTs calm down after a big S2 signal.

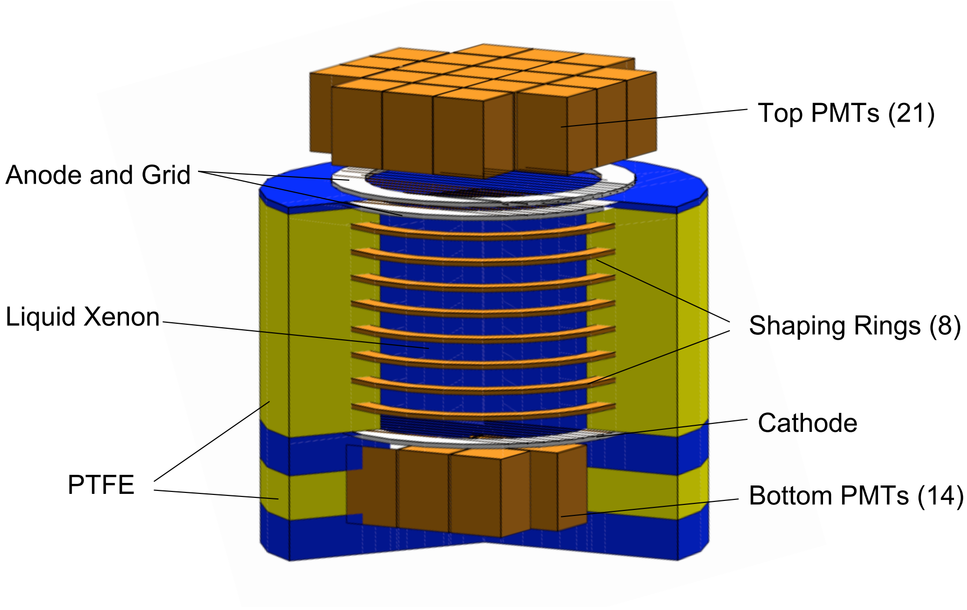

Figure 5.18: XENON3 inner chamber with 21 PMTs on top and 14 PMTs on bottom.

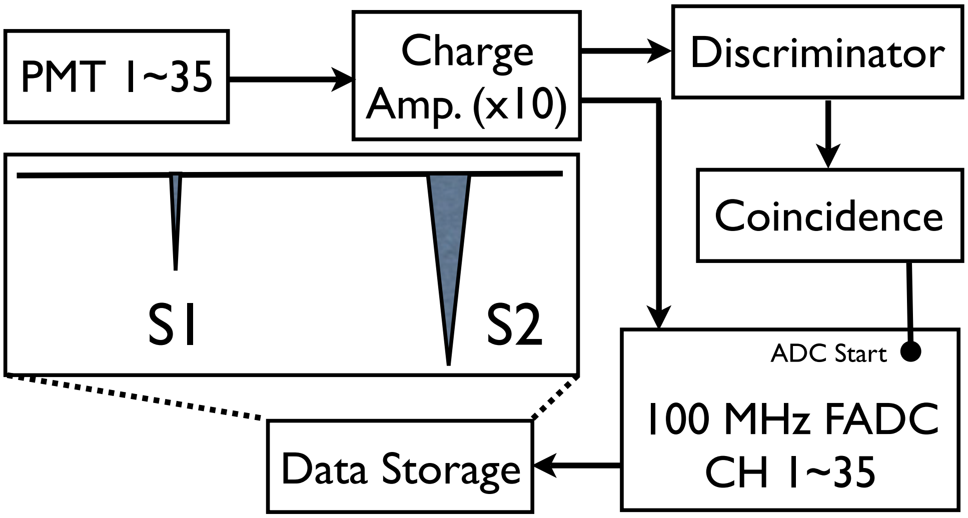

Figure 5.19: A simplified diagram of XENON3 DAQ.

5.3.1 XY position sensitivity

XENON3 represent the first detector in the XENON program with 3D position sensitivity. The Z position of an event can be precisely determined from the drift time between $S1$ and $S2$. The small electron diffusion coefficient in liquid xenon with an electric field, *drift field*, applied in liquid xenon, provides a very localized $S2$ signal in x and y. With an array of photon-sensors right above the xenon gas, where $S2$ signal is generated, the x and y positions can be determined from the signal distribution along the array of photon-sensors. In the following, we use S as the symbol for $S2$.

In XENON3 detector, each of the 21 top PMTs gives a proportional light S_i (i=1 to 21) from an event. S_i is in the unit of number of photoelectrons (pe) for the analysis. The simplest way to get the event position is to use a *Center of Gravity* method as in equation 5.8, with x_i and y_i the positions of ith PMT.

$$x = \left(\sum_{i=1}^{21} x_i \, S_i \right) \; / \; \sum_{i=1}^{21} S_i \quad \text{and} \quad \mathrm{y} = \left(\sum_{\mathrm{i}=1}^{21} \mathrm{y_i} \, \mathrm{S_i} \right) \; / \; \sum_{\mathrm{i}=1}^{21} \mathrm{S_i} \tag{5.8}$$

The *Center of Gravity* method usually gives a biased position towards the center of the detector, with a symmetric PMT configuration, such as in the case of XENON3 detector. If we obtain the response of $S2$ signals along the array of PMTs with known event XY positions in the detector, the position of a future event can be determined by comparing with the known instrumental response. The best instrumental response will be obtained from an experimental measurement of events distributed uniformly across the volume of the detector. For XENON3 this was not possible, thus a simulation

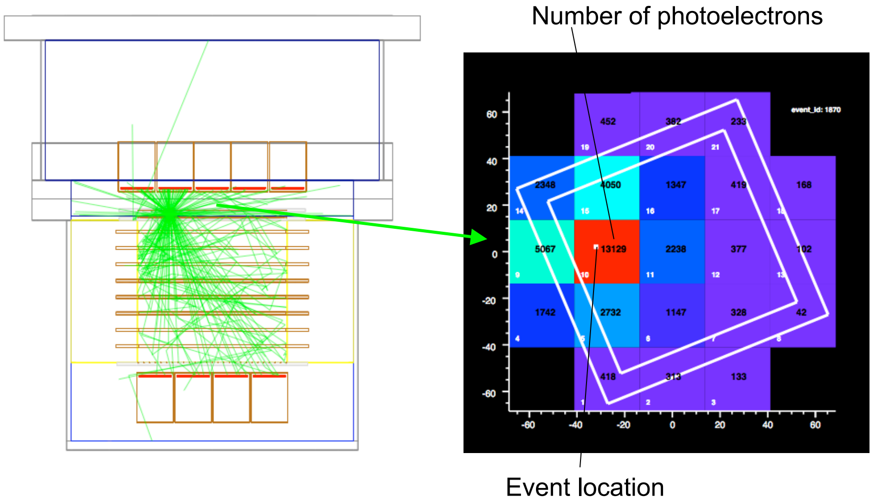

Figure 5.20: Simulation of proportional light from a 100 keV electron recoil event near [-30, 0] mm in XENON3 detector.

program with as many details (see Table 5.2) as in the real detector, was developed, based on GEANT4, to obtain the response of the PMTs. The program tracks each UV photon, produced from a specific location in the gas phase. The geometry of the detector and the PMT arrays, as well as the material properties of xenon and structural materials are described with sufficient detail to enable realistic UV photon tracking. A large number of UV photons are produced in the region between anode and grid to simulate the proportional scintillation light (Figure 5.20). In the simulation, the PMT response information was obtained for each 1 mm^2 grid in XY plane for the detector's sensitive area (10 cm diameter circular plane). It takes about 1 day to generate the full *S2 Hit Map* with 10^5 photons/event produced for each 1 mm^2 grid. Here we use s_i (i=1 to 21) as the simulated number of photoelectrons from an event at specific location in XY. Since the simulation gives the probability p_i (or light collection efficiency) of photon hits on the ith PMT, s_i is estimated as below, where S_i is the real number of photoelectrons from experiment for ith PMT.

$$s_i = p_i \cdot \sum_{i=1}^{21} S_i / \sum_{i=1}^{21} p_i \tag{5.9}$$

Once the instrumental response is obtained, several methods can be used to reconstruct the event position from a real measurement. We have also studied *Minimum Chisq* and *Maximum Likelihood* methods, which are described below. A new method based on *Neural Network* is also under development.

The *Minimum Chisq* method calculates the χ^2 value as in equation 5.10 by comparing a real S_i output with s_i from all simulated positions. The

Item	Value
LXe index of refraction	1.61
Light absorption length	100 cm
Light scattering (Rayleigh) length	30 cm
PTFE reflectivity for UV light	95%
Steel/Copper reflectivity for UV light	20%
PMT QE (inclulding collection efficiency)	14%

Table 5.2: Parameters assumed in the simulation of PMT's response to S2 signals.

minimum χ^2 value corresponds to the event X and Y positions.

$$\chi^2(x,y) = \sum_{i=1}^{21} \frac{[S_i - s_i(x,y)]^2}{\sigma_i^2} \tag{5.10}$$

Here $\sigma_i^2(x,y)$ is the uncertainty, which includes the statistical fluctuation of photoelectrons emission ($\sigma_{pe,i}$) from the photocathode of ith PMT and the PMT's gain fluctuation (σ_{g_i}). σ_{pe} is simply equal to $\sqrt{S_i}$, providing S_i is sufficiently large. σ_{g_i} was measured for each PMT based on its single photoelectron spectrum, where g_i is the gain of that PMT. Thus we have,

$$\sigma_i^2 = \sigma_{pe,i}^2 \left[1 + (\sigma_{g_i}/g_i)^2\right] = S_i \left[1 + (\sigma_{g_i}/g_i)^2\right] \tag{5.11}$$

The *Maximum Likelihood* method is similar to the *Minimum Chisq* method. If the fluctuation of PMT gains is ignored, a Log-Likelihood function (equation 5.12) can be used to estimate the best matched positions. The **maximum** value of $L(x,y)$ corresponds to the reconstructed position x and y.

$$L(x,y) = \sum_{i=1}^{21} \left[S_i \log(s_i(x,y)) - s_i(x,y) \right] \tag{5.12}$$

The *Maximum Likelihood* method can be used to treat data with a small number of photoelectrons (including zero), while the *Minimum Chisq* way works well if the signal is sufficiently large, which is the case for the proportional light in the XENON experiment. We compare the performance of both methods in the following section by using simulated data. The *Minimum Chisq* method also provides the 'goodness-of-fit', which can be used to identify multiple scattering events in the detector.

Comparison of different methods from simulated data

We first used simulated data to check the performance of the various methods for position reconstruction. The results were obtained for the detector geometry as shown in Figure 5.18. To get the *S2 Hit Map*, we generated 10^5 photons/event for each 1 x 1 mm^2 grid in the gas phase, between anode and grid. We also simulated 10,000 events with10^5 photons/event at the location of [-30, 0] mm. To get the number of photoelectrons seen by each PMT for these simulated events, we used the number of photon hits from simulation multiplied by the PMT quantum efficiency, with a Gaussian smearing. The spread that we put in the Gaussian smearing depends on the energy that we are interested in and its dependence on energy is approximately written as below, where σ_E is the 1σ energy resolution.

$$\sigma_E/E = 0.05/\sqrt{E(\text{MeVee})} \tag{5.13}$$

To simulate events with 10 keVee energy, the spread that we entered into the Gaussian smearing is $\sigma_E/E = 50\%$. The reconstructed positions, relative to their original positions, are shown in Figure 5.21 for the three methods as discussed above. The *Center of Gravity* methods apparently gives an offset of 4.8 mm for x. It doesn't give a similar offset for y since the event locations are at $y = 0$ in this simulation. Both *Minimum Chisq* and *Maximum Likelihood* methods give less offsets. The spread of the reconstructed positions for the two latter methods are both less than 5 mm (σ), with the *Minimum Chisq* giving a slightly better performance.

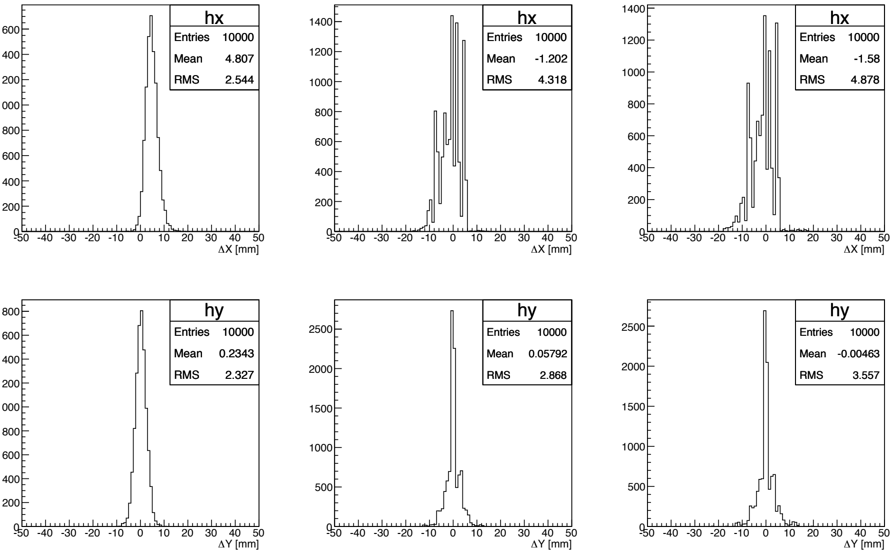

Figure 5.21: Reconstructed positions relative to their actual position at [-30, 0] mm from Center of Gravity (left), Minimum Chisq (center) and Maximum Likelihood (right) methods for 10 keVee electron recoils.

We further verified the performance of position reconstruction for 10 keVr nuclear recoil events. The amount of electrons produced by 10 keVr nuclear

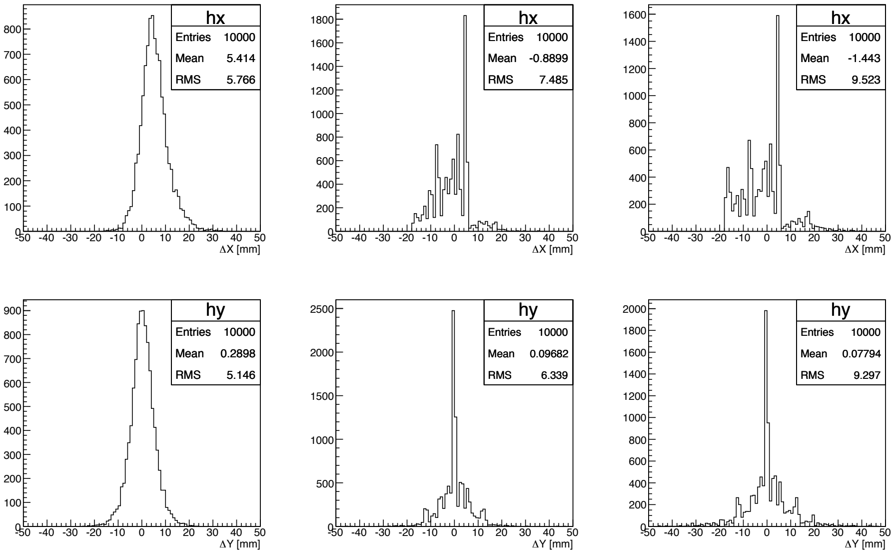

Figure 5.22: Reconstructed positions relative to their actual position at [-30, 0] mm from Center of Gravity (left), Minimum Chisq (center) and Maximum Likelihood (right) methods for 10 keVr nuclear recoils.

recoils at 1 kV/cm is about 40, which is similar to that from 1 keVee electron recoils. Thus we need a Gaussian smearing of $\sigma_E/E \sim 150\%$ for 10 keVr nuclear recoil events. The results are shown in Figure 5.22. The *Center of Gravity* gives again an offset for x. The *Minimum Chisq* method still gives a slightly better performance than *Maximum Likelihood*. The spread of reconstructed positions is less than 1 cm (σ) in both cases.

Based on the simulation results, we adopted *Minimum Chisq* as the main method for the position reconstruction for the data from real experiment.

Results from XENON3 with PTFE on bottom

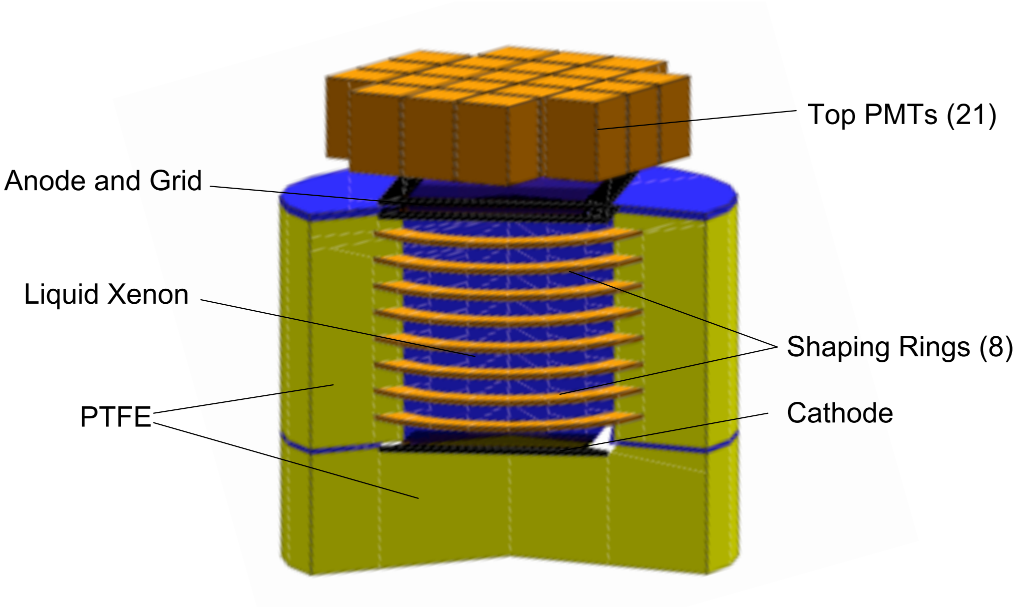

Figure 5.23: XENON3 detector with 21 PMTs on top and PTFE on bottom. Square rings with 8 x 8 cm^2 openings were used for anode, grid and cathode.

The XENON3 calibration runs started with PTFE, instead of an array of 14 PMTs, on the bottom. The anode and grid rings were square rings with 8 x 8 cm^2 openings (see Figure 5.23). The cathode ring was also square in shape, with an alpha source disc (Po-210, 1 cm diameter) deposited on the wire structure, with its center located at [-24.5, -10.1] mm. Wires with 120 μm diameter and 2 mm spacings were used for these grids. The highly localized 5.3 MeV alpha particles emitted from the source disc gave a unique source position to verify the detector's position resolution. We also used an external gamma ray source (Co-57), which emits 122 keV γ rays, at different locations on the detector's cryostat to check the detector's position sensitivity. The short attenuation length of 122 keV in liquid xenon allows us to check specially the position sensitivity near the edges of the sensitive target.

Since the alpha source was located on the cathode wires, the 5.3 MeV alpha events have the maximum drift time ($\sim$50 μs) at 1 or 2 kV/cm drift field. The alpha events can be selected by a maximum drift time cut. The S2 distribution of events with maximum drift time is shown in Figure 5.24. The reconstructed X&Y position for events in the alpha peak are shown in Figure 5.25, with position resolution (σ) better than 3 mm for both X and Y.

The attenuation length of 122 keV γ rays in liquid xenon is very short. With the Co-57 source placed outside of the cryostat, most of the events interact very close to the edge of the detector's sensitive volume. Figure 5.26 (right) is from a simulation of reconstructed 122 keV event positions, for the case of the source located at [-116,-138] mm (marked as Position 3). The other two positions that were used for the measurement are [290,0] mm

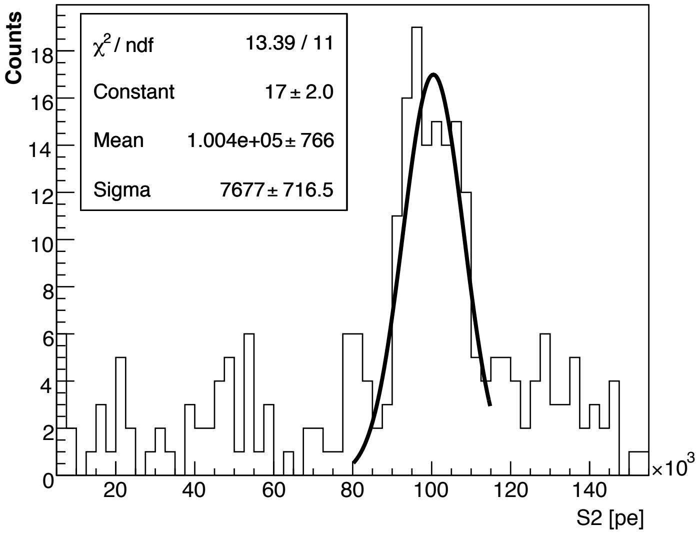

Figure 5.24: S2 distribution for events at maximum drift time. The 5.3 MeV alpha events give about 100,000 photoelectrons for this run.

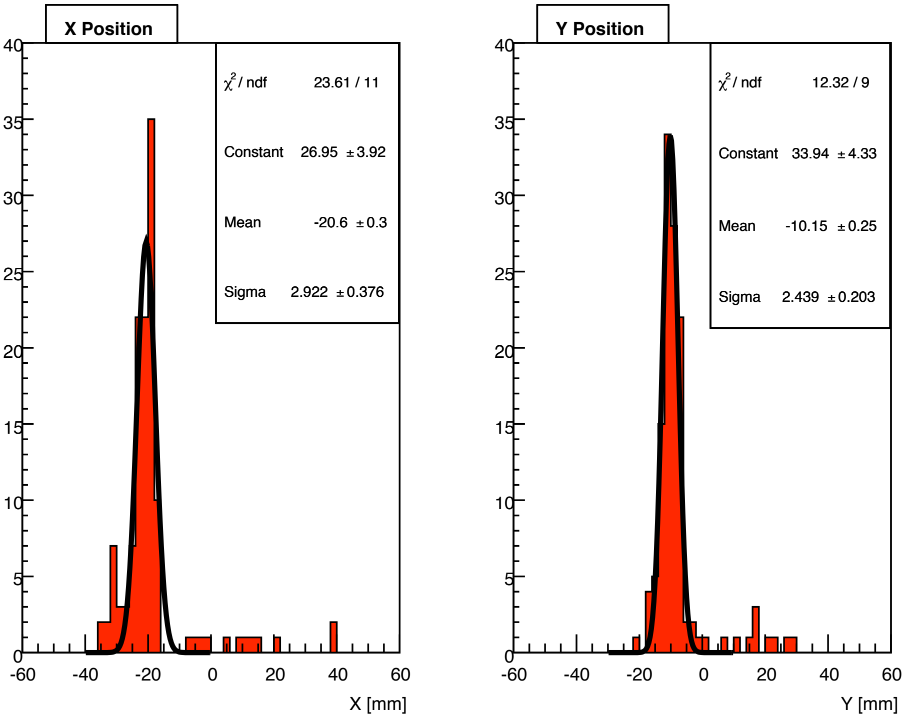

Figure 5.25: The reconstructed X&Y distribution for 5.3 MeV alpha events.

(marked as Position 1) and [-116,138] mm (marked as Position 2).

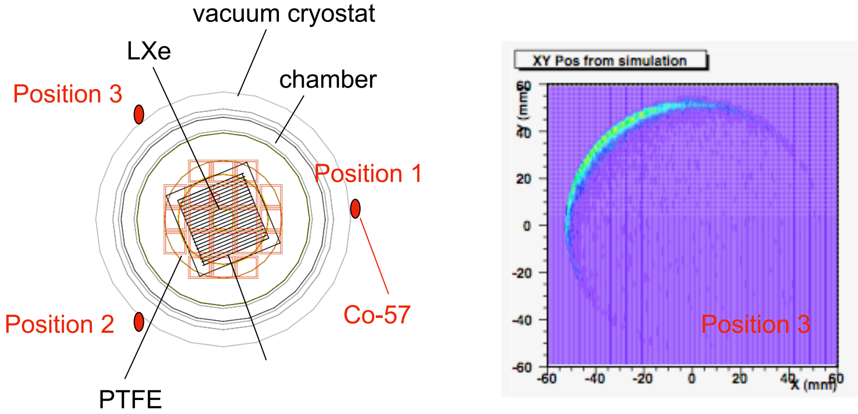

Figure 5.26: Co-57 positions for the calibration of XENON3 detector.

Figure 5.27 shows reconstructed positions for Co-57 at these three different positions on the external wall of the cryostat, compared with simulated positions. Only S2 from those events with x and y inside of the square grid openings (8 x8 cm^2) can be seen by the PMTs array on the top. For a realistic comparison, we made a cut for the simulated results. The reconstructed positions from the experiment are well reproduced, with a slight offset compared to the simulated positions. This might be due to a slight offset of the square rings in the actual detector's geometry.

Improved performance with a circular grid on the top

The square shape of the rings (anode and grid) blocks the events from the edge and its shape is well imaged with the XY position sensitivity of the detector. Later, a pair of circular rings were used to replace the square rings,

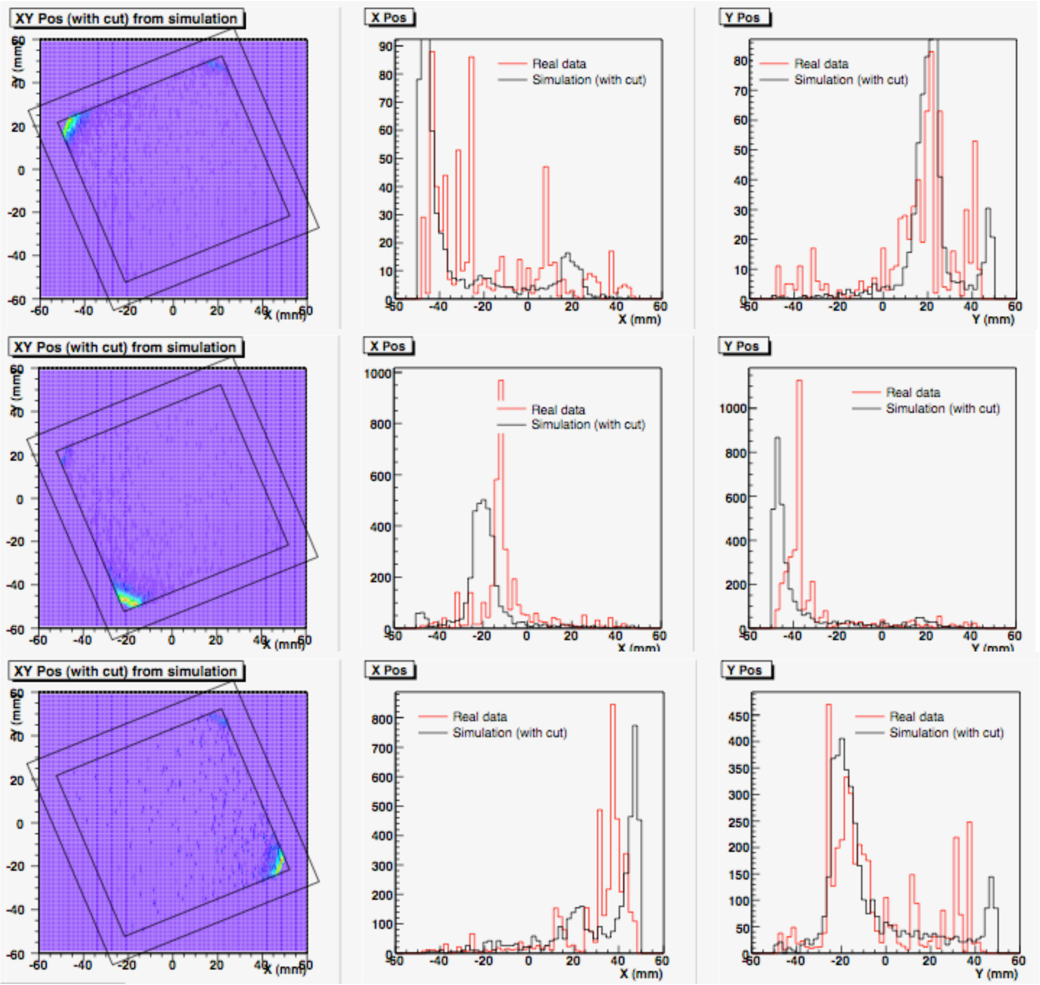

Figure 5.27: Reconstructed XY positions for Co-57 at Position 1 (bottom), 2 (middle) and 3 (top), compared with expected positions from simulation.

as shown in Figure 5.18. The change improves the position sensitivity, as well as enlarge the sensitive volume of the detector. The reconstructed radial and angular distributions from Co-57 at the one of the three locations are shown in Figure 5.28. The improved position sensitivity, especially near the edge of the detector, will allow us to achieve a better background discrimination since background events have more chance to happen near the edges. We will discuss the performance of the detector in the next section.

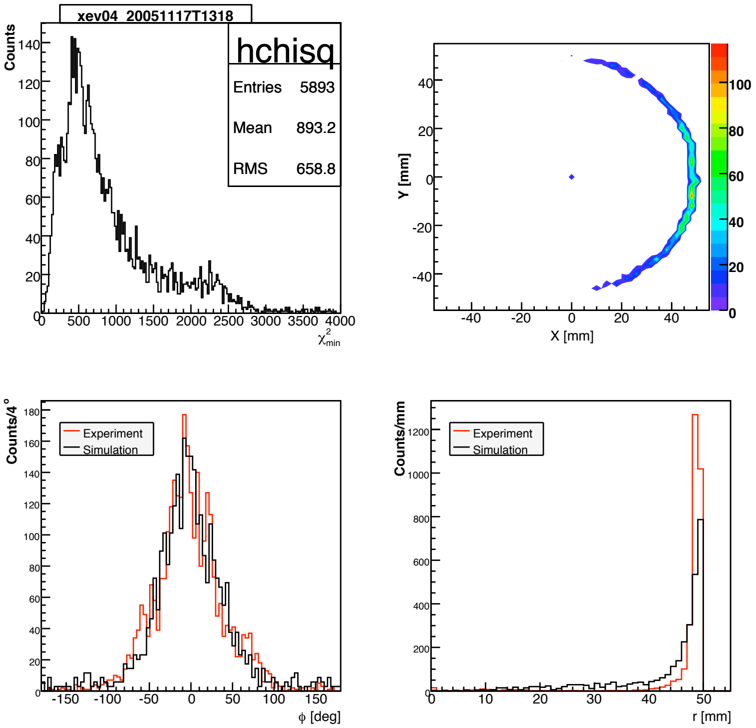

Figure 5.28: Reconstructed XY positions (radial and angular distributions) for Co-57 from XENON3 detector with circular rings on top.

5.3.2 Energy calibration and position dependence

XENON3 has been tested extensively with a Cf-252 neutron source, as well as a neutron generator producing 2.5 MeV neutrons. Elastic scattering events from nuclear recoils were recorded. The following results are from the prototype with circular rings for cathode, anode and grid as in Figure 5.18.

At the beginning of the experiment, the gain of each PMT was measured from the single photoelectron peak by using the light emitted by two LEDs installed in the detector (see Section 3.3 and Figure 3.4). The voltages of the PMTs were adjusted to have similar gain values ($\sim 2 \times 10^6$) for all PMTs.

For the energy calibration of the detector, we used 122 keV γ rays emitted from a Co-57 source placed outside of the cryostat. Number of photoelectrons for both S1 (direct scintillation light) and S2 (proportional light) were obtained by dividing the integral charge from each PMT by its gain. The summed value of 35 PMTs (21 on the top and 14 on the bottom) was used. The energy calibration runs were made at least once each day to monitor the detector's stability. We also placed the source at different locations around the detector, in order to avoid systematic uncertainty from the detector's non-uniform response at different locations, since the 122 keV γ rays mainly interact near the edge of the detector. The drift time, as well as the reconstructed XY positions, was obtained to study the position dependency of the energy calibration.

Figure 5.29 shows the drift time (dt) dependence of S1 and S2 from the 122 keV γ ray events. Since a large fraction of the direct scintillation light S1 is seen by the PMTs on the bottom, the events near the bottom (larger dt) have higher S1 signal than the events with smaller dt. The dependence is fit by an exponential function $S1(dt) = \exp(a_1 + b_1 \cdot dt)$ with parameters a_1 (Constant) and b_1 (Slope) shown in the figure. S2 is also dependent on the drift time, as the electrons will attach to impurities while drifting to the gas phase. So events with a large dt have a smaller value of S2. While the S1 dependency on drift time is not changing during the whole experiment, the S2 dependency on drift time is affected by the amount of time that the xenon gas circulates through the purifier. The S2 dependency on dt is also fit by an exponential function $S2(dt) = \exp(a_2 + b_2 \cdot dt)$, with a_2 (Constant) and b_2 (Slope) shown in Figure 5.29. The electron lifetime τ, a constant that is used to describe the purity level of liquid xenon, can be found as $\tau = -1/b_2$. An electron lifetime of a few hundred μs was achieved with the 3 kg prototype. This allowed only a small loss of the electrons signal due to the impurities in LXe. If we take the average drift time of 25 μs (electron drift velocity is about 2 mm/mus in the case of 1 kV/cm drift field), the average percentage loss of electrons is about $1 - \exp(-25/\tau) = 8\%$ for the run shown in Figure 5.29 with an electron lifetime $\tau = 280\mu$s.

Once the dependency of S1 and S2 on the drift time is found, S1 and S2 signals can be corrected by normalizing the measured value to that at a fixed dt. For S1, we normalize the signal to $dt = 25\mu s$ (average drift time at 1 kV/cm drift field) as the mean light signal. For S2, we normalize the signal to $dt = 0\mu s$, which is the S2 signal without any electron loss due to impurities. Spectra of S1 and S2, after correcting the drift time dependency, for Co-57 events are shown in Figure 5.30. The XENON3 detector shows a high S1 light collection of 2.2 pe/keVee at 1 kV/cm, with energy resolution about 19% (σ). S2 signal from the 122 keV γ ray is about 61,400 photoelectrons for the run in Figure 5.30, with an energy resolution about 27% (σ). The amount of primary ionization electrons from 122 keV γ ray interactions in liquid xenon is about 7,800 (by dividing the energy by a W value of 15.6 eV). At 1 kV/cm, about 65% (Shutt *et al.*, 2005) of these electrons escape the initial recombination, become free electrons, and drift from the liquid to the gas phase. This gives about 12 photoelectrons per electron drifting into the gas phase. The detector is thus capable to detect events with energy as low as 1 keVee (from S1) and as is sensitive to a single electron drifting in the liquid. The systematic error due to S1 calibration at different location around the detector's cryostat is very small (less than 1%), while the systematic error for S2 due to Co-57 at different locations is about 12%. The difference of S2 calibration for Co-57 at different locations around the detector's cryostat might comes from the fact that grid and anode are not truly horizontal, resulting in a different gas gap, thus a different gas gain for proportional light at different sides of the detector. The accuracy of the PMT gain calibration may also contribute to this difference, as the S2 light strikes primarily only a few PMTs right above the event location.

In fact, the S2 is also dependent on the radial position of an event. Part of the S2 radial position dependency is due to the light collection non-uniformity, since the events in the center are always viewed by more PMTs on the top, giving a higher S2 signal. This is shown in Figure 5.31 from simulation. Based on the simulation, the S2 light collection efficiency for events near the edge can be 10–15% lower than the mean value in the detector. S2 signal for events near the edge of the detector can also be reduced due to drift field non-uniformity and due to field lines ending up on the PTFE wall. Both

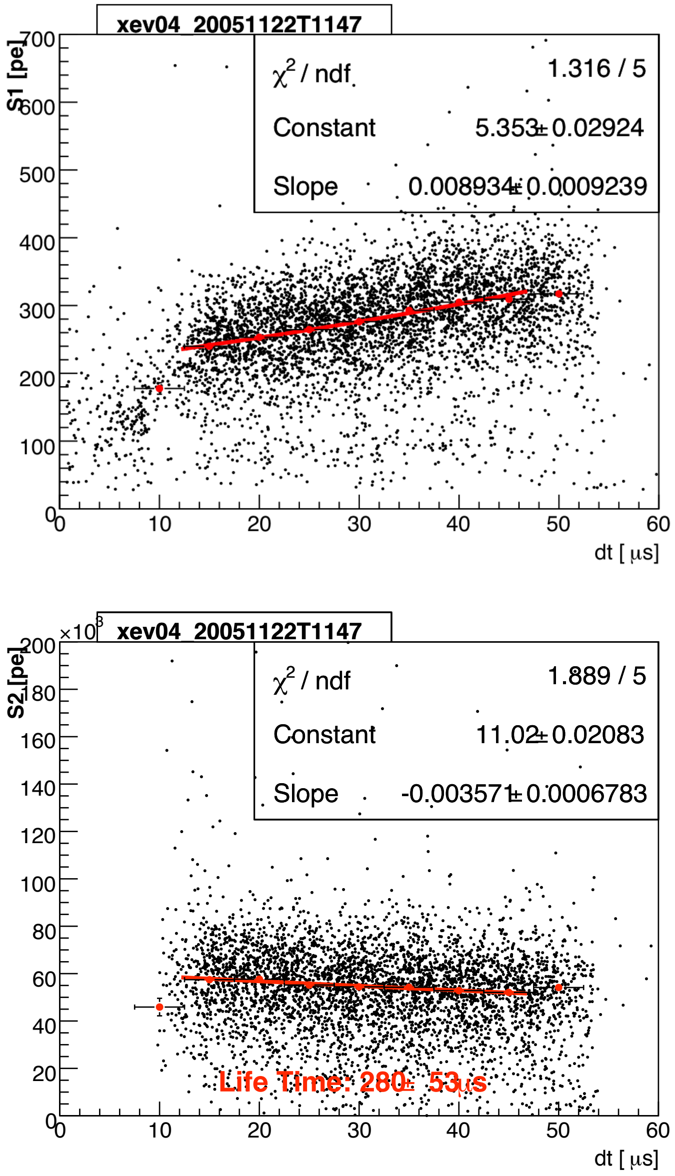

Figure 5.29: Drift time dependence of S1 and S2 signals from Co-57 at position 1 (see Figure 5.26), with the detector operating at $V_{\text{cathode}} = 10\text{kV}$ and $V_{\text{anode}} = 4\text{kV}$. The pressure in the chamber was 2.6 atm and the gas gap is around 3 mm.

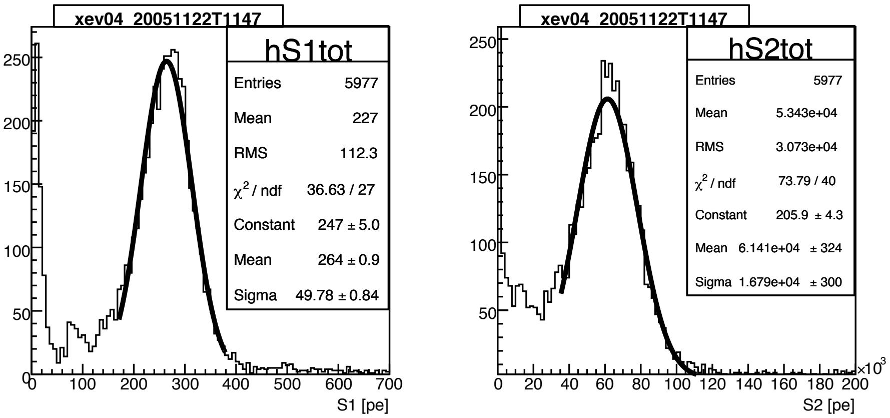

Figure 5.30: Energy spectra of S1 and S2 for Co-57 at 1 kV/cm.

the light collection effect and the field line effect will give a smaller S2 signal for events near the edge. This effect is particularly relevant as the current detector uses a calibration source (122 keV γ ray emitted from Co-57 from outside) with most events interacting near the edge of the sensitive liquid xenon target.

In order to obtain an accurate energy calibration value, we fit the S1 and S2 (both signals are after drift time dependency corrections) as a function of radius for 122 keV gamma rays from Co-57, as shown in Figure 5.32. The ratio of S1(r)/S1 and S2(r)/S2 is plotted as a function of r, where S1(r) and S2(r) are signal at radial position r, and S1 and S2 are the values found for all 122 keV events in the detector. Due to the small attenuation length of 122 keV γ rays in liquid xenon, this radial dependency can only be studied for events at a radius larger than 35 mm. We fit the radial dependency with linear functions $S1(r)/S1 = c_1 + d_1 \times r$ and $S2(r)/S2 = c_2 + d_2 \times r$, which

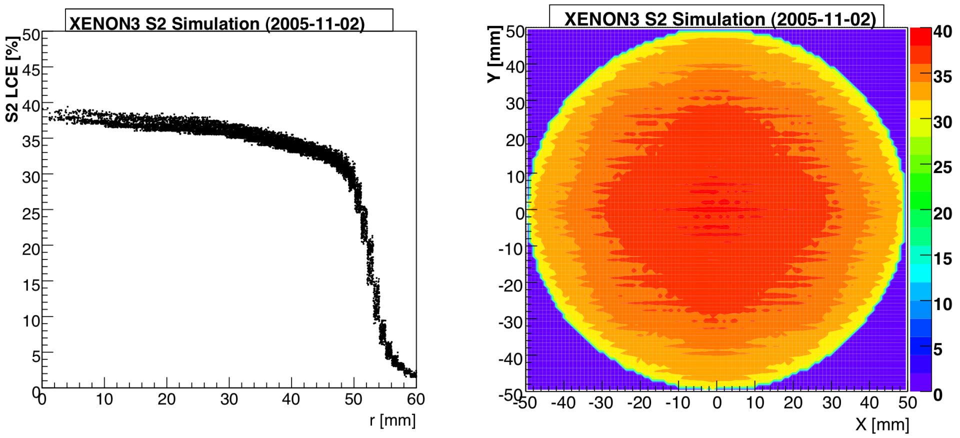

Figure 5.31: Simulation of S2 light collection efficiency as a function of event radial position (left) and XY position dependency (right) for XENON3 detector.

gives $c_1 = 1.529 \pm 0.050$, $d_1 = -0.0113 \pm 0.0011$, $c_2 = 2.496 \pm 0.098$ and $d_2 = -0.0320 \pm 0.0021$. These parameters are only valid for $35mm < r < 50mm$. The uncertainties are statistical only. At $r = 40$ mm, the S1 and S2 are: S1(r=40)/S1 $= 1.078 \pm 0.064$ and S2(r=40)/S2 $= 1.22 \pm 0.13$, where $S1$ and $S2$ are values from all of the 122 keV events from Co-57 after drift time correction.

Although we find a strong radial dependency of the S1 and S2 signal for events happening at radius between 35 and 55 mm, the dependency at smaller radius can't be obtained from the Co-57 events, as the 122 keV γ rays interact mostly near the edges. Fortunately, neutrons make inelastic scattering on ^{129}Xe in liquid xenon and produce 40 keV gammas (see Figure 5.35). Although the scintillation light from these events does not correspond

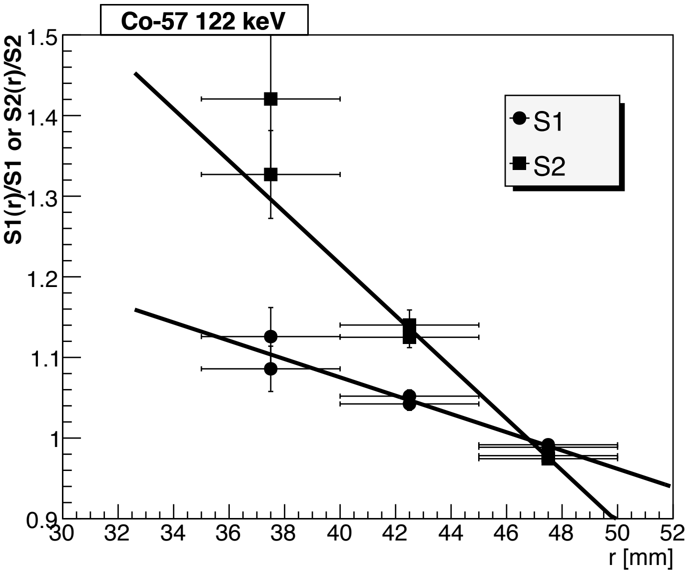

Figure 5.32: Radial dependency of S1 and S2 signal for 122 keV γ rays in the XENON3 detector for 35mm < r < 50mm.

exactly to a value at 40 keV based on the energy calibration with 122 keV γ rays, those events are located all over the sensitive volume of the detector and can be used to obtain the radial position dependency of S1 and S2 at smaller radii. Due to the limited statistics and resolution of the "40 keV line", we choose to obtain the radial position dependency for events with $r < 40mm$, which can be a radial position cut for the final results, and $35mm < r < 45mm$, which can be used as the mean value for events at r = 40 mm, to compare with Co-57 calibration. Figure 5.33 are the S1 and S2 (after drift time correction) distributions for "40 keV line" at $r < 40$ mm and $35mm < r < 45mm$, separately. We obtain, from the peak positions of the "40 keV line" in these distributions, $S1(r < 40)/S1(r = 40) = 0.956 \pm 0.015$ and $S2(r < 40)/S2(r = 40) = 1.136 \pm 0.022$.

Based on the above studies of radial position dependency of S1 and S2 signals, we apply the following correction factors for S1 and S2 for using the energy calibration from all 122 keV γ rays from Co-57: $S1(r < 40)/S1 = 1.030 \pm 0.063$ and $S2(r < 40)/S2 = 1.39 \pm 0.15$.

5.3.3 Nuclear recoil ionization yield

During the experiment, the detector was irradiated with a Cf-252 neutron source at 5.8 meters away and later with neutrons from a generator about 1 meter away from the detector. The Cf-252 source produced 1.3×10^7 neutrons/sec, with a mean neutron energy around 1 MeV (see Figure 5.34). The rate in the detector with the Cf-252 was controlled to be less than 2 kHz, by changing the distance of the source to the detector. It was further shielded with 10 cm of lead blocks to reduce γ ray activity.

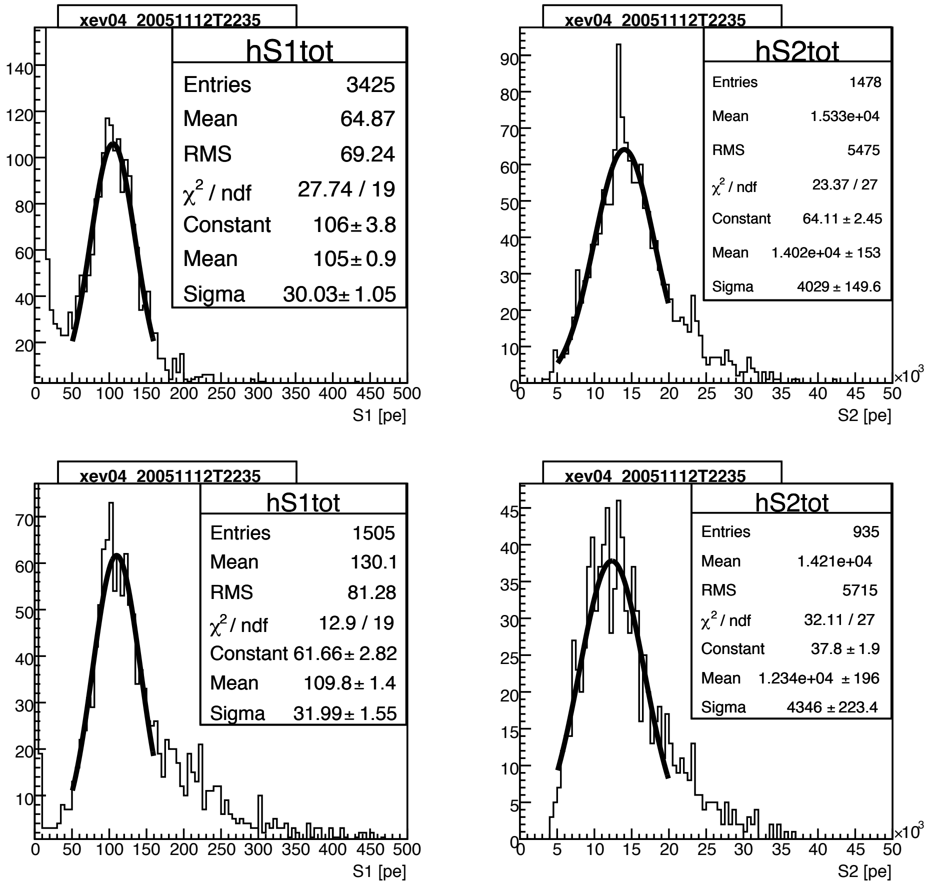

Figure 5.33: S1 and S2 distributions for *40 keV line* at $r < 40$ mm (two on top) and 35mm < r < 45mm (two on bottom). Both S1 and S2 have been corrected for drift time dependency.

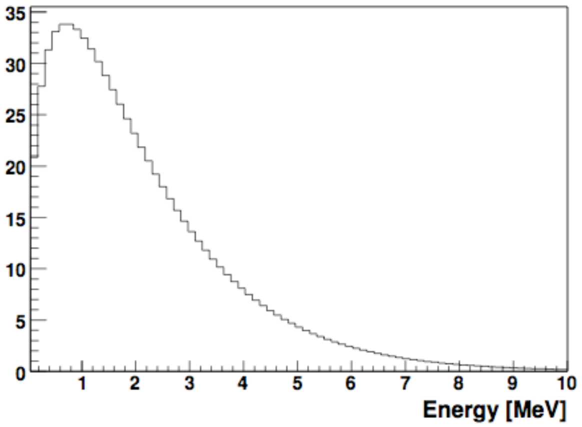

Figure 5.34: Neutron spectrum from Cf-252 source.

After correcting the Z dependence of S1 and S2 by using the parameters obtained from Co-57 calibration runs, the response of the XENON3 detector to Cf-252 is shown in Figure 5.35 for an operating condition with 13 kV at cathode (corresponding to 1.3 kV/cm drift field in the liquid) and 4 kV at anode. The pressure in the chamber is about 2.5 atm.

The nuclear recoil events are identified with a different S2/S1 ratio from that of γ ray events. To define the nuclear recoil band, we first fit log10(S2/S1) with a Gaussian function to find the mean and sigma for each 5 keVee energy window. An exponential function is used to fit the mean plus/minus the sigma of log10(S2/S1) for all energy windows to obtain the band for nuclear recoil events. The two lines represent the elastic scattering nuclear recoil band (68%). The upper line is $Log10(S2/S1) = \exp(0.777 - 0.00723 \times E_{ee})$, the lower line is $Log10(S2/S1) = \exp(0.516 - 0.00354 \times E_{ee})$. The vertical thick line (5 keVee) represents the energy threshold of the current run.

Similar to the calculation for the XeBaby experiment (see Section 5.2), the nuclear recoil energy is calculated based on $E_r = E_e/f_q \cdot L_e/L_n$, where E_e is the electron equivalent energy from S1 calibration of ^{57}Co. f_q is the nuclear recoil scintillation efficiency in liquid xenon at zero field. L_n and L_e are scintillation light quenching due to drift field for nuclear recoils and 122 keV γ rays separately. At 1.3 kV/cm drift field, L_n is about 95% (Aprile *et al.*, 2005b), and L_e is about 50% (Aprile *et al.*, 2005a). The nuclear recoil scintillation efficiency was measured by several groups and we adopt an empirical formula $f_q = 0.06E_r^{0.34}$, based on the measured value in (Aprile *et al.*, 2005a).

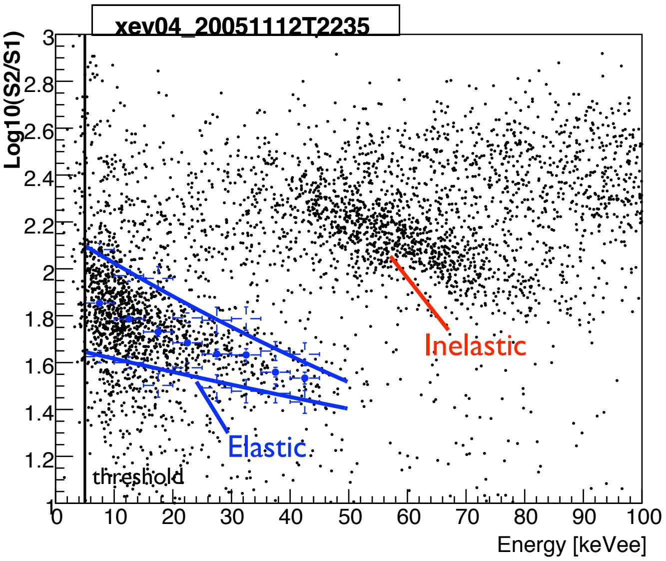

Figure 5.35: XENON3 response to Cf-252 source.

The S2 distribution for nuclear recoil events at each 10 keVr nuclear recoil energy window was further selected to obtain the nuclear recoil ionization yield, the procedure being the same as discussed in Section 5.2. Co-57 calibration runs were taken before and after the Cf-252 run. The calibration gave $S1(r < 40) = 230 \pm 14$ pe and $S2(r < 40) = 43.5 \pm 4.7$ kpe for 122 keV gamma rays.

The result of nuclear recoil ionization yield for the Cf-252 run at 1.3 kV/cm is shown in Figure 5.36, compared with the results obtained from the XeBaby detector at 1.0 and 2.0 kV/cm drift field. Considering the large statistical and systematic errors for the current measurement, the two detectors give rather consistent results. The shown error for XENON3 result is statistical only, based on the statistical error from Co-57 calibration and nuclear recoils. The systematic error from the Co-57 S2 calibration for XENON3 might be as large as 12%.

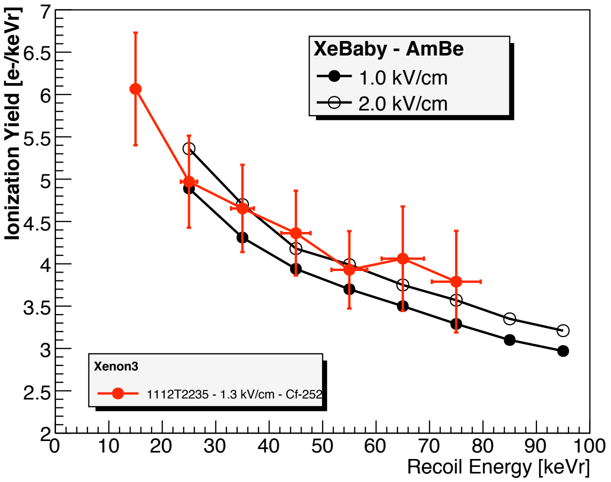

Figure 5.36: Nuclear recoil ionization yield, combined results from XENON3 and XeBaby detectors.

5.3.4 Background discrimination with position cut

XENON3's 3D position sensitivity allows identification of events in X and Y. For the events interact near the edge of the LXe sensitive target, the field non-uniformity may cause none-sufficient electron drifting from the liquid to the gas, which results a small $S2$ signal, while $S1$ is not affected. This makes the $S2/S1$ of these *edge* electron recoils events similar to the nuclear recoil events. With a radial cut of the event position, these edge events can be removed. A preliminary study from the XENON3 data indicates an improved background rejection efficiency after cutting out the edge events.

Figure 5.37 shows the background rejection efficiency from pure gamma ray exposure ^{137}Cs to the detector. The nuclear recoil acceptance is 68% [-σ, σ], as defined in Figure 5.35. A better background rejection can be achieved by making a selection with event radial position less than 45 mm. The statistical errors are shown.

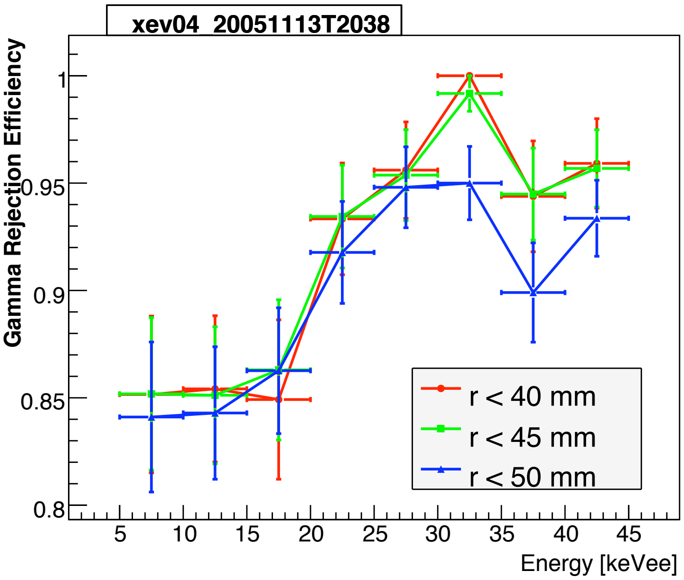

Figure 5.37: XENON3 background rejection efficiency with different position cut.

Chapter 6

The XENON10 Experiment

Based on the results obtained from the XENON R&D program, a larger scale dual phase xenon TPC prototype has been designed and constructed with optimized light collection efficiency, PMT signal readout, LXe purity monitoring, HV handling and 3D position sensitivity. The XENON10 detector, with a sensitive target mass of about 10 kg after fiducial volume cut, will be operated underground in Gran Sasso National Lab starting from 2006.

In this section, we will first illustrate the baseline design of the XENON10 detector. The expected performance of the detector will be studied with Monte Carlo simulations. We then will discuss various background contributions to the detector. The detector's sensitivity to the SUSY parameter space for WIMP detection will be presented in the end.

6.1 Detector design and operation

The baseline design of XENON10 detector is shown in Figure 6.1. The dual phase xenon TPC has an active volume of about 5 liter (15 kg of LXe), defined by a PTFE cylinder with 8 inch inner diameter and 6 inch drift length (from cathode to grid). A low radioactivity cathode HV feed-through of custom design has been built and shown to allow at least 1 kV/cm drift field, and up to a few kV/cm, in the LXe region. The high UV-reflectivity of the PTFE improves the light collection efficiency for both direct and proportional light. An array of field shaping copper wires is placed between grid and cathode, to ensure the drift field uniformity. Several capacitance liquid level meters are placed on the top near the grid to measure the liquid xenon level with a precision of much less than 1 mm. An additional purity monitor (Arneodo *et al.*, 2002) will be implemented to monitor the liquid xenon purity in the detector. The XENON10 detector will be cooled by the same pulse tube refrigerator (PTR), which has been extensively tested and operated with XENON3 and previous prototypes, since 2003. An additional LN_2 cooling coil is installed around the inner wall of the chamber, for emergency cooling in case of power loss or PTR failure. The LN_2 flow is activated by a battery-powered solenoid valve which opens at a preset value of over pressure in the detector.

Above the grid that is immersed in the LXe, additional grids are used to create the electric field for the proportional scintillation light. The four grids (cathode, grid, anode and top grid) are all made with meshes (2 x 2 mm^2 holes, 100 μm bar width, 80μm thickness). These mesh grids will produce a much more uniform electric field, which improves the energy resolution of

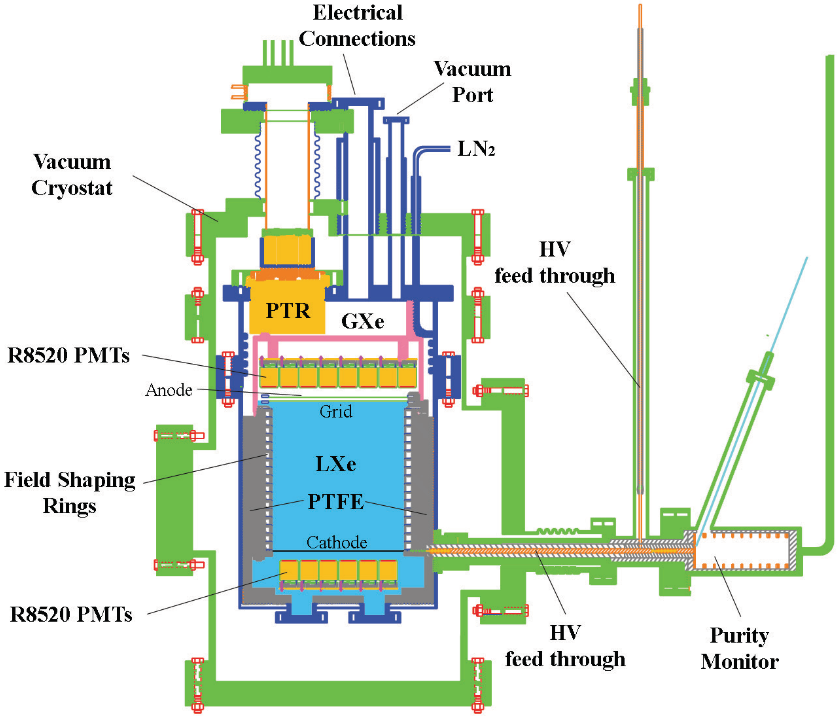

Figure 6.1: Baseline design of the XENON10 detector.

the proportional light. Two PMT arrays are installed in the detector. One with 48 PMTs, located about 1 cm above the top grid, is installed on the top in the gas phase. Another one with 41 PMTs, located about 1 cm below the cathode grid, is installed on the bottom, in the LXe. The PMTs are the same type (Hamamatsu R8520, 1 inch square) used in the XENON3 detector. An illustration of the detector's inner chamber is shown in Figure 6.2. The signals from the PMTs will be readout by the same DAQ system as used in XENON3 (see section 5.3) with increased number of channels.

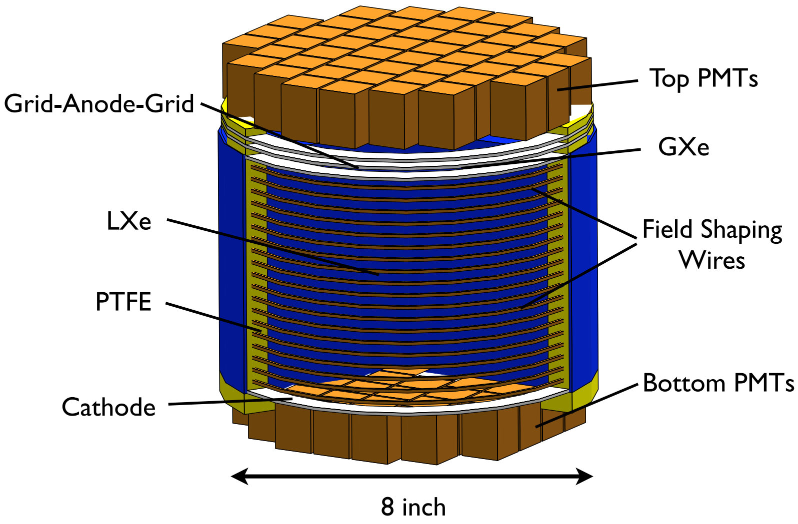

Figure 6.2: XENON10 inner detector illustration.

The detector system with its vacuum cryostat will be installed in a passive shield consisting of a 30 cm thickness of polyethylene (total mass of 2.2 ton) for neutron moderation and 23 cm of Pb (total mass 27 ton) to reduce external gamma activity.

6.2 Light detection simulations

The XENON10 detector's performance was simulated with a GEANT4 program for direct light and proportional light detection, using a detailed detectors mass model (Figure 6.2). The simulation of light detection for proportional light also produces a lookup table for XY position reconstruction, as discussed in section 5.3.1 for the case of XENON3. The assumptions for the simulation are listed in Table 6.2, where the nuclear recoil scintillation efficiency and ionization yield functions are obtained from the measurements in section 5.1 and 5.2, respectively. E_n is the nuclear recoil energy in keVr. The scintillation light is partly absorbed by the detector materials (LXe, wires, grids, PTFE, etc.). We define the *light collection efficiency (LCE)* as the ratio of the number of photons reaching the photocathodes of PMTs over the total number of scintillation photons produced by an event.

6.2.1 Direct light detection

The direct scintillation light produced by electron recoils and nuclear recoils are detected by both the PMTs on the top and bottom. Due to the total internal reflection of the scintillation light on the liquid-gas interface, most of the photons are collected by the PMT array on the bottom. The solid angle effect makes the light detection dependent on the Z position of an event. Figure 6.3 shows the simulated LCEs for the top, bottom arrays and their combined value as a function of Z. The LCEs has approximately a linear relationship to Z, as shown in the plots separately. In order to have a better energy resolution, we can correct the light collection using parameters

Item	Value
PTFE reflectivity	92%
Light absorption length	100 cm
Rayleigh scattering length	30 cm
Liquid xenon index of refraction	1.61
W value of light for electron recoil	21.6 eV
Gas gain for proportional light	200
Nuclear recoil scintillation efficiency	$0.06E_n^{0.34}$
Quenching of $S1$ at 1 kV/cm for nuclear recoil	95%
Quenching of $S1$ at 1 kV/cm for electron recoil	50%
Nuclear recoil ionization yield at 1 kV/cm [e-]	$15.4E_n^{0.643}$
Charge collection for electron recoils at 1 kV/cm	65%
PMT quantum efficiency	20%
PMT collection efficiency	70%

Table 6.1: Assumptions for the simulation of light collection efficiency.

found in Figure 6.3. The corrected LCE distributions for all events uniformly distributed in the detectors sensitive volume are shown in Figure 6.3. The mean LCEs for the top, bottom and total are about 8%, 26% and 34% separately. The total light collection efficiency for $S1$ corresponds to 2.3 pe/keV electron recoils at zero field. At high field, its about 1 pe/keV.

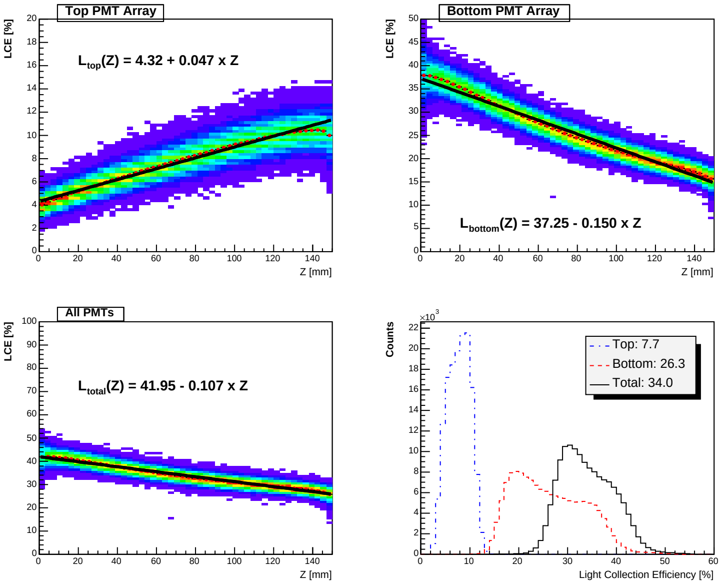

Figure 6.3: Simulated XENON10 light collection efficiency and its dependence on drift time.

From the simulation values of the LCEs, we calculate the triggering efficiency for low energy events. A physical event is identified by seeing one or more photoelectrons on at least two PMTs (coincidence of two). This coincidence-triggering scheme avoids false triggering on the dark current of an individual PMT. By taking into account the scintillation efficiency, field quenching for nuclear recoils and quantum efficiency of PMTs, a distribution

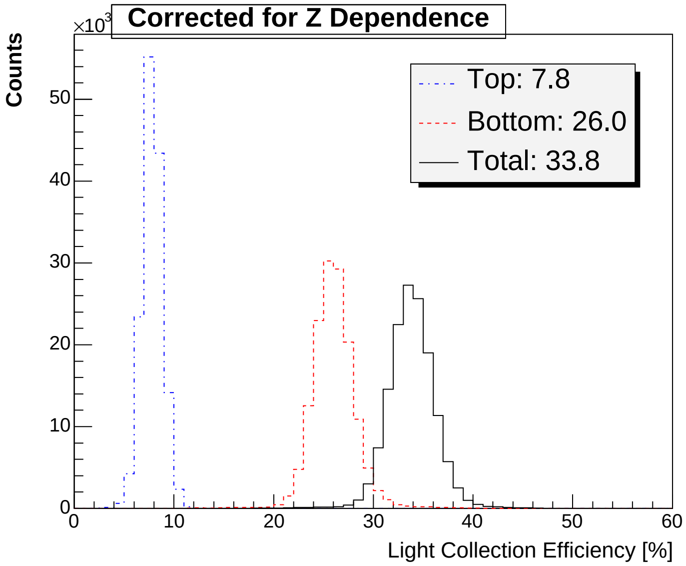

Figure 6.4: Light collection efficiency for XENON10 after correcting for drift time dependency.

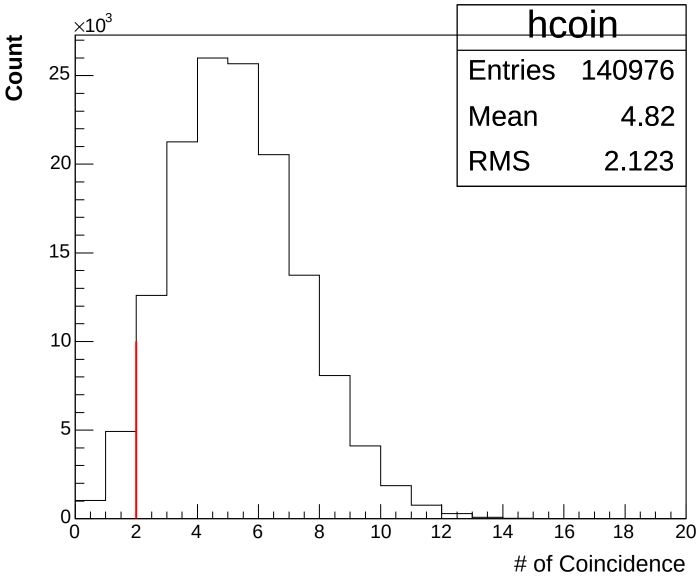

Figure 6.5: PMT coincidence distribution for 16 keV nuclear recoil events uniformly distributed in the sensitive target.

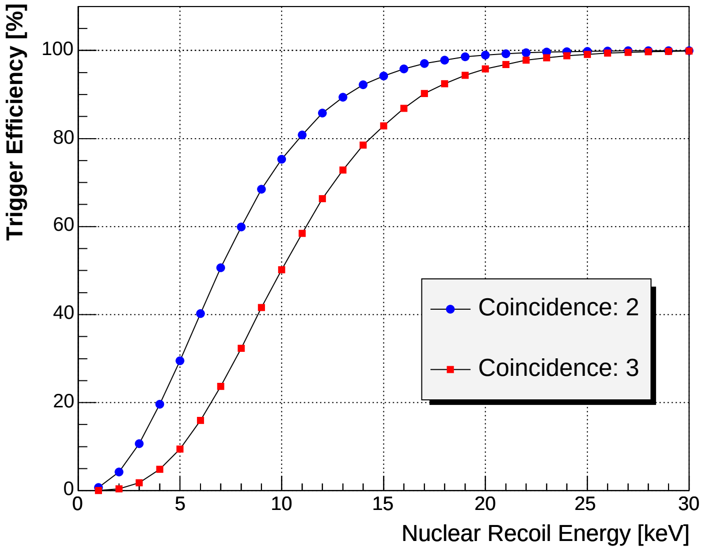

Figure 6.6: Low energy nuclear recoil trigger efficiency for XENON10.

of number of coincidence (number of PMTs seeing at least one photoelectron) for 16 keVr nuclear recoil events uniformly distributed in the detector's sensitive target is shown in Figure 6.5, with a mean coincidence value about 5. More than 95% of the events have at least coincidence value of 2. The XENON10 trigger efficiency for different energy of nuclear recoils is shown in Figure 6.6.

6.2.2 Proportional light detection

Proportional scintillation light $S2$ was simulated for event positions located between the anode and bottom grid. An approximation was made to produce light as a point source, instead of the electron-accelerating track along the field line. This approximation should not affect the results too much as the gas gap is very small (less than 5 mm). The light collection efficiency for $S2$ at different event XY positions is shown in Figure 6.7. It has an average value about 29% for events located less than 8 cm to the center. It drops down to 24% for events near the edge (8 cm $<$ r $<$ 10 cm). Assuming a gas gain value of 200 and PMT efficiencies listed in Table 6.2, we expect to see about 8 photoelectrons per electron drifting in the gas.

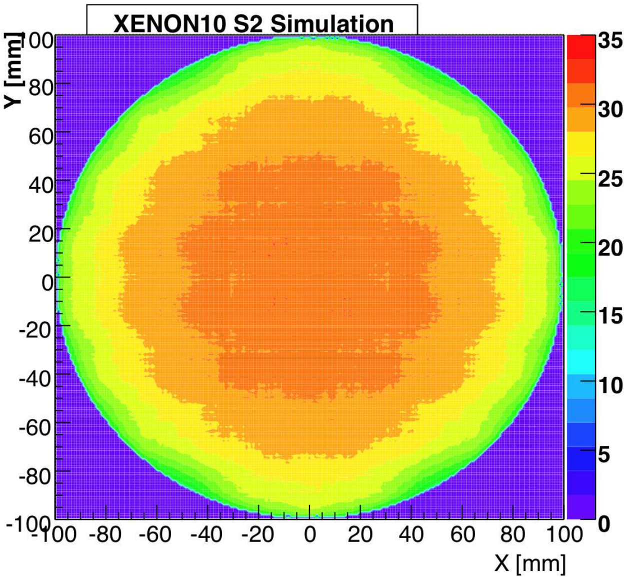

Figure 6.7: S2 light collection efficiency for XENON10. Color unit is in %.

6.2.3 Expected XY position sensitivity

From the $S2$ signal distribution across the PMT array on the top, the XY position of an event can be reconstructed by using variety of methods (e.g. Maximum Likelihood, Minimum-Chisq, Neural Network, etc.). The *Minimum-Chisq* method (see section 5.3.1) was used to obtain the current results for

XENON10.

The expected XY position sensitivity of XENON10 was studied by using simulated 10 keV nuclear recoil events. The mean number of generated proportional light photons, N_γ, is based on the nuclear recoil ionization yield and gas gain values given in Table 6.2. It is further smeared by a Gaussian distribution, with a resolution $\sigma_\gamma = 10\sqrt{N_\gamma}$. The number of photoelectrons, N_{pe}, is calculated by using the simulated photon hits on the PMTs, multiplied by the PMT efficiencies with a binomial distribution. Events were generated at different radii in the detector and the number of photoelectrons, from each of the PMTs on the top, was used for the position reconstruction. Figure 6.8 shows the calculated $1/\chi^2$ distribution for two typical events located at (0,0) and (0,60) mm. The X&Y positions are found at the peak of $1/\chi^2$ distribution. The reconstructed positions and position resolutions at different radii are shown in Figure 6.9.

The *Minimum-Chisq* method can also be used to identify multiple-scatter events if the Z difference between event steps is too small to tell (e.g. less than 2 mm) based only on the drift time information. Although the current method does not reconstruct XY position for each of the steps from one multiple-scatter event, the minimum chisq values, χ^2_{min}, can be used to discriminate between the single-step and multiple-scatter events. χ^2_{min} values for single-step events are smaller than that for multiple-scatter events. This information can be used to reject multiple-scatter nuclear recoil events for a large-scale liquid xenon dark matter detector. Figure 6.10 shows the χ^2_{min} distribution for two-5keV-step nuclear recoil events (total energy is 10 keV), with steps separated by $\Delta L = \sqrt{\Delta X^2 + \Delta Y^2}$ in XY. To simulate the number

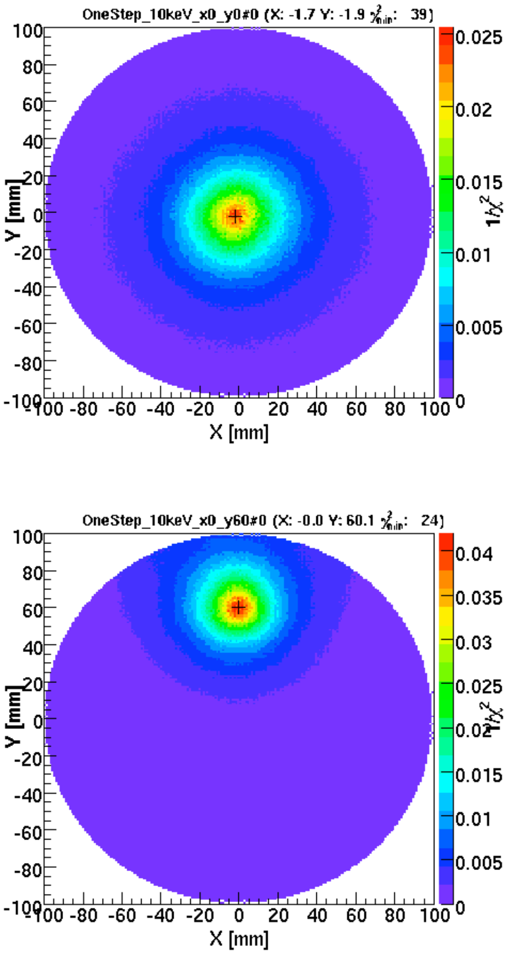

Figure 6.8: $1/\chi^2$ distribution for two simulated events from [0,0] mm (left) and [0,60] mm (right). The reconstructed X&Y positions (+ in the plot) and the χ^2_{min} values are shown on top of the plots.

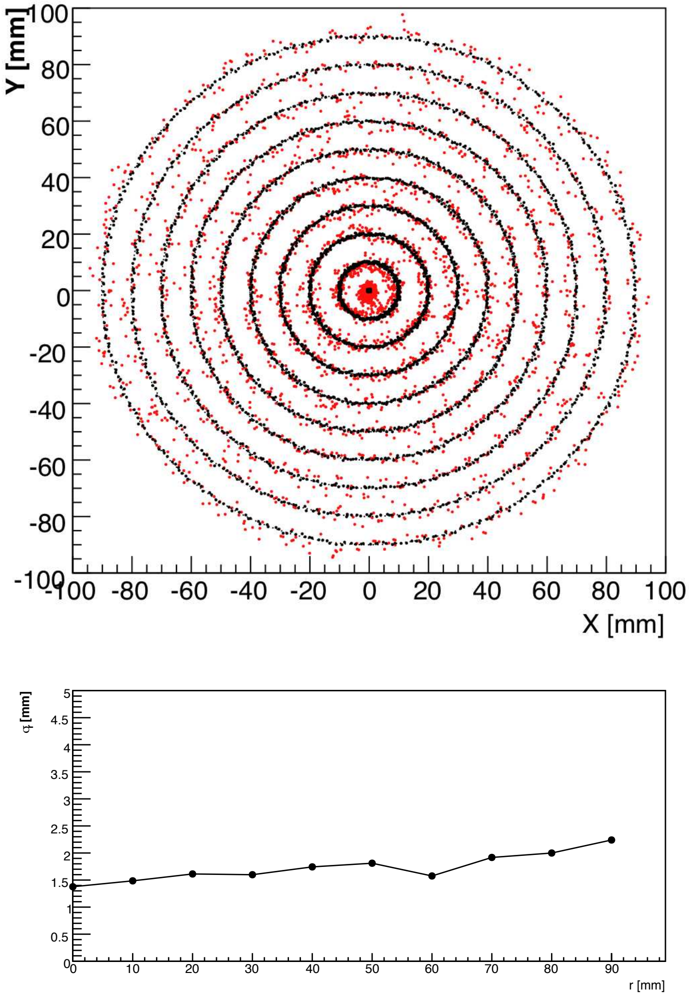

Figure 6.9: Expected XY position sensitivity of XENON10 detector for 10 keV nuclear recoil events. The figure above shows the reconstructed event positions (red dots), compared with the original event positions (black dots). The figure below shows the dependence of position resolution (σ) on the event location. The resolution is best at the center (1.4 mm at r = 0), and becomes larger near the edge (2.4 mm at r = 9 cm).

of photoelectrons in the PMTs, we follow the same procedure for the single step events discussed above. The only difference is that the summed signal from the two steps is used for the position reconstruction. From the χ^2_{min} values, more than 50% of events, with two steps separated by $\Delta L = 2$ cm, can be identified. Events with steps separated by $\Delta L \geq 3$ cm can be fully identified.

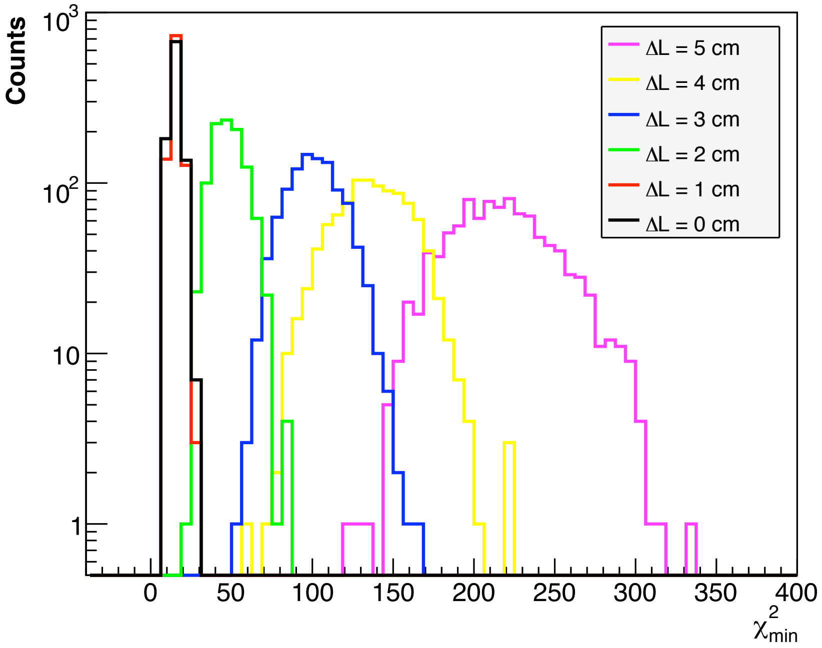

Figure 6.10: The distribution of minimum chisq from position reconstruction for two-5keV-step nuclear recoil events with two steps separated by ΔL in XY.

6.2.4 Electron recoil rejection efficiency

In order to achieve the designed goal of the XENON10 experiment (see section 6.3.3), the electron recoil rejection efficiency based on $S2/S1$ ratio should be about 99.5% or better with a detector threshold of 16 keVr nuclear recoil energy. The ultimate rejection efficiency will only be limited and determined by the statistical fluctuation of the S1 and S2 signals, both of which are partly determined by the S1 and S2 light collection efficiency.

Based on the assumption values listed in Table 6.2, we estimated that 16 keVr nuclear recoil events will produce an average of 110 UV photons for $S1$ and 32 electrons for $S2$. In order to produce the same value of $S1$, an electron recoil energy of about 4.8 keVee is required; this will produce an average value of 72 electrons for $S2$. $S1$ and $S2$ were smeared with Gaussian distributions, taking into account the energy resolution for both signals. The energy resolutions for 16 keVr nuclear recoils and 4.8 keVee electron recoils are derived with $\sigma = \sqrt{FN}$, where N is the number of direct scintillation photons (110 for 16 keVr nuclear recoil) for $S1$ resolution, and number of primary ionization electrons (32 for 16 keVr nuclear recoil) for $S2$ resolution. F is a factor describing the energy resolution. Here we assume a value $F = 10$. The smeared number of photons for both $S1$ and $S2$ were further smeared by binomial distributions, taking into account the PMT effective quantum efficiency (14%), and a final Gaussian smearing due to the PMT gain fluctuation, which is about 0.5 pe from the single photoelectron measurement. The resulting distributions of $S2/S1$ for both 16 keVr nuclear recoils and 4.8 keVee electron recoils are plotted in Figure 6.11. At higher energies, the separation of the nuclear and electron recoil bands will be larger.

We further investigate the rejection efficiency of electron recoil events based on the S2/S1 value. By setting a lower S2/S1, the rejection efficiency of electron recoils will be better, but it also limits the nuclear recoil acceptance. Figure 6.12 shows the electron rejection efficiency as a function of nuclear recoil acceptance efficiency. An electron recoil rejection efficiency of 99.5% can be achieved with a nuclear recoil acceptance of 30%. While a 95% and 90% electron recoil rejection corresponds to a nuclear recoil acceptance of 59% and 70%, respectively. At higher recoil energies, the rejection efficiency will be better.

6.3 Background consideration and sensitivity

To achieve a sensitivity of WIMP-nucleon cross-section down to 2×10^{-44} cm^2, a factor of 10 below the current best limit set by the CDMS II experiment (CDMS Collaboration, 2005b), the total background event rate for XENON10 is required to be below 0.005 evts/kg/day after rejection based on ionization and scintillation ratio $S2/S1$. Such a low background event rate can be achieved by selecting special detector materials with much less radioactive contaminations, a very efficient electron recoil rejection based on $S2/S1$, a 3D sensitivity for rejecting surface/edge events and multiple scattering events. Placing the detector in a deep underground lab and with passive shielding will suppress the background induced by muons and reduce the neutron and gamma background from the environment.

In the following, we will discuss the background in two main categories, the *gamma* rays, which mostly can be rejected based on $S2/S1$ ratio, and the

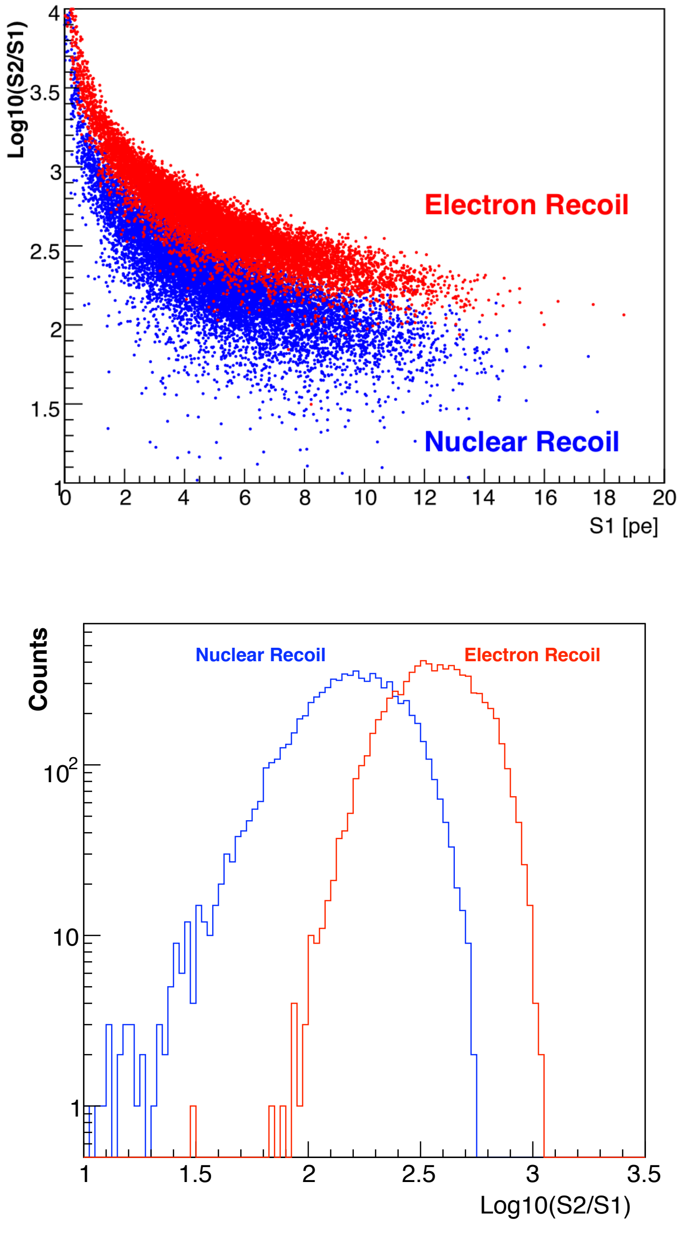

Figure 6.11: Expected S2/S1 distribution for 16 keVr nuclear recoil events (and equivalent electron recoils) in XENON10 detector.

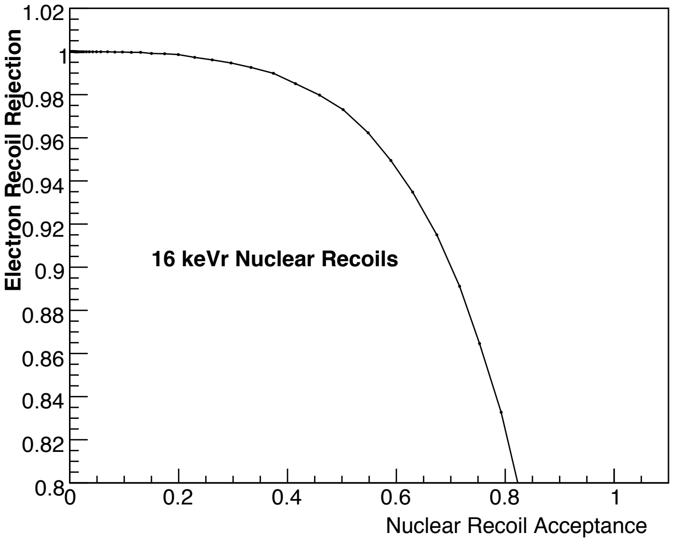

Figure 6.12: Expected electron recoil rejection efficiency vs. nuclear recoil acceptance at 16 keVr level for XENON10 detector.

neutron background, which may cause nuclear recoils similar to those produced by WIMP events. In the end, the projected sensitivity of XENON10 experiment will be presented.

6.3.1 Gamma ray background

The detector materials contain^{238}U, ^{232}Th and ^{40}K. The decay chain of ^{238}U and ^{232}Th, and ^{40}K will produce gamma rays. Natural xenon contains about 5-10 ppm Krypton. The main long-lived radioisotope ^{85}Kr undergoes beta decay with a 690 keV end-point and 10.76 year half-life. Gamma rays from the underground cavern and from the passive shielding materials will also contribute to the total gamma activity.

Gamma rays from detector components

The XENON10 baseline design uses stainless steel for both the inner chamber and outer cryostat. A total mass of about 100 kg stainless steel will be used. The activity from stainless steel (for example, AISL316L) for U/Th/K/^{60}Co is 4/3/<100/23 mBq/kg (1 Bq is 1 disintegration per second) separately. Monte Carlo simulations have been performed using these values. We expect to have 220 mdruee (10^{-3} evts/keVee/kg/day), in the energy range 8–32 keVee, after a fiducial volume cut out of 1 cm from the edge, from the gamma event rate from the stainless steel vessels. Among these events, the single scatters contribute 14 mdruee. The rest are multiple scattering events which can be rejected with the 3D sensitivity of the detector.

Another major gamma ray background is from the PMTs. The PMTs made by Hamamatsu Co. were specially designed for low radioactivity.

The activity of the 1 inch R8520 PMT in U/Th/K/^{60}Co is about 15/3/5/5 mBq/tube (based on value provided by the company and our screening results). The overall gamma activity from two arrays of PMTs on top and bottom will contribute a total activity about of 400 mdruee (8–32 keVee). Since the gamma rays originate from the detectors top and bottom regions , a fiducial volume cut of 1 cm from top and bottom will reduce the value to 200 mdruee. Additional cuts based on multiple scattering events rejection will leave about 35 mdruee, from the single scattering events.

The PTFE material has a representative upper limit of radioactivity for U/Th/K at 0.4/0.2/40 mBq/kg. The gamma ray contribution will be less than 1 mdruee (8–32 keVee) for single scattering events. Similarly, the resistors used for the field shaping wires will contribute about 1.6 mdruee (8–32 keVee) for single scattering events.

The beta-decay of ^{85}Kr contributes a significant background in a liquid xenon experiment. The commercial available xenon (¡10 ppm contamination of Kr) will give a total electron recoil activity at about 300 druee at low energies (Yamashita, 2003a).The Kr contamination should be reduced below the 1 ppb level to insure a low contribution of background (1 ppb level of Kr gives 30 mdruee). Krypton-free xenon can be purchased from Spectra Gas with $<$ 5 ppb Kr, which is close to the level required to satisfy the XENON10 experiment. Within the XENON collaboration, a Kr separation system was built, based on chromatographic adsorption in a charcoal column at room temperature. The system also concentrates the removed Kr, allowing it to be measured at the ppt level. A high-purity version of the system has been built and should allow a removal of Kr down to 100 ppt level and should be capable of processing 10 kg Xe in a few days. The Krypton contamination can also be measured to much less than 1 ppt level by atom counting using a magneto-optical trap (MOT) technique (McKinsey and Orzel, 2005a).

The 2.2 ton polyethylene shield (U/Th/K of 0.37/0.24/31 mBq/kg) will contribute 50 mdruee gamma activity in the fiducial volume, among which 9 mdruee are single scatters.

External gamma ray background

The gamma ray activity from the rock and concrete of the underground lab can be reduced by using passive Pb shield (23 cm). The estimated activity is about 90 mdruee, among which 9 mdruee are single scatters. The U/Th/^{210}Pb in the lead shielding will create gamma activity in the detector. The shielding Pb blocks will be screened to insure a background contribution from the ^{210}Pb to be less than 10 mdruee and U/Th to be less than 5 mdruee after cut on multiple scatters.

Table 6.2 lists various contributions to the gamma ray activity in the XENON10 detector. The total gamma activity, after cut on the fiducial volume (10 kg) and multiple scatters, is about 115 mdru. Assume a 99.5% electron recoil rejection efficiency based on $S2/S1$ ratio, this leaves 0.6 mdru electron recoil events that can't be identified as gamma background. This rate needs to be further reduced by at least a factor of 3, for instance by replacing the stainless vessel with OFHC copper and by further reducing the Kr level in Xe, in order to achieve the XENON10 designed WIMP sensitivity goal.

Table 6.2: Gamma ray background of XENON10 experiment.

Source	Activity [mdruee]	Actitity after cut [mdruee]
Kr-85 (1ppb)		30
PMTs	400	35
Stainless Steel	220	14
Resistor, PTFE		< 2.6
Polyethylene	50	9
External	90	24
Total		115

6.3.2 Neutron background

The U and Th contamination in the detector construction materials can produce neutrons via (α, n) reaction and spontaneous fission. This neutron background needs to be suppressed by using active veto detectors (Carson *et al.*, 2005). The cosmic muons can also induce neutrons when passing through the rocks. And the radioactive component in the rock itself also produces neutrons. This external neutron background needs to be reduced by passive shielding (e.g. polyethylene) surrounding the detector.

Neutrons from (α, n) reaction

Alpha particles themselves will deposit their energy immediately after they enter the liquid xenon from external sources. Those events are very close to the edge of the detector and can be rejected by a fiducial volume cut once their positions are known. Alphas from the U and Th decay chains will produce neutrons via (α, n) reaction, producing neutrons in the energy of 0-10 MeV. Based on the U/Th levels as in the previous sections, the estimated neutron event rate from (α, n) reaction is about 10^{-4} mdrur (r represents recoil energy) negligible for XENON10.

Neutrons from rock

The underground laboratory for placing the WIMP detectors has rock walls around, with U/Th level at the 60 ppb and 130 ppb, respectively. The radioactive isotopes in the decay chains of U/Th produce neutrons with a total rate of about 10^{-8}n/cm^3/s and mean energy of 1-2 MeV in a typical underground lab. The neutron flux at the rock-lab boundary is about 2×10^{-6}n/cm^2/s above 10 keV (Davies *et al.*, 2005). To reduce the level of neutron flux originating from the rock, a passive shield with hydrocarbon material is needed. By using 30 cm polyethylene shield around the XENON10 detector, the neutron from external cavern is moderated and reduced to 0.02 mdrur in the detector's sensitive volume.

Muon induced neutrons

Neutrons can be induced in the rock by atmospheric muons penetrating deep into the underground. Most of the neutrons are thermal neutrons from the muon induced hadronic and electromagnetic cascades. They are moving slowly and get captured by protons or other nuclei. Some of the neutrons will make elastic scatterings off the target nucleus and produce irreducible signals similar to those from WIMPs. Gamma rays activity can also be increased by the neutron activation. Together with an active veto shield to distinguish these neutrons, a fully understanding of the neutron flux induced by muons is crucial for WIMP dark matter detectors underground. The muon-induced neutron production and detection can be calculated by Monte Carlo simulations with GEANT4 (GEANT4) and FLUKA (FLUKA) toolkits, which should yield similar results for liquid xenon detector underground (Araujo *et al.*, 2005).

The muon flux in Gran Sasso, at a depth of 3700 mwe, is 12 $\mu/\mathrm{m}^2/\mathrm{day}$. The muon electromagnetic showers, hadron showers and direct spallation in the shielding Pb and Polyethylene will produce $4 \times 10^{-3}\mathrm{n}/\mu/(\mathrm{g\ cm}^{-2})$ and $0.23 \times 10^{-3}\mathrm{n}/\mu/(\mathrm{g\ cm}^{-2})$ separately. The resulted nuclear recoil rates in the LXe target at 16 keVr threshold are 0.005 mdrur and 0.003 mdrur, respectively.

The high energy neutrons (20-600 MeV) generated in the cavern rock by muon interaction tend to *punch-through* the moderator shielding (polyethylene). The estimated XENON10 event rate due to high energy punch-through neutron events will be less than 0.003 mdrur.

Combining all the studied possible neutron sources, the overall nuclear recoil event rate due to neutron background is in the order of 0.02 mdrur, which is much lower than expected WIMP event rate in XENON10 (see section 6.3.3).

6.3.3 Projected sensitivity

The design goal of the XENON10 experiment is to be able to probe a spin-independent WIMP-nucleon cross-section as low as 2×10^{-44} cm^2, a 10 folds lower than the current lowest limit set by CDMS experiment at Soudan.

The total event rate, for a WIMP mass of 100 GeV, of XENON10 with 16 keVr threshold, will be 2.3 evts/10kg/month, based on the calculation in section 2.2.4. This corresponds to a differential event rate of 6.4×10^{-4} evts/keVr/kg/day at 16 keVr (0.64 mdrur).

The background event rate for XENON10, including nuclear recoils from neutron elastic scattering and electron recoil after fiducial cut and rejection based on $S2/S1$ ratio with 99.5% discrimination capability, will be lower (see previous section on background) than the WIMP event rate. Thus, by operating the detector with a net exposure of 300 kg·day (10 kg for one month), XENON10 should be able to see at least an average of 2.3 WIMP candidate events if WIMP-nucleon cross-section is above 2×10^{-44} cm^2. While seeing no events would indicate, with 90% C.L. (based on Poisson distribution), that WIMP-nucleon cross-section is below that level (2×10^{-44} cm^2 for 100 GeV WIMP).

Figure 6.13 shows the projected sensitivity of XENON10 experiment. The successful operation of XENON10 experiment will pave the way for the XENON100 module, which increases the target LXe mass to 100 kg level. Operating the XENON100 experiment at the Gran Sasso laboratory for three months, with a background level below 1×10^{-5} druee, would provide a sensitivity to WIMP-nucleon cross-section at 10^{-45}cm^2 level. This sensitivity will allow testing SUSY models at a comparable level with accelerator constraints. An eventual finding of WIMP events at XENON100 stage would require future tonne scale experiments (XENON1T) to gather more WIMP events to study their unique properties in the lab.

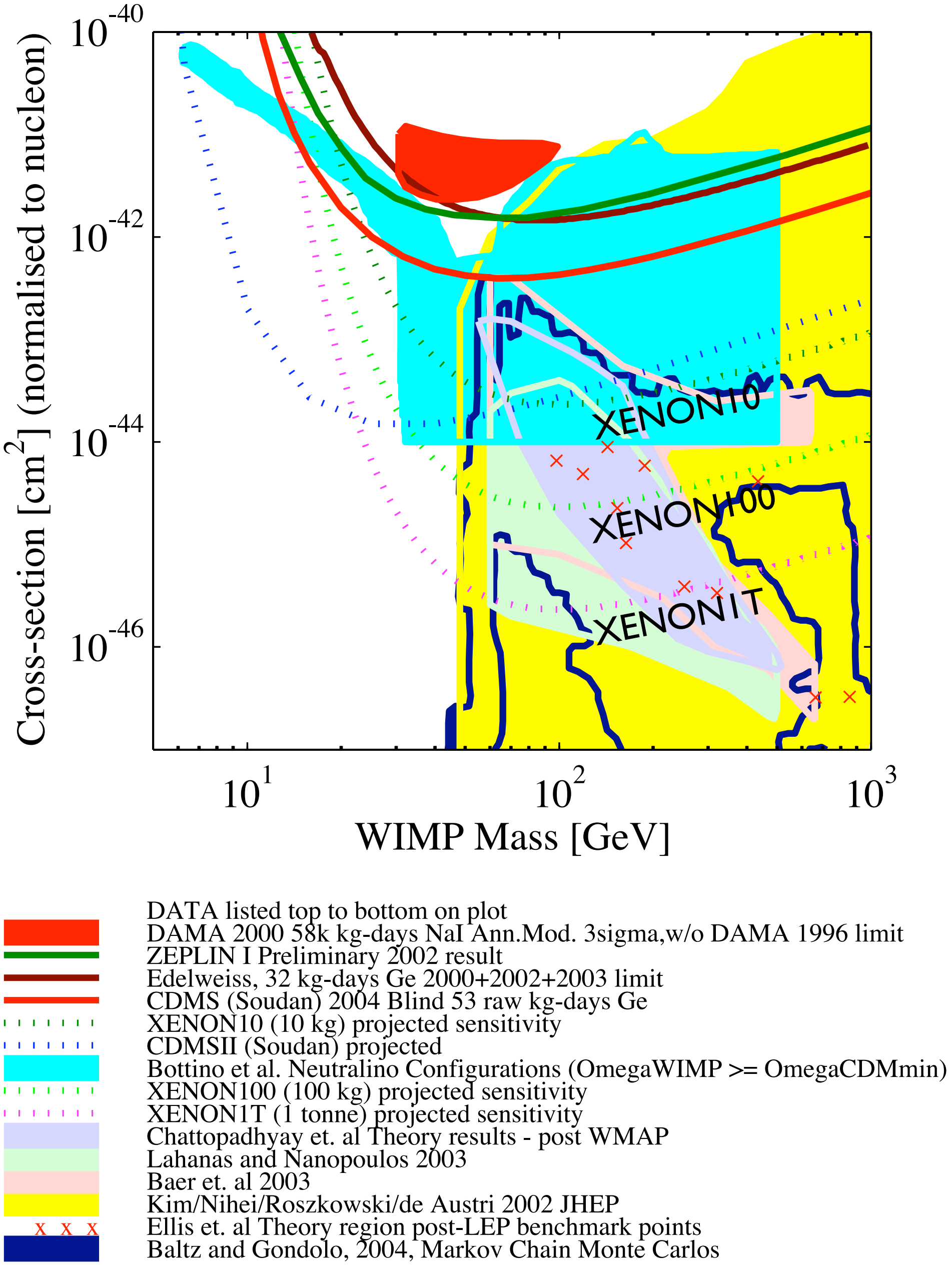

Figure 6.13: Projected spin-independent WIMP sensitivity of XENON10 experiment. Plotted from http://dmtools.brown.edu.

Bibliography

Agostinelli, S. *et al.*, Nucl. Inst. and Meth. A **506**, 250 (2003).

Alkhazov, G.D. *et al.*, Nucl. Instr. Meth. **48**, 1 (1967).

Akimov, D. *et al.*, Phys. Lett. B **524**, 245 (2002).

Allen, A.W., Schmidt, R.W., & Fabian, A.C., MNRAS **334**, L11 (2002).

ANTARES Collaboration: http://antares.in2p3.fr/.

Aprile, E. *et al.*, IEEE Trans. on Nucl. Sci., Vol. 37, No. 2, 553 (1990).

Aprile, E. *et al.*, Nucl. Instr. Meth. A **302**, 177 (1991a).

Aprile, E. *et al.*, Nucl. Instr. Meth. A **307**, 119 (1991b).

Aprile, E. *et al.*, Phys. Rev. A **48**, 1313 (1993).

Aprile, E. *et al.*, Nucl. Instr. and Meth. A **338**, 328 (1994).

Aprile, E. *et al.*, Nucl. Instr. and Meth. A **461**, 256 (2001).

Aprile, E. *et al.*, astro-ph/0212005.

Aprile, E. *et al.*, Nucl. Inst. and Meth. A **480**, 636 (2002b).

Aprile, E. *et al.*, IEEE Trans. on Nucl. Sci., Vol. 50, No. 5, 1303 (2003).

Aprile, E., et al, IEEE Trans. Nucl. Sci., **51** 1986 (2004).

Aprile, E. *et al.*, *Scintillation Spectroscopy with Photomultipliers in Liquid Xenon*, to be submitted to Nucl. Inst. and Meth. A (2005a).

Aprile, E. *et al.*, Phys. Rev. D **72**, 072006 (2005b).

Araújo, H.M. *et al.*, Nucl. Instr. and Meth. A **545**, 398 (2005).

Arneodo, F. *et al.*, Nucl. Inst. and Meth. A **449**, 147 (2000).

Arneodo, F. *et al.*, *Electron lifetime and purity monitor for the ICARUS T600 detector*, ICARUS-TM/02-14.

Asztalos, S.J. *et al.*, ApJ **571**, L27 (2002).

Bahcall, J.N. *et al.*, ApJ. **265**, 730 (1983).

Bakele, G. *et al.*, J. Phys. Chem. **80**, 2556 (1976).

Baldini, A. *et al.*, Nucl. Instr. and Meth. A **545**, 753 (2005).

Baltz, E.A., and Gondolo, P., Phys. Rev. D **67**, 063503 (2003).

Baltz, E.A., astro-ph/0412170.

Barkov, L.M. *et al.*, Nucl. Instr. and Meth. A **379**, 482 (1996).

Barrau, A. *et al.*, Phys. Rev. D **72**, 063507 (2005).

Begeman, K.G. *et al.*, MNRAS **249**, 523 (1991).

Belli, P. *et al.*, Phys. Rev. D **66**, 043503 (2002) 043503.

Bekenstein, J.D., Phys. Rev. D **70**, 083509 (2004); Bekenstein, J.D., Phys. Rev. D **71** 069901(2005).

Bennett, G.W. *et al.*, Phys. Rev. Lett. **89**, 101804 (2002).

Bergstrom, L. *et al.*, Phys. Rev. Lett. **94**, 131301 (2005).

Bernabei, R. *et al.*, Phys. Lett. B **389**, 757 (1996).

Bernabei, R. *et al.*, Phys. Lett. B **436**, 379 (1998).

Bernabei, R. *et al.*, Phys. Lett. B **480**, 23 (1998).

Bernabei, R. *et al.* EPJdirect **C11**, 1 (2001).

Bernabei, R. *et al.* Riv. Nuovo Cim. **26**, 1 (2003), astro-ph/0307403.

Bevington, P.R., and Robinson, D.K., *Data Reduction and Error Analysis for the Physical Science*, 2nd ed., pp.45.

Birkedal-Hansen, A. and Wacker, J.G., Phys. Rev. D **69**, 065022 (2004)

Birkedal, A., Matchev, K., and Perelstein, M., Phys. Rev. D **70**, 077701 (2004).

Bolozdynya, A.I., Nucl. Instr. and Meth. A **422**, 314 (1999).

Boulay, M.G. *et al.*, nucl-ex/0410025.

Bondarenko, G. *et al.*, Nucl. Instr. and Meth. A **442**, 187 (2000).

Bottino, A. *et al.*, Phys. Rev. D **69**, 037302 (2004).

Bottino, A. *et al.*, Phys. Rev. D **72**, 083518 (2005).

Boukhira, N. *et al.*, Astropart. Phys. **14**, 227 (2000).

Braem, A. *et al.*, Nucl. Instr. and Meth. A **320**, 228 (1992).

Bringmann, T., JCAP **0508** (2005) 006, astro-ph/0506219.

Buzhan, P. *et al.*, Nucl. Instr. and Meth. A **504**, 48 (2003).

Bunemann, O. *et al.*, Can. J. of Res. **27**, 191 (1947).

Caldwell, R.R., and Ostriker, J.P., ApJ **251**, 61 (1981).

Carson, M.J. *et al.*, Nucl. Instr. and Meth. A **548**, 418 (2005).

CAST Collaboration, Phys. Rev. Lett. **94**, 121301 (2005).

Catena, R. *et al.*, Phys. Rev. D **70**, 063519 (2004).

CDMS Collaboration, Phys. Rev. Lett. **84**, 5699 (2000).

CDMS Collaboration, Phys. Rev. D **66**, 122003 (2002).

CDMS Collaboration, Phys. Rev. D **68**, 082002 (2003).

CDMS Collaboration, Phys. Rev. Lett. **93**, 211301 (2004).

CDMS Collaboration, Phys. Rev. D **72**, 052009 (2005a).

CDMS Collaboration, astro-ph/0509259.

CDMS Collaboration, astro-ph/0509269.

Cembranos, J.A.R., Dobado, A. and Maroto, A.L., Phys. Rev. Lett. **90**, 241301 (2003).

Chepel, V.Y. *et al.*, Nucl. Instr. and Meth. A **349**, 500 (1994).

Chepel, V.Y. *et al.*, Nucl. Instr. and Meth. A **392**, 427 (1997).

Cheng, H.-C., Feng, J.L., and Matchev, K.T., Phys. Rev. Lett. **89**, 211301 (2002).

Cline, D.B. *et al.*, Nucl. Phys. B (Proc. Suppl.) **124**, 229 (2002).

Clowe, D. *et al.*, ApJ **604**, 596 (2004).

Collar, J.I. *et al.*, Phys. Rev. Lett. **85**, 3083 (2000).

Collar, J.I. *et al.*, astro-ph/0503398.

Conti, E. *et al.*, Phys. Rev. B **68**, 054201 (2003).

Crawford, H.J. *et al.*, Nucl. Instr. and Meth. A **256**, 47 (1987).

CRESST Collaboration, Astropart. Phys. **23**, 325 (2005).

Cushman, P. *et al.*, Nucl. Instr. and Meth. A **442**, 289 (2000).

Danilov, M. *et al.*, Phys. Lett. B **480**, 12 (2000).

Davies, J.C. *et al.*, Nucl. Intr. and Meth. A **546**, 509 (2005).

Diemand, J. *et al.*, MNRAS **353**, 624 (2004).

Diemand, J. *et al.*, Nature **433**, 389 (2005).

Doke, T., Portugal. Phys. **12**, 9 (1981).

Doke, T., Nucl. Instr. and Meth. **196**, 87 (1982).

Doke, T., and Masuda, K., Proc. SPIE 2305, 19 (1994).

Doke, T. *et al.*, Nucl. Instr. and Meth. A **420**, 62 (1999).

Doke, T., Proceedings of the International Workshop on Technique and Application of Xenon Detectors (Xenon01), pp.17, (2001).

Doke, T. *et al.*, Jpn. J. Appl. Phys. **41**, 1538 (2002).

Doke, T. *et al.*, Nucl. Instr. and Meth. A **503**, 290 (2003).

Drukier, A. *et al.*, Phys. Rev. D **33**, 3495 (1986).

EDELWEISS Collaboration, Phys. Lett. B **513**, 15 (2001).

EDELWEISS Collaboration, Phys. Lett. B **545**, 43 (2002).

EDELWEISS Collaboration, Phys. Rev. D **71**, 122002 (2005a).

EDELWEISS Collaboration, Phys. Lett. B **616**, 25 (2005b).

Einasto, J. *et al.*, Nature **250**, 309 (1974).

Ellis, J. *et al.*, Nucl. Phys. B **238**, 453 (1984).

Ellis, J. *et al.*, Phys. Rev. D **71**, 095007 (2005).

Elsaesser, D., and Mannheim, K., Phys. Rev. Lett. **94**, 171302 (2005).

Engel, J., Phys. Lett. B **264**, 114 (1991).

EXO Experiment, see online http://www-project.slac.stanford.edu/exo/.

Faber, S.M. and Gallagher, J.S., Ann. Rev. Astron. Astrophys. **17**, 135 (1979).

Fano, U., Phys. Rev. **70**, 44 (1946); and Phys. Rev. **72**, 26 (1947).

Feng, J.L., and Smith, B.T., Phys. Rev. D **71**, 015004 (2005).

Fernandes, L.M.P. *et al.*, IEEE Trans. on Nucl. Sci., Vol. 51, No. 4, 1575 (2004a).

Fernandes, L.M.P. *et al.*, Nucl. Instr. Meth. A **531**, 566 (2004b).

Fornengo, N, Pieri, L., and Scopel, S., Phys. Rev. D **70**, 103529 (2004).

Freedman, W. and Turner, M., Rev. Mod. Phys. **75**, 1433 (2003).

FLUKA Simulation Package, available at http://www.fluka.org/.

Fuke, H *et al.*, Phys. Rev. Lett. **95**, 081101 (2005).

Gaitskell, R.J., Annu. Rev. Nucl. Part. Sci. **54**, 315 (2004).

GEANT4 Collaboration, Nucl. Instr. and Meth. A **506**, 250 (2003); GEANT4 Simulation Packge, available at http://wwwasd.web.cern.ch/wwwasd/geant4/.

Georgadze, A.Sh. *et al.*, Astropart. Phys. **7**, 173 (1997).

Giuliani, F. *et al.*, hep-ex/0504022.

GLAST Facility Science Team, Gehrels, N, and Michelson, P., Astropart. Phys. **11**, 277 (1999).

Goldberg, H., Phys. Rev. Lett. **50**, 19 (1983).

Goodman, M.K., and Witten, E., Phys. Rev. D **31**, 3059 (1985).

Grandi, L., "WARP: an argon double phase technique for Dark Matter search", Ph.D. Thesis, University of Pavia, available online http://warp.pv.infn.it/phd_luca.pdf.

Griest, K., and Kamionkowski, M., Phys. Rep. **333**, 167 (2000).

Hailey, C.J. *et al.*, Nucl. Instr. and Meth. B **214**, 122 (2004).

Hailey, C.J. *et al.*, astro-ph/0509587.

Hamaguchi, K. *et al.*, Phys. Rev. D **70**, 115007 (2004).

Haruyama, T. *et al.*, AIP Conference Proceedings, Vol.710, Issue 1, 1459-1466 (2004). see also http://www.joho-kyoto.or.jp/ cryomini/.

HESS Project, Science, **307**, 1938 (2005).

Hitachi, A. *et al.*, Phys. Rev. B **27**, 5279 (1983).

Hitachi, A. *et al.*, Phys. Rev. B **46**, 11463 (1992).

Hitachi, A, in *The Identification of Dark Matter* Proceedings of the Fourth International Workshop, York, UK 2 - 6 September 2002, edited by Neil J C Spooner and Vitaly Kudryavtsev (University of Sheffield, UK) p 357-362; 5th International Workshop on the Identification of Dark Matter, IDM2004, Edinburgh, Scotland, 6th-10th September (2004).

Hitachi, A., to be submitted to Phys. Rev. D (2005).

Hunter, S.D. *et al.*, ApJ **481**, 205 (1997).

IceCube website: http://www.icecube.wisc.edu/.

Ichinose, H. *et al.*, Nucl. Inst. and Meth. A **305**, 111 (1991).

Ichinose, H. *et al.*, Nucl. Inst. and Meth. A **322**, 216 (1992).

Ishida, N. *et al.*, Nucl. Instr. and Meth. A **384**, 380 (1997).

Jortner, J. *et al.*, J. Chem. Phys. **42**, 4250 (1965).

Jungman, G., Kamionkowski, M., and Griest, K., Phys. Rep. **267**, 195 (1996).

Kaluza, T., Sitzungsber. Preuss. Akad. Wiss. Berl. Math. Phys. K1, 966 (1921); Klein, O., Z. Phys. **37**, 895 (1926) [Surv. High-Energy Phys. **5**, 241 (1986)].

Kapusta, M. *et al.*, IEEE Trans. on Nucl. Sci., Vol. 49, No. 4, 1693 (2002).

Kaufmann, L., Talk presented at 7th UCLA Symposium on sources and detection of dark matter and dark energy in the universe, available online at http://www.physics.ucla.edu/hep/dm06/talks/kaufmann.pdf.

KIMS Collaboration, astro-ph/0509080.

Klapdor-Kleingrothaus, H.V. *et al.*, hep-ph/9910205.

Knoll, G.F., *Radiation Detection and Measurement, 3rd Ed.*, John Wiley & Sons, (2000).

Knop, R.A. *et al.*, ApJ **598**, 102 (2003).

Kobayashi, S. *et al.*, Nucl. Instr. and Meth. A **531**, 327 (2004).

Kubota, S. *et al.*, Phys. Rev. B **17**, 2762 (1978).

Lewin, J.D., and Smith, P.F., Astropart. Phys. **6**, 87 (1996).

Lindhard, J., Mat. Fys. Medd. Dan. Vid. Selsk. **33**, 1 (1963).

Lopes, J.A.M. *et al.*, IEEE Trans. on Nucl. Sci., Vol.48, No. 3, 312 (2001).

Lopes, M.I. *et al.*, IEEE Trans. on Dielectrics and Electrical Insulation, Vol.10, No. 6, 994 (2003).

Lowder, D.M. *et al.*, Nature **353**, 331 (1991).

Marcoux, J., Can. J. Phys., **48**, 244 (1970).

Marrone, S. *et al.*, Nucl. Inst. and Meth. A **490**, 299 (2002).

McKinsey, D.N., and Orzel, C., Nucl. Instr. and Meth. A **545**, 524 (2005a).

McKinsey, D.N. *et al.*, Phys. Rev. Lett. **95**, 111101 (2005b).

McKinsey, D.N., Talk presented in SNOLAB workshop, August 15, 2005. Online available at http://snolab2005.snolab.ca/.

MEG Collaboration, Nucl. Instr. Meth. A **503**, 290 (2003).

Milgrom, M., ApJ **270**, 371 (1983).

Miller, L.S. *et al.*, Phys. Rev., **166**, 871 (1968).

Mitchell, J.W. *et al.*, Adv. Space Res. **35**, 151 (2005).

Mitra, S., astro-ph/0409121.

Miyajima, M. *et al.*, Phys. Rev. A, **9**, 1438 (1974); Phys. Rev. A, **10**, 1452 (1974).

Miyajima, M. *et al.*, Nucl. Instr. and Meth. B **63**, 297 (1992).

Morales, A., hep-ex/0111089.

Moszynski, M. *et al.*, Nucl. Instr. and Meth. A **497**, 226 (2003).

Moulin, E. *et al.*, Phys. Lett. B **614**, 143 (2005).

Namba, T. *et al.*, in the proceedings of NOON2004 (The 4th workshop on Neutrino Oscillations and their Origins) page 387-394, February 11-15, 2004, Tokyo, Japan.

Ni, K. *et al.*, Nucl. Instr. and Meth. A, **551**, 356 (2005).

NIST STAR database: http://physics.nist.gov/PhysRefData/Star/Text/.

NIST Fluid: Thermophysical Properties of Fluid System, online: http://webbook.nist.gov/chemistry/fluid/.

Nusser, A., MNRAS **331**, 909 (2002).

Ostriker, J.P. *et al.*, ApJ **193**, L1 (1974).

Ozone, K., *Liquid Xenon Scintillation Detector for the New $\mu \rightarrow e\gamma$ Search Experiment*, Ph.D. Thesis, Department of Physics, University of Tokyo, Japan, (2005).

Pacheco, J.A.F. and Peirani, S., astro-ph/0503380.

Paling, S.M. *et al.* Nucl. Instr. and Meth. A **535**, 644 (2004).

Peccei, R.D., and Quinn, H.R., Phys. Rev. Lett. **38**, 1440 (1977).

Peacock, J.A. *et al.*, Nature **410**, 169 (2001).

Percival, W.J. *et al.*, Mon. Not. R. Astron. Soc. **327**, 1297 (2001).

Perlmutter, S. *et al.* (The Supernova Cosmology Project), ApJ **517**, 565 (1999).

PICASSO Collaboration, Phys. Lett. B **624**, 186 (2005).

Profume, S. and Ullio, P., JCAP **0311**, 006 (2003).

Readhead, A.C.S. *et al.*, Science, **306**, 836 (2004).

Salati, P., Phys. Lett. B **571**, 121 (2003).

Sanders, R.H., McGaugh, S.S., Ann. Rev. of Astron. and Astrophys. **40**, 263 (2002).

Seguinot, J. *et al.*, Nucl. Instr. and Meth. A **323**, 583 (1992).

Schmidt, W.F., *Liquid State Electronics of Insulating Liquids*, CRC Press, New York, 1997.

Schmidt, B.P. *et al.* (The High-Z Supernova Search), ApJ **507**, 46 (1998).

Seidel, G.M. *et al.*, Nucl. Instr. and Meth. A **489**, 189 (2002).

Shagin, P. *et al.*, Nucl. Instr. and Meth. A **556**, 215 (2006).

Shutt, T. *et al.*, Nucl. Instr. and Meth. A **444**, 340 (2000).

Shutt, T. *et al.*, *Measurement of low energy γ ray ionization in liquid xenon*, in preparation.

Slosar, A *et al.*, Phys. Rev. D **72**, 101301 (2005).

Smith, P.F. *et al.* Phys. Lett. B **379**, 299 (1996).

SNO Collaboration, Phys. Rev. Lett. **89**, 011301 (2002).

Snowden-Ifft, D.P. *et al.*, Phys. Rev. D **61**, 101301 (2000).

Snowden-Ifft, D.P. *et al.*, Nucl. Instr. and Meth. A **498**, 155 (2003).

Sofue, Y *et al.*, Publ. Astron. Soc. Jpn. **51**, 737 (1999).

Sofue, Y, and Rubin, V, Ann. Rev. Astron. Astrophys. **39**, 137 (2001).

Solovov, V.N. *et al.*, IEEE Trans. on Nucl. Sci., Vol. 47, No. 4, 1307 (2000).

Solovov, V.N. *et al.*, Nucl. Instr. and Meth. A **488**, 572 (2002).

Solovov, V.N. *et al.*, Nucl. Instr. and Meth. A **516**, 462 (2004).

Spergel, D.N., Phys. Rev. D **37**, 1353 (1988).

Spergel, D.N. *et al.*, Astrophys. J. Suppl. **148**, 175 (2003).

Springel, V. *et al.*, Nature **435**, 629 (2005).

SRIM website: http://www.srim.org/.

Storm, E, and Isreal, H.I., *Photon cross section from 0.001 to 100 MeV for elements 1 through 100*, Los Alamos Scientific Laboratory, LA-3753 (1967).

Super-Kamiokande Collaboration, Phys. Rev. Lett. **81**, 1562 (1998)

Takahashi, T. *et al.*, Phys. Rev. A, **12**, 1771 (1975).

Thomas, J. *et al.*, Phys. Rev. A, **38**, 5793 (1988).

Tovey, D.R. *et al.*, Phys. Lett. B **488**, 17 (2000).

Trimble, V., Ann. Rev. Astron. Astrophys. **25**, 425 (1987).

Turner, M.S., Phys. Rept. **197**, 67 (1990).

UKDMC Collaboration, in Proceedings of the 3th International Workshop on the Identification of Dark Matter, York, 2001, Eds. N. Spooner and V. Kudryavtsev, p.452.

UKDMC Collaboration, in Proceedings of the 4th International Workshop on the Identification of Dark Matter, York, 2002, Eds. N. Spooner and V. Kudryavtsev (World Scientific 2003)

UKDMC Collaboration, Phys. Lett. B **616**, 17 (2005a).

UKDMC Collaboration, Astropart. Phys. **23**, 444 (2005b).

Vergados, J.D., Phys. Rev. D **67**, 103003 (2003).

WARP Collaboration, WARP Experimental Proposal (2004), available online at http://warp.pv.infn.it/proposal.pdf.

WebElements Periodic Table, online http://www.webelements.com/.

Weekes, T.C. *et al.*, ApJ **342**, 379 (1989).

Weekes, T.C. *et al.*, Astropart. Phys. **17**, 221 (2002).

Weidner, V.R., and Hsia, J.J., J. Opt. Soc. Am. **71**, 856 (1981).

Weinberg, S., Phys. Rev. Lett. **40**, 223 (1978).

Wilczek, F., Phys. Rev. Lett. **40**, 279 (1978).

WMAP Collaboration, ApJ. Suppl., **148**, 1 (2003); ApJ. Suppl., **148**, 175 (2003).

XMASS Experiment, Suzuki, Y, hep-ph/0008296.

XENON Collaboration, Proceedings of the International Workshop on Technique and Application of Xenon Detectors (Xenon01) (2001), astro-ph/0207670.

XENON Collaboration, New Astronomy Review, **49** 289 (2005), astro-ph/0407575.

Xu, F., *Development of A LXe-TPC Compton Telescope for Gamma-Ray Astronomy*, Ph.D. Thesis, Physics Department, Columbia University (1998).

Yamashita, M., *Dark matter search experiment with double phase Xe detector*, Ph.D. Thesis, Waseda University, Japan, (2003a).

Yamashita, M. *et al.*, Astropart. Phys. **20**, 79 (2003b).

Yamashita, M. *et al.*, Nucl. Instr. and Meth. A **535**, 692 (2004).

Zwicky, F., Helv. Phys. Acta **6**, 110 (1933).